XAS studies of metal speciation in hydrothermal fluids

Yuan TIAN

B.Eng. (2007), East China University of Science and Technology, Shanghai, China

This thesis is submitted for the degree of Doctor of Philosophy
in
School of Chemical Engineering
at
The University of Adelaide

May 2013
Adelaide, Australia

Table of Contents

Abstract

Knowledge of metal speciation and thermodynamic properties underpins our capability to model metal transport and deposition in natural and engineered systems. Using synchrotron-based X-ray Absorption Spectroscopy and high temperature – high pressure experimental techniques, this project aims to elucidate nickel and manganese speciation in hydrothermal chloride solutions, and obtain the thermodynamic properties for predominant species.

Ab initio XANES simulation methods were used in this study to provide independent or complementary information about the nature (stoichiometry and geometry) of aqueous complexes. Application of this technique to the calculation of XANES spectra of Mo(VI) complexes in hydrothermal systems confirmed that $[MoO_4]^{2-}$ is stable in neutral and basic solutions over a wide range of temperature and salinity, and chlorinated Mo complexes (e.g., $[MoCl_2O_2(H_2O)_2]_{(aq)}$, $[MoOCl_4]_{(aq)}$) exist in strongly acidic solutions. XANES simulations of Te complexes added additional evidence that $[Te(OH)_3]$ and $[TeO_3]$ species predominate in basic and acidic solutions, respectively, and that the deprotonation process to convert $[Te(OH)_3]$ to $[TeO_3]$ is associated with a distance contraction for the Te-O bond.

Ni(II) speciation in hydrothermal brines was investigated over a wide range of temperatures (25-434 °C) and fluid compositions (0-7.68 m Cl^-) at 400 and 600 bar. Quantitative XAS data interpretation revealed that Ni(II) chloroaqua complexes undergo a structural transition from octahedral at room temperature to distorted tetrahedral at elevated temperatures. Both heating and an increase in salinity promote the stability of tetrahedral complexes relative to octahedral complexes. The $NiCl_{2(aq)}$ species exists in both octahedral $[NiCl_2(H_2O)_4]_{(aq)}$ and tetrahedral $[NiCl_2(H_2O)_2]_{(aq)}$ forms, with the ratio of octahedral to tetrahedral decreasing at

high temperature (> 200 °C). The highest order Ni chloride complex identified in this work is not the fully chlorinated $[NiCl_4]^{2-}$ but the tri-chloro mono-aqua complex $[NiCl_3(H_2O)]^-$, confirmed by both EXAFS analysis and XANES simulations.

A similar coordination change of Mn(II) chloroaqua complexes has been quantitatively identified by analysis of both XANES and EXAFS data collected between 30 to 550 °C at 600 bar, with chlorinity ranging from 0.100 to 10.344 m. Octahedral species predominate at room temperature within the whole salinity range and persist up to ~400 °C in low salinity solutions ($m_{Cl} < 1$ m), and tetrahedral species become significant at temperatures above 300 °C. Compared with Fe(II) chloride complexation, the octahedral to tetrahedral structural transition occurs at higher temperature for Mn(II) complexes. A combination of EXAFS refinements, Density Functional Theory calculations and *ab initio* XANES simulations confirmed that at elevated temperatures (≥ 400 °C) the highest order chloride complex predominating in highly saline brines ($m_{Cl} > 3$ m, Cl:Mn ratio > 53) is $[MnCl_3(H_2O)]^-$ with $[MnCl_4]^{2-}$ being unstable through all T-P-salinity range, while a lower order chlorocomplex, $[MnCl_2(H_2O)_2]_{(aq)}$, is the major species in low salinity solutions ($m_{Cl} < 0.5$ m, Cl:Mn ratio < 10). The differences regarding to the stoichiometry and stability of highest order metal chloride complexes identified in this study, $[NiCl_3(H_2O)]^-$ and $[MnCl_3(H_2O)]^-$, and in previous studies (i.e., $[CoCl_4]^{2-}$ and $[FeCl_4]^{2-}$) may play a role in the fractionation between metals with closely related geochemical properties in hydrothermal systems (e.g., Ni/Co; Mn/Fe).

Overall, the combination of XANES and EXAFS data provided us with a molecular level understanding of Ni and Mn speciation in hydrothermal brines and improved our capability for modeling metal mobility in the Earth's crust.

Declaration

I certify that this work contains no material which has been accepted for the award of any other degree or diploma in any university or other tertiary institution and, to the best of my knowledge and belief, contains no material previously published or written by another person, except where due reference has been made in the text. In addition, I certify that no part of this work will, in the future, be used in a submission for any other degree or diploma in any university or other tertiary institution without the prior approval of the University of Adelaide and where applicable, any partner institution responsible for the joint-award of this degree.

I give consent to this copy of my thesis when deposited in the University Library, being made available for loan and photocopying, subject to the provisions of the Copyright Act 1968.

The author acknowledges that copyright of published works contained within this thesis resides with the copyright holder(s) of those works.

I also give permission for the digital version of my thesis to be made available on the web, via the University's digital research repository, the Library catalogue and also through web search engines, unless permission has been granted by the University to restrict access for a period of time.

Signature: Date: 29-05-2013

Acknowledgements

I always feel lucky that I made the right decision to come to down under to pursue something I was really interested in 3.5 years ago, because I was introduced to a great project and some great people, although I had a steep learning curve in the beginning of this project, which is far away from what I've learnt for my undergraduate study. This PhD experience is a unique journey in my life when it comes to the final stage, and everything in the past three and a half years comes to my mind all together.

This thesis has been benefited from so many people. Firstly, I am extremely grateful to all my supervisors: A/Prof. Joël Brugger, Dr Yung Ngothai, Dr Weihua Liu, and A/Prof. Brian O'Neil for their infinite patience, invaluable discussions, unreserved help, and constant encouragement to my research. Without these key factors, this thesis would not be able to come into being.

I am particularly thankful to the scientists based in SA Museum Dr Barbara Etschmann, Prof. Allan Pring, Dr Ben McHenry, Dr Peter Elliot, Dr Mike Snow and other scientists Dr Stacey Borg, Dr Fang Xia, Dr Pascal Groundler, Dr Denis Testemale, Prof. David Sherman, Dr Yves Joly, Dr Frank Reith and PhD fellow Blake Tooth for their kind suggestions and assistances to my research and critical discussions and comments for some research articles, which significantly improved the quality of this project. I am also grateful to Jason Peak and Michael Jung, the technicians based in School of Chemical Engineering workshop, for building and maintaining the HP-HT hydrothermal autoclave for this project. I thank Nick Rae and beamline scientists Dr Bernt Johannessen, Dr Chris Glover for their contributions to the intensive experiments at Australian Synchrotron, and Dr Denis Testemale for the

experiment at ESRF. A special thank is attributed to Dr Haipeng Wang (previously Associate Professor of Curtin University of Technology), who provided valuable assistance to my PhD admission and scholarship applications, as well as suggestions of doing research. Thanks a lot to those who helped me with administrations via the School of Chemical Engineering of the University of Adelaide and Mineralogy Division of SA Museum.

I would like to acknowledge Australian Synchrotron and European Synchrotron Radiation Facility for providing precious beamtime, Australian International Synchrotron Access Program for travel funding, and iVEC for the EPIC advanced computing resource. I also acknowledge ASI scholarship from the University of Adelaide. This thesis has been examined by Prof. John Mavrogenes and Prof. Terry Seward, whose helpful reviews and comments are greatly appreciated.

Last but not least, I thank my dear wife Yuan Mei for accompanying me in Adelaide and this thesis would not be completed without her endless understanding and patience, in particular during the last six months of my PhD. I thank all my families in China for their continual encouragement and support. I wish this thesis will comfort my grandparents in the heaven.

List of publications

Part of the thesis has been published in the following peer-reviewed conference paper and abstract.

1. **Tian, Y.**, Brugger, J., Liu, W., Borg, S., Etschmann, B., O'Neill, B., Testemale, D., Hazemann, J-L., Glover, C., Ngothai, Y., Jung, M., Peak, J., 2010. High-temperature and pressure spectroscopic cell for in-situ XAS study of supercritical fluids at the Australian Synchrotron, Chemeca 2010, Adelaide, S. A., Australia. (Copyright of this paper belongs to RMIT Publishing, Appendix A)
2. **Tian, Y.**, Brugger, J., Liu, W., Etschmann, B., Borg, S., Testemale, D., O'Neill, B., Ngothai, Y., 2011. Speciation and Thermodynamic Properties of Manganese(II) and Nickel(II) Chloride Complexes in Hydrothermal Fluids: In situ XAS Study. Goldschmidt Conference Abstract, August 14-19, 2011, Prague, Czech Republic. (published in Mineralogical Magazine 75, 2011; copyright of this abstract belongs to the Mineralogical Society of Great Britain and Ireland, Appendix B)

The following peer-reviewed journal paper and manuscript are based on this PhD project, and they comprise the main body of this thesis (chapters 4 and 5):

3. **Tian, Y.**, Etschmann, B., Liu, W., Borg, S., Mei, Y., Testemale, D., O'Neill, B., Rae, N., Sherman, D.M., Ngothai, Y., Johannessen, B., Glover, C., Brugger, J., 2012. Speciation of nickel (II) chloride complexes in hydrothermal fluids: In situ XAS study. Chemical Geology 334, 345-363. (Copyright of this paper belongs to Elsevier Ltd.)
4. **Tian, Y.**, Etschmann, B., Mei, Y., Grundler, P., Testemale, D., Hazemann, J.-L., Elliott, P., Ngothai, Y., Brugger, J., Speciation and thermodynamic properties of

Manganese (II) chloride complexes in hydrothermal fluids: *in situ* XAS study. (under review for Geochimica Cosmochimica Acta)

The XANES simulation work (chapter 3) of this PhD project contributes to the following peer-reviewed research paper and manuscript:

5. Borg, S., Liu, W., Etschmann, B., **Tian, Y.**, Brugger, J., 2012. An XAS study of molybdenum speciation in hydrothermal chloride solutions from 25–385 °C and 600 bar. Geochimica et Cosmochimica Acta 92, 292-307. (Copyright of this paper belongs to Elsevier Ltd., Appendix C).
6. Grundler, P., Brugger, J., Etschmann, B., Helm, L., Liu, W., Spry, P., **Tian, Y.**, Testemale, D., Pring, A., Speciation of aqueous tellurium(IV) in hydrothermal solutions and vapors, and the role of oxidized tellurium species in gold metallogenesis. (in revision for Geochimica Cosmochimica Acta, Appendix D)

Chapter 1

Introduction

1.1 Metal speciation and hydrothermal ore deposits

Hydrothermal processes are ubiquitous in the Earth's crust and lead to the formation of hydrothermal ore deposits. In addition, many other deposit types can undergo hydrothermal alteration to varying extents that result in changes in mineralogy and in local remobilization of the metals (Robb, 2004). Hydrothermal fluids play an important role in hydrothermal ore forming process, as metals are re-distributed by hydrothermal fluids in the Earth's crust through fluid-rock interaction, transport and deposition (Seward and Barnes, 1997). In these hot aqueous fluids, metals exist mostly as metal complexes with different ligands (e.g., Cl^-, HS^-, OH^-) in very low concentrations. A single metal species may predominate, or a mixture of metal species may co-exist, depending on the temperature, pressure and fluid composition of the hydrothermal fluid. Therefore, metal speciation is a key factor in determining metal solubility and stability in hydrothermal fluids. In addition, metal speciation in hydrothermal solutions also plays an important role in man-made systems; it can control the porosity creation / destruction and scaling in geothermal and CO_2-injection wells, corrosion in power plants, and the efficiency of hydrometallurgical processes (e.g., Brugger et al. 2010; Seward and Driesner 2004).

Hydrothermal processes occur over a wide range of temperature (from room-T to above 600 °C), pressure (from atmospheric pressure to up to several kbar), and fluid chemistry (e.g., highly concentrated brines, volatile-rich low-density fluids), which leads to complex mechanisms and processes for metal precipitation and ore formation. For instance, changes of fluid environment and chemistry (e.g., cooling, dilution, decompression) may result in a change of metal speciation and a decrease of mineral solubility, thus leading to ore deposition. In order to shed light on the mechanisms and processes that cause metal precipitation and ore formation, it is critical to investigate the metal speciation that is largely responsible for metal solubility in hydrothermal fluids, and to understand the effects of physical and chemical factors (temperature, pressure and fluid composition) on metal speciation in hydrothermal systems (Seward and Barnes, 1997). Moreover, numerical modeling of metal mobility in the Earth's crust relies on a comprehensive and correct metal speciation model and the availability of reliable thermodynamic properties for each of the relevant species as a function of temperature, pressure, and fluid chemistry (Seward and Driesner, 2004; Brugger et al., 2010).

The chloride anion is one of the primary ligands in hydrothermal systems, and metal chloride complexes are important for transport of many metals (e.g, Seward and Barnes, 1997). In particular, the halide complexes of the first row transition metals, such as Fe(II), Co(II), Ni(II), and Cu(II), undertake a coordination change from octahedral to tetrahedral with increasing temperature and/or salinity which has a profound impact on the mineral solubility in the fluid, as discovered by Susak and Crerar (1985) via systematic UV-Vis experiments. In the past decade there has been an increasing number of *in situ* studies dedicated to the quantitative understanding of the speciation of chloroaqua complexes of the first row transition metals in hydrothermal fluids. These studies include an examination of chloride interactions with Fe(II) (Testemale et al., 2009), Co(II) (Liu et al., 2011), Cu(II) (Brugger et al., 2001; Trevani et al., 2010), and interactions of chloride and bromide with Zn(II) (Anderson et al., 1998; Mayanovic et al., 1999, 2001; Mibe et al., 2009; Liu et al., 2007, 2012), which have greatly improved our understanding of the transport and deposition of these first row transition metals in hydrothermal fluids by molecular level understanding of metal halide complexation and geological implications of these new findings.

A number of previous studies examining Ni(II) and Mn(II) chloride coordination have been carried out in order to understand the mobility of Ni and Mn in the Earth's crust. There is general agreement that higher order Mn and Ni chloride complexes (e.g., $NiCl^+$, $NiCl_{2(aq)}$, $MnCl^+$, and $MnCl_{2(aq)}$) become more important with increasing temperature and Cl^- concentration (e.g., Lüdemann and Franck, 1968; Susak and Crerar, 1985; Gammons and Seward, 1996; Suleimenov and Seward, 2000; Suleimenov, 2004). However, most of these speciation/solubility studies were limited to *ex situ* solubility measurements, confined P-T-salinity range, and suffered from unavailability of molecular level characterization of the nature (stoichiometry and geometry) and thermodynamic properties of Ni and Mn chloride complexes. The main discrepancy among these studies lies in the assigned speciation and thermodynamic models, in particular the nature and stability of predominant tetrahedral Ni and Mn chloride complexes at elevated temperature and pressure (e.g., Lin and Popp, 1984; Fahlquist and Popp, 1989; Boctor, 1985; Uchida et al., 1995, 1996, 2003; Uchida and Tsutsui, 2000). Thus there is still some controversy over the exact speciation of Ni and Mn chloroaqua complexes with varying temperature, pressure, fluid composition. Recent *in situ* XAS studies of Ni-Br and Mn-Br complexation (Wallen et al., 1998; Hoffmann et al., 1999; Chen et al., 2005) investigated the structural transition of Ni and Mn bromide complexes with increasing temperature. However, chloride (Cl) is the most abundant ligand in many geological fluids, and Seward and Barnes (1997) suggested that chloride complexes are the main species responsible for Ni and Mn transport in the Earth's crust. The lack of XAS studies for Mn-Cl and Ni-Cl complexation has hindered our understanding of Ni and Mn speciation in hydrothermal brines and our capability of modelling Ni and Mn mobility in hydrothermal fluids.

1.2 Research objectives

This project aims to achieve a molecular level understanding of manganese and nickel speciation in hydrothermal chloride solutions over a wide range of conditions (from ambient to supercritical) using x-ray absorption spectroscopy. The main objectives of the project are:

1) Document the effects of temperature and salinity on the speciation of Ni(II) and Mn(II) chloroaqua complexes.

2) Constrain the nature (stoichiometry and geometry) of Ni(II) and Mn(II) chloroaqua complexes at elevated temperatures and pressures using a combination of XAS data processing strategies and Density Functional Theory calculations.

3) Derive formation constants of nickel and manganese chloride complexes in Cl-rich fluids, based on the new information derived in 2), and regress HKF or MRB parameters of these metal species for a wide range of P-T.

4) Obtain a better understanding of Ni and Mn mobility in the Earth's crust.

1.3 Experimental approaches and advances of XAS technology

Over the past several decades, numerous studies have been conducted to investigate the properties of hydrothermal solutions and to measure metal speciation and mineral solubility at elevated temperatures as reviewed by Sverjensky et al. (1997), Seward and Barnes (1997), Wood and Samson (1998), Seward and Driesner (2004) and Oelkers et al. (2009). In these experimental studies, the changes of metal speciation and coordination in aqueous solutions as a function of temperature, pressure, and fluid composition of interest are investigated by several experimental techniques, e.g., solubility experiments, UV-Vis (Ultraviolet-Visible) spectroscopy, XAS (x-ray absorption spectroscopy) spectroscopy, etc.

Solubility experiments have been the most commonly used technique in the past several decades for examining the behaviour of metals under hydrothermal conditions in order to better understand the formation of ore deposits (e.g., Wood and Samson, 1998; McKibben and Williams, 1989). Given the known chemical composition of starting materials in both the solid (often metal oxide or sulfide crystals) and the liquid phase (often S- or Cl-bearing solutions), solubility experiments measure the dissolved metal concentration at equilibrium conditions. Therefore, the stoichiometries and stability constants of metal speciation can be determined by dissolved metal concentration as a function of physical and chemical variables (e.g., ligand concentration, pH, temperature, pressure) (e.g., Fleet and Knipe, 2000; Gammons and Barnes, 1989; Gammons and Seward, 1996; Hayashi et al, 1990; McKibben and Williams, 1989; Palmer et al., 2011; Stefánsson and Seward 2003, 2004; Shenberger and Barnes, 1989; Simon et al, 2004; Ziemniak and Goyette, 2004). The effects of ligand concentration on metal speciation were measured at elevated temperature by varying ligand:metal molal ratios (e.g., Fahlquist and Popp, 1989; Uchida et al., 1995; Tagirov et al., 2007). The effects of pH and redox condition on mineral solubility were examined in many solubility studies (e.g., Wesolowski et al., 1998; Krupp, 1988; Mountain and Seward, 1999; Palmer et al., 2011). Synthetic fluid inclusions were also studied to measure metal solubility at elevated temperatures and pressures (e.g., Hack and Mavrogenes, 2006; Duc-Tin et al., 2007). However, the lack of structural information makes direct application of solubility data to thermodynamic modelling difficult. Hence, solubility experiments are often combined with spectroscopic methods, such as UV-Vis and XAS spectroscopy (e.g., Bazarkina et al., 2010; Migdisov et al., 2011; Ulrich and Mavrogenes, 2008).

UV-Vis spectroscopy is an important method applied to investigate *in situ* metal speciation at elevated temperature and pressure. Several HP-HT UV-Vis solution cells have been built for *in situ* UV-Vis spectroscopic studies of metal complexes at elevated temperatures (e.g., Migdisov and Williams-Jones, 2002; Suleimenov, 2004). Susak and Crerar (1985) have reported the coordination changes for Fe(II), Co(II), Ni(II) and Cu(II) chloride complexes by analyzing UV-Vis spectral changes upon increasing temperature and salinity. Similar UV-Vis measurements have been conducted to investigate metal speciation as a function of temeprature, pressure, pH, ligand concentration (e.g., Pan and Susak 1989; Heinrich and Seward, 1990; Suleimenov and Seward, 2000). However, UV-Vis spectroscopy is affected by the deviation from Beer-Lambert law due to the change in the refractive index of solvent, which may affect the accuracy for concentrated electrolytes (e.g., Vinokurov and Kankare 1998). In addition, the detailed information of the geometry and stoichiometry of metal species is not fully retrievable from UV-Vis data. Potentiometric experiments and Raman spectroscopy have also been employed to study metal speciation and to measure equilibrium constants of aqueous species at elevated temperatures (e.g., Bénézeth and Palmer, 2000; Mibe et al., 2009). However, like solubility experiments and UV-Vis spectroscopy, these techniques are limited by the unavailability of full geometric characterization of metal complexes.

The advance of third generation synchrotron radiation facilities over the past two decades makes x-ray absorption spectroscopy (XAS) a powerful experimental technique. Since the principles of XAS theory have been provided in great detail in the literature (e.g., Bunker, 2010; Teo, 1986), and its application to soil and mineral analysis discussed by Kelly et al. (2008), only a brief introduction of the advantages of XAS technology is given here: (1) XAS is element selective, hence minimizing the interference from other components of the sample; (2) the focused and tunable synchrotron x-ray source has high brightness, tight collimation and polarization, is well-suited for investigations on dilute sample solutions (metal concentrations << 1 wt%); (3) XAS technology can be applied to samples in any physical state (solid, liquid and vapour), enabling *in situ* data acquisition from ambient to supercritical conditions; (4) XAS exploits the quantum interference resulting from the scattering of a photoelectron (generated by the excitation of a core level electron) by the potential of the surrounding atoms. This scattering is sensitive to the distance, atomic weight and average distribution of the nearest neighbours from the photo-absorbing atom (Filipponi, 2001), providing a molecular level understanding of coordination chemistry: EXAFS quantifies coordination number, identity of neighbouring ligands and distance to neighbours around the absorbing atom while XANES is particular sensitive to the valence state, local electronic structure and symmetry; (5) XAS is not influenced by the deviation from Beer-Lambert law for concentrated solutions compared with UV-Vis spectroscopy, ensuring higher data quality and better experimental precision over wide range of fluid composition (e.g., $\geqslant$ 15 m Cl^-). Combined with novel high-pressure high-temperature experimental cells (e.g., Testemale et al., 2005), XAS is increasingly and extensively used for *in situ* experiments, which allow metal speciation to be investigated over a wide range of conditions (P, T and composition) (e.g., Seward et al, 1996; Pokrovski et al, 2000). It is also possible to use XAS techniques to determinine mineral solubility *in situ,* as well as liquid-vapour partitioning co-efficients by measuring the x-ray absorption in the liquid and vapour phase separately (e.g., Pokrovski et al., 2005; Liu et al., 2008). The results gained via conventional techniques (e.g., solubility experiments, UV-Vis spectroscopy) are often combined with structural data determined from XAS methods to get more precise overall picture of speciation and thermodynamic properties for aqueous metal species (e.g., Etschmann et al., 2011; Liu et al., 2006; Migdisov et al., 2011).

Recent XAS studies have greatly improved our understanding of metal speciation in hydrothermal fluids. For example, in the case of Fe(II) speciation in hydrothermal brines, most solubility studies concluded that $FeCl_{2(aq)}$ was the highest order complex at elevated temperature even in concentrated brines (e.g., Ding and Seyfried, 1992; Fein et al., 1992; Ohmoto et al., 1994). Using XAS spectroscopy, Liu et al. (2007) and Testemale et al. (2009) detected the strong stability of the tetrahedral $FeCl_4^{2-}$ complex and derived formation constants by extending experimental conditions to a higher T-P-salinity range (450 °C, 500 bar, 12 m Cl^-). The speciation and thermodynamic properties of Cu(I) chloride complexes in the past decade provide another illustration of the power of XAS for hydrothermal studies. Solubility and UV-Vis experiments were carried out to investigate Cu(I) speciation in hydrothermal brines, and to obtain thermodynamic properties of a series of copper species - $CuCl_n^{1-n}$ (n=1, 2, 3, 4) (e.g., Xiao et al., 1998; Liu et al., 2001, 2002, 2005). However, the tetrahedral $CuCl_4^{3-}$ was proved to be unstable and the linear $CuCl_2^-$ predominates copper speciation at elevated temperatures (> 200 °C) with $CuCl_3^{2-}$ playing a minor role in chloride-rich brines at low temperature according to several *in situ* XAS studies (Berry et al., 2006, 2009; Brugger et al., 2007; Fulton et al., 2000a, b; Mavrogenes et al., 2002). These XAS results were also confirmed by Molecular Dynamics simulation (Sherman 2007). Hence, the new Cu(I) speciation model was used to re-interpret the earlier solubility and UV-Vis data to obtain new thermodynamic properties for each copper species (e.g., Brugger et al,. 2007). These new discoveries reconstructed Fe and Cu speciation in hydrothermal brines and provided more reliable thermodynamic properties for their aqueous metal species, thus improving our understanding of Fe and Cu mobility in hydrothermal systems.

Overall, XAS spectroscopy is a powerful technique, providing molecular level information for the nature (geometry and stoichiometry) of metal species over a wide range of conditions. This technique, with its unique advantages, complements the conventional experimental techniques (e.g., solubility experiment and UV-Vis spectroscopy), and is particularly suitable for investigation of metal speciation under hydrothermal-magmatic conditions. In this project, *in situ* XAS will be used for the investigation of Ni and Mn speciation of chloroaqua complexes from ambient to hydrothermal conditions.

1.4 Thesis organization

To perform *in situ* XAS experiments and collect high quality XAS data at synchrotron radiation facilities, a HP-HT cell (mAESTRO autoclave) was designed and constructed in partnership between the University of Adelaide, CSIRO, and CNRS (Grenoble) scientists. The detailed information of the mAESTRO autoclave and the commissioning experiment for Ni chloride sample solutions at the XAS beamline of Australian Synchrotron is described in chapter 2, which is based on the paper presented at the Chemeca 2010 conference (appendix A, related publications of this project are included as appendices).

The main body of the thesis consists of chapters 3, 4 and 5. Chapter 3 describes the use of *ab initio* methods to calculate XANES spectra for solid standards and aqueous metal complexes, and highlights the significance of investigating metal speciation using the XANES region as independent or complementary information compared to the EXAFS region. This chapter is mainly based on the results of *ab initio* XANES simulations for metal solid compounds and aqueous complexes that comprise two journal papers and two manuscripts (see appendices C and D). Chapter 4 is dedicated to a molecular level understanding of Ni-Cl complexation in hydrothermal brines, and is directly based on appendix D. In a similar manner, chapter 5 provides *in situ* XAS investigation of Mn-Cl and Mn-Br complexing from ambient to supercritical conditions (550 °C, 600 bar, 0.100-10.344 m Cl and 0.110 – 2.125 m Br). This chapter is based on a manuscript to be submitted to a geochemistry journal. The final conclusions and future works are discussed in chapter 6.

1.5 References

Anderson, A. J., Mayanovic, R. A., and Bajt, S., 1998. A microbeam XAFS study of aqueous chlorozinc complexing to 430 °C in fluid inclusions from the Knaumuehle granitic pegmatite, Saxonian granulite massif, Germany. *The Canadian Mineralogist* **36**, 511-524.

Bazarkina, E. F., Pokrovski, G. S., Zotov, A. V., and Hazemann, J.-L., 2010. Structure and stability of cadmium chloride complexes in hydrothermal fluids. *Chemical Geology* **276**, 1-17.

Bénézeth, P. and Palmer, D. A., 2000. Potentiometric determination of cadmium–acetate complexation in aqueous solutions to 250 °C. *Chemical Geology* **167**, 11-24.

Berry, A. J., Hack, A. C., Mavrogenes, J. A., Newville, M., and Sutton, S. R., 2006. A XANES study of Cu speciation in high-temperature brines using synthetic fluid inclusions. *American Mineralogist* **91**, 1773-1782.

Berry, A. J., Harris, A. C., Kamenetsky, V. S., Newville, M., and Sutton, S. R., 2009. The speciation of copper in natural fluid inclusions at temperatures up to 700 °C. *Chemical Geology* **259**, 2-7.

Boctor, N. Z., 1985. Rhondonite solubility and thermodynamic properties of aqueous $MnCl_2$ in the system $MnO-SiO_2-HCl-H_2O$. *Geochimica et Cosmochimica Acta* **49**, 565-575.

Brugger, J., Etschmann, B., Liu, W., Testemale, D., Hazemann, J. L., Emerich, H., van Beek, W., and Proux, O., 2007. An XAS study of the structure and thermodynamics of Cu(I) chloride complexes in brines up to high temperature (400 °C, 600 bar). *Geochimica et Cosmochimica Acta* **71**, 4920-4941.

Brugger, J., McPhail, D. C., Black, J., and Spiccia, L., 2001. Complexation of metal ions in brines: application of electronic spectroscopy in the study of the Cu(II)-LiCl-H_2O system between 25 and 90 °C. *Geochimica et Cosmochimica Acta* **65**, 2691-2708.

Brugger, J., Pring, A., Reith, F., Ryan, C., Etschmann, B., Liu, W., O'Neill, B., and Ngothai, Y., 2010. Probing ore deposits formation: New insights and challenges from synchrotron and neutron studies. *Radiation Physics and Chemistry* **79**, 151-161.

Bunker, G., 2010. *Introduction to XAFS: a practical guide to X-ray absorption fine structure spectroscopy*. Cambridge University Press Cambridge, UK.

Chen, Y., Fulton, J. L., and Partenheimer, W., 2005. The Structure of the Homogeneous Oxidation Catalyst, $Mn(II)(Br^{-1})_x$, in Supercritical Water: An X-ray Absorption Fine-Structure Study. *Journal of the American Chemical Society* **127**, 14085-14093.

Ding, K. and Seyfried Jr, W. E., 1992. Determination of Fe-Cl complexing in the low pressure supercritical region (NaCl fluid): Iron solubility constraints on pH of subseafloor hydrothermal fluids. *Geochimica et Cosmochimica Acta* **56**, 3681-3692.

Duc-Tin, Q., Audétat, A., and Keppler, H., 2007. Solubility of tin in (Cl, F)-bearing aqueous fluids at 700 °C, 140 MPa: A LA-ICP-MS study on synthetic fluid inclusions. *Geochimica et Cosmochimica Acta* **71**, 3323-3335.

Etschmann, B. E., Black, J. R., Grundler, P. V., Borg, S., Brewe, D., McPhail, D. C., Spiccia, L., and Brugger, J., 2011. Copper(I) speciation in mixed thiosulfate-chloride and ammonia-chloride solutions: XAS and UV-Visible spectroscopic studies. *RSC Advances* **1**, 1554-1566.

Fahlquist, L. S. and Popp, R. K., 1989. The effect of NaCl on bunsenite solubility and Ni-complexing in supercritical aqueous fluids. *Geochimica et Cosmochimica Acta* **53**, 989-995.

Fein, J. B., Hemley, J. J., D'Angelo, W. M., Komninou, A., and Sverjensky, D. A., 1992. Experimental study of iron-chloride complexing in hydrothermal fluids. *Geochimica et Cosmochimica Acta* **56**, 3179-3190.

Filipponi, A., 2001. EXAFS for liquids. *Journal of Physics: Condensed Matter* **13**, R23.

Fleet, M. E. and Knipe, S. W., 2000. Solubility of Native Gold in H-O-S Fluids at 100–400 °C and High H_2S Content. *Journal of Solution Chemistry* **29**, 1143-1157.

Fulton, J. L., Hoffmann, M. M., and Darab, J. G., 2000a. An X-ray absorption fine structure study of copper(I) chloride coordination structure in water up to 325 °C. *Chemical Physics Letters* **330**, 300-308.

Fulton, J. L., Hoffmann, M. M., Darab, J. G., Palmer, B. J., and Stern, E. A., 2000b. Copper(I) and Copper(II) Coordination Structure under Hydrothermal Conditions at 325 °C: An X-ray Absorption Fine Structure and Molecular Dynamics Study. *The Journal of Physical Chemistry A* **104**, 11651-11663.

Gammons, C. H. and Barnes, H. L., 1989. The solubility of Ag_2S in near-neutral aqueous sulfide solutions at 25 to 300 °C. *Geochimica et Cosmochimica Acta* **53**, 279-290.

Gammons, C. H. and Seward, T. M., 1996. Stability of manganese (II) chloride complexes from 25 to 300 °C. *Geochimica et Cosmochimica Acta* **60**, 4295-4311.

Hack, A. C. and Mavrogenes, J. A., 2006. A synthetic fluid inclusion study of copper solubility in hydrothermal brines from 525 to 725 °C and 0.3 to 1.7 GPa. *Geochimica et Cosmochimica Acta* **70**, 3970-3985.

Hayashi, K., Sugaki, A., and Kitakaze, A., 1990. Solubility of sphalerite in aqueous sulfide solutions at temperatures between 25 and 240 °C. *Geochimica et Cosmochimica Acta* **54**, 715-725.

Heinrich, C. A. and Seward, T. M., 1990. A spectrophotometric study of aqueous iron (II) chloride complexing from 25 to 200 °C. *Geochimica et Cosmochimica Acta* **54**, 2207-2221.

Hoffmann, M. M., Darab, J. G., Palmer, B. J., and Fulton, J. L., 1999. A transition in the Ni^{2+} complex structure from six-to four-coordinate upon formation of ion pair species in supercritical water: An X-ray absorption fine structure, near-infrared, and molecular dynamics study. *The Journal of Physical Chemistry A* **103**, 8471-8482.

Kelly, S., Hesterberg, D., Ravel, B., Ulery, A., and Drees, L., 2008. Analysis of soils and minerals using X-ray absorption spectroscopy. *Methods of soil analysis. Part* **5**, 387-463.

Krupp, R. E., 1988. Solubility of stibnite in hydrogen sulfide solutions, speciation, and equilibrium constants, from 25 to 350 °C. *Geochimica et Cosmochimica Acta* **52**, 3005-3015.

Lin, S. and Popp, R. K., 1984. Solubility and complexing of Ni in the system $NiO-H_2O-HCl$. *Geochimica et Cosmochimica Acta* **48**, 2713-2722.

Liu, W., Borg, S., Etschmann, B., Mei, Y., and Brugger, J., 2012. An XAS study of speciation and thermodynamic properties of aqueous zinc bromide complexes at 25–150 °C. *Chemical Geology* **298–299**, 57-69.

Liu, W., Borg, S. J., Testemale, D., Etschmann, B., Hazemann, J.-L., and Brugger, J., 2011. Speciation and thermodynamic properties for cobalt chloride complexes in hydrothermal fluids at 35–440 °C and 600 bar: An in-situ XAS study. *Geochimica et Cosmochimica Acta* **75**, 1227-1248.

Liu, W., Brugger, J., Etschmann, B., Testemale, D., and Hazemann, J. L., 2008. The solubility of nantokite ($CuCl_{(s)}$) and Cu speciation in low-density fluids near the critical isochore: An in-situ XAS study. *Geochimica et Cosmochimica Acta* **72**, 4094-4106.

Liu, W., Brugger, J., McPhail, D. C., and Spiccia, L., 2002. A spectrophotometric study of aqueous copper(I)-chloride complexes in LiCl solutions between 100 °C and 250 °C. *Geochimica et Cosmochimica Acta* **66**, 3615-3633.

Liu, W., Etschmann, B., Brugger, J., Spiccia, L., Foran, G., and McInnes, B., 2006. UV-Vis spectrophotometric and XAFS studies of ferric chloride complexes in hyper-saline LiCl solutions at 25-90 °C. *Chemical Geology* **231**, 326-349.

Liu, W., Etschmann, B., Foran, G., Shelley, M., and Brugger, J., 2007. Deriving formation constants for aqueous metal complexes from XANES spectra: Zn^{2+} and Fe^{2+} chloride complexes in hypersaline solutions. *American Mineralogist* **92**, 761-770.

Liu, W. and McPhail, D. C., 2005. Thermodynamic properties of copper chloride complexes and copper transport in magmatic-hydrothermal solutions. *Chemical Geology* **221**, 21-39.

Liu, W., McPhail, D. C., and Brugger, J., 2001. An experimental study of copper(I)-chloride and copper(I)-acetate complexing in hydrothermal solutions between 50 °C and 250 °C and vapor-saturated pressure. *Geochimica et Cosmochimica Acta* **65**, 2937-2948.

Lüdemann, H. D. and Franck, E. U., 1968. Absorptionsspektren bei hohen Drucken und Temperaturen. II [1] Kobalt(II)- und Nickel(II)-halogenide in konzentrierten Alkalihalogenid-Lösungen. *Berichte der Bunsengesellschaft für physikalische Chemie* **72**, 514-523.

Mavrogenes, J. A., Berry, A. J., Newville, M., and Sutton, S. R., 2002. Copper speciation in vapor-phase fluid inclusions from the Mole Granite, Australia. *American Mineralogist* **87**, 1360-1364.

Mayanovic, R. A., Anderson, A. J., Bassett, W. A., and Chou, I., 1999. XAFS measurements on zinc chloride aqueous solutions from ambient to supercritical conditions using the diamond anvil cell. *Journal of Synchrotron Radiation* **6**, 195-197.

Mayanovic, R. A., Anderson, A. J., Bassett, W. A., and Chou, I. M., 2001. Hydrogen bond breaking in aqueous solutions near the critical point. *Chemical Physics Letters* **336**, 212-218.

McKibben, M. A. and Williams, A. E., 1989. Metal speciation and solubility in saline hydrothermal fluids; an empirical approach based on geothermal brine data. *Economic Geology* **84**, 1996-2007.

Mibe, K., Chou, I. M., Anderson, A. J., Mayanovic, R. A., and Bassett, W. A., 2009. The speciation of aqueous zinc(II) bromide solutions to 500 °C and 900 MPa determined using Raman spectroscopy. *Chemical Geology* **259**, 48-53.

Migdisov, A. A. and Williams-Jones, A. E., 2002. A spectrophotometric study of neodymium(III) complexation in chloride solutions. *Geochimica et Cosmochimica Acta* **66**, 4311-4323.

Migdisov, A. A., Zezin, D., and Williams-Jones, A. E., 2011. An experimental study of Cobalt (II) complexation in Cl^- and H_2S-bearing hydrothermal solutions. *Geochimica et Cosmochimica Acta* **75**, 4065-4079.

Mountain, B. W. and Seward, T. M., 1999. The hydrosulphide/sulphide complexes of copper(I): experimental determination of stoichiometry and stability at 22 °C and reassessment of high temperature data. *Geochimica et Cosmochimica Acta* **63**, 11-29.

Oelkers, E. H., Bénézeth, P., and Pokrovski, G. S., 2009. Thermodynamic Databases for Water-Rock Interaction. *Reviews in Mineralogy and Geochemistry* **70**, 1-46.

Ohmoto, H., Hayashi, K.-I., and Kajisa, Y., 1994. Experimental study of the solubilities of pyrite in NaCl-bearing aqueous solutions at 250–350 °C. *Geochimica et Cosmochimica Acta* **58**, 2169-2185.

Palmer, D. A., Benezeth, P., Xiao, C. B., Wesolowski, D. J., and Anovitz, L. M., 2011. Solubility Measurements of Crystalline NiO in Aqueous Solution as a Function of Temperature and pH. *Journal of Solution Chemistry* **40**, 680-702.

Pan, P. and Susak, N. J., 1989. Co(II)-chloride and -bromide complexes in aqueous solutions up to 5 m NaX and 90 °C: Spectrophotometric study and geological implications. *Geochimica et Cosmochimica Acta* **53**, 327-341.

Pokrovski, G. S., Martin, F., Hazemann, J.-L., and Jacques, S., 2000. An X-ray absorption fine structure spectroscopy study of germanium-organic ligand complexes in aqueous solution. *Chemical Geology* **163**, 151-165.

Pokrovski, G. S., Roux, J., Hazemann, J.-L., and Testemale, D., 2005. An X-ray absorption spectroscopy study of argutite solubility and aqueous Ge(IV) speciation in hydrothermal fluids to 500 °C and 400 bar. *Chemical Geology* **217**, 127-145.

Robb, L., 2004. *Introduction to ore-forming processes*. Wiley-Blackwell, pp. 129-174

Seward, T., Henderson, C., Charnock, J., and Dobson, B., 1996. An X-ray absorption (EXAFS) spectroscopic study of aquated Ag^+ in hydrothermal solutions to 350 °C. *Geochimica et Cosmochimica Acta* **60**, 2273-2282.

Seward, T. M. and Barnes, H. L., 1997. Metal transport by hydrothermal ore fluids. In: Barnes, H. L. (Ed.), *Geochemistry of Hydrothermal Ore Deposits*. Wiley, New York.

Seward, T. M. and Driesner, T., 2004. Hydrothermal solution structure: Experiments and computer simulations. In: Donald, A. P., Roberto, F.-P., and Allan, H. H. Eds.), *Aqueous Systems at Elevated Temperatures and Pressures*. Academic Press, London.

Shenberger, D. M. and Barnes, H., 1989. Solubility of gold in aqueous sulfide solutions from 150 to 350 °C. *Geochimica et Cosmochimica Acta* **53**, 269-278.

Sherman, D. M., 2007. Complexation of Cu^+ in Hydrothermal NaCl Brines: Ab initio molecular dynamics and energetics. *Geochimica et Cosmochimica Acta* **71**, 714-722.

Simon, A. C., Pettke, T., Candela, P. A., Piccoli, P. M., and Heinrich, C. A., 2004. Magnetite solubility and iron transport in magmatic-hydrothermal environments. *Geochimica et Cosmochimica Acta* **68**, 4905-4914.

Stefánsson, A. and Seward, T. M., 2003. Stability of chloridogold(I) complexes in aqueous solutions from 300 to 600 °C and from 500 to 1800 bar. *Geochimica et Cosmochimica Acta* **67**, 4559-4576.

Stefánsson, A. and Seward, T. M., 2004. Gold(I) complexing in aqueous sulphide solutions to 500 °C at 500 bar. *Geochimica et Cosmochimica Acta* **68**, 4121-4143.

Suleimenov, O. and Seward, T., 2000. Spectrophotometric measurements of metal complex formation at high temperatures: the stability of Mn (II) chloride species. *Chemical Geology* **167**, 177-192.

Suleimenov, O. M., 2004. Simple, compact, flow-through, high temperature high pressure cell for UV-Vis spectrophotometry. *Review of Scientific Instruments* **75**, 3363-3364.

Susak, N. J. and Crerar, D. A., 1985. Spectra and coordination changes of transition metals in hydrothermal solutions: Implications for ore genesis. *Geochimica et Cosmochimica Acta* **49**, 555-564.

Sverjensky, D. A., Shock, E. L., and Helgeson, H. C., 1997. Prediction of the thermodynamic properties of aqueous metal complexes to 1000 °C and 5 kb. *Geochimica et Cosmochimica Acta* **61**, 1359-1412.

Tagirov, B. R., Suleimenov, O. M., and Seward, T. M., 2007. Zinc complexation in aqueous sulfide solutions: Determination of the stoichiometry and stability of complexes via ZnS(cr) solubility measurements at 100 °C and 150 bars. *Geochimica et Cosmochimica Acta* **71**, 4942-4953.

Teo, B. K., 1986. *EXAFS: basic principles and data analysis*. Springer-Verlag, Berlin.

Testemale, D., Argoud, R., Geaymond, O., and Hazemann, J. L., 2005. High pressure/high temperature cell for x-ray absorption and scattering techniques. *Review of Scientific Instruments* **76**, 043905.

Testemale, D., Brugger, J., Liu, W., Etschmann, B., and Hazemann, J. L., 2009. In-situ X-ray absorption study of Iron (II) speciation in brines up to supercritical conditions. *Chemical Geology* **264**, 295-310.

Trevani, L., Ehlerova, J., Sedlbauer, J., and Tremaine, P. R., 2010. Complexation in the Cu(II)–LiCl–H_2O system at temperatures to 423K by UV-Visible spectroscopy. *International Journal of Hydrogen Energy* **35**, 4893-4900.

Uchida, E., Goryozono, Y., and Naito, M., 1996. Aqueous speciation of magnesium, strontium, nickel and cobalt chlorides in hydrothermal solutions at 600 °C and 1 kbar. *Geochemical Journal* **30**, 99-109.

Uchida, E., Goryozono, Y., Naito, M., and Yamagami, M., 1995. Aqueous speciation of iron and manganese chlorides in supercritical hydrothermal solutions. *Geochemical Journal* **29**, 175-188.

Uchida, E., Haitani, T., Suetsugu, T., Kashima, T., and Tsutsui, K., 2003. Experiments on the Element Distribution between the Granodiorite JG-1a and 2M NaCl Hydrothermal Solution at Temperatures of 300 to 800 °C and a Pressure of 1 kb. *Resource Geology* **53**, 155-161.

Uchida, E. and Tsutsui, K., 2000. Cation Leaching from the Basalt JB–1a by 2M NaCl Hydrothermal Solutions. *Resource Geology* **50**, 93-102.

Ulrich, T. and Mavrogenes, J., 2008. An experimental study of the solubility of molybdenum in H_2O and KCl–H_2O solutions from 500 °C to 800 °C, and 150 to 300 MPa. *Geochimica et Cosmochimica Acta* **72**, 2316-2330.

Vinokurov, I. A. and Kankare, J., 1998. Beer's law and the Isosbestic Points in the Absorption Spectra of Conductive Polymers. *The Journal of Physical Chemistry B* **102**, 1136-1140.

Wallen, S. L., Palmer, B. J., and Fulton, J. L., 1998. The ion pairing and hydration structure of Ni in supercritical water at 425 °C determined by x-ray absorption fine structure and molecular dynamics studies. *The Journal of chemical physics* **108**, 4039-4046.

Wesolowski, D. J., Bénézeth, P., and Palmer, D. A., 1998. ZnO Solubility and Zn^{2+} Complexation by Chloride and Sulfate in Acidic Solutions to 290 °C with In-Situ pH Measurement. *Geochimica et Cosmochimica Acta* **62**, 971-984.

Wood, S. and Samson, I., 1998. Solubility of ore minerals and complexation of ore metals in hydrothermal solutions. *Reviews in Economic Geology* **10**, 33-80.

Xiao, Z., Gammons, C. H., and Williams-Jones, A. E., 1998. Experimental study of copper(I) chloride complexing in hydrothermal solutions at 40 to 300 °C and saturated water vapor pressure. *Geochimica et Cosmochimica Acta* **62**, 2949-2964.

Ziemniak, S. and Goyette, M., 2004. Nickel (II) oxide solubility and phase stability in high temperature aqueous solutions. *Journal of Solution Chemistry* **33**, 1135-1159.

Chapter 2

XAS spectroscopy of solutions at high P-T: the mAESTRO autoclave[*]

[*]This chapter is mainly based on the following paper:

Tian, Y., Brugger, J., Liu, W., Borg, S., Etschmann, B., O'Neill, B., Testemale, D., Hazemann, J-L., Glover, C., Ngothai, Y., Jung, M., Peak, J., 2010. High-temperature and pressure spectroscopic cell for *in-situ* XAS study of supercritical fluids at the Australian Synchrotron, Chemeca 2010, Adelaide, S. A., Australia.

(Copyright of this paper belongs to RMIT Publishing, Appendix A)

2.1 Introduction

The development of third generation synchrotron sources has provided advanced beam techniques to characterise the structure of matters in different states, e.g., disordered state under extreme conditions. To investigate the structure of hydrothermal fluids, special devices are required to achieve high pressure and high temperature sample environment corresponding to natural hydrothermal conditions and these devices need to be installed at XAS beamlines of synchrotron facilities in order to undertake *in situ* XAS experiments over wide range of conditions.

Two main types of experimental devices have been used for *in situ* XAS measurements under hydrothermal conditions in the past two decades. (i) The Hydrothermal Diamond Anvil Cell (HyDAC) (e.g., Bassett et al., 1993; Bassett et al., 2000; Chou et al., 2008) is capable of higher temperature and especially pressure (up to >8000 bar) than other XAS cells. Its limitations are the minuscule volume (< 0.1 μl), the high attenuation of X-ray by diamond, and the difficulty to control pressure accurately. (ii) Various autoclave cells (e.g., Fulton et al., 2001; Fulton et al., 2004; Seward et al., 1996; Tamura et al., 1995; Testemale et al., 2005) offer easy sample loading, flexible geometric design and accurate control over temperature and pressure but they are usually limited to lower pressures (≤ 2000 bar).

A hydrothermal XAS cell named mAESTRO (Australian Extreme SpecTROscopy) was developed in partnership between the University of Adelaide, CSIRO (Australia) and the Centre National de la Recherche Scientifique (CNRS, France) based on the design of Testemale et al. (2005). This system can provide near-routine capability for the XAS investigation of solutions up to 800 ˚C and 600 bar. In this chapter, the setup is described in section 2.2 and the commissioning of this system at the Australian Synchrotron and preliminary results are reported in section 2.3. This chapter is based on Tian et al. (2010) (see appendix A).

2.2 Instrument description

The mAESTRO system consists of a stainless steel autoclave with an internal sample cell, a pressure generation and regulation unit, a temperature controlling system and a controlling PC (Figure 2.1). The external water-cooled and internally heated autoclave is the core of the system. The pressure within the autoclave is transmitted to the sample via a set of two moving pistons inside the sample cell. The heat transfer to the sample cell is achieved by an internal wire-coil heater in the heating block. This set-up enables the temperature and pressure to be adjusted independently. The system is designed to provide steady temperatures and pressures over 10's of minutes to hours, a feature critical for enabling collection of high-quality XAS data, especially for low-density fluids.

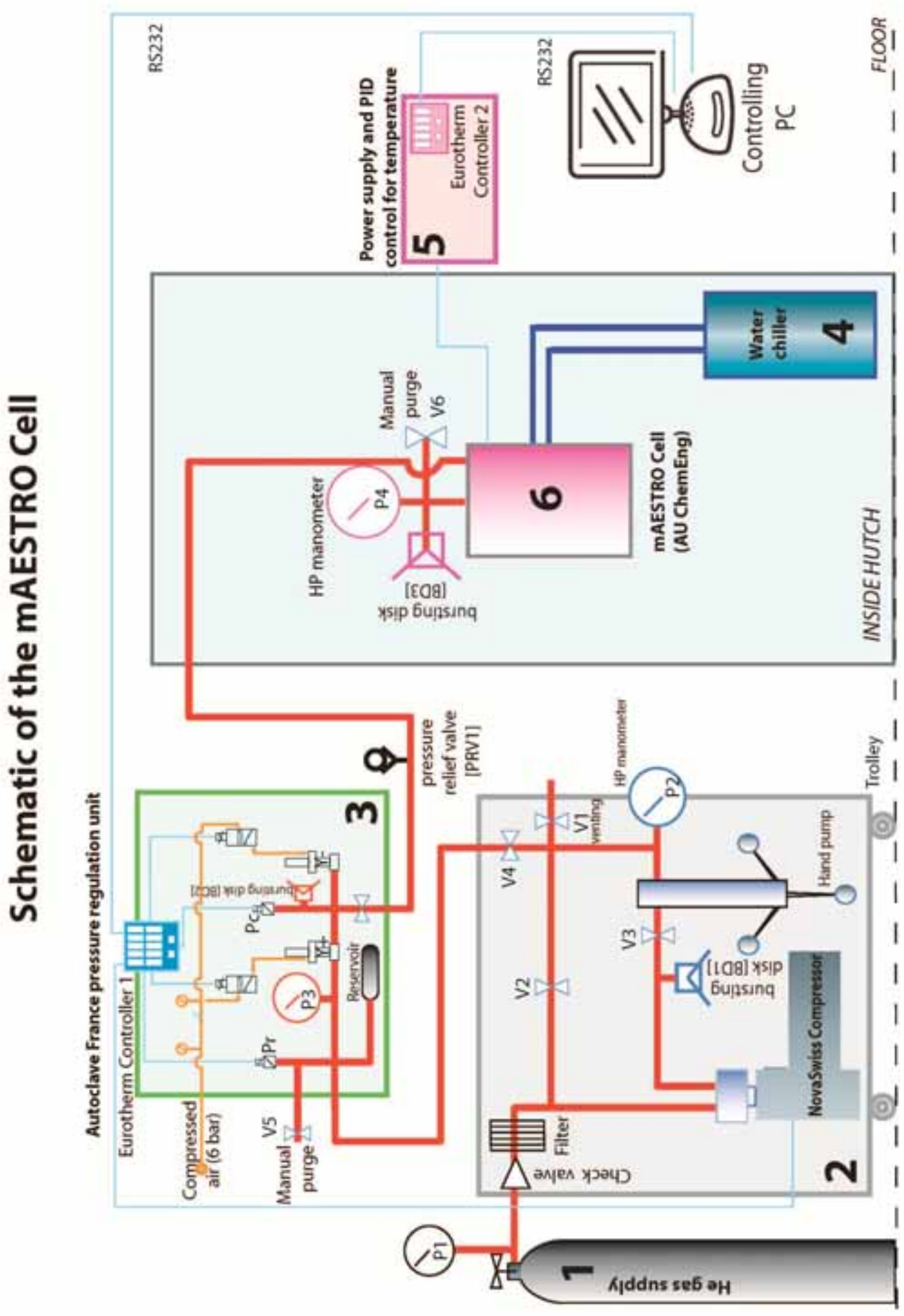

Figure 2.1 Schematic for installation of the mAESTRO cell at high T-P at the Australian Synchrotron (not to scale). 1: Helium gas supply; 2: pressure generation and back-up manual pressure generation unit; 3: automatic (PID-controlled) pressure regulation unit; 4: water chiller for cooling XAS mAESTRO autoclave; 5: power supply and (PID controlled) temperature controlling unit for internal heated mAESTRO autoclave; 6: mAESTRO autoclave.

2.2.1 Stainless steel autoclave and internal sample cell

The stainless steel autoclave consists of a lid with a heating block and a body that is cooled by the circulation of chilled water using an external circulation chiller (NESLAB, ThermoFlex 900). The heating block (Figure 2.2a) is a vessel-like module covered by a brass sleeve and is attached to the autoclave lid. It contains two copper sleeves with ceramic stuffing at two ends and one insulating ceramic sleeve in the middle. The insulating ceramic sleeve hosts an internal wire-coil heater, on which the internal sample cell is inserted from the bottom of the heater (Figure 2.3a, b). The internal heater is a cylindrical resistive furnace, consisting of a copper housing as inner layer and a macor tube as outer layer. The copper housing encloses the internal sample cell (glassy carbon tube) and resistive metallic wires (kanthal, molybdenum, nichrome, or tungsten) are coiled around the macor tube for heating.

Figure 2.2 Pictures of mAESTRO autoclave: (a) the autoclave body and heating block; (b) internal glassy carbon cell with two alumina pistons; (c) Beryllium window and holder.

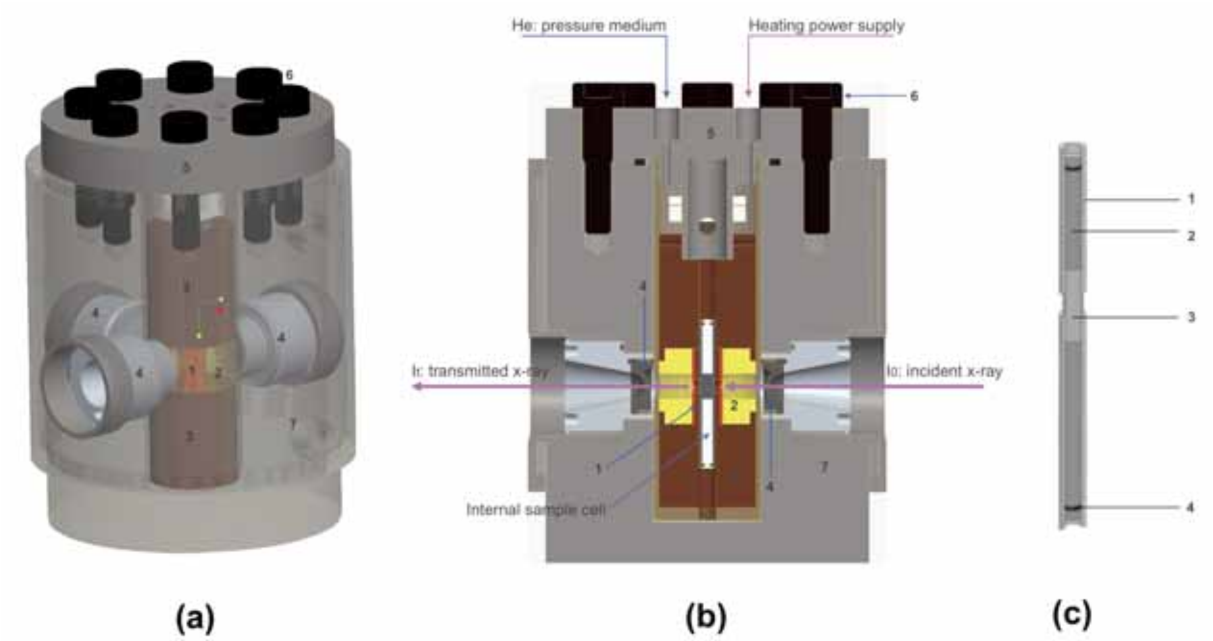

Figure 2.3 (a / b) transparent 3-D / 2-D design of mAESTRO autoclave (1: internal heater; 2: ceramic sleeve; 3: copper sleeve with ceramic stuffing; 4: Beryllium window; 5: autoclave lid; 6: sealing screw; and 7: autoclave wall); (c) internal sample cell (1: glassy carbon tube; 2: alumina piston; 3: sample space; and 4: Viton O-ring).

Three beryllium windows (Testemale et al., 2005) are mounted to the autoclave wall (Figures 2.2c and 2.3a, b), and three beam holes in the heating block enable concurrent measurements of the fluorescence and transmission XAS signals: one entrance window for incident x-ray, one exit window for transmitted x-ray (axial) and one exit window for fluorescence signals (at 90° relative to the incident x-ray beam). Beryllium is chosen as window material because of its low x-ray absorption properties and high pressure resistance. The thickness of the Be-windows dictates the maximum working pressure for the system. Thinner windows are typically chosen to minimize absorption (x-ray energy < 10 keV), or to minimize contamination from impurities contained in the Be windows. The thinnest windows (0.7 mm) are rated to a working pressure (P_{work}) of 400 bar, and 31% of the beam is absorbed by two windows at the Fe *K*-edge energy (7112 eV), compared to 41% absorption by a pair of 1 mm windows rated to P_{work} = 600 bar.

The sample solution is contained within a glassy carbon tube (Sigradur G grade, HTW®) that has a length of 85 mm, an internal diameter of 4 mm and a wall thickness of 1 mm (Figures 2.2b and 2.3c). The part of the glassy carbon tube exposed to the x-ray beam can be machined to have thinner wall to reduce its x-ray absorption when a relatively low x-ray absorption edge energy (< 8 keV) is investigated. Glassy carbon is chosen as the material of sample container according to its properties of low x-ray absorption, resistance to high temperature and chemical stability. The sample solution is sealed by two alumina pistons with Viton O-rings, which allows pressure equalisation through expansion or contraction. Consequently, the sample volume can change between ~25 and 100 μl. Depending upon the amount of sample loaded at room-T, the density of the sample can be controlled by imposing appropriate P-T conditions. This feature enables difficult experiments involving low-density supercritical fluid near the critical isochore (Liu et al., 2008) or concurrent measurement of metal-speciation in co-existing liquids and vapours (Pokrovski et al., 2008).

2.2.2 Pressure and temperature control

The pressure for the XAS cell is generated with a high-pressure compressor (NovaSwiss) and maintained within ±1 bar of set pressure by a novel PID-controlled pressure regulation device (Bruyère et al., 2008). Helium is used as a pressure medium due to its low x-ray absorption cross section. The PID-controlled programmable power supply (Delta, SM 1500-70-22) provides voltage and current for the internally heated autoclave, so that the sample temperature is controlled to ±1 ˚C of set temperature. The pressure controller (Eurotherm, 3504) and temperature controller (Eurotherm, 3216) are both connected to the controlling PC via RS232 cable, allowing Graphic User Interface (GUI) and integration with the XAS beamline controls. Power supply, pressure medium hoses and thermocouple wires are connected to internal parts of cell (heating block and glassy carbon tube) through the plugs at the top of autoclave lid (Figure 2.4).

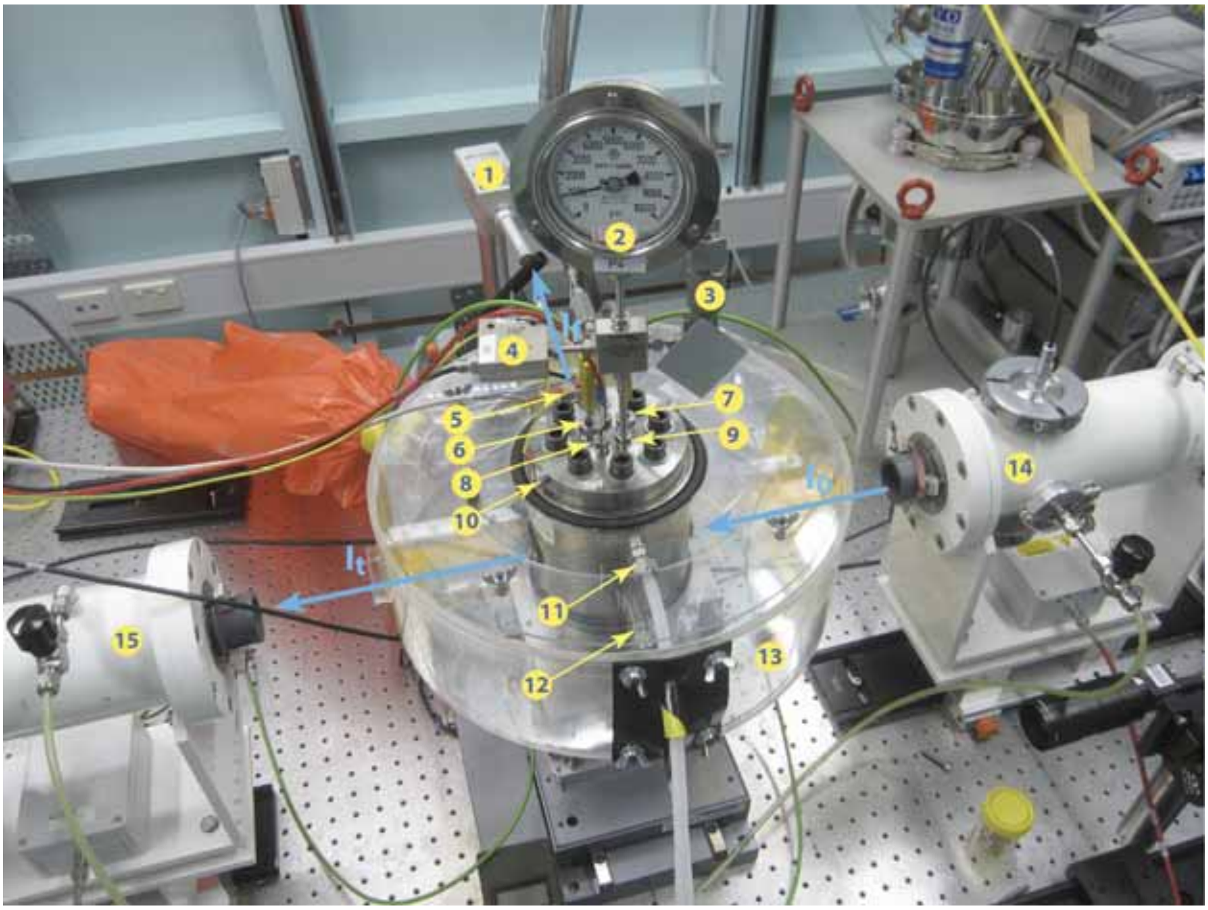

Figure 2.4 setup of the mAESTRO cell on the XAS beamline of the Australian Synchrotron (I_0: incident x-ray; I_t: transmitted x-ray; I_f: fluorescence signal; 1: fluorescence detector; 2: calibrated manometer; 3: rupture disk; 4: purge valve; 5: thermostat; 6 / 7: thermocouples ports; 8: power inlet; 9: pressure medium inlet; 10: earthing; 11: hot water outlet; 12: cooling water inlet; 13: Perspex case; 14 / 15: ionisation chamber 1 / 2).

2.2.3 Safety measures

The safety of the autoclave operation on the beamline is ensured by the following processes. (i) A safety factor of 1.5 is applied to the pressure components; i.e., hydrostatic tests of the system were conducted at $1.5*P_{work}$. To insure the mechanical strength of the Be-windows, an explosion test was conducted using a window from each different batch. In this test increasing pressure was applied until the Be window(s) exploded. On the basis of this test, the maximum working pressure (P_{work}) for each batch was set at one third of the measured explosion pressure. Each individual Be window was then tested at P_{work}*2 to insure its mechanical integrity. (ii) A redundant system was put in place to ensure that the pressure in the autoclave remains below 1.2*P_{work} at all time; this system includes PID-controlled pressure regulation that compensates for pressure variations, for example upon heating; a pressure relief valve that ensures that the maximum pressure delivered by the pressure generation system is $\leq 1.2*P_{work}$. In addition, a rupture disk was mounted on top of the autoclave (Figure 2.4). (iii) The autoclave is enclosed in a protective Perspex case with expandable volume (Figure 2.4), which protects users in case of catastrophic failure of the Be window and contains most of the Be-fragments. (iv) The temperature of autoclave surface is kept at ~25 ˚C via chilled water (~15 ˚C) using a circulation chiller. (v) The thermostat connected to the temperature control loop switches off heating if the cell body exceeds 60 ˚C (Figure 2.4).

2.3 Commissioning and results

The mAESTRO system was commissioned at the XAS beam line at the Australian Synchrotron (AS), Melbourne, Australia in October, 2009. The XAS beamline of AS has a 1.9T wiggler source, and a Si (111) double-crystal monochromator with energy resolution of 1.5×10^{-4} ($\Delta E/E$). The energy resolution was 1.25 eV at Ni *K*-edge (8333 eV, 1.5×10^{-4} $\Delta E/E$). The beam spot size used was 140×400 μm^2. The sample solutions were prepared by dissolving solid $NiCl_2 \cdot 6H_2O$ powder in slightly acidified water (to prevent hydrolysis), and adding different amount of NaCl to control the chlorinity and Cl:Ni ratio of solutions. Solutions were loaded into the sample cell at ambient conditions. Since a suitable fluorescence detector was not available at XAS beamline of AS at the time of commissioning, all Nickel *K*-edge XAS spectra were collected in transmission mode. Energy calibration was achieved using the Ni foil placed in the reference holder at the first experimental hutch. The mAESTRO system installed at the XAS beamline of AS is shown in figure 2.4. Isobaric heating was carried out to measure each sample solution in a repeatable routine. (i) The cell was pressurized to target pressure by the pressure generation-regulation unit in the second experimental hutch (Figure 2.5) at a rate of 15 bar per minute until it reached a constant level (400 bar). (ii) The sample cell was heated to target temperature by the temperature control unit near the control cabin (Figure 2.5) at a rate of 10 ˚C per minute. (iii) XAS data were acquired at the set pressure and temperature. (iv) The cell was then heated to the next target temperature. Up to 6 scans were performed at each temperature from 25 to 427 ˚C (at around 50 ˚C intervals) for the commissioning. The temperature and pressure of the sample were adjusted independently and maintained within ±1 bar and ±0.5 ˚C of the set values during XAS data collection. Note that all concentrations are reported in molal units, since the solution volumes vary as a function of T and P. As thermocouples are placed outside the glassy carbon tube, not exactly at the position where the beam interacts with sample solutions, the real sample temperature at the beam spot is usually lower than the thermocouple temperature. The solution temperature at the beam position was calibrated by measuring the absorption of pure water as a function of temperature at 400 bar. Using the mass attenuation coefficients from Chantler (1995), the pathlength of the solution at room-T (known density) was determined, and the experimentally measured densities were used to calculate the solution temperature by comparing with the tabulated water density values from the NIST database (Lemmon et al., 2000). Details of temperature calibration can be seen in Etschmann et al., (2010).

Figure 2.5 mAESTRO system at the XAS beamline of Australian Synchrotron (1: mAESTRO autoclave in the first experimental hutch, 2: pressure generation-regulation unit in the second experimental hutch, and 3: temperature control unit near the control cabin).

The speciation of Ni was investigated at a pressure of 400 bar at temperatures ranging from 25 to 427 ˚C. Figure 2.5 shows XANES and EXAFS spectra of the solutions containing 0.2 m $NiCl_2$ (Cl:Ni ratio = 2) at 25 ˚C, 400 bar and 0.2 m $NiCl_2$ and 5.5 m NaCl (Cl:Ni ratio = 30) at 427 ˚C, 400 bar, respectively. Qualitatively, the XANES spectra show that the intensity of the pre-edge feature increases while the white line intensity decreases, and the position of the edge shifts towards lower energies with increasing temperature and chlorinity (Figure 2.6a). This is consistent with the trends with increasing temperature and chlorinity observed in previous XAS studies for other first row transition metals (Liu et al., 2007; Testemale et al., 2009a), suggesting a transition from six-coordinated octahedral to four-coordinated tetrahedral-like structures, as noted by Susak and Crerar (1985) in their qualitative UV-Vis study. EXAFS data were analysed with the HORAE package (Ravel and Newville, 2005), following the procedure of Testemale et al. (2009a). Quantitative EXAFS refinements (Figure 2.6b, c; Table 2.1) confirm the reduction of Ni coordination number and ligand substitution around the Ni^{2+} ion from $Ni(H_2O)_6^{2+}$ to $Ni(H_2O)_{(4-n)}Cl_n^{-(n-2)}$ (n=2.83) with increasing temperature and chlorinity. From the EXAFS fitting results reported in Table 2.1, structural information of Nickel complexes in the two solutions can be inferred. (i) At room-T, Ni(II) speciation is dominated by the octahedral hexaaquo complex - $Ni(H_2O)_6^{2+}$ in dilute solutions with a Ni-O bond distance of 2.043(2) Å. (ii) At 427 ˚C, 400 bar and much higher salinity most Ni^{2+} cations tend to form four-coordinated higher order chloride complexes - $Ni(H_2O)_{(4-n)}Cl_n^{-(n-2)}$ (n=2.83) with a Ni-O bond distance of 2.083(20) Å and a Ni-Cl bond distance of 2.244(20) Å. Measured raw absorption data in energy space was converted to photoelectron momentum k-space by a serious of data reduction procedures which include background remove, conversion of E to k, normalisation, μ_0 correction, weighting scheme, etc; then the signal in k-space was converted to R-space by Fourier transform (Teo, 1986). R-space spectra reflect a radial distribution function from central atom to scattering shell. For the k-space EXAFS spectra (Figure 2.6b), the amplitude of the oscillations is lower at 450 ˚C than at 25 ˚C because of the reduced number of ligands around Ni^{2+}. The EXAFS spectra at higher temperature and chlorinity have higher degree of noise and disorder, although its fit has a lower goodness of fit. In Figure 2.5c, the position of the main peak increases with increasing T and salinity while its intensity decreases, reflecting the replacement of water ligands by Cl^- and the decrease in coordination number. These results are in good agreement with previous studies about Ni bromide complexes (Hoffmann et al., 1999; Wallen et al., 1998).

Table 2.1 EXAFS refinements for two typical Ni-chloride solutions (0.2 m $NiCl_2$ at 25 °C and 0.2 m $NiCl_2$ plus 5.5 m NaCl at 427 °C).

Temperature (Sample)	25 °C (0.2 m $NiCl_2$)	427 °C (0.2 m $NiCl_2$ + 5.5 m NaCl)
Model (N)	One shell Ni-O (5.87±0.48)	Two shells Ni-O (1.17±0.32), Ni-Cl (2.83±0.32)
R(Ni-O, Å)	2.043±0.002	2.083±0.020
R(Ni-Cl, Å)	-	2.244±0.020
σ^2(Ni-O, $Å^2$)	0.005±0.001	0.002*
σ^2(Ni-Cl, $Å^2$)	-	0.005±0.002
ΔE_0 (eV)	0.27±0.78	4.2±8.1 2.3±2.7
R-factor	0.0240	0.0198

(*) indicates parameters that were fixed during refinement. The parameters are: type of scattering shell and coordination model number (N), bond distance from Ni^{2+} to scattering shell (R), Debye-Waller factor (σ^2) which is mean squared displacement of the bond length, energy shift (ΔE_0) which accounts for a misalignment of energy between theoretical calculations and experiments, and the goodness of fit (R-factor) which is the fraction of the sum of the squares of the differences between data and fit to the sum of the squares of the data.

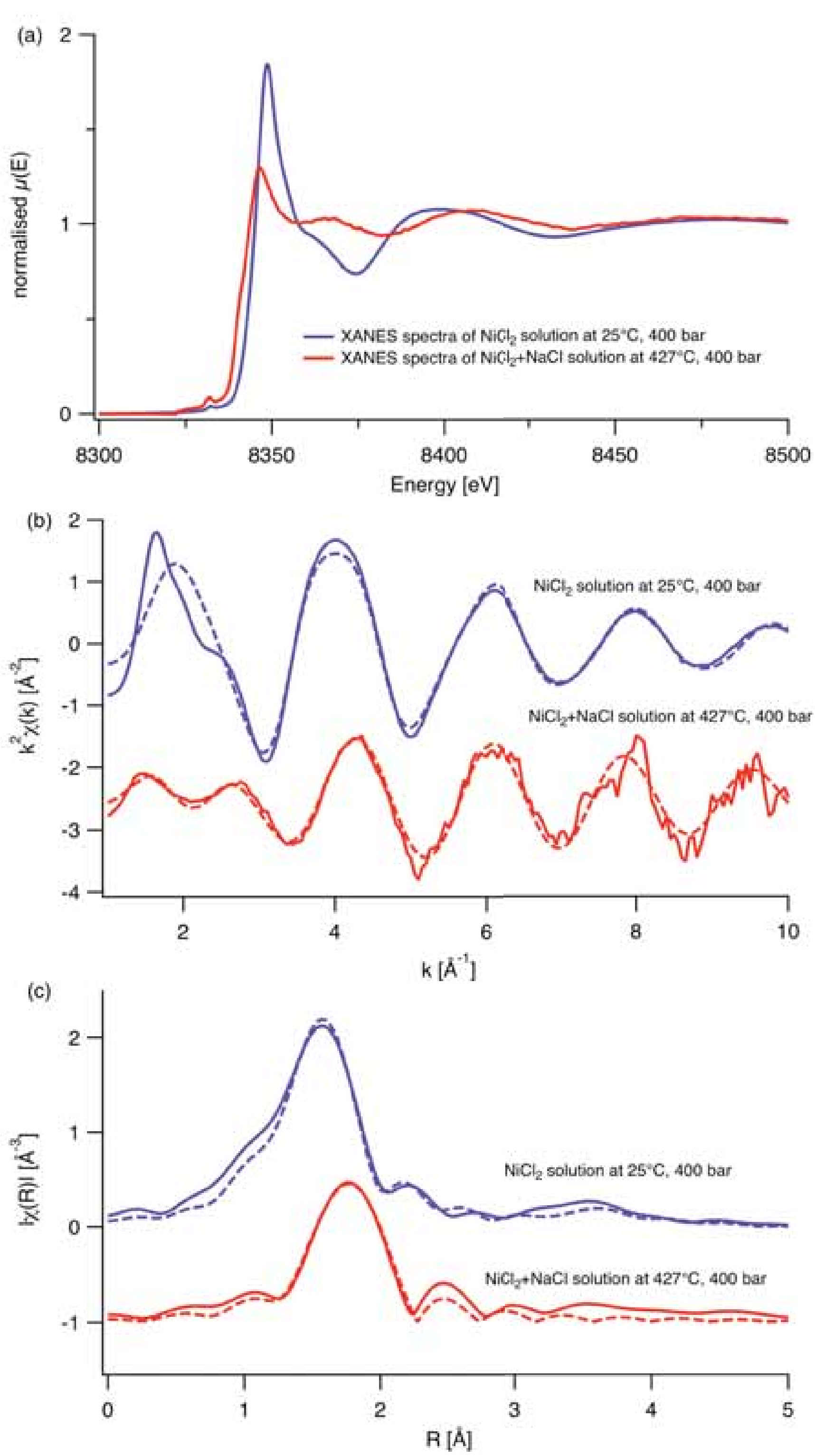

Figure 2.6 XAS spectra and fits of the $NiCl_2$ solution at 25 °C, 400 bar and $NiCl_2$/NaCl solution at 427 °C, 400 bar. (a) XANES spectra; (b) k-space EXAFS spectra and fits; (c) R-space spectra and fits. Blue lines and red lines represent the data of $NiCl_2$ solution and $NiCl_2$/NaCl solution, respectively. Solid lines represent experimental data, and dashed lines the fits based on the parameters in Table 2.1.

2.4 Conclusions

High quality XAS data have been obtained for solutions using mAESTRO system at high T-P conditions at the Australian Synchrotron (T to 600 ˚C; P current limited to 600 bar, though the technology is suitable for pressures > 1000 bar). Coordination changes of Ni (II) aqueous chloride complexes have been detected *in situ* from 25 to 427 ˚C, at 400 bar. The Structural information of six-coordinated octahedral $Ni(H_2O)_6^{2+}$ and four-coordinated $Ni(H_2O)_{(4-n)}Cl_n^{-(n-2)}$ (n=2.83) have been derived from EXAFS analysis. The trend of these changes lies in the decrease of coordination number and the ligand replacement of water molecule by halide anion with increasing temperature and salinity. Such coordination changes have been described for other transition metals (e.g., Mn^{2+}, Fe^{2+}, Fe^{3+}, Co^{2+}, Zn^{2+}, Cd^{2+}).

The mAESTRO system provides new opportunities for synchrotron-based structural information at high temperature and pressure. *In situ* XAS measurements provide information about fluid density, elemental concentration, and metal speciation via XANES and EXAFS (Fulton et al., 1996). All these measurements can be combined in a single experiment, opening the way to complex experiments. Examples include measurement of the partitioning and speciation of metals during phase separation at high temperature/pressure (Etschmann et al., 2010; Pokrovski et al., 2008); derivation of formation constants and thermodynamic properties of aqueous metal complexes (Liu et al., 2007; Testemale et al., 2009a); measuring the solubility and dissolution kinetics *in situ* (Testemale et al., 2009b); deciphering the solvation of ion-pairing and structure of water under supercritical conditions (Da Silva et al., 2009; Wernet et al., 2005). The potential applications of the mAESTRO system include, but are not limited to: ore deposit research and mineral exploration (Brugger et al., 2010), geothermal systems, CO_2 geosequestration

(Testemale et al., 2009b), hydrometallurgy (Azimi and Papangelakis, 2010), and synthetic chemistry in near- and supercritical solvents (Van Eldik and Merbach, 1992; Eckert et al., 1996; Watanabe et al., 2004).

2.5 References

Azimi, G. and Papangelakis, V. G., 2010. The solubility of gypsum and anhydrite in simulated laterite pressure acid leach solutions up to 250 °C. *Hydrometallurgy* **102**, 1-13.

Bassett, W., Shen, A., Bucknum, M., and Chou, I., 1993. A new diamond anvil cell for hydrothermal studies to 2.5 GPa and from -190 to 1200 °C. *Review of Scientific Instruments* **64**, 2340-2345.

Bassett, W. A., Anderson, A. J., Mayanovic, R. A., and Chou, I., 2000. Hydrothermal diamond anvil cell for XAFS studies of first-row transition elements in aqueous solution up to supercritical conditions. *Chemical Geology* **167**, 3-10.

Brugger, J., Pring, A., Reith, F., Ryan, C., Etschmann, B., Liu, W., O'Neill, B., and Ngothai, Y., 2010. Probing ore deposits formation: New insights and challenges from synchrotron and neutron studies. *Radiation Physics and Chemistry* **79**, 151-161.

Bruyère, R., Prat, A., Goujon, C., and Hazemann, J., 2008. A new pressure regulation device using high pressure isolation valves. *Journal of Physics: Conference Series* **121**, 122003.

Chou, I., Bassett, W. A., Anderson, A. J., Mayanovic, R. A., and Shang, L., 2008. Containment of fluid samples in the hydrothermal diamond-anvil cell without the use of metal gaskets: Performance and advantages for in situ analysis. *Review of Scientific Instruments* **79**, 115103-115103-4.

Da Silva, C., Proux, O., Hazemann, J. L., James-Smith, J., Testemale, D., and Yamaguchi, T., 2009. X-ray absorption spectroscopy study of solvation and ion-pairing in aqueous gallium bromide solutions at supercritical conditions. *Journal of Molecular Liquids* **147**, 83-95.

Eckert, C. A., Knutson, B. L., and Debenedetti, P. G., 1996. Supercritical fluids as solvents for chemical and materials processing. *Nature* **383**, 313-318.

Etschmann, B. E., Liu, W., Testemale, D., Müller, H., Rae, N. A., Proux, O., Hazemann, J. L., and Brugger, J., 2010. An in situ XAS study of copper(I) transport as hydrosulfide complexes in hydrothermal solutions (25-592 °C, 180-600 bar): Speciation and solubility in vapor and liquid phases. *Geochimica et Cosmochimica Acta* **74**, 4723-4739.

Fulton, J., Pfund, D., Wallen, S., Newville, M., Stern, E., and Ma, Y., 1996. Rubidium ion hydration in ambient and supercritical water. *The Journal of chemical physics* **105**, 2161.

Fulton, J. L., Chen, Y., Heald, S. M., and Balasubramanian, M., 2004. High-pressure, high-temperature x-ray absorption fine structure transmission cell for the study of aqueous ions with low absorption-edge energies. *Review of Scientific Instruments* **75**, 5228-5231.

Fulton, J. L., Darab, J. G., and Hoffmann, M. M., 2001. X-ray absorption spectroscopy and imaging of heterogeneous hydrothermal mixtures using a diamond microreactor cell. *Review of Scientific Instruments* **72**, 2117-2122.

Hoffmann, M. M., Darab, J. G., Palmer, B. J., and Fulton, J. L., 1999. A transition in the Ni^{2+} complex structure from six-to four-coordinate upon formation of ion pair species in supercritical water: An X-ray absorption fine structure, near-infrared, and molecular dynamics study. *The Journal of Physical Chemistry A* **103**, 8471-8482.

Lemmon, E., McLinden, M., Friend, D., Linstrom, P., and Mallard, W., 2000. Thermophysical Properties of Fluid Systems. In: 69, n. (Ed.), *NIST chemistry WebBook, Nist standard reference database* National Institute of Standards and Technology, Gaithersburg.

Liu, W., Brugger, J., Etschmann, B., Testemale, D., and Hazemann, J. L., 2008. The solubility of nantokite ($CuCl_{(s)}$) and Cu speciation in low-density fluids near the critical isochore: An in-situ XAS study. *Geochimica et Cosmochimica Acta* **72**, 4094-4106.

Liu, W., Etschmann, B., Foran, G., Shelley, M., and Brugger, J., 2007. Deriving formation constants for aqueous metal complexes from XANES spectra: Zn^{2+} and Fe^{2+} chloride complexes in hypersaline solutions. *American Mineralogist* **92**, 761-770.

Pokrovski, G. S., Roux, J., Hazemann, J. L., Borisova, A. Y., Gonchar, A., and Lemeshko, M., 2008. In situ X-ray absorption spectroscopy measurement of vapour-brine fractionation of antimony at hydrothermal conditions. *Mineralogical Magazine* **72**, 667-681.

Ravel, B. and Newville, M., 2005. ATHENA, ARTEMIS, HEPHAESTUS: data analysis for X-ray absorption spectroscopy using IFEFFIT. *Journal of synchrotron radiation* **12**, 537-541.

Seward, T., Henderson, C., Charnock, J., and Dobson, B., 1996. An X-ray absorption (EXAFS) spectroscopic study of aquated Ag^+ in hydrothermal solutions to 350 °C. *Geochimica et Cosmochimica Acta* **60**, 2273-2282.

Susak, N. J. and Crerar, D. A., 1985. Spectra and coordination changes of transition metals in hydrothermal solutions: Implications for ore genesis. *Geochimica et Cosmochimica Acta* **49**, 555-564.

Tamura, K., Inui, M., and Hosokawa, S., 1995. XAFS measurements at high temperatures and pressures. *Review of Scientific Instruments* **66**, 1382-1384.

Testemale, D., Argoud, R., Geaymond, O., and Hazemann, J. L., 2005. High pressure/high temperature cell for x-ray absorption and scattering techniques. *Review of Scientific Instruments* **76**, 043905-043905-5.

Testemale, D., Brugger, J., Liu, W., Etschmann, B., and Hazemann, J. L., 2009a. In-situ X-ray absorption study of Iron (II) speciation in brines up to supercritical conditions. *Chemical Geology* **264**, 295-310.

Testemale, D., Dufaud, F., Martinez, I., Bénézeth, P., Hazemann, J. L., Schott, J., and Guyot, F., 2009b. An X-ray absorption study of the dissolution of siderite at 300 bar between 50 °C and 100 °C. *Chemical Geology* **259**, 8-16.

Tian, Y., Brugger, J., Liu, W., Borg, S., Etschmann, B., O'Neill, B. K., Testemale, D., Hazemann, J. L., Glover, C., and Ngothai, Y. M., 2010. High-temperature and pressure spectroscopic cell for in-situ XAS study of supercritical fluids at the Australian synchrotron *CHEMECA 2010*, Adelaide, Australia.

Van Eldik, R. and Merbach, A. E., 1992. High pressure kinetics. A decisive dimension in mechanistic studies of inorganic reactions. *Comments on Inorganic Chemistry* **12**, 341-378.

Wallen, S. L., Palmer, B. J., and Fulton, J. L., 1998. The ion pairing and hydration structure of Ni in supercritical water at 425 °C determined by x-ray absorption fine structure and molecular dynamics studies. *The Journal of chemical physics* **108**, 4039.

Watanabe, M., Sato, T., Inomata, H., Smith, R. L. J., Arai, K., Kruse, A., and Dinjus, E., 2004. Chemical reactions of C1 compounds in near-critical and supercritical water. *Chemical Reviews* **104**, 5803-5821.

Wernet, P., Testemale, D., Hazemann, J. L., Argoud, R., Glatzel, P., Pettersson, L., Nilsson, A., and Bergmann, U., 2005. Spectroscopic characterization of microscopic hydrogen-bonding disparities in supercritical water. *The Journal of chemical physics* **123**, 154503.

Chapter 3

Ab initio XANES simulations for metal solid standards and aqueous species*

*This chapter is mainly based on the following paper and submitted manuscript:

Borg, S., Liu, W., Etschmann, B., Tian, Y., Brugger, J., 2012. An XAS study of molybdenum speciation in hydrothermal chloride solutions from 25–385 °C and 600 bar. *Geochimica et Cosmochimica Acta* 92, 292-307. (see appendix C) Copyright of this paper belongs to Elsevier Ltd.

Grundler, P., Brugger, J., Etschmann, B., Helm, L., Liu, W., Spry, P., Tian, Y., Testemale, D., Pring, A., Speciation of aqueous tellurium(IV) in hydrothermal solutions and vapors, and the role of oxidized tellurium species in gold metallogenesis. (in revision for *Geochimica et Cosmochimica Acta*)

3.1 Introduction

XAS (X-ray Absorption Spectroscopy) studies the x-ray absorption coefficient of an absorbing element as a function of energy due to the absorption of incident x-ray photon, excitation of electron from the core level orbital of the absorbing atom, and consequent quantum interference between the outgoing and scattered photoelectron wavefunction by the potential of the surrounding atoms (Bunker, 2010). The principles and applications of XAS have been discussed for example by Teo (1986), Koningsberger and Prins (1987) and Kelly et al (2008). XAS can be divided into two regimes: XANES (X-ray Absorption Near Edge Structure) and EXAFS (Extended X-ray Absorption Fine Structure) (Figure 3.1). XANES (from pre-edge to within approximately 50 eV above the absorption edge) probes the excitation of photoelectron near the binding energy E_0 of the element from core-level ground state to continuum final state, and is particularly sensitive to the formal valence state, electronic structure and local geometry of the absorbing atom; EXAFS (from ~50 eV up to >1000 eV above the absorption edge) stands for the energy-dependent oscillation resulted from this quantum interference, and is sensitive to the nature, number, and distance of nearest neighbours around the central atom. Compared to XANES, the basic principle and theory of EXAFS region has been better understood (i.e., Rehr and Albers, 2000), and there is an analytical expression of EXAFS that has been routinely used for refining structural parameters since the 1970's (e.g., Sayers et al., 1971). One can identify ligand identity and quantitatively refine the ligation number and bond distance from absorbing atom to neighbouring ligands through EXAFS analysis and data fitting. In contrast, there is no analytical expression for the information of the XANES region, making quantitative XANES interpretation relatively difficult. Molecular orbital theory, crystal field theory and/or ligand field theory have been used to interpret the XANES spectral features and their origins in earlier XANES studies (e.g., Shulman et al., 1976).

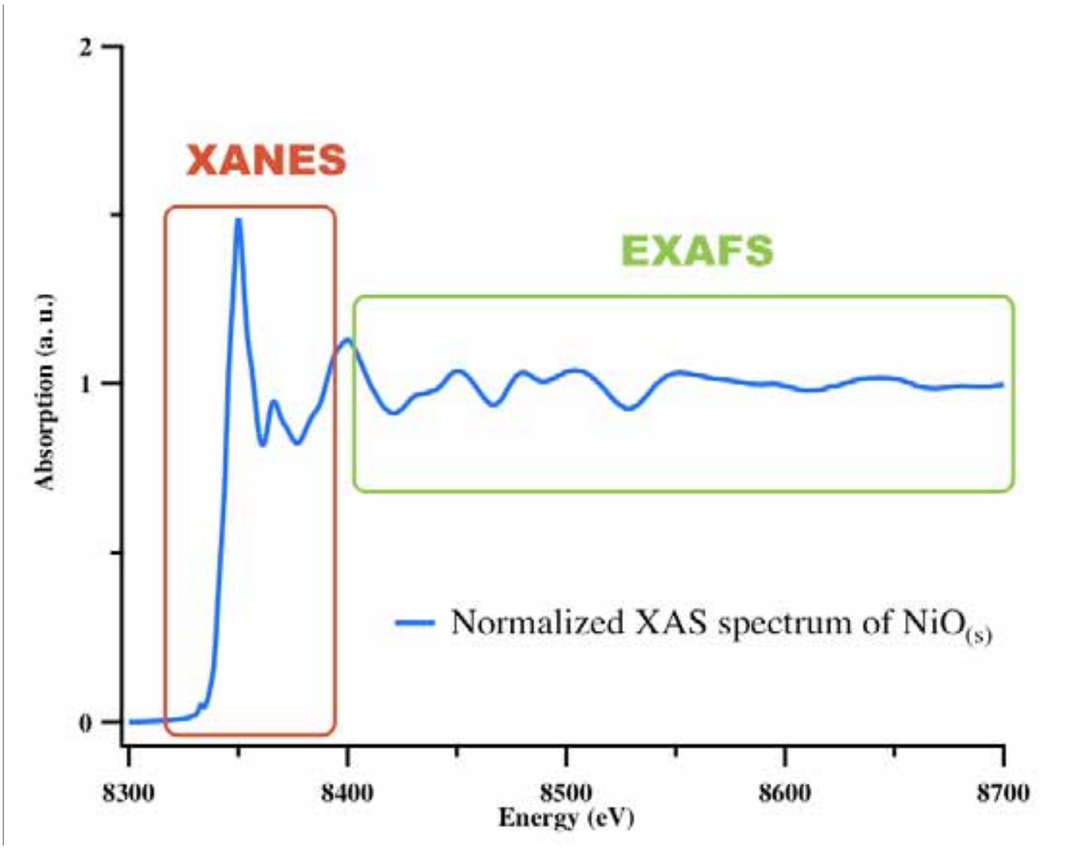

Figure 3.1 XAS spectrum of $NiO_{(s)}$: XANES and EXAFS regions

XANES may provide additional and complementary information (oxidation state, electronic and geometric structures) to EXAFS analysis when both XANES and EXAFS data are available. In order to better constrain the coordination around the absorbing atom, it is desirable to have information derived from both XANES and EXAFS analysis. However, in some cases XANES may be the only source of information, due to demanding analytical requirements. For example, only XANES data could be collected on very dilute samples (ppm level, e.g., Lombi and Susini 2009) and on samples sensitive to beam damage (e.g., Berry et al., 2006; James-Smith et al., 2010). In some situations, EXAFS is not sensitive to coordination geometry around absorbing metal cation but XANES may show higher sensitivity. For example, it's hard to tell whether the hydrated Cu^{2+} complex at room-T is six-coordinated octahedron or five-coordinated square-pyramidal by EXAFS analysis. This issue was addressed by *ab initio* XANES calculations based on the two models that five-fold square-pyramidal $Cu(H_2O)_5^{2+}$ was in better agreement with experimental XANES spectrum while using five-fold square pyramidal $Cu(H_2O)_5^{2+}$ and six-fold distorted octahedron $Cu(H_2O)_6^{2+}$ coordination geometries yielded nearly identical calculated EXAFS spectra (Benfatto et al., 2002).

XANES simulations need to calculate the spectroscopic transition of the core electron of absorbing atom from an initial core state to upper empty level - the final state. The initial state is easy to solve and the difficulty of XANES calculations lies in improving the accuracy of determining the final electronic state of the absorbing atom. To evaluate the final state, the Schrödinger equation for a given cluster needs to be solved (Joly, 2001). Since analytical solutions for the general Schrödinger equation are not available, one has to rely on numerical approximations. For XANES simulations, Multiple Scattering Theory (MST) has been developed to calculate x-ray absorption cross-section, which generally uses the muffin tin approximation to solve the Schrödinger equation and evaluate the inter-atomic potentials (e.g., Rehr and Albers, 1990). The muffin tin approximation uses spherically averaged potential around the absorbing atom (Rehr et al., 1992). There are several programs developed to perform XANES simulations based on the muffin tin approximation, such as CONTINUUM (Natoli et al., 1980), FEFF (Ankudinov et al., 1998), MXAN (Benfatto et al., 2001). Numerous XANES calculations have been conducted in the past three decades to explore the valence and geometric information around absorbing atoms based on the muffin tin approximation (e.g., Garcia et al., 1986; Farges et al., 1997). It is now possible to extract quantitative geometrical information by such XANES calculations using some theoretical codes (e.g., MXAN, FitIt) (e.g., Benfatto et al., 1997, 2002, 2003; Chaboy et al., 2006; D'Angelo et al., 2006; Smolentsev and Soldatov, 2007) which are still developing with the progress in the theory and interpretation of XANES

(Rehr and Ankudinov, 2005). The MST methods relying on the muffin tin approximation used in early studies are still popular since they are computationally trivial on modern personal computers, and they provide accurate results, especially for relatively symmetrical structures (e.g., octahedral geometry; D'Angelo et al., 2002). However, for some cases of low-symmetry and/or non-dense structures, the muffin tin approximation does not accurately reproduce the experimental spectra. To address this issue, several groups have developed methods that go beyond the muffin tin approximation. In particular, the Finite Difference Method (FDM) has emerged to be a powerful technique to explore the local structure for solid compounds and aqueous solutions over wide range of conditions, because this method avoids the limitations of muffin tin approximation by allowing a free potential shape. The FMD method is especially valuable for asymmetrical structures in disordered systems where calculations using MST with the muffin tin approximation may not be satisfactory (Joly, 2001). In an early seminal study of hydrothermal speciation, Testemale et al. (2004) showed that the XANES spectra of the asymmetrical trigonal pyramid species $As(OH)_{3(aq)}$ can be more accurately reproduced by calculations using the FDM method rather than the MST method. More recently, many XAS studies of aqueous species at elevated temperatures and pressures have used *ab initio* XANES simulations following the FDM method as a complementary tool to constrain the stoichiometries and geometries of aqueous metal complexes (e.g., Brugger et al., 2007; Pokrovski et al., 2009; Testemale et al., 2009; Bazarkina et al., 2010; Etschmann et al., 2010, 2011; Liu et al., 2011, 2012; Borg et al., 2012; Tian et al., 2012).

As a mixture of different chemical species may co-exist in the same sample, the measured XANES spectrum represents a linear combination of the XANES spectra of each individual species, and the ratio of each species can be obtained by fitting the experimental data with a linear combination of spectra from standards of known structure and composition (Kelly et al., 2008). Hence, one can derive the formation constants of each metal species by XANES fitting in a similar manner to linear combination fitting: the spectra for each aqueous species need to be identified and extracted from multiple experimental XANES spectra, and the distribution and ratio of all species (with varying temperature, salinity, pH) can be obtained based on the XANES spectrum of each individual species (e.g., Liu et al., 2007). This method assumes that different complexes have different XANES spectra. In many systems, single species cannot be isolated (i.e., they exist as a mixture with a number of different species). *Ab initio* XANES calculations can therefore play an important role in assessing the influence of stoichiometry and geometry on the XANES spectra of different species and the impact of different geometries for an individual species, and here guide the derivation of thermodynamic formation constants from XANES data.

This chapter is dedicated to *ab inito* XANES simulations to explore the structure of solid and aqueous species of Mo, Te, Ni and Mn chloride and oxide complexes. The aims of this chapter include: i) determining the calculation method (FDM vs MST) based on the site symmetry of absorbing atom and evaluate the impact of cluster size on calculations for metal solid standards so as to assess the capability of XANES calculations to reproduce spectral features for known structures; ii) determining the influence of structural and electronic parameters (e.g., bond length, distortion, stoichiometry, self consistent calculations, etc) on the calculated XANES spectra of aqueous complexes in order to confirm the results of EXAFS analysis or to obtain additional information regarding the nature (stoichiometry and geometry) of aqueous complexes where EXAFS results may be unavailable or ambiguous; iii) validating the process of retrieving thermodynamic properties by XANES spectra fitting; and iv) assessing the effect of second shell on the calculated XANES spectra.

3.2 Method

In this study *ab initio* XANES simulations were conducted for solid standards and aqueous complexes using the FDMNES program developed by Joly (2001). This program uses full potential calculations within the real space cluster, and the final states and resulting absorbing cross sections can be calculated using either the MST or the FDM method. The raw calculations represent the photo-absorption cross-section, related to the transition amplitudes between initial and final states. To compare to the experimental spectra, the calculated raw data were convoluted with: i) a Lorentzian function of energy-dependent width to reproduce the core-hole lifetime broadening and the inelastic plasmon interactions with the photoelectron (core-hole width can be found in Krause and Oliver, 1979 for each absorbing element); and ii) a Gaussian function to account for the energy resolution determined by beamline setup. These convolution parameters were fixed for all calculations and not fitted in the subsequent analyses. Another convolution parameter - Fermi level represents the potential energy of a core level electron for the absorbing atom in a given cluster, as a cutting energy beneath which the electronic states are occupied and the absorption cross-section is set to zero before convolution (Joly, 2012). The Fermi level was by default calculated by FDMNES program. In most cases, this calculated Fermi level energy was applied to convolute the raw spectrum. In some case the Fermi level was adjusted manually by examination of the density of state (DOS) evolution of the different electronic states and alignment of the calculated pre-edge peak position to experimental spectra (Bazarkina et al., 2010). For example, a value of -4 eV was used for the convolution of the spectra of all Mn(II) clusters in chapter 5. Manually adjusting the value of Fermi level

(±3 eV around default value determined by FDMNES program) yielded minor variations of convoluted spectra, but the key spectral features were unchanged. Self-consistent field (SCF) calculations available in the recent versions of FDMNES (Bunău and Joly, 2009) have also been applied to provide a rigorous evaluation of the Fermi level based on more accurate final state calculations. These authors have suggested that of the choice of FDM versus the MST method plays a first order control in improving the accuracy of the calculated spectra, rather than the effect of SCF over non-SCF calculations. Therefore, the FDM method with non-SCF calculations was conducted first; if the XANES spectral features were not well reproduced, SCF calculations based on FDM method were performed to attempt to improve the agreement between the experimental and calculated spectra. All calculations in this study were carried out with neutral atoms for metals at *K*-edges, and the evolution of the charges in the clusters was not investigated (Joly et al., 1999; Testemale et al., 2004).

3.3 *Ab initio* XANES simulations for solid standards

The XANES spectra of selected solid standards with known coordination geometries were simulated to assess the reliability of XANES simulations to reproduce spectral features for known structures; and the agreement between calculation and experiment was used to validate the simulations for aqueous species. The results of simulations will be discussed for different solids by using different calculation methods, e.g., multiple scattering theory using muffin tinapproximation (MST) and finite differential method (FDM) and showing the effect of cluster size on the calculated XANES spectra.

3.3.1 Calculation method: MST vs FDM

Compared to the MST method, the FDM method is computationally intensive (up 1000's of processor-hours, and high memory usage of up to > 4 GB per processor), and does not significantly improve the calculated spectra for symmetrical geometries. Therefore, the MST method has been used in this study for some symmetrical structures, e.g., $Na_2MoO_4.2H_2O_{(s)}$, $MoO_{2(s)}$ $MoO_2Cl_{2(s)}$ and $MoO_{3(s)}$ (Borg et al., 2012). In this case, use of larger cluster size in the MST calculations trumps the more accurate electronic state calculations of the FDM method. Calculations for solids - $NiSO_4.6H_2O_{(s)}$ and $Te(OH)_{6(s)}$ with symmetrical geometry show that the agreement between calculation and experiment by MST is similar to or better than by FDM (Figure 3.2). In $NiSO_4.6H_2O_{(s)}$, Ni exists as the octahedral $[Ni(H_2O)_6]$ moiety (Rousseau et al., 2000, ICSD 89697). The calculated intensity of feature (B) by MST (7 Å) agrees slightly better with experimental data than FDM (6 Å), and the shape and position of band (C) are better reproduced in the MST (one peak at 8400 eV) than in the FDM (two peaks at 8387 and 8402 eV) calculations. The MST and FDM methods yield very similar spectra for $Te(OH)_{6(s)}$, in which Te(VI) is coordinated to six hydroxide ligand to form an octahedral $[Te(OH)_6]$ moiety (Falck and Lindqvist, 1978, ICSD 2390). The key spectral features - white line (A), shoulder (B) and band (C) are all properly reproduced by both MST and FDM. Although the shoulder (B) is not significant on the convoluted spectra by either MST or FDM, it is present at the prominent peak at 31842 eV on the raw FDM spectrum.

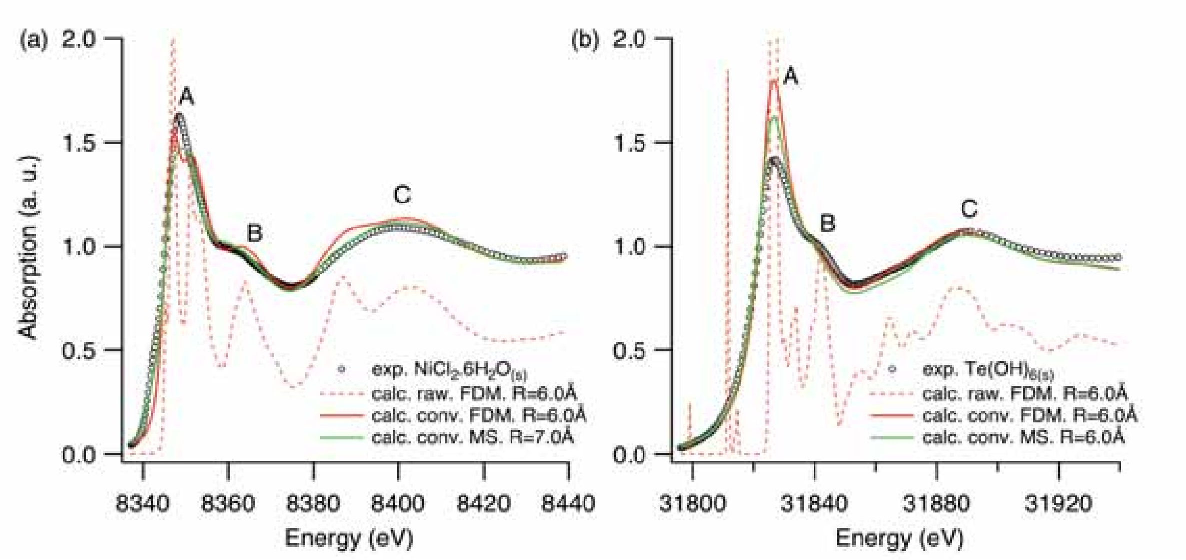

Figure 3.2 XANES simulations of solid standards: (a) $NiSO_4.6H_2O_{(s)}$ at Ni *K*-edge and (b) $Te(OH)_{6(s)}$ at Te *K*-edge.

For some asymmetrical geometries or non-dense structures, the FDM method yields better agreements than the MT method. XANES simulation for $K_2TeO_{3(s)}$ provides a typical example (see Figure 3.3). Te(IV) exists as a trigonal pyramidal [TeO_3] moiety in $K_2TeO_{3(s)}$ (Andersen et al., 1989, ICSD 65640). The calculated spectrum (FDM, 6 Å) is in excellent agreement with the experimental spectrum. In particular, the white line (A) and the shoulder (B) at 31,845 eV are accurately calculated. The only discrepancy is the band (C): there is one broad peak at about 31,895 eV on the experimental spectrum, whereas there are two small peaks at 31,885 and 31,905 eV on the calculated raw spectrum. The spectrum calculated using the MT approximation shows a much poorer agreement; in particular, the shoulder (B) is poorly reproduced. The large difference between the FDM and MT methods can be attributed to the low local symmetry (trigonal pyramid TeO_3) around Te(IV) (Andersen et al., 1989; Joly, 2001; Testemale et al., 2004).

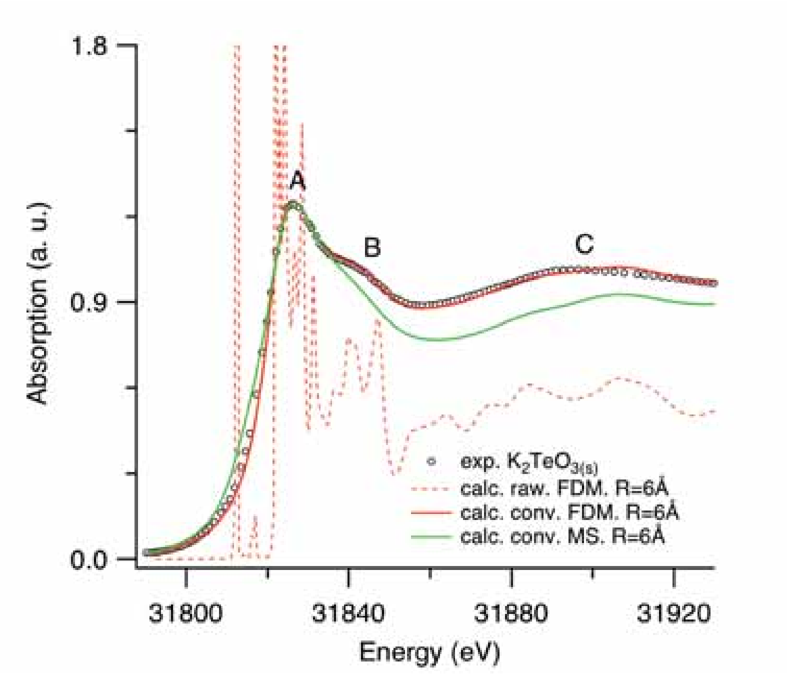

Figure 3.3 XANES simulations for $K_2TeO_{3(s)}$ at Te *K*-edge.

3.3.2 Effect of cluster size

As crystal structures are periodically repeated, contributions from beyond the first coordination sphere may have an effect on the XANES spectrum. Figure 3.4 shows the calculations of $MoO_{2(s)}$ and $MnCO_{3(s)}$ with increasing calculation range. For $MoO_{2(s)}$, in which Mo(IV) exist as a [MoO_6] moiety (Brandt and Skapski, 1967; Bolzan et al., 1995), MST was used to calculate the XANES spectra as a function of radii around the central atom varying from 2.1 Å (7 atoms included in the cluster) to 7.0 Å (121 atoms in the cluster). Figure 3.4a shows that the XANES spectra of a known crystal structure can be better simulated with a longer radius (bigger cluster size).

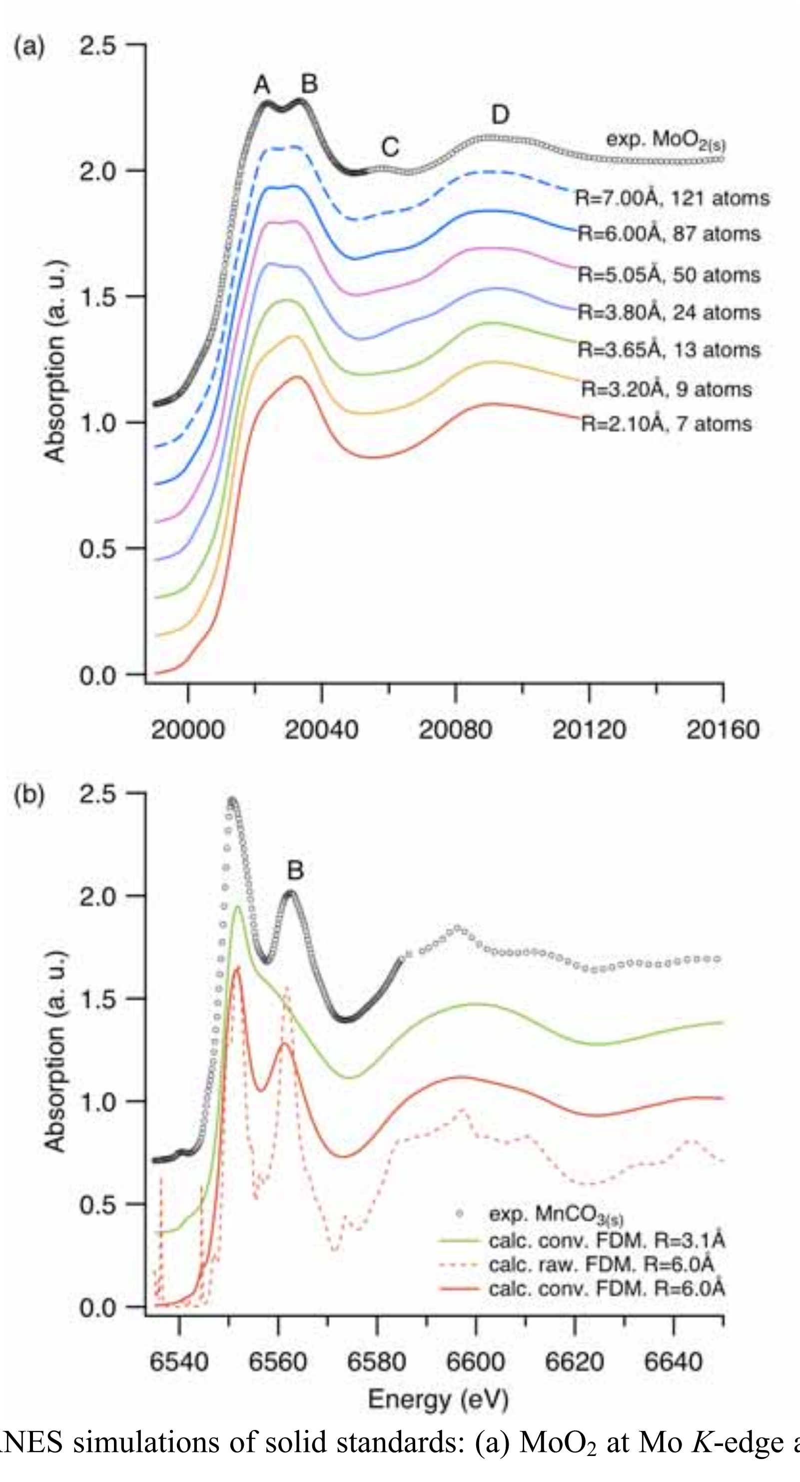

Figure 3.4 XANES simulations of solid standards: (a) MoO_2 at Mo *K*-edge and (b) $MnCO_3$ at Mn *K*-edge.

In particular, band (C) is correctly calculated only in the calculations with radius ≥ 6.0 Å, and the shape of the white line (A) from 3.8 Å, i.e. where the calculation includes a full second shell of Mo atoms. Further increase of calculation radius from 6 Å to 7 Å does not produce significant changes in the calculated spectra. Mn(II) exists as a [MnO_6] moiety in $MnCO_{3(s)}$ (Maslen et al., 1995). As can be seen from Figure 3.4b, the peak (B) at 6562 eV is missing on the convoluted spectrum of 3.1 Å by FDM but well reproduced by the FDM calculation of 6.0 Å. Therefore, inclusion of only first shell around the absorbing atom is not sufficient to calculate all spectral features for solid standards, and a calculation range of up to 6 or 7 Å is needed to correctly reproduce some fine spectral features.

3.4 *Ab initio* XANES simulations for aqueous species

Combined with the results of EXAFS analysis (coordination number, bond distance), *ab initio* XANES calculations were performed to simulate unknown solution spectra to explore the structure of aqueous species. Calculated XANES spectra for different geometries and structures are compared to experimental spectra in order to assess the influence of electronic and structural parameters, and to use the qualitative agreement with experimental spectra to ascertain the presence or absence of different species. Many factors such as SCF calculations, geometrical distortion, bond distance, stoichiometry, hydrogen, second shell may influence the XANES spectra, and these factors are discussed below.

3.4.1 Effect of the self-consistent field (SCF) calculations

As XANES and EXAFS analysis suggest that [TeO_3] and [$Te(OH)_3$] species may predominate Te(IV) speciation in strongly basic and acidic solutions, respectively. XANES calculations (without SCF) for these two species were performed via FDM method as a first attempt to reproduce experimental spectra (blue lines in Figure 3.5). It was found that the calculated spectrum was in good agreement with experimental data but white line (A) was over-estimated. Hence, SCF calculations were conducted in a second step and the white line peak (A) of SCF calculations (red lines in Figure 3.5) were more accurately reproduced, resulting in a better intensity ratio of the white line (A) and band (B). Although Bunău and Joly (2009) concluded that the choice of FDM versus the MST method plays a first order control on the amelioration of calculated spectra compared to the effect of SCF over non-SCF calculations, in the case of Te(IV) species here, SCF calculations were able to further improve the agreement between experiment and theoretical calculations.

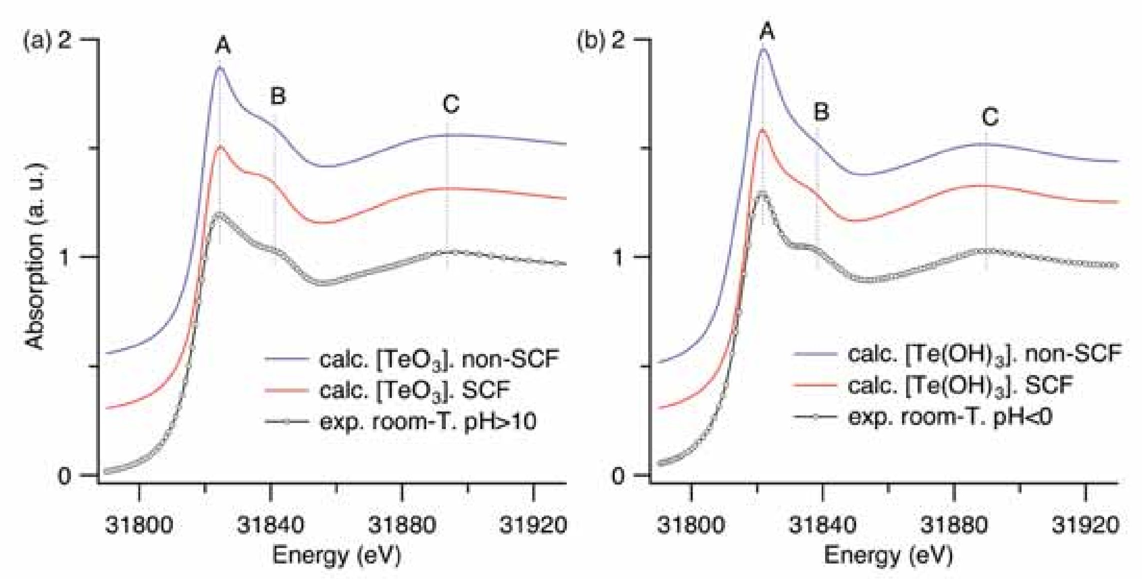

Figure 3.5 Comparisons of experimental spectra with calculated XANES spectra of (a) [TeO_3] and (b) [$Te(OH)_3$] with and without SCF.

3.4.2 Effect of bond distance

The bond distance can have some impact on the calculated XANES spectra. EXAFS refinements of experimental solutions with 0-5.8 m Cl from room-T up to 340 ˚C suggest that $[MoO_4]^{2-}$ is the predominant species over a wide range of T and salinity at near neutral and basic conditions and the fitted Mo=O bond length is 1.777 Å for the dilute solution at 25 ˚C (Borg et al., 2012). The XANES spectra of experimental solutions (0.41 m Na_2MoO_4 with 0 m NaCl at 25 ˚C and 0.17 m Na_2MoO_4 with 5.8 m NaCl at 340 ˚C) are compared to the calculated spectra using a Mo-O distance of 1.777 Å, as derived from EXAFS refinements (see Figure 3.6a and Borg et al., 2012). The models used in the calculation for the [MoO_4] cluster were a regular tetrahedron (T_d) and a slightly distorted tetrahedron with angles taken from the $Na_2MoO_4.2H_2O_{(s)}$ compound (Capitelli et al., 2006). Both pre-edge and white-line features observed in the experiments have been well reproduced in the convoluted spectra. The only significant difference between the two models lies in the pre-edge intensity, where the distorted tetrahedron has higher intensity. This is attributed to increased d-p orbital mixing and site asymmetry in the distorted tetrahedron, where electric dipole plays an important role (Shulman et al., 1976; Westre et al., 1997; Yamamoto, 2008; de Groot et al., 2009). Figure 3.6b shows that the pre-edge intensity and position of the white line peak (most intense line at ~20040 eV) are highly sensitive to the average Mo=O distance used in calculations. The tendency is that the longer Mo-O bond distance, the shorter the pre-edge peak and the higher energy position of white line peak, which is consistent with the spectral evolution of tetrahedral cluster as a function of Mn-O bond distance as noted by Bunker (2010). Thus, XANES simulations confirm that a tetrahedral $[MoO_4]^{2-}$ species (T_d or slightly distorted) predominates in near neutral and basic solutions over a wide range of salinity (0-5.8 m NaCl) and temperature (25-340 ˚C) at 600 bars pressure, and that the geometry of the complex does not change over the investigated P-T-composition range.

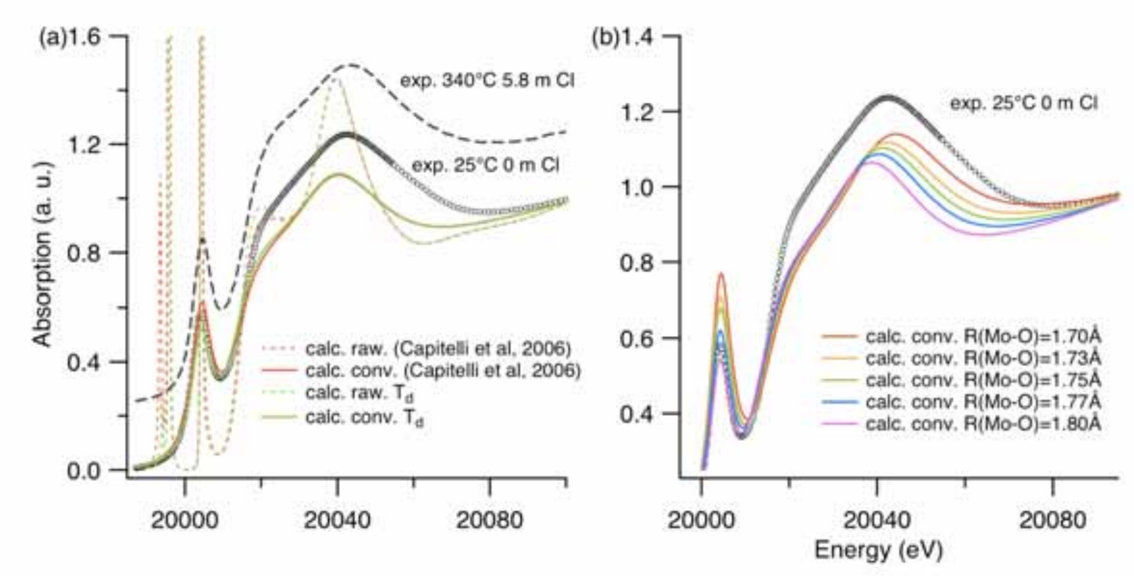

Figure 3.6 XANES calculations of the [MoO_4] cluster at Mo *K*-edge: (a) standard tetrahedral [MoO_4] and distorted [MoO_4] with angles taken from the Na_2MoO_4•$2H_2O_{(s)}$ compound (Capitelli et al., 2006); (b) distorted [MoO_4] as a function of Mo=O bond distances.

3.4.3 Effect of stoichiometry and distortion

XANES analysis and EXAFS refinements suggest that H_2O molecules are progressively substituted by Cl^- ligands around the central metal cation within an octahedral or tetrahedral coordination sphere upon increasing salinity and / or temperature (e.g., Bazarkina et al., 2010; Liu et al., 2011, 2012). Here we present *ab initio* XANES simulations for a series of octahedral Mo species - $[MoO_2Cl_n(H_2O)_{(4-n)}]^{-(n-2)}$ (n = 1, 2 and 3). The calculated spectra display four main spectral features, labelled A, B, C and D (Figure 3.7a). The substitution of Cl^- ions for H_2O ligands in the first coordination shell of the complex results in an increase of the intensity of features A and D. This trend is consistent with the spectral evolution observed experimentally with increasing temperature for solution S9b (0.226 m Na_2MoO_4 and 6.21 m HCl). The band at around 20033 eV (feature B) shows a growth of intensity, but also a shift to higher energy with increasing number of chlorines. The small bump at 20055 eV (feature C) and the pre-edge peak at 20007 eV are properly calculated in the raw spectrum but are not clearly visible in convoluted spectra. Among the series, $MoO_2Cl_2(H_2O)_{2(aq)}$ has the highest intensity in feature C, and is considered to be in better agreement with the experimental spectrum at 166 ˚C. Calculations based on a distorted octahedron as in the crystal structure of $MoO_2Cl_2(H_2O)_2$•H_2O•Et_4NCl (Taylor et al., 1993) have a more intense pre-edge, and better match the measured pre-edge. We also calculated the cis- and trans-configurations for a distorted octahedral geometry; the configuration has a relatively large effect on the C and D bands, with the trans-configuration matching the experiment better (prominent C band). The above analysis supports that $MoO_2Cl_2(H_2O)_{2(aq)}$ in distorted octahedral coordination is an abundant species in strongly acidic solutions from room temperature up to 166 ˚C. XANES spectra of higher-order Mo-oxo-chloride complexes are calculated and compared with the experimental spectrum collected from solution S9b at 340 ˚C in Figure 3.7b. The clusters calculated here include a square pyramidal [$MoOCl_4$] unit, an octahedral [$MoOCl_5$] unit with bond lengths derived from the EXAFS refinements (see details in appendix B), and a distorted octahedron as in the crystal structure of $MoOCl_{4(s)}$ (Taylor and Waugh, 1980). The calculated spectra from above square pyramidal and octahedral clusters are broadly similar to each other and to the experimental spectra. The main differences are the pre-edge, which is absent in the $MoOCl_5$ cluster with undistorted octahedral coordination and most prominent in the square pyramidal structure; and the small band at C, which is absent from the octahedral $MoOCl_5$ clusters with a single Mo-Cl distance, but well reproduced in a $MoOCl_5$ cluster that contains 4 Cl ligands at 2.39 Å and one Cl at 2.90 Å. The feature C is also present, but less prominent, in the square pyramidal [$MoOCl_4$] structure. These calculations show that square pyramidal and distorted octahedral structures with a long Mo-Cl bond are difficult to distinguish on the basis of XANES data.

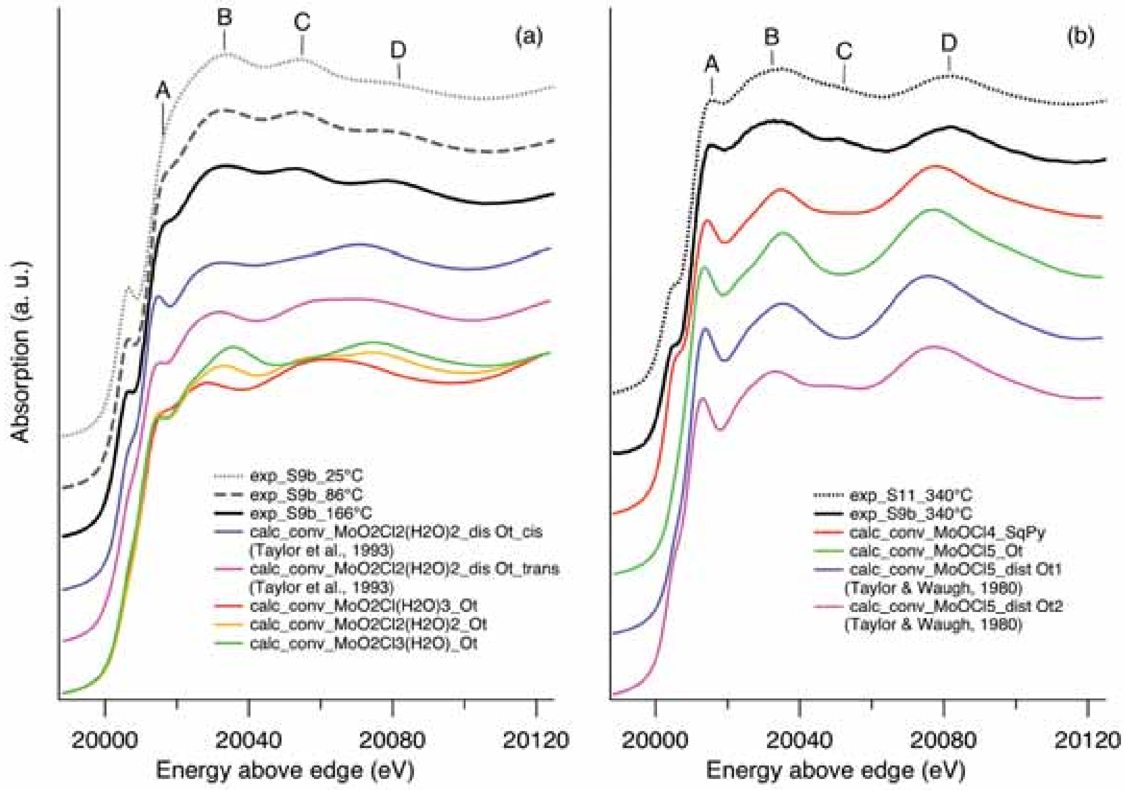

Figure 3.7 (a) XANES calculations of Mo complexes $[MoO_2Cl_n(H_2O)_{(4-n)}]^{(2-n)}$ (n = 1, 2 and 3) existing in strongly acidic solutions at low temperature (25 – 166 °C), and (b) XANES calculations of higher order complexes $[MoOCl_4]_{(aq)}$ and $[MoOCl_5]^-$ at 340 °C.

In addition, *ab initio* XANES simulations for a series of octahedral and tetrahedral species with different stoichiometry provided additional evidence for the predominance of $[M(H_2O)_6]^{2+}$ (M = Ni and Mn) at room-T in low salinity solutions and of $[MCl_3(H_2O)]^-$ (M = Ni and Mn) species in concentrated brines at elevated T-P (see details in chapters 4 and 5). Another example for the effect of distortion is that calculation for a distorted tetrahedral $[NiCl_3(H_2O)]$ cluster optimized by Density Functional Theory (DFT) is in better agreement with experimental spectrum (S8, 7.682 m Cl, 434 ˚C, 600 bar) than those of regular tetrahedral and square planar structural models (see details in chapter 4).

3.4.4 Effect of hydrogen

It is shown in Figure 3.8a that XANES calculations of [Ni(H_2O)$_6$] and [NiO_6] yielded only minor differences regarding the intensity of feature (B) and the position of band (C). The effect of hydrogen atoms on the calculated spectra is relatively small in this case. However, in some cases, the effect of hydrogen is significant, and inclusion of hydrogen in the calculations is compulsory to reproduce the experimental spectra. For instance, *ab initio* XANES calculations show that the spectral differences of acidic and basic Te(IV) solutions are not due to a change in coordination, but are attributed to a deprotonation process associated with changes of Te-O bond distances and the O-Te-O bond angles. To test the effect of hydrogen atoms, we calculated the spectra of four clusters – [Te$(OH)_3$], [TeO(OH)-$_2$], [TeO_2(OH)], and [TeO_3] in a similar manner to the As counterparts (Testemale et al., 2011). These species have the same TeO_3 entity that is present in $K_2TeO_{3(s)}$ (Andersen et al., 1989) with a Te-O distance of 1.90 Å and O-Te-O angles of 101.5°. The O-H bond lengths of 0.97 Å and Te-O-H angles of 117.6° were fixed so that the [Te$(OH)_3$] moiety has a C_{3v} symmetry. Deprotonation causes the white line (A) and the shoulder (B) to shift to higher energy, a reduction in the intensity for feature (A), and an increase in the intensity of feature (B) (see Figure 3.8b). Band (C) remained unchanged during this deprotonation process, as it is strongly related to the Te-O bond length. Changing the Te-O bond distance from 1.90 Å to 1.80 Å within the same [TeO_3] geometry resulted in a systematic spectral alteration in which the shorter the distance, the lower the white line (A) and the higher the energy positions of shoulder (B) and band (C). Deprotonation and bond distance contraction happen simultaneously; calculations that took into account both effects correctly reproduced the key spectral features of basic and acid solutions: [TeO_3] (1.83 Å dashed blue in Figure 3.8b) and [Te$(OH)_3$] (1.90 Å solid blue), indicating that these are the predominant species in the two extreme pH conditions.

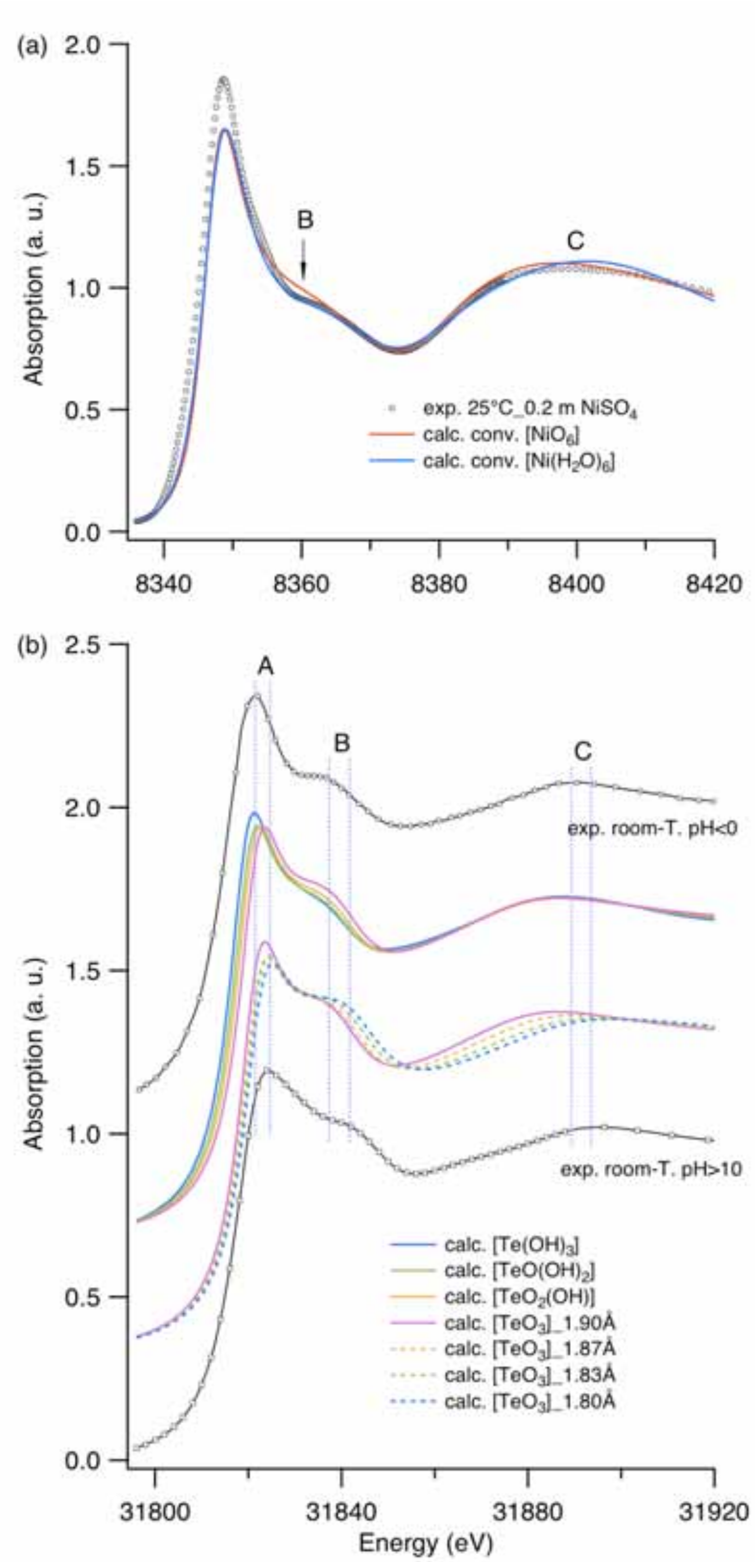

Figure 3.8 (a) Effect of hydrogen: XANES calculations of $[Ni(H_2O)_6]$ and $[NiO_6]$ at Ni *K*-edge; (b) Effect of deprotonation and bond length contraction: XANES calculations of $[Te(OH)_3]$, $[TeO(OH)_2]$, $[TeO_2(OH)]$ and $[TeO_3]$ at Te *K*-edge.

3.4.5 Contributions of second hydration shell

To assess the effect of hydration beyond the first shell, classical MD code - MOLDY (Refson, 2000) was used to generate atomic configurations around the metal complexes of interest, e.g., $[MnCl_3(H_2O)]^-$. Detailed information for the setup of classical MD simulation can be seen in chapter 5. Twenty frames were randomly selected from atomic configurations run by MOLDY which were used as the input file for XANES calculations. The calculated convoluted spectrum for each frame was averaged and shown as the blue solid line and the raw spectrum of one typical frame was shown as the green dashed line in Figure 3.9. The main discrepancies between calculation of first shell and experiment lie in the missing shoulder (B) at 6546 eV on the convoluted spectrum and double peaks (B) present at the white line. Inclusion of the second shell has a minor effect on the convoluted XANES spectrum, and results mainly in a better visual agreement with the experimental spectra: reduced intensity of pre-edge (A) and feature (D); and a more correct shape of white line (C) at the edge region. A peak at 6548 eV corresponding to shoulder (B) on the experimental spectrum appeared in the raw spectrum of some frames (green dashed line); this shows that feature B is probably related to solvation.

In the simple simulations reported here, the structures of $[MnCl_3(H_2O)]^-$ and water molecules are rigid. *Ab initio* MD simulations are expected to provide more information for the structural disorder for the first shell and to further improve the agreement between experiment and theoretical calculations (e.g., D'Angelo et al., 2006).

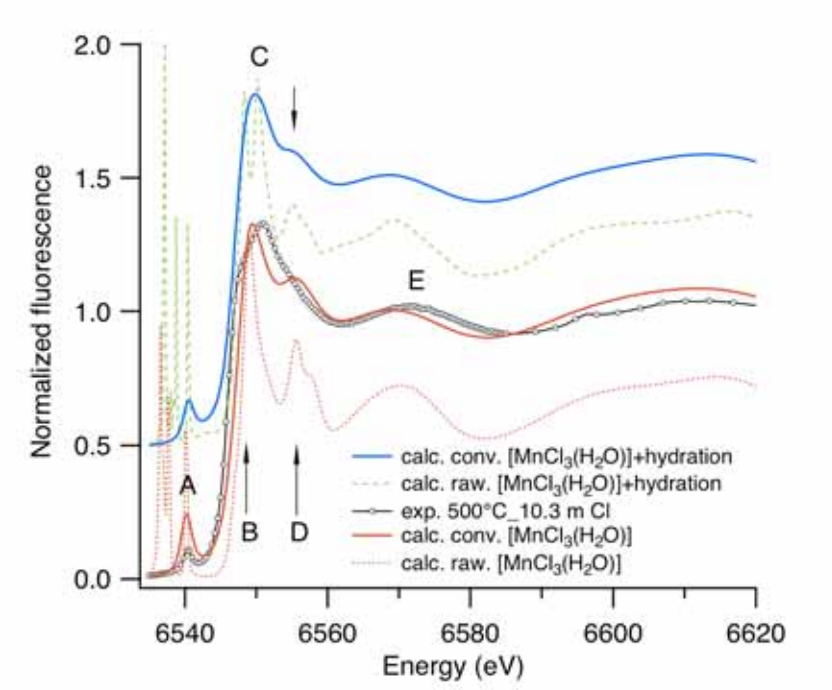

Figure 3.9 Effect of second hydration shell: XANES calculations of [$MnCl_3(H_2O)$] cluster with and without second hydration shell at Mn *K*-edge (blue solid line is the average of 20 frames from classical MD simulation; green dashed line is from one single frame; red solid and dotted lines are convoluted and raw spectra from DFT optimized geometry, respectively).

3.5 Conclusions

Overall, *ab initio* XANES simulation is a powerful technique to investigate the local geometric and electronic structure of absorbing atoms, which can provide complementary or addition information regarding the stoichiometry and geometry for the complexes of interest. By using *ab inito* XANES simulations, several issues have been addressed and some conclusions can be drawn as below:

1) The XANES spectra for known structures (e.g., solid standards) can be correctly calculated by *ab initio* XANES simulations via either the MST or FDM method. Calculations with a cluster size of 6 or 7 Å can reproduce even minor spectral features

accurately. For aqueous species, structural and thermal disorder and second shell may contribute to the XANES spectra, resulting in some discrepancies between experiments and calculations if only a rigid first shell cluster is taken into account (e.g., intensity and shape of key spectral features such as pre-edge and white line). Classical MD simulations provide useful insights into these effects. More accurate *ab initio* Molecular Dynamics (MD) simulations will generate more realistic configurations of aqueous species and surrounding shells (Sherman, 2007, 2010; D'Angelo et al., 2006; Migliorati et al., 2011).

2) XANES simulations successfully distinguished different aqueous metal complexes with different stoichiometry, where EXAFS results were ambiguous or had a larger uncertainty. For example, XANES simulations provided additional evidence for the predominance of tri-chloro one aqua complex – $[MCl_3(H_2O)]^-$ (M = Ni and Mn) rather than the fully chlorinated MCl_4^{2-} complexes in highly saline solutions at elevated temperature. The predominance of the MoO_4^{2-} species over a wide range of temperature and salinity (25-340 ˚C, 0-5.76 m Cl) in basic, neutral, and even weakly acidified solutions was supported by XANES calculations.

3) XANES simulations suggested that the O-Te-O bond angle and Te-O bond distance of the $[TeO_3]$ moiety may be dynamic and stable over a limited range (1.80 - 1.90 Å and 90 - 120°), and that the species $MoO_2Cl_2(H_2O)_{2(aq)}$, with a distorted octahedral geometry, is abundant in strongly acidic solutions from room temperature up to 166 ˚C. In addition, XANES simulations provided experimental evidence for a distorted tetrahedral structure rather than a square planar one for the $NiCl_3(H_2O)^-$ complex, confirming that predictions from DFT structure optimization calculations.

4) XANES simulations provided strong support for retrieving thermodynamic properties for aqueous complexes. The XANES calculations help to constrain the nature of the complexes present in the experimental solutions, and to validate the speciation model that underpins thermodynamic fitting.

Acknowledgement: The FDMNES calculations were supported by iVEC through the use of the EPIC advanced computing resource located in Perth, Australia.

3.6 References

Andersen, L., Langer, V., Stromberg, A., Stromberg, D., 1989. The structure of K_2TeO_3 - an experimental and theoretical study. *Acta Crystallographica Section B* **45**, 344-348.

Ankudinov, A.L., Ravel, B., Rehr, J.J., Conradson, S.D., 1998. Real-space multiple-scattering calculation and interpretation of x-ray-absorption near-edge structure. *Physical Review B* **58**, 7565-7576.

Bazarkina, E.F., Pokrovski, G.S., Zotov, A.V., Hazemann, J.-L., 2010. Structure and stability of cadmium chloride complexes in hydrothermal fluids. *Chemical Geology* **276**, 1-17.

Benfatto, M., Congiu-Castellano, A., Daniele, A., Della Longa, S., 2001. MXAN : a new software procedure to perform geometrical fitting of experimental XANES spectra. *Journal of Synchrotron Radiation* **8**, 267-269.

Benfatto, M., D'Angelo, P., Della Longa, S., Pavel, N.V., 2002. Evidence of distorted fivefold coordination of the Cu^{2+} aqua ion from an x-ray-absorption spectroscopy quantitative analysis. *Physical Review B* **65**, 174205.

Benfatto, M., Della Longa, S., Natoli, C.R., 2003. The MXAN procedure: a new method for analysing the XANES spectra of metalloproteins to obtain structural quantitative information. *Journal of Synchrotron Radiation* **10**, 51-57.

Benfatto, M., Solera, J.A., Chaboy, J., Proietti, M.G., García, J., 1997. Theoretical analysis of x-ray absorption near-edge structure of transition-metal aqueous complexes in solution at the metal K edge. *Physical Review B* **56**, 2447-2452.

Berry, A.J., Hack, A.C., Mavrogenes, J.A., Newville, M., Sutton, S.R., 2006. A XANES study of Cu speciation in high-temperature brines using synthetic fluid inclusions. *American Mineralogist* **91**, 1773-1782.

Bolzan, A., Kennedy, B., Howard, C., 1995. Neutron Powder Diffraction Study of Molybdenum and Tungsten Dioxides. *Australian Journal of Chemistry* **48**, 1473-1477.

Borg, S., Liu, W., Etschmann, B., Tian, Y., Brugger, J., 2012. An XAS study of molybdenum speciation in hydrothermal chloride solutions from 25–385 °C and 600 bar. *Geochimica et Cosmochimica Acta* **92**, 292-307.

Brandt, B. G., and Skapski, A. C., 1967. A refinement of the crystal structure of molybdenum dioxide. *Acta Chemica Scandinavica* **21**, 661-672.

Brugger, J., Etschmann, B., Liu, W., Testemale, D., Hazemann, J.L., Emerich, H., van Beek, W., Proux, O., 2007. An XAS study of the structure and thermodynamics of Cu(I) chloride complexes in brines up to high temperature (400 °C, 600 bar). *Geochimica et Cosmochimica Acta* **71**, 4920-4941.

Bunău, O., Joly, Y., 2009. Self-consistent aspects of x-ray absorption calculations. *Journal of Physics: Condensed Matter* **21**, 345501.

Bunker, G., 2010. *Introduction to XAFS: A Practical Guide to X-ray Absorption Fine Structure Spectroscopy*, 1st ed. Cambridge University Press, New York.

Capitelli, F., Selim, M.D., Mukherjea, K.K., 2006. Synthesis and crystal structure determination of sodium molybdate dihydrate. *Asian Journal of Chemistry* **18**, 2856-2860.

Chaboy, J., Munoz-Paez, A., Merkling, P.J., Marcos, E.S., 2006. The hydration of Cu^{2+}: Can the Jahn-Teller effect be detected in liquid solution? *The Journal of Chemical Physics* **124**, 064509-064509.

D'Angelo, P., Benfatto, M., Della Longa, S., Pavel, N.V., 2002. Combined XANES and EXAFS analysis of Co^{2+}, Ni^{2+}, and Zn^{2+} aqueous solutions. *Physical Review B* **66**, 064209.

D'Angelo, P., Roscioni, O.M., Chillemi, G., Della Longa, S., Benfatto, M., 2006. Detection of second hydration shells in ionic solutions by XANES: computed spectra for Ni^{2+} in water based on molecular dynamics. *Journal of the American Chemical Society* **128**, 1853-1858.

de Groot, F., Vanko, G., Glatzel, P., 2009. The 1s x-ray absorption pre-edge structures in transition metal oxides. *Journal of Physics: Condensed Matter* **21**, 104207.

Etschmann, B.E., Black, J.R., Grundler, P.V., Borg, S., Brewe, D., McPhail, D.C., Spiccia, L., Brugger, J., 2011. Copper(I) speciation in mixed thiosulfate-chloride and ammonia-chloride solutions: XAS and UV-Visible spectroscopic studies. *RSC Advance* **1**, 1554-1566.

Etschmann, B.E., Liu, W., Testemale, D., Müller, H., Rae, N.A., Proux, O., Hazemann, J.L., Brugger, J., 2010. An in situ XAS study of copper(I) transport as hydrosulfide complexes in hydrothermal solutions (25-592 °C, 180-600 bar): speciation and solubility in vapor and liquid phases. *Geochimica et Cosmochimica Acta* **74**, 4723-4739.

Falck, L., Lindqvist, O., 1978. X-ray refinement of the structure of cubic telluric acid. *Acta Crystallographica Section B* **34**, 3145-3146.

Farges, F., Brown, G.E., Jr., Rehr, J.J., 1997. Ti K-edge XANES studies of Ti coordination and disorder in oxide compounds: Comparison between theory and experiment. *Physical Review B* **56**, 1809-1819.

Garcia, J., Bianconi, A., Benfatto, M., Natoli, C.R., 1986. Coordination geometry of transition-metal ions in dilute-solutions by XANES. *Journal De Physique* **47**, 49-54.

James-Smith, J., Cauzid, J., Testemale, D., Liu, W., Hazemann, J.-L., Proux, O., Etschmann, B., Philippot, P., Banks, D., Williams, P., Brugger, J., 2010. Arsenic speciation in fluid inclusions using micro-beam X-ray absorption spectroscopy. *American Mineralogist* **95**, 921-932.

Joly, Y., 2001. X-ray absorption near-edge structure calculations beyond the muffin-tin approximation. *Physical Review B* **63**, 125120.

Joly, Y., Cabaret, D., Renevier, H., Natoli, C.R., 1999. Electron Population Analysis by Full-Potential X-Ray Absorption Simulations. *Physical Review Letters* **82**, 2398.

Joly, Y., 2012. *FDMNES users' guide*. Institut Néel, CNRS, Grenoble, France.

Kelly, S., Hesterberg, D., Ravel, B., Ulery, A., and Drees, L., 2008. Analysis of soils and minerals using X-ray absorption spectroscopy. *Methods of soil analysis. Part* **5**, 387-463.

Koningsberger, D.C., Prins, R., 1987. X-ray absorption: Principles, applications, techniques of EXAFS, SEXAFS and XANES.

Krause, M.O., Oliver, J.H., 1979. Natural widths of atomic *K* and *L* levels, *Kα* x-ray lines and several *KLL* Auger lines. *Journal of Physical and Chemical Reference Data* **8**, 329-338.

Liu, W., Borg, S.J., Testemale, D., Etschmann, B., Hazemann, J.-L., Brugger, J., 2011. Speciation and thermodynamic properties for cobalt chloride complexes in hydrothermal fluids at 35–440°C and 600bar: An in-situ XAS study. *Geochimica et Cosmochimica Acta* **75**, 1227-1248.

Liu, W., Borg, S., Etschmann, B., Mei, Y., Brugger, J., 2012. An XAS study of speciation and thermodynamic properties of aqueous zinc bromide complexes at 25-150 °C. *Chemical Geology* **298–299**, 57-69.

Liu, W., Etschmann, B., Foran, G., Shelley, M., and Brugger, J., 2007. Deriving formation constants for aqueous metal complexes from XANES spectra: Zn^{2+} and Fe^{2+} chloride complexes in hypersaline solutions. *American Mineralogist* **92**, 761-770.

Lombi, E., Susini, J., 2009. Synchrotron-based techniques for plant and soil science: opportunities, challenges and future perspectives. *Plant Soil* **320**, 1-35.

Maslen, E.N., Streltsov, V.A., Streltsova, N.R., Ishizawa, N., 1995. Electron density and optical anisotropy in rhombohedral carbonates. III. Synchrotron X-ray studies of $CaCO_3$, $MgCO_3$ and $MnCO_3$. *Acta Crystallographica Section B* **51**, 929-939.

Migliorati, V., Mancini, G., Chillemi, G., Zitolo, A., D'Angelo, P., 2011. Effect of the Zn^{2+} and Hg^{2+} Ions on the Structure of Liquid Water. *The Journal of Physical Chemistry A* **115**, 4798-4803.

Natoli, C.R., Misemer, D.K., Doniach, S., Kutzler, F.W., 1980. First-principles calculation of x-ray absorption-edge structure in molecular clusters. *Physical Review A* **22**, 1104-1108.

Pokrovski, G.S., Tagirov, B.R., Schott, J., Bazarkina, E.F., Hazemann, J.-L., Proux, O., 2009. An in situ X-ray absorption spectroscopy study of gold-chloride complexing in hydrothermal fluids. *Chemical Geology* **259**, 17-29.

Refson, K., 2000. Moldy: a portable molecular dynamics simulation program for serial and parallel computers. *Computer Physics Communications* **126**, 310-329.

Rehr, J.J., Albers, R.C., 1990. Scattering-matrix formulation of curved-wave multiple-scattering theory: Application to x-ray-absorption fine structure. *Physical Review B* **41**, 8139-8149.

Rehr, J.J., Albers, R.C., 2000. Theoretical approaches to x-ray absorption fine structure. *Reviews of Modern Physics* **72**, 621-654.

Rehr, J.J., Ankudinov, A.L., 2005. Progress in the theory and interpretation of XANES. *Coordination Chemistry Reviews* **249**, 131-140.

Rousseau, B., Maes, S.T., Lenstra, A.T.H., 2000. Systematic intensity errors and model imperfection as the consequence of spectral truncation. *Acta Crystallographica Section A* **56**, 300-307.

Sayers, D.E., Stern, E.A., Lytle, F.W., 1971. New Technique for Investigating Noncrystalline Structures: Fourier Analysis of the Extended X-Ray—Absorption Fine Structure. *Physical Review Letters* **27**, 1204-1207.

Sherman, D. M., 2007. Complexation of Cu^+ in Hydrothermal NaCl Brines: Ab initio molecular dynamics and energetics. *Geochimica et Cosmochimica Acta* **71**, 714-722.

Sherman, D. M., 2010. Metal complexation and ion association in hydrothermal fluids: insights from quantum chemistry and molecular dynamics. *Geofluids* **10**, 41-57.

Shulman, G.R., Yafet, Y., Eisenberger, P., Blumberg, W.E., 1976. Observations and interpretation of x-ray absorption edges in iron compounds and proteins. *Proceedings of the National Academy of Sciences of the United States of America* **73**, 1384-1388.

Smolentsev, G., Soldatov, A.V., 2007. FitIt: New software to extract structural information on the basis of XANES fitting. *Computational Materials Science* **39**, 569-574.

Taylor, J.C., Waugh, A.B., 1980. Crystal and molecular structure of molybdenum tetrachloride oxide by neutron and X-ray diffraction. *Journal of the Chemical Society, Dalton Transactions*, 2006-2009.

Taylor, M.J., Jirong, W., Rickard, C.E.F., 1993. Preparation and crystal structure of $MoO_2Cl_2(H_2O)_2{\cdot}H_2O{\cdot}Et_4NCl$ in relation to the nature of the molybdenum(VI) species in hydrochloric acid solutions. *Polyhedron* **12**, 1433-1435.

Teo, B.K., 1986. *EXAFS: basic principles and data analysis*. Springer-Verlag, Berlin.

Testemale, D., Brugger, J., Liu, W., Etschmann, B., Hazemann, J.-L., 2009. In-situ x-ray absorption study of iron(II) speciation in brines up to supercritical conditions. *Chemical Geology* **264**, 295-310.

Testemale, D., Hazemann, J.L., Pokrovski, G.S., Joly, Y., Roux, J., Argoud, R., Geaymond, O., 2004. Structural and electronic evolution of the $As(OH)_3$ molecule in high temperature aqueous solutions: An x-ray absorption investigation. *Journal of Chemical Physics* **121**, 8973-8982.

Testemale, D., Pokrovski, G. S., and Hazemann, J. L., 2011. Speciation of As(III) and As(V) in hydrothermal fluids by in situ X-ray absorption spectroscopy. *European Journal of Mineralogy* **23**, 379-390.

Tian, Y., Etschmann, B., Liu, W., Borg, S., Mei, Y., Testemale, D., O'Neill, B., Rae, N., Sherman, D.M., Ngothai, Y., Johannessen, B., Glover, C., Brugger, J., 2012. Speciation of nickel (II) chloride complexes in hydrothermal fluids: In situ XAS study. *Chemical Geology* **334**, 345-363.

Westre, T.E., Kennepohl, P., DeWitt, J.G., Hedman, B., Hodgson, K.O., Solomon, E.I., 1997. A multiplet analysis of Fe *K*-edge 1s → 3d pre-edge features of iron complexes. *Journal of the American Chemical Society* **119**, 6297-6314.

Yamamoto, T., 2008. Assignment of pre-edge peaks in K-edge X-ray absorption spectra of 3d transition metal compounds: electric dipole or quadrupole? *X-Ray Spectrometry* **37**, 572-584.

Chapter 4

Speciation of Nickel (II) chloride complexes in hydrothermal fluids: *in situ* XAS study*

*This chapter is based on the following paper:

Tian, Y., Etschmann, B., Liu, W., Borg, S., Mei, Y., Testemale, D., O'Neill, B., Rae, N., Sherman, D.M., Ngothai, Y., Johannessen, B., Glover, C., Brugger, J., 2012. Speciation of nickel (II) chloride complexes in hydrothermal fluids: In situ XAS study. Chemical Geology 334, 345-363.

Y. Tian, B. Etschmann, W. Liu, S. Borg, Y. Mei, D. Testemale, B. O'Neill, N. Rae, D.M. Sherman, Y. Ngothai, B. Johannessen, C. Glover and J. Brugger (2012) Speciation of nickel (II) chloride complexes in hydrothermal fluids: In situ XAS study.
Chemical Geology, v. 334, pp. 345-363, December 2012

Chapter 5

Speciation and thermodynamic properties of Manganese (II) chloride complexes in hydrothermal fluids: *in situ* XAS study*

*This chapter is based on the following manuscript:

Tian, Y., Etschmann, B., Mei, Y., Grundler, P., Testemale, D., Hazemann, J.-L., Elliott, P., Ngothai, Y., Brugger, J., Speciation and thermodynamic properties of Manganese (II) chloride complexes in hydrothermal fluids: *in situ* XAS study. (under review for Geochimica Cosmochimica Acta)

Speciation and thermodynamic properties of Manganese (II) chloride complexes in hydrothermal fluids: *in situ* XAS study

Yuan Tian[1, 2], *Barbara Etschmann*[2, 3], *Yuan Mei*[2, 3, 4], *Pascal V. Grundler*[2, 3†], *Denis Testemale*[5], *Jean-Louis Hazeman*[5], *Peter Elliott*[2], *Yung Ngothai*[1], *Joël Brugger*[2, 3*]

1. School of Chemical Engineering, The University of Adelaide, Adelaide 5000, South Australia, Australia
2. Division of Mineralogy, South Australian Museum, Adelaide 5000, South Australia, Australia
3. Tectonics, Resources and Exploration (TRaX), School of Earth and Environmental Sciences, The University of Adelaide, Adelaide 5000, South Australia, Australia
4. CSIRO Earth Science and Resource Engineering, Clayton, Victoria, 3168, Australia
5. Institut Neel, Département MCMF, 38042 Grenoble, France; and FAME beamline, ESRF, 38043 Grenoble, France

† Present address: Laboratory for Nuclear Materials, Paul Scherrer Institute, CH-5232 Villigen PSI, Switzerland

* Corresponding author: joel.brugger@adelaide.edu.au

Abstract

The speciation of Mn(II) in acidic brines under a wide range of conditions (30-550 ˚C, 600 bar, 0.100 - 10.344 *m* chloride and 0.110 - 2.125 *m* bromide) was investigated using *in situ* X-ray Absorption Spectroscopy (XAS). Increasing temperature and/or salinity results in a structural change of the Mn(II) complexes from octahedral to (distorted) tetrahedral. Octahedral species predominate at room temperature within the whole salinity range and persist up to ~400 ˚C in low salinity solutions ($m_{Cl} < 1$ *m*), and tetrahedral species become significant above 300 ˚C. A combination of EXAFS refinements, Density Functional Theory calculations and *ab initio* XANES simulations shows that at temperatures ≥ 400 ˚C, the highest order chlorocomplex predominating in high salinity solutions ($m_{Cl} > 3$ m, Cl:Mn ratio > 53) is $MnCl_3(H_2O)^-$, and that a lower order chlorocomplex, $MnCl_2(H_2O)_{2(aq)}$, is the predominant species in low salinity solutions ($m_{Cl} < 0.5$ *m*, Cl:Mn ratio < 10). A similar result was also found in Mn bromide solutions: $MnBr_3(H_2O)^-$ and $MnBr_2(H_2O)_{2(aq)}$ are the dominant species at 500 ˚C in high salinity solutions (e.g., 2.125 *m*, Br:Mn ratio = 33.73) and in low salinity solutions (e.g., 0.110 *m*, Br:Mn ratio = 2.04), respectively. XANES spectra of Mn(II) chloride solutions were used to retrieve formation constants of $MnCl_2(H_2O)_{2(aq)}$ and $MnCl_3(H_2O)^-$ at 600 bar. The speciation and thermodynamic model of this study are consistent with previous solubility and UV-Vis spectroscopic studies.

Keywords: XAS, speciation, thermodynamic properties, Mn(II) chloride complexes, coordination change, EXAFS, XANES, hydrothermal fluids.

5.1 Introduction

Manganese is the second most abundant transition element in the Earth's crust. It is highly mobile in hydrothermal systems, occurring in high concentrations in geothermal waters, with values up to 59 ppm Mn recorded in Mid Oceanic Ridge fluids with Cl concentrations close to that of seawater (~0.5 *m* Cl; James et al., 1995) and values up to 1900 ppm in hypersaline brines (>5 *m* Cl; Salton Sea, McKibben and Williams, 1989). In general, Mn concentrations in natural fluids increase with increasing temperature and with increasing chlorine concentrations, and hypersaline magmatic brines can carry in excess of one wt% Mn (Yardley, 2005). The formation of much of the world's Mn resources is related to shallow hydrothermal circulation and interaction with surface waters (Brugger and Gieré, 1999; Brugger and Meisser 2006; Cornell and Schütte, 1995; Roy, 1992), but due to its mobility, Mn is an important metal in many hydrothermal processes (e.g. epithermal deposits; Davies et al., 2008).

Accurate modeling of the transport and deposition of Mn under hydrothermal conditions is required to improve predictive mineral exploration and to increase the efficiency of mineral and metallurgical processing techniques (e.g., Brugger et al., 2007; Seward and Driesner, 2004). Understanding Mn transport and deposition relies on our knowledge of the aqueous complexes responsible for the mobility of Mn in hydrothermal fluids and on the availability of thermodynamic properties for each of the relevant species as a function of pressure, temperature, and fluid composition (Brugger et al., 2010; Seward and Barnes, 1997). Mn is widely accepted to exist mainly in the form of the Mn(II) aqua ion and Mn(II) chloro complexes in hydrothermal waters (McKibben and Williams, 1989; Gammons and Seward, 1996; Yardley, 2005), and a number of studies have been carried out to investigate Mn(II) aqueous speciation over a wide range of conditions using different techniques (Table 5.1).

At temperatures to 300 ˚C, there is good agreement that the Mn^{2+} aqua ion, $[Mn(H_2O)_6]^{2+}$ (e.g., Koplitz et al., 1994) and low order octahedral chlorocomplexes (mainly $MnCl^+$) predominate in acidic waters containing up to ~1 m Cl. $MnCl^+$ was identified on the basis of potentiometric (Libuś and Tialowska, 1975), electron spin resonance (Wheat and Carpenter, 1988), solubility (Gammons and Seward, 1996) and spectrophotometric (Libuś and Tialowska, 1975; Suleimenov and Seward, 2000) measurements. In highly saline solutions (Cl >> 2 *m*) and with increasing temperature (150-300 ˚C), octahedral $MnCl_{2(aq)}$ becomes an important complex; however no evidence for a higher order Mn(II) chloride complex, e.g., $MnCl_3^-$ and $MnCl_4^{2-}$ was found in solutions up to 300 ˚C (Gammons and Seward, 1996; Suleimenov and Seward, 2000). Boctor (1985) found that Mn(II) speciation was dominated by $MnCl_{2(aq)}$ in supercritical solutions with low Cl:Mn ratio (2-7) over the temperature range 400 to 700 ˚C at 1 and 2 kbar. At higher Cl:Mn ratios (Cl:Mn >> 7), Uchida et al. (1995, 2003) and Uchida and Tsutsui (2000) concluded that $MnCl_3^-$ was the predominant species in 2 mole/(kg H_2O) (*m*) NaCl solutions at similar T-P conditions.

XAS studies of Mn complexing with halide ions at ambient conditions confirmed the existence of a series of six-fold octahedral Mn(II) species $[MnX_n(H_2O)_{(6-n)}]^{(2-n)+}$ (X = Cl and Br; n=0, 1, 2) in solutions containing 0.10 – 4.95 *m* $MnCl_2$, 0.10 – 5.2 *m* $MnBr_2$ and 0.05 – 6 *m* $MnBr_2$ (Beagley et al., 1991; Chen et al., 2005a). Currently, there is no XAS characterization of the structure of Mn(II) chloroaqua complexes in aqueous solutions under hydrothermal conditions, but Chen et al., (2005b) reported a structural transition of Mn(II) bromoaqua complexes from octahedral at room-T, 1 bar to tetrahedral under supercritical conditions (400 ˚C, 310 bar, 0.4 - 1.2 *m* Br_{tot}); this transition mainly occurs below 325 ˚C at 140 bar. The highest order complex identified by Chen et al., (2005b) was $MnBr_3(H_2O)^-$, similarly to the $MnCl_3(H_2O)^-$ complex found in concentrated 2 *m* NaCl solutions at high temperature (Uchida et al., 1995, 2003; Uchida and Tsutsui, 2000).

Table 5.1 Previous studies of aqueous Mn(II) speciation under ambient and hydrothermal conditions.

T, P and composition	Species identified	Reference
Solubility		
400 – 700 °C at 1 and 2 kbar, Cl:Mn ratio = 2 – 7	$MnCl_{2(aq)}$	Boctor,1985
25 – 275 °C at P_{sat}, 4 < pH < 10	Mn^{2+}, $MnHCO_3^+$, $MnCO_{3(aq)}$, $Mn(OH)CO_3$, $Mn(OH)_{2(aq)}$	Wolfram and Krupp, 1996
25 – 300 °C at P_{sat}, 0.01-6.0 *m* HCl and Cl:Mn ratio ⩾ 2	Mn^{2+}, $MnCl^+$, $MnCl_{2(aq)}$	Gammons and Seward, 1996
400 – 600 °C at 1 kbar, 2 *m* NaCl	$MnCl_3^-$	Uchida et al., 1995
300 – 800 °C at 1 kbar, 0.5 – 1 kbar at 600 °C, 2 *m* NaCl	$MnCl_{2(aq)}$, $MnCl_3^-$	Uchida and Tsutsui, 2000
300 – 800 °C at 1 kbar, 2 *m* NaCl	$MnCl_{2(aq)}$, $MnCl_3^-$	Uchida et al., 2003
Electron Spin Resonance spectroscopy		
20 °C at 1 bar, 50 ppb – 15 ppm Mn in marine and lacustrine pore waters	Mn^{2+}, $MnCl^+$, $MnSO_{4(aq)}$, $MnCO_{3(aq)}$, $Mn(HCO_3)^+$	Carpenter, 1983
50 – 170 °C at 1 – 100 bar, ≤ 1.0 *m* Cl	Mn^{2+}, $MnCl^+$, $MnSO_{4(aq)}$	Wheat and Carpenter, 1988
Potentiometry and UV spectroscopy		
25 °C at 1 bar, 0.01*m* Cl	Mn^{2+}, $MnCl^+$	Libuś and Tialowska, 1975
UV-Vis spectroscopy		
25 – 250 °C at P_{sat}, 0.9 *m* $Mn(ClO_4)_2$ with 0.01 *m* $HClO_4$	$Mn(H_2O)_6^{2+}$	Koplitz et al., 1994
25 – 300 °C at P_{sat}, 0.022 – 0.80 *m* Cl	Mn^{2+}, $MnCl^+$, $MnCl_{2(aq)}$	Suleimenov and Seward, 2000
XAS spectroscopy		
Ambient conditions, 0.1 *m* (n-C_4H_9)NXO_4 (X=Cl, Br) in hexamethylphosphoric triamide solution	$MnCl^+$, $MnCl_{2(aq)}$, $MnCl_3^-$, $MnBr^+$, $MnBr_{2(aq)}$, $MnClBr_{(aq)}$, $MnCl_2Br^-$	Ozutsumi et al., 1994
Ambient conditions, 0.10 – 4.95 *m* $MnCl_2$, 0.10 – 5.2 *m* $MnBr_2$	$Mn(H_2O)_6^{2+}$, $MnCl(H_2O)_5^+$, $MnCl_2(H_2O)_{4(aq)}$, $MnBr(H_2O)_5^+$, $MnBr_2(H_2O)_{4(aq)}$	Beagley et al., 1991
Ambient conditions, 0.05 – 6 *m* $MnBr_2$	$Mn(H_2O)_6^{2+}$, $MnBr(H_2O)_5^+$, $MnBr_2(H_2O)_{4(aq)}$	Chen et al., 2005a
25 – 400 °C at 1 – 310 bar, 0.4 – 1.2 *m* Br and Cl:Mn ratio = 2 – 6	$Mn(H_2O)_6^{2+}$, $MnBr(H_2O)_3^+$, $MnBr_2(H_2O)_{2(aq)}$, $MnBr_3(H_2O)^-$	Chen et al., 2005b

This study is dedicated to providing a molecular-level understanding of Mn(II) chloride complexing in chloride solutions ($0.100\ m \leq Cl_{tot} \leq 10.344\ m$) by *in situ* synchrotron-based XAS analysis over a wide temperature range (30 to 550 ˚C, 600 bar). The experimental results are supported by Density Functional Theory (DFT) calculations. This study aims to: i) map the effects of temperature and salinity on the coordination changes of Mn(II) chloroaqua complexes; ii) identify whether high order tetrahedral Mn(II) chloroaqua complexes exist at elevated temperatures and determine the structure (stoichiometry and geometry) of the predominant Mn(II) complexes by EXAFS refinements, DFT calculations and *ab initio* XANES simulations; iii) use the molecular-level understanding of Mn chloride complexing to establish a Mn(II) speciation model that is consistent with the available experimental data (e.g., Suleimenov and Seward, 2000).

5.2 Materials and methods

5.2.1 Experimental samples

Millipore doubly deionized water and analytical grade chemicals ($MnCl_2$•$4H_2O_{(s)}$, $MnBr_2$•$4H_2O_{(s)}$, $NaCl_{(s)}$, $NaBr_{(s)}$, $HCl_{(aq)}$, $HBr_{(aq)}$) purchased from Sigma-Aldrich were used without further treatment. All sample solutions were prepared by dissolving $MnCl_2$•$4H_2O_{(s)}$ or $MnBr_2$•$4H_2O_{(s)}$ in Millipore® doubly deionized water, slightly acidified with HCl/HBr to prevent hydrolysis of Mn^{2+} (Table 5.2). Accurately weighed amounts of $NaCl_{(s)}$/$NaBr_{(s)}$ were added to prepare a series of solutions with the desired chloride/bromide concentration. $LiCl_{(s)}$ was used to achieve the highest chloride concentration (solution 8, $10.344\ m\ Cl_{tot}$) instead of $NaCl_{(s)}$ due to its higher solubility. Distribution of species calculations performed using the HCh package (Shvarov and Bastrakov, 1999) confirms that the hydrolysis of Mn^{2+} can be neglected throughout the whole temperature range in this study based on the thermodynamic properties of $Mn(OH)^+$ from Shock et al. (1997) and of $Mn(OH)_{2(aq)}$ from Wolfram and Krupp (1996) (hydrolysis constants are -9.87, -5.31 for $Mn(OH)^+$ and -17.88, -14.93 for $Mn(OH)_{2(aq)}$ at 30 ˚C and 300 ˚C, 600 bar, respectively).

Table 5.2 List of sample solutions.

Solution No.	Mn [m]	NaCl [m]	HCl [m]	Total Cl [m]	Cl:Mn molar ratio
1	0.050	0	0.0003	0.100	2.00
11	0.050	0.054	0.0026	0.157	3.14
6	0.050	0.154	0.0026	0.257	5.14
13	0.051	0.411	0.0026	0.516	10.12
7	0.053	0.941	0.0027	1.050	19.81
12	0.056	2.001	0.0043	2.117	37.80
9	0.058	2.959	0.0028	3.078	53.07
14	0.061	3.982	0.0028	4.107	67.33
3	0.064	5.000	0.0029	5.131	80.17
Solution No.	Mn [m]	LiCl [m]	HCl [m]	Total Cl [m]	Cl:Mn molar ratio
8	0.141	10.045	0.0167	10.344	73.36
Solution No.	Mn [m]	NaBr [m]	HBr [m]	Total Br [m]	Br:Mn molar ratio
5	0.054	0	0.0016	0.110	2.04
15	0.105	0.990	0.0043	1.204	11.47
4	0.063	1.997	0.0016	2.125	33.73

The oxygen- and moisture-sensitive solid compound tetraethylammonium tetrachloromanganate(II), $(NEt_4)_2MnCl_{4(s)}$, which contains tetrahedral $[MnCl_4]$ moieties (Cotton et al., 1962), was synthesized for use as a solid standard using the following procedure: i) 16.8 g (0.101 mol) $NEt_4Cl_{(s)}$ were dissolved in 14 ml dry ethanol solution and the resulting solution heated to 75 ˚C; ii) 5.3 g (0.042 mol) of $MnCl_{2(s)}$ were dissolved in 34 ml of dry hot ethanol and added to the hot NEt_4Cl solution; iii) upon mixing a creamcolored thick precipitate of $(NEt_4)_2MnCl_{4(s)}$ formed; iv) the solution was cooled down and the precipitate of $(NEt_4)_2MnCl_{4(s)}$ was recovered by filtration on a glass frit and rinsed with three portions of dry ethanol and then dried under dynamic vacuum overnight. All synthetic work was done under anhydrous conditions (dried reactants, inert gas/vacuum line). A micro-chemical CHN analysis was carried out for the $(NEt_4)_2MnCl_{4(s)}$ product (Campbell Microanalytical Laboratory, University of Otago, Dunedin, NZ); the resulting composition of C 42.2%, H 9.04% and N 5.96% (errors not provided) is close to the theoretical values of C 42.0%, H 8.82% and N 6.13%. Crystals suitable for single crystal X-ray diffraction analysis were obtained by recrystallizing the product from anhydrous methanol-ethanol; details of the crystal structure solution and refinement are given in Section 5.8.1. For standards containing Mn in octahedral coordination, rhodochrosite ($MnCO_3$) from the Sweet Home Mine, Colorado (South Australian Museum collection number G9806; $[MnO_6]$ moieties; Maslen et al., 1995) and $MnCl_2{\bullet}4H_2O_{(s)}$ (Sigma-Aldrich; $[MnCl_2(H_2O)_4]$ moieties; Zalkin et al., 1964; El Saffar and Brown, 1971) were used. The identity of these standards was confirmed via X-ray powder diffraction.

5.2.2 XAS Measurements

XAS measurements were conducted at beamline BM-30B (FAME) at the European Synchrotron Research Facility (ESRF). The ESRF is a 6.03 GeV synchrotron, which has a maximum current of 200 mA when operating in 7/8 multi-bunch mode. The FAME beamline is a bending magnet beamline with a double crystal Si(220) monochromator, and an energy resolution of 0.34 eV at the Mn *K*-edge of 6539 eV (Proux et al., 2005). A focused beam size of 145×270 μ m^2 was used, with a beam flux of 2×10^{11} photons/s/200 mA at the Mn *K*-edge. The fluorescence data were measured using a 30 element solid state Canberra fluorescence detector, while transmission data were collected concurrently with Si diodes.

The spectroscopic cell developed by the Laboratoire de Cristallographie, CNRS, Grenoble (Testemale et al., 2005) was used for the XAS measurements. The setup consists of an external water-cooled autoclave equipped with three 1.5 mm thick beryllium windows that allow collection of fluorescence and transmission signals concurrently up to a pressure of 750 bar. The sample solution is enclosed inside a glassy carbon tube, and the pressure is transmitted to the sample by two glassy carbon pistons. The glassy carbon tube is placed inside a small cylindrical resistive heater; the heater and tube are then installed inside the autoclave, which is pressurised using He. The Mn contents of the high purity beryllium (Brush Wellman grade PF60) were ≤ 0.01 wt%, and baseline XAS data show that the Mn signals from the Be windows and scattering off the autoclave components are negligible.

Each solution was loaded into the cell using a syringe at ambient conditions. The autoclave was pressurized to 600±1 bar (Bruyère et al., 2008) at a rate of ~20 bar/min, then the sample solution was heated to the target temperature (±0.5 ˚C). Up to 6 scans were performed at each temperature (30 to 550 ˚C). As the thermocouples are placed outside the glassy carbon tube, not exactly at the position where the beam interacts with the solution, the sample temperature at the beam position is lower than the thermocouple temperature. The solution temperature at the beam position was calibrated by using XAS to measure the density of pure water as a function of thermocouple temperature at 600 bar (e.g. Etschmann et al., 2010; Borg et al., 2012). The mass attenuation coefficients from Chantler (1995) (8.55 keV) and the water densities tabulated in the NIST database (Lemmon et al., 2000) were used in the calculations. The temperatures used throughout this paper are the calibrated temperatures, with estimated precisions better than ± 5 °C.

5.2.3 EXAFS data analysis

EXAFS fluorescence data were analyzed by the HORAE package (Ravel and Newville, 2005), using the procedure outlined in Brugger et al. (2007), Testemale et al. (2009) and Etschmann et al. (2010). EXAFS calculations were performed using FEFF8 (Ankudinov et al., 1998). The FLUO (http://www.aps.anl.gov/xfd/people/haskel/fluo.html) and BOOTH (Booth and Bridges, 2003) algorithms (part of HORAE) were used to check the effect of self-absorption on the fluorescence XANES and EXAFS data, respectively. We found that self-absorption was negligible, and therefore raw data were used in the XANES and EXAFS analysis. A 'spike' at about 6596 eV (~3.6 $Å^{-1}$ in k-space), present on all Mn(II) spectra (feature F in Figures 5.1-5.3), is attributed to a multielectron excitation ($KM_{II,III}$ transition; Chen et al., 2005a). Removal of this feature had negligible effect on the EXAFS refinements, thus the raw spectra were analyzed without further correction. All EXAFS refinements were performed based on k^2-weighted data in R-space using a Hanning window. The goodness of fit was evaluated by two parameters: the R-factor, defined as the fraction of the sum of the squares of the differences between data and fit over the sum of the squares of the data (Newville et al., 1995); and the reduced chi-square, χ^2, which allows a statistical comparison between fits based on different numbers of parameters and different data quality (Kelly et al., 2008).

5.2.4 Density Functional Theory calculations

DFT calculations were performed using the Amsterdam Density Functional program, ADF2010.02 (Te Velde et al., 2001) to optimize the geometries for the proposed Mn(II) complexes. ADF implements DFT for finite clusters and molecules by using linear combinations of atomic orbitals. The basis functions are localized Slater-type orbitals. The Vosko-Wilk-Nusair (VWN) parameterization (Vosko et al., 1980) was used for Local Density Approximation (LDA), together with the Perdew-Burke-Ernzerhof (PBE; Perdew et al., 1996) generalized gradient approximation (GGA) for calculating the exchange-correlation energy (Parr and Yang, 1989). For all atoms, an uncontracted, triple-zeta basis set (TZP) was used with polarization functions (Van Lenthe and Baerends, 2003). Frozen core orbitals (1s, 2s, 2p for Mn; 1s, 2s, 2p for Cl; 1s, 2s, 2p, 3s, 3p for Br and 1s for O) were applied during the calculations to reduce the computational time (Peacock and Sherman, 2004; Te Velde et al., 2001). All calculations were done using the spin-unrestricted formalism to account for the five unpaired 3d-electrons of Mn(II) (Sherman, 2009). The Conductor-like Screening model (COSMO) (Klamt and Schuurmann, 1993; Pye and Ziegler, 1999; Sherman, 2010) was employed to account for long-range solvation in aqueous solutions. In COSMO models, each atom is surrounded by a sphere of radius $R_a = 1.17 \times R_a^{vDW}$ (where R_a^{vDW} is the van der Waals radius of the atom) as optimized by Klamt et al. (1998) in order to define a molecular cavity; radii of 2.1 Å for Mn, 1.72 Å for O, 1.3 Å for H, and 2.05 Å for Cl and Br were used. Outside of this cavity, the solvent is represented as a dielectric continuum. A dielectric constant of 10 and a solvent radius of 1.3 Å were applied to represent hydrothermal fluids at 500 ˚C, 600 bar (Fernandez et al., 1997; Sherman, 2007). The geometry optimizations of Mn(II) clusters were based on a Newton-Raphson approach incorporating a Hessian matrix as coded in ADF. The bond lengths and angles converged to 0.01 Å and 0.5˚, respectively.

5.2.5 Ab initio XANES simulations

Ab initio XANES simulations were conducted using the FDMNES program (Joly, 2001) following the method developed in recent studies of metal complexing (Brugger et al., 2007; Testemale et al., 2009; Etschmann et al., 2010; Liu et al., 2011, 2012; Borg et al., 2012; Tian et al., 2012; Tooth et al., 2012). FDMNES calculates the photo-absorption cross section using two different methods: i) multiple scattering theory, which uses the Muffin Tin (MT) approximation to evaluate the inter-atomic potentials; and ii) the Finite Difference Method (FDM), which avoids the limitations of the MT approximation by allowing a free potential shape (Joly, 2001). To compare to the experimental spectra, the calculated raw data were convoluted with a Lorentzian function of energy-dependent width to reproduce the core-hole lifetime broadening (1.16 eV; Krause and Oliver, 1979) and the inelastic plasmon interactions with the photoelectron. In addition, the spectra were convoluted with a Gaussian function (0.34 eV FWHM) to account for the energy resolution of the beamline. The Fermi energy was fixed to -4 eV for all calculations; this value corresponds to ~five 3*d* electrons (Mn^{2+}) based on examination of the calculated density of state (DOS). These convolution parameters were fixed for all calculations and not fitted in the subsequent analyses. All calculations were carried out with neutral atoms. The calculated spectra were aligned so that the pre-edge and white line peaks are at the same energy position as that of experimental data.

5.3 Qualitative analysis of XAS spectra

5.3.1 Effect of temperature

The Mn *K*-edge XAS spectra of the two solutions containing the lowest and highest Cl concentrations (S1: 0.10 m Cl, Cl:Mn ratio = 2.00; and S8: 10.34 m Cl, Cl:Mn ratio = 73.36) are shown in Figure 5.1 as a function of temperature at 600 bar. With increasing temperature, the changes in XANES spectra include (Figure 5.1a, b): i) the intensity of the pre-edge at ~6540.5 eV (feature A) increases; ii) the shoulder at the lower energy side of the white line (feature B) becomes more prominent; iii) the intensity of the white line (feature C) decreases and its position shifts towards lower energy; and iv) reduced intensity of the oscillation in the 6570 to 6610 eV range (features E and F). This evolution is similar to that observed for Mn^{2+} in bromide solutions (Chen et al., 2005a, b) and for some other divalent transition metals in halide solutions (e.g., Fe^{2+} in chloride solutions, Testemale et al., 2009; Co^{2+} in chloride and bromide solutions, Liu et al., 2011; Ni^{2+} in chloride and bromide solutions, Hoffman et al., 1999, Tian et al., 2012; Cd^{2+} in chloride solutions, Barzakina et al., 2010), and reflects a structural transition from octahedral to tetrahedral-like.

The transition from octahedral to tetrahedral–like structures occurs at higher temperatures for S1 than for S8 (Figure 5.1a-c). For solution S1, only small spectral changes can be observed in the XANES and EXAFS spectra from 25 ˚C to 200 ˚C (Figure 5.1a, c), implying that octahedral complexes are largely dominant over this temperature range. Spectra of S1 change dramatically upon heating from 200 to 500 ˚C, but show only subtle systematic changes upon further heating to 550 ˚C. In contrast, the spectra of solution S8 change rapidly from 30 to 300 ˚C, but evolve slowly at temperatures above 300 ˚C (Figure 5.1b, c), which suggests that Mn speciation in this solution is dominated by a single species at $T > 300$ ˚C. The Fourier-transformed spectra reflect the radial distribution function around Mn^{2+} ions, and the main peaks for $MnCO_{3(s)}$ and $(NEt_4)_2MnCl_{4(s)}$ correspond to six Mn-O and four Mn-Cl bonds, respectively (Figure 5.1d). The centroids of the main peaks of the S1 and S8 solutions are close to those of $MnCO_{3(s)}$ at 30 ˚C, and move to larger R values at 550 ˚C, close to $(NEt_4)_2MnCl_{4(s)}$. The increase of bond distances to neighboring ligands upon heating is related to a chlorination process, which results in the replacement of H_2O by Cl^- in the first shell of Mn^{2+} associated with a structural transition from six-coordination to four-coordination.

The XANES pre-edge feature is strongly indicative of the local geometry of Mn(II) in solids (Farges, 2005; Chalmin et al., 2009) and in aqueous solutions (Chen et al., 2005a, b). The pre-edge peak is due to the 1s→3d transition that is forbidden in symmetrical sites; a small pre-edge in octahedrally coordinated environments is related to a weak electric quadrupole caused by distortion and p-d hybridization (e.g., $MnCl_2 \cdot 4H_2O_{(s)}$; feature A in Figure 5.2b; Shulman et al., 1976; Westre et al., 1997). Intense pre-edges are characteristic of electric dipole transitions, such as those allowed in tetrahedral symmetry (de Groot et al., 2009; Shulman et al., 1976; Westre et al., 1997; Yamamoto, 2008). Hence the pre-edge data are consistent with octahedral complexes dominating at low temperature (Figure 5.2a, b) and tetrahedral complexes at high temperature (Figure 5.2f). Feature B (Figures 5.1 and 5.2) is attributed to the 1s→4p electronic transition (Chen et al., 2005a, b), indicating a strong interaction between metal cation and surrounding ligands, e.g., Cl^-/Br^- and H_2O, like Ca(II) (Fulton et al., 2003), Fe(II) (Testemale et al., 2009), Co(II) (Liu et al., 2011) and Ni(II) (Tian et al., 2012) in chloride solutions, and Mn(II) in bromide solutions (Chen et al., 2005a).

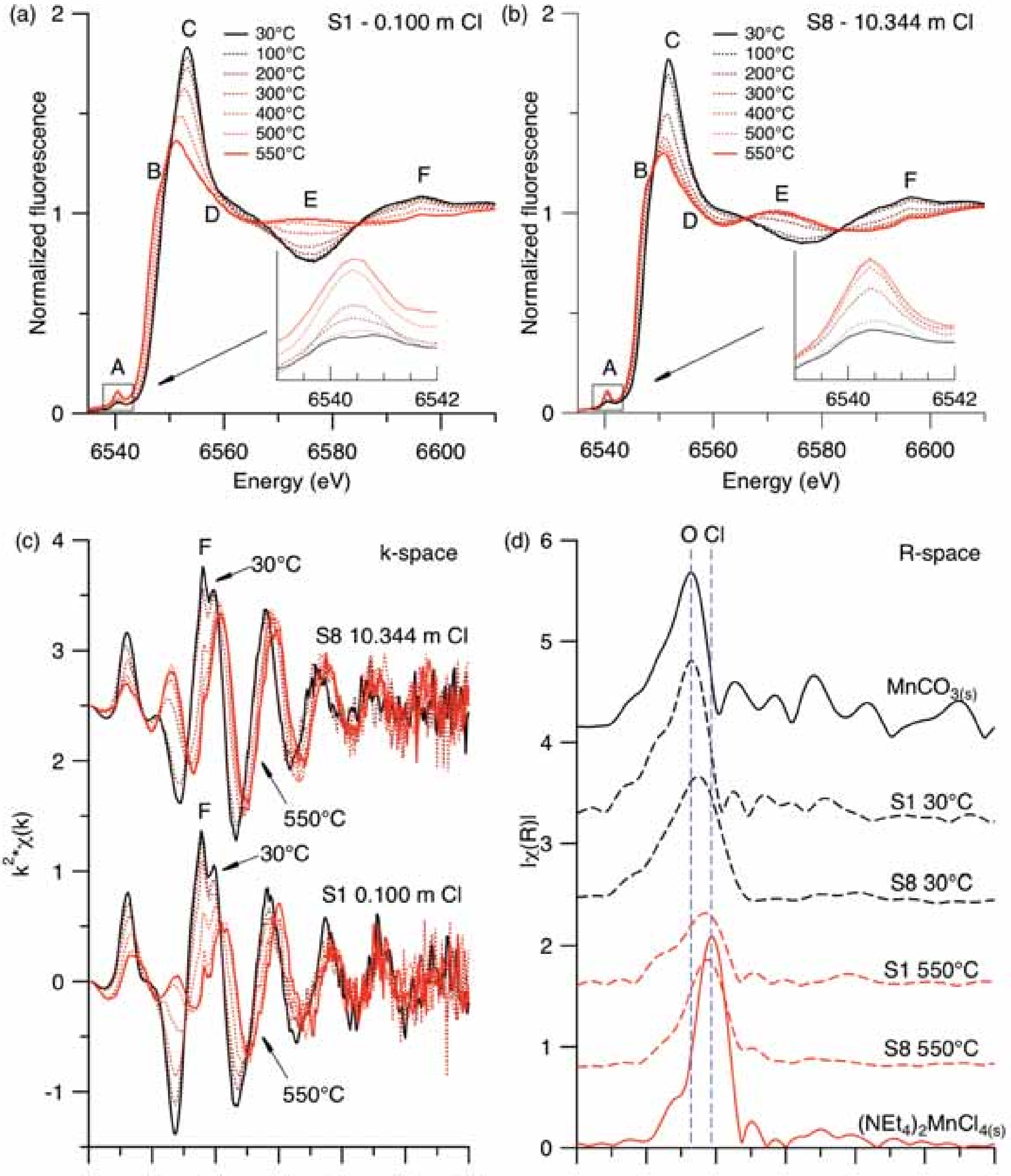

Figure 5.1 XANES spectra of S1 (0.100 *m* Cl) and S8 (10.344 *m* Cl) as a function of temperature from 30 to 550 °C (a and b). The growth of the pre-edge peak at about 6540 eV is shown in the insets upon heating. EXAFS spectra in k-space of S1 and S8 with increasing temperature (c), and R-space spectra of of S1 and S8 at two extreme temperatures (30 and 550 °C) compared with those of Mn solid reference compounds – $MnCO_{3(s)}$ and $(NEt_4)_2MnCl_{4(s)}$.

5.3.2 Effect of salinity

Mn *K*-edge XANES spectra of chloride solutions are shown as a function of salinity at fixed temperatures (30, 100, 200, 300, 400, and 500 ˚C) in Figure 5.2. The effect of increasing salinity at room-T and at 100 ˚C is small (Figure 5.2a, b). A salinity increase from 3.078 to 10.344 *m* results in a slight decrease of white line intensity, an energy shift (1.4 eV) of the white line peak to lower energy, and the growth of a band at ~6575 eV. The XANES spectra of the highest salinity solution (S8) resemble that of $MnCl_2•4H_2O_{(s)}$ (Figure 5.2b), containing octahedral $MnCl_2(H_2O)_4$ moieties. Hence, octahedral species dominate Mn speciation at low temperature throughout the whole salinity range (Farges, 2005; Chalmin et al., 2009).

The effect of salinity is more pronounced at elevated temperatures, in particular at 300 ˚C (Figure 5.2d). S1 has a typical octahedral spectrum, while the spectrum of S8 is characteristic of tetrahedral-like coordination. At 500 ˚C, Mn exists in tetrahedral-like complexes, with XANES spectra similar to $(NEt_4)_2MnCl_{4(s)}$ (Figure 5.2f), and no spectral changes occur upon further heating to 550 ˚C (Figures 5.1a, b). At ≥ 500 ˚C, the solutions can be categorized into two groups based on the shape of the white line (feature C) and intensities of the features B and E: the low salinity (S1, S11, and S6) and high salinity groups (S14, S3, and S8). In particular, feature E is strongest for $(NEt_4)_2MnCl_{4(s)}$, is significant for solutions of the high salinity group, but is absent for the low salinity group (Figure 5.2f). These differences suggest that two tetrahedral species with a different ration of water to chloride ligands dominate Mn(II) speciation in low and high salinity solutions at high temperature. A similar situation was found for Co(II) chlorocomplexes at 440 ˚C, with tetrahedral $CoCl_2(H_2O)_{2(aq)}$ and $CoCl_4^{2-}$ complexes dominating in low and high salinity solutions, respectively (Liu et al., 2011).

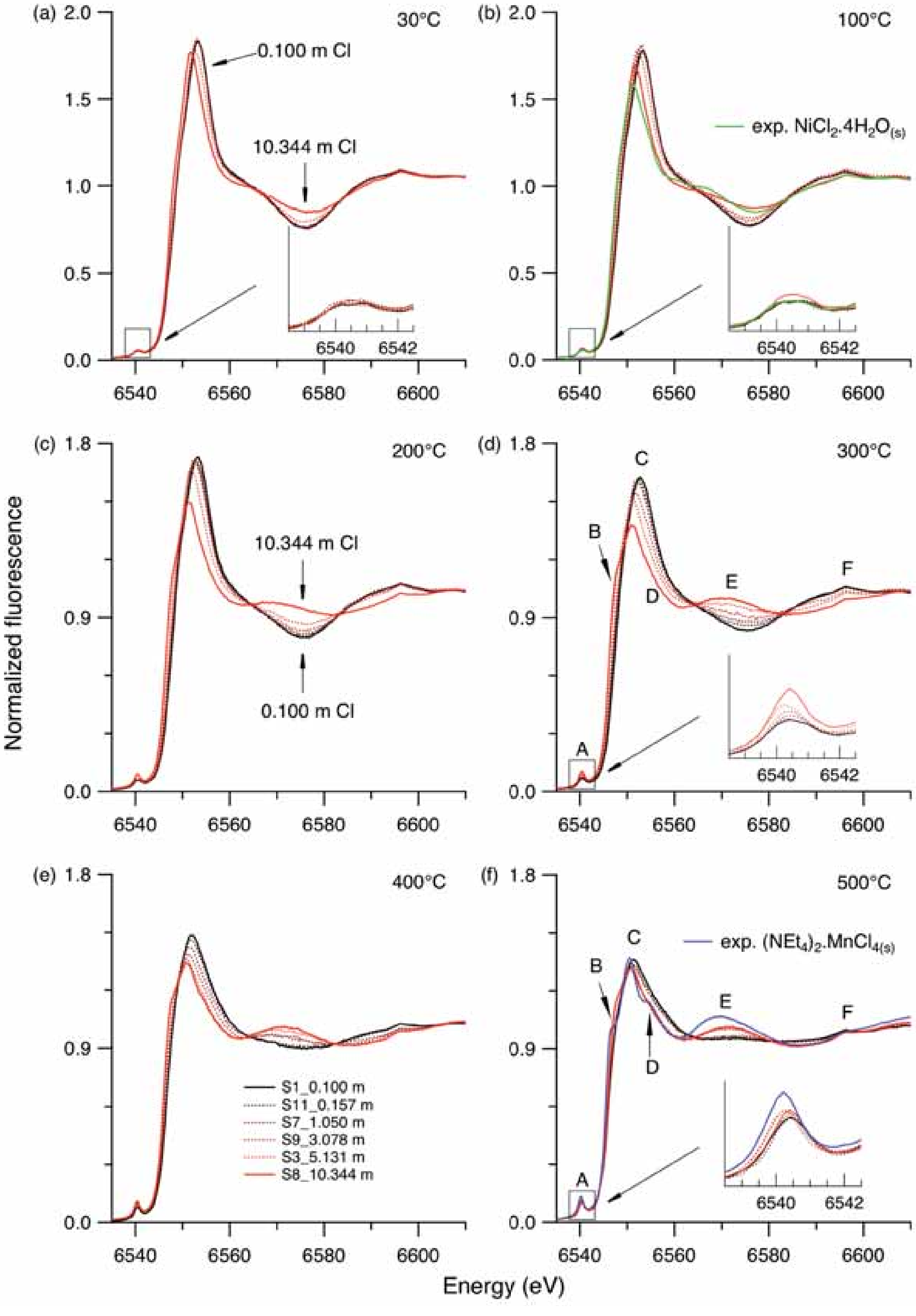

Figure 5.2 XANES spectra of Mn(II) chloride solutions as a function of salinity from 0.100 to 10.344 *m* Cl at (a) 30 °C, (b) 100 °C, (c) 200 °C, (d) 300 °C, (e) 400 °C and (f) 500 °C. The growth of pre-edge peak at around 6540 eV with increasing chloride concentration for

the 30 °C, 100 °C, 300 °C and 500 °C datasets are shown in insets. XANES spectra of Mn reference compounds – $MnCl_2.4H_2O_{(s)}$ and $(NEt_4)_2MnCl_{4(s)}$ are also shown in (b) and (f) for comparison.

5.3.3 XANES spectra of bromide solutions

The spectral evolution of the Mn(II) bromide solutions follows a similar trend to that of the Mn-Cl solutions (Figure 5.3). The octahedral to tetrahedral transition for Mn(II) complexes occurs at higher temperature in Br solutions than in Cl solutions, similarly to Co(II) (Liu et al., 2011). Two isosbestic points at around 6565 and 6583 eV in the XANES spectra of both chloride and bromide solutions also support this structural transition as a function of both temperature and salinity (Figures 5.1-5.3). At 400 ˚C, Linear Combination Fits (LCF; Athena program, Ravel and Newville, 2005; energy range 6519 to 6589 eV) show that in the dilute solutions S5 (0.110 *m* Br) and S1 (0.100 *m* Cl), tetrahedral species account for 57% and 71%; in the more concentrated solutions S4 (2.125 *m* Br) and S12 (2.117 *m* Cl), tetrahedral species account for 63% and 80%. Note that at 500 ˚C the solutions with the lowest and highest Br contents (0.110 - 2.125 *m* Br) show only slight differences and a similar feature E (Figure 5.3c).

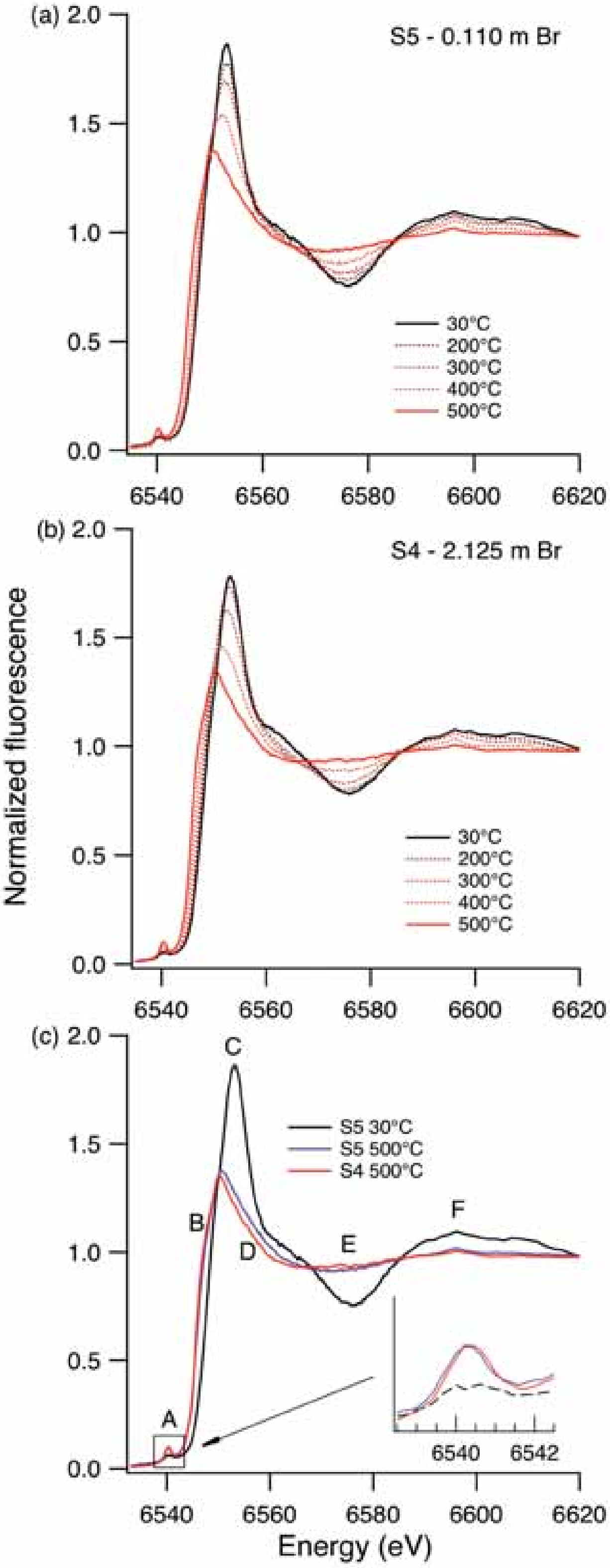

Figure 5.3 XANES spectra of S5 (0.110 *m* Br) and S4 (2.125 m Br) as a function of temperature from 30 to 500 °C (a and b). The representative individual XANES spectra are shown in (c) with the pre-edge around 6540 eV shown in the inset.

5.4 EXAFS refinements

Quantitative EXAFS analysis was conducted to constrain the coordination number and bond distances for Mn(II) chloride and bromide complexes. Fitting EXAFS data of $(NEt_4)_2MnCl_{4(s)}$ by taking into account only the first shell (fixed coordination number at four, avoiding issues with disorder among the NEt groups) yielded an amplitude factor (S_0^2) of 0.68(6) and an average Mn-Cl bond distance of 2.37(1) Å that is slightly longer than the value of 2.334(6) Å obtained by single crystal X-ray diffraction measurement (see Section 5.8.1). The same S_0^2 value of 0.68(5) was refined by fitting the known octahedral structure of aqueous $Mn(H_2O)_6^{2+}$ with a fixed coordination number of six to the EXAFS data of S1 (0.050 m $MnCl_2$, Cl:Mn molar ratio = 2.00) at 30 ˚C and 1 bar (Table 5.3). Hence, a S_0^2 value of 0.68 was used in all subsequent EXAFS refinements. This value is similar to that of 0.72 used in the study of Mn-bromide complexing by Chen et al. (2005a, b).

Table 5.3 Summary of EXAFS refinements of Mn solid standard - $(NEt_4)_2MnCl_{4(s)}$ and solution S1 (0.100 m Cl, Cl:Mn molar ratio = 2.00) at ambient condition.

Sample	$(NEt_4)_2MnCl_{4(s)}$	Solution S1 at 1 bar
Model	One shell, Mn-Cl (4)	One shell, Mn-O (6)
S_0^2	0.68(6)	0.68(4)
ΔE_0 (eV)	6.1(7)	-0.9(7)
R(Mn-X) (X=O / Cl) (Å)	2.37(1)	2.16(1)
σ^2(Mn-X) (X=O / Cl) (Å^2×10^{-3})	2.5(8)	3.9(1.0)
R- / k-range	1.0-3.0 / 2.2-11.5	1.0-4.3 / 2.2-11.0
R-factor / χ^2	0.015 / 24.44	0.020 / 12.98

The ΔE_0 parameter accounts for a misalignment of energy between theoretical calculations and experiments (Kelly et al., 2008). Metal-ligand distances are strongly correlated with ΔE_0 (Bunker, 2010), and in some cases assigning different ΔE_0 to different ligands can result in more physically significant fits (Kelly et al., 2008). For example, using a single ΔE_0 to fit the 500 ˚C data for S1 (0.100 m Cl, Cl:Mn ratio = 2.00), assuming a coordination number of four (Section 5.3), resulted in poor agreement (R-factor > 0.50) and in a Mn-O distance of 2.27 Å, far longer than the room temperature octahedral Mn-O distance of 2.16 Å. This 2.27 Å Mn-O distance is close to the tetrahedral Mn-Cl distance of 2.31 Å, suggesting that O and Cl are interchangeable during the fitting. Therefore, we chose to use different ΔE_0 values for the Mn-Cl and Mn-O scattering shells. In order to limit the number of fit parameters, the ΔE_0 values were determined from fitting the standards $(NEt_4)_2MnCl_{4(s)}$ [ΔE_0(Mn-Cl) = 6.1(7)] and $Mn(H_2O)_6^{2+}$ [solution S1 at 30 ˚C, 1 bar; ΔE_0(Mn-O) = -0.9(7)]. The two ΔE_0 values were allowed to vary within the error range obtained on the standards for each individual fit. A similar approach was used for example by Mayanovic et al. (2002, 2009) to refine EXAFS data for aqueous Yb^{3+} and Nd^{3+} chloroaqua complexes.

5.4.1 Mn-Cl solutions

5.4.1.1 Solutions with one dominant coordination geometry

The XANES analysis showed that octahedral complexes dominate Mn(II) speciation at 30 ˚C and 100 ˚C (Figure 5.2a, b), and tetrahedral complexes at 500 ˚C and 550 ˚C (Figure 5.2f). The EXAFS fit of S1 at 30 ˚C (Figure 5.4) confirms that the octahedral $Mn(H_2O)_6^{2+}$ complex (6.1(4) water) is the predominant species in chloride-poor solutions (e.g., Chen et al., 2005a). Solutions containing 0.100 – 3.078 *m* Cl at 30 ˚C have similar XANES spectra (Figure 5.2a), and the fitted water numbers for these data were around 6 within error (Table 5.4). Attempts to add one chloride into the first octahedral shell resulted in a statistically worse fit (i.e. the statistically significant change in reduced χ^2 for the two fits is greater than two standard deviations, as defined by Kelly et al. (2008); equation 19 on page 445). The refined Mn-O bond distance of 2.16(1) Å is in good agreement with the literature value of 2.169(7) Å (Chen et al., 2005a) for the Mn(II) hexaaqua complex in a 0.05 *m* $MnBr_2$ solution at 25 ˚C and 1 bar. With increasing salinity, the presence of chloride within the octahedral complex was detected by the EXAFS analysis for solutions with chloride concentrations ≥ 4.107 *m* at 30 ˚C, ≥ 2.117 *m* at 100 ˚C, and all chloride concentrations at T $\geq$ 200 ˚C (Table 5.4 and Figure 5.4). The refined Mn-O and Mn-Cl bond lengths for solution S8 at 100 ˚C are 2.17(2) Å and 2.49(2) Å, respectively, in excellent agreement with the averaged Mn-O lengths of 2.20(2) Å and Mn-Cl length of 2.49(2) Å of $MnCl_2{\bullet}4H_2O_{(s)}$ (Zalkin et al., 1964; El Saffar and Brown, 1971) and of $MnCl_2$ solutions (Beagley et al., 1991).

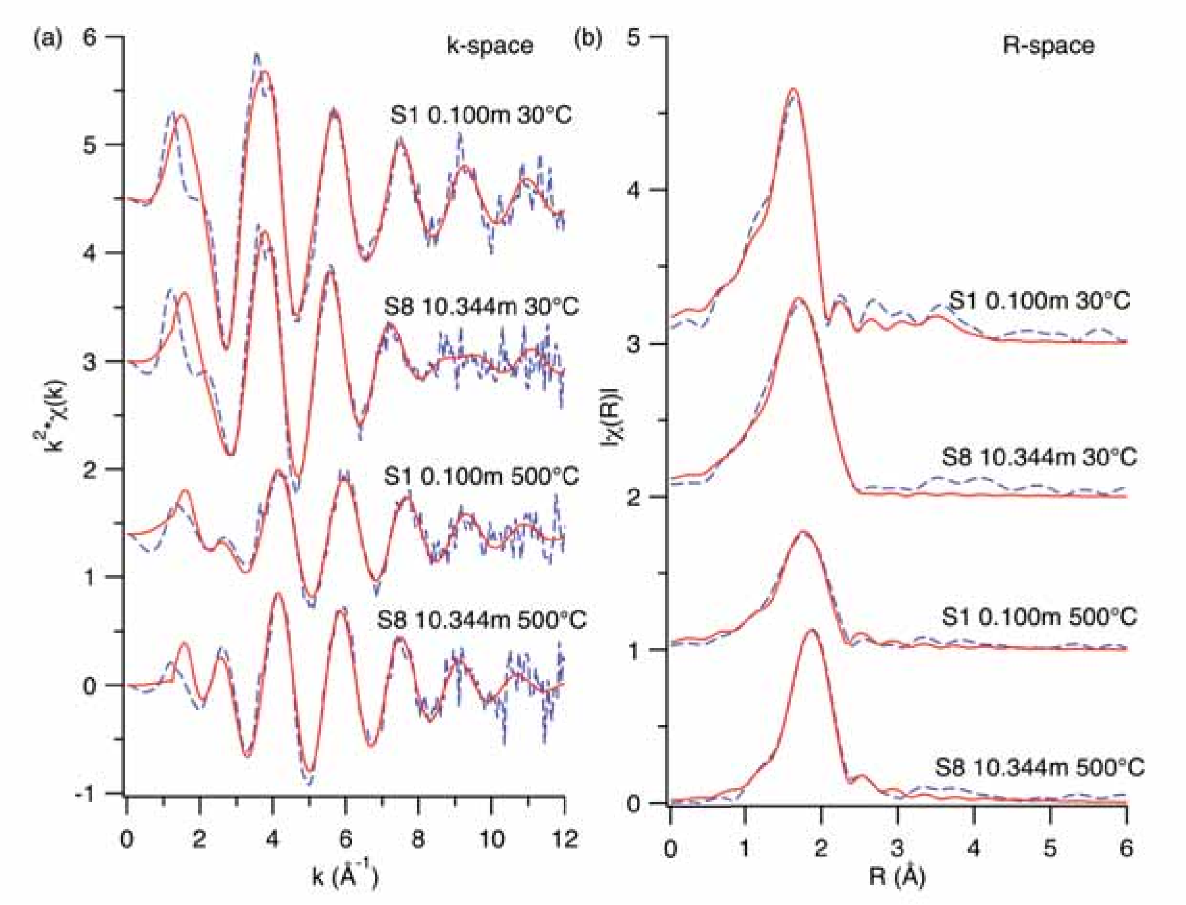

Figure 5.4 Experimental (blue dashed line) and fitted (red solid line) EXAFS spectra of S1 (0.100 m Cl) and S8 (10.344 m Cl) at 30 ˚C and 500 ˚C in (a) k-space and (b) R-space. All fits are shown with k^2 weighting.

The coordination number of Mn was constrained to be four for all EXAFS refinements of solutions at 500 ˚C and 550 ˚C (Section 5.3). For the weakly saline solutions ($0.100 \leq m\mathrm{Cl_{tot}} \leq 0.257$; $2 \leq$ Cl:Mn molal ratio ≤ 5), the numbers of water and chloride were both around two, revealing predominance of the $MnCl_2(H_2O)_{2(aq)}$ complex. At high salinity, the best fit was $MnCl_{3.0(4)}O_{1.0(4)}$ for all solutions with $\geqslant$5.131 m $\mathrm{Cl_{tot}}$ (Table 5.4), consistent with the $MnBr_{3.4(1.6)}O_{0.9(4)}$ average ligation identified by Chen et al. (2005b). The refined Mn-Cl bond length was 2.37(1) Å for solution S8 at 500 ˚C (Figure 5.4; Table 5.4), identical to that of 2.37(1) Å for $(NEt_4)_2MnCl_{4(s)}$; the fitted Mn-O bond length was 2.13(5) Å, within error of the room-T bonds length of 2.18(2) Å for S8 and 2.16(1) Å for S1. EXAFS refinement using a $MnCl_4$ model resulted in a statistically worse fit.

Table 5.4 Summary of EXAFS refinements of Mn chloride solutions at 30 - 550 °C, 600 bar.

T (°C)	Mn-O interaction				Mn-Cl interaction				R-range	k-range	R-factor	χ^2
	ΔE_0 (eV)	N_O	$R_{Mn\text{-}O}$ (Å)	σ_O^2 (Å$^2\times10^{-3}$)	ΔE_0 (eV)	N_{Cl}	$R_{Mn\text{-}Cl}$ (Å)	σ_{Cl}^2 (Å$^2\times10^{-3}$)				
S1, 0.100 m Cl, Cl:Mn molar ratio = 2.00												
30	-1.0	6.1(0.4)	2.16(0.01)	4.6(1.0)	-	-	-	-	1-4.3	2.2-11	0.016	16.84
100	-1.6	6.2(0.4)	2.15(0.01)	6.5(1.3)	-	-	-	-	1-4.3	2.2-10.5	0.019	14.64
†200	-1.3	5.9(0.4)	2.17(0.01)	7.5(1.3)*	6.8	0.2(0.3)	2.31(0.17)	7.5(1.3)*	1-4.3	2.2-11	0.020	10.64
†300	-1.6	4.9(0.4)	2.16(0.01)	9.2(1.4)*	5.4	0.7(0.3)	2.37(0.05)	9.2(1.4)*	1-3	2.2-10.5	0.023	24.98
†400	-1.6	3.3(0.3)	2.14(0.03)	8.9(4.1)	5.4	1.4(0.3)	2.34(0.03)	8.5(4.4)	1-3	2.2-10.5	0.013	9.71
500	-1.6	1.9(0.3)	2.13(0.05)	9.6(6.2)	6.8	2.1(0.3)	2.33(0.01)	7.4(3.0)	1-3	2.2-11	0.015	17.94
550	-1.6	2.0(0.6)	2.15(0.10)	12.9(16.2)	6.8	2.0(0.6)	2.32(0.02)	6.2(4.2)	1-3	2.2-11	0.034	10.72
S11, 0.157 m Cl, Cl:Mn molar ratio = 3.14												
30	-1.2	6.1(0.5)	2.16(0.01)	4.0(1.3)	-	-	-	-	1-4.3	2.2-11	0.032	10.09

(continued)

Table 5.4 continued

100	-1.3	6.3(0.4)	2.16(0.01)	7.1(1.2)	-	-	-	-	1-4.3	2.2-10.5	0.015	3.94
†200	-1.6	6.0(0.4)	2.16(0.01)	7.7(1.3)*	6.8	0.2(0.3)	2.31(0.16)	7.7(1.3)*	1-4.3	2.2-11	0.025	6.89
†300	-1.6	5.1(0.4)	2.16(0.03)	10.2(2.2)	6.8	0.6(0.3)	2.41(0.05)	4.1(6.7)	1-3	2.2-11	0.036	17.18
†400	-1.6	3.3(0.3)	2.14(0.02)	11.4(1.9)	6.8	1.4(0.3)	2.37(0.01)	5.4(1.4)	1-3	2.2-11	0.014	9.26
†450	-1.6	2.4(0.3)	2.13(0.02)	13.0(3.4)	6.8	1.8(0.3)	2.35(0.01)	6.2(1.3)	1-3	2.2-11	0.020	7.08
500	-1.6	2.0(0.3)	2.12(0.08)	8.9(2.1)*	6.8	2.0(0.3)	2.32(0.02)	8.9(2.1)*	1-3	2.2-9.2	0.031	12.27
S6, 0.257 m Cl, Cl:Mn molar ratio = 5.14												
30	-1.6	6.6(0.6)	2.16(0.01)	5.8(1.4)	-	-	-	-	1-4.3	2.2-11	0.030	8.88
100	-1.3	6.2(0.5)	2.15(0.01)	5.9(1.4)	-	-	-	-	1-4.3	2.2-10.5	0.025	20.75
†200	-1.6	5.8(0.5)	2.16(0.01)	6.7(1.2)*	6.8	0.2(0.2)	2.32(0.14)	6.7(1.2)*	1-4.3	2.2-10.5	0.020	5.25
†300	-1.6	4.9(0.4)	2.16(0.03)	8.9(3.1)	6.3	0.7(0.2)	2.41(0.09)	7.8(12.3)	1-3	2.2-10	0.013	9.02
†400	-1.6	3.3(0.3)	2.14(0.01)	5.6(2.1)	5.7	1.5(0.2)	2.34(0.04)	11.6(5.1)	1-3	2.2-10.5	0.012	6.19
500	-1.6	1.7(0.2)	2.12(0.01)	6.4(4.5)	6.8	2.3(0.2)	2.34(0.01)	9.4(2.5)	1-3	2.2-11	0.011	16.39
550	-1.6	1.8(0.2)	2.11(0.06)	9.3(1.3)*	6.8	2.2(0.2)	2.32(0.02)	9.3(1.3)*	1-3	2.2-10.5	0.026	6.74
S13, 0.516 m Cl, Cl:Mn molar ratio = 10.12												
30	-0.9	6.1(0.4)	2.16(0.01)	4.0(1.1)	-	-	-	-	1-4.3	2.2-11	0.024	13.37
100	-0.6	6.0(0.5)	2.17(0.01)	5.6(1.4)	-	-	-	-	1-4.3	2.2-11	0.031	13.51
†200	-1.6	5.4(0.5)	2.17(0.01)	6.6(1.2)*	5.4	0.3(0.4)	2.32(0.07)	6.6(1.2)*	1-4.3	2.2-11	0.030	5.94
†300	-1.6	4.5(0.5)	2.16(0.01)	8.6(1.6)	5.4	0.9(0.4)	2.39(0.03)	4.6(2.4)	1-3	2.2-11	0.010	15.88
†400	-1.6	2.4(0.4)	2.14(0.02)	7.8(2.9)	5.9	2.1(0.4)	2.35(0.02)	7.9(1.7)	1-3	2.2-11	0.010	11.87
†450	-1.6	1.5(0.4)	2.13(0.02)	2.8(3.4)	6.8	2.6(0.4)	2.35(0.01)	9.4(2.0)	1-3	2.2-9.8	0.015	28.26
S7, 1.050 m Cl, Cl:Mn molar ratio = 19.81												
30	-0.2	6.3(0.5)	2.16(0.01)	5.5(1.3)	-	-	-	-	1-4.3	2.2-11	0.025	10.74
100	-1.2	5.8(0.2)	2.16(0.01)	5.0(0.9)*	6.8	0.2(0.2)	2.53(0.09)	5.0(0.9)*	1-4.3	2.2-11	0.021	5.00
†200	-1.6	5.1(0.2)	2.16(0.01)	7.1(1.0)	6.8	0.6(0.2)	2.48(0.04)	9.2(6.9)	1-3	2.2-10.2	0.009	9.37
†300	-0.2	4.0(0.2)	2.18(0.02)	7.9(2.3)*	6.6	1.2(0.2)	2.42(0.09)	7.9(2.3)*	1-3	2.2-9.2	0.054	42.95
†400	-1.6	2.4(0.4)	2.13(0.05)	7.6(3.8)	6.8	2.2(0.4)	2.38(0.02)	8.9(2.9)	1-3	2.2-10	0.025	13.42
S12, 2.117 m Cl, Cl:Mn molar ratio = 37.80												
30	-1.2	6.4(0.6)	2.15(0.01)	5.1(1.6)	-	-	-	-	1-4.3	2.2-11	0.038	12.29
100	-1.6	5.5(0.2)	2.15(0.01)	5.0(0.9)*	6.8	0.5(0.2)	2.52(0.04)	5.0(0.9)*	1-4.3	2.2-11	0.025	6.16
†200	-1.6	4.9(0.2)	2.15(0.01)	5.9(1.7)*	6.8	0.8(0.2)	2.54(0.04)	5.9(1.7)*	1-3	2.2-10.5	0.040	20.28
†300	-1.6	3.3(0.3)	2.15(0.02)	4.7(1.9)	6.8	1.7(0.3)	2.40(0.02)	12.2(4.3)	1-3	2.2-10.5	0.022	6.34
†400	-1.6	2.0(0.4)	2.11(0.05)	5.4(4.3)	6.8	2.4(0.4)	2.38(0.02)	10.0(3.3)	1-3	2.2-10.2	0.043	35.54

(continued)

Table 5.4 continued

S9, 3.078 m Cl, Cl:Mn molar ratio = 53.07											
30	-0.7	6.3(0.4)	2.15(0.01)	5.6(1.1)	-	-	-	-	1-4.3	2.2-11	0.018	7.13
100	-1.6	5.5(0.4)	2.15(0.02)	4.6(1.4)*	6.8	0.5(0.4)	2.51(0.06)	4.6(1.4)*	1-4.3	2.2-10	0.038	18.10
†200	-1.6	4.8(0.4)	2.16(0.02)	6.7(1.1)*	5.4	0.9(0.4)	2.42(0.04)	6.7(1.1)*	1-3	2.2-11	0.019	11.30
†300	-0.3	3.4(0.4)	2.17(0.03)	5.9(3.1)	5.4	1.6(0.4)	2.37(0.03)	9.4(4.7)	1-3	2.2-10.5	0.016	7.61
†400	-1.6	1.9(0.4)	2.12(0.02)	2.2(2.9)	6.3	2.5(0.4)	2.37(0.03)	11.3(3.0)	1-3	2.2-10.2	0.018	11.39
†450	-1.6	1.3(0.4)	2.13(0.03)	3.5(3.9)	6.4	2.8(0.4)	2.36(0.02)	8.2(1.5)	1-3	2.2-11	0.017	30.73
S14, 4.107 m Cl, Cl:Mn molar ratio = 67.33												
30	-1.0	5.6(0.3)	2.16(0.01)	4.6(1.0)*	5.4	0.4(0.3)	2.53(0.07)	4.6(1.0)*	1-4.5	2.2-11	0.031	8.51
100	-1.6	5.3(0.2)	2.16(0.01)	6.2(0.8)*	5.8	0.7(0.2)	2.51(0.04)	6.2(0.8)*	1-4.5	2.2-11	0.018	6.09
†200	-1.6	4.4(0.2)	2.16(0.03)	6.9(2.2)	5.4	1.2(0.2)	2.46(0.05)	6.2(4.8)	1-3	2.2-10.2	0.018	15.62
†300	-1.6	2.8(0.3)	2.15(0.05)	6.4(5.0)	5.9	2.0(0.3)	2.39(0.03)	6.9(4.1)	1-3	2.2-10.2	0.020	30.70
†400	-1.6	1.7(0.4)	2.12(0.02)	5.0(3.0)	6.8	2.6(0.4)	2.38(0.01)	6.6(1.3)	1-3	2.2-11	0.021	12.17
†450	-1.6	1.3(0.4)	2.12(0.03)	4.2(2.0)	6.8	2.8(0.4)	2.37(0.01)	7.8(0.9)	1-3	2.2-11	0.007	2.10
500	-1.6	1.1(0.4)	2.11(0.09)	3.9(8.4)	6.8	2.9(0.4)	2.36(0.01)	7.3(2.9)	1-3	2.2-10	0.017	12.80
S3, 5.131 m Cl, Cl:Mn molar ratio = 80.17												
30	-1.1	5.1(0.4)	2.16(0.01)	5.6(1.1)	6.8	0.9(0.4)	2.53(0.03)	7.1(5.4)	1-4.5	2.2-11	0.022	12.18
100	-1.6	5.1(0.3)	2.16(0.01)	5.8(0.8)	6.8	0.9(0.4)	2.53(0.03)	6.9(3.3)	1-4.5	2.2-11	0.011	9.89
†200	-1.6	4.1(0.3)	2.15(0.01)	6.5(0.8)	6.8	1.4(0.4)	2.48(0.01)	11.4(2.6)	1-4.3	2.2-10.5	0.015	5.72
†300	-1.6	2.6(0.4)	2.14(0.05)	7.4(3.0)	6.8	2.2(0.4)	2.40(0.01)	6.4(2.1)	1-3	2.2-10.5	0.024	21.26
†400	-1.6	1.5(0.4)	2.12(0.05)	6.4(3.5)	6.8	2.8(0.4)	2.38(0.01)	6.7(1.3)	1-3	2.2-10.5	0.013	9.07
500	-1.6	1.0(0.4)	2.14(0.10)	5.9(1.0)*	6.5	3.0(0.4)	2.37(0.02)	5.9(1.0)*	1-3	2.2-10	0.013	8.27
S8, 10.344 m Cl, Cl:Mn molar ratio = 73.36												
30	-0.3	4.4(0.5)	2.18(0.02)	6.1(1.3)	5.4	1.6(0.5)	2.51(0.02)	5.5(2.8)	1-4.7	2.2-11	0.024	12.28
100	-1.6	4.0(0.4)	2.17(0.02)	7.5(1.4)	5.4	2.0(0.4)	2.49(0.02)	7.9(2.3)	1-4.3	2.2-11	0.019	14.51
†200	-1.6	2.4(0.3)	2.15(0.05)	6.5(3.2)	6.8	2.5(0.3)	2.41(0.01)	7.4(2.2)	1-3	2.2-10.5	0.026	23.66
†300	-1.6	1.5(0.3)	2.12(0.03)	6.8(4.3)	6.8	2.8(0.3)	2.40(0.01)	5.5(1.1)	1-3	2.2-10.5	0.018	24.58
†400	-1.6	1.2(0.3)	2.11(0.03)	4.7(4.0)	6.8	2.9(0.3)	2.39(0.01)	6.5(1.1)	1-3	2.2-10.5	0.015	8.60
500	-1.6	1.0(0.3)	2.13(0.05)	7.3(1.0)*	6.2	3.0(0.3)	2.37(0.01)	7.3(1.0)*	1-3	2.2-11	0.016	16.13
550	-1.6	1.0(0.4)	2.12(0.10)	8.1(1.0)*	6.2	3.0(0.4)	2.37(0.02)	8.1(1.0)*	1-3	2.2-11	0.013	12.32

* Debye-waller factor set to be identical for Mn-O and Mn-Cl interactions.

† data refined by linear combination fit (LCF) of octahedral and tetrahedral complexes (see text for details).

5.4.1.2 Solutions with mixed octahedral and tetrahedral complexes

Based on the qualitative XANES analysis, most chloride solutions contain mixtures of octahedral and tetrahedral complexes at intermediate temperatures (200 – 450 ˚C). As each complex has different Mn-O and Mn-Cl distances, Cl/O ratio, and Debye-Waller factors, fitting EXAFS of solutions that contain a few species is challenging. To reduce the number of fit parameters, EXAFS data at intermediate temperatures for each solution were analyzed assuming that they consist of a mixture of the species that exist at low (100 ˚C; octahedral coordination) and high temperatures (500 ˚C; tetrahedral coordination). For each solution, the fraction of tetrahedral and octahedral species was derived from XANES data via LCF (Table 5.5). These fractions were fixed in the EXAFS refinements, and the Mn-Cl and Mn-O bond lengths and corresponding Debye-Waller factors were fitted (Table 5.4), and represent average values of octahedral and tetrahedral complexes in each solution.

Table 5.5 Summary of linear combination fits (LCF) of XANES spectra using ATHENA for each chloride solution at intermediate temperatures (200 - 450 ˚C). XANES data of solution S14 at 500 ˚C was used as one standard to fit the intermediate spectra for solutions S13, S7, S12 and S9 due to lack of reliable XANES data at 500 ˚C for these solutions.

Sample - T (˚C)	**S1-100 °C**	**S1-500 °C**
S1(0.100m) - 100	1.0	0
S1(0.100m) - 200	0.920	0.080
S1(0.100m) - 300	0.690	0.310
S1(0.100m) - 400	0.316	0.684
S1(0.100m) - 500	0	1.0
Sample - T (˚C)	**S11-100 °C**	**S11-500 °C**
S11(0.157m) - 100	1.0	0
S11(0.157m) - 200	0.921	0.079
S11(0.157m) - 300	0.724	0.276
S11(0.157m) - 400	0.304	0.696
S11(0.157m) - 450	0.093	0.907
S11(0.157m) - 500	0	1.0

(continued)

Table 5.5 continued

Sample - T (°C)	**S6-100 °C**	**S6-500 °C**
S6(0.257m) - 100	1.0	0
S6(0.257m) - 200	0.911	0.089
S6(0.257m) - 300	0.716	0.284
S6(0.257m) - 400	0.354	0.646
S6(0.257m) - 500	0	1.0
Sample - T (°C)	**S13-100 °C**	**S14-500 °C**
S13(0.516m) - 100	1.0	0
S13(0.516m) - 200	0.886	0.114
S13(0.516m) - 300	0.695	0.305
S13(0.516m) - 400	0.268	0.732
S13(0.516m) - 450	0.087	0.913
S14(4.107m) - 500	0	1.0
Sample - T (°C)	**S7-100 °C**	**S14-500 °C**
S7(1.050m) - 100	1.0	0
S7(1.050m) - 200	0.845	0.155
S7(1.050m) - 300	0.623	0.377
S7(1.050m) - 400	0.273	0.727
S14(4.107m) - 500	0	1.0
Sample - T (°C)	**S12-100 °C**	**S14-500 °C**
S12(2.117m) - 100	1.0	0
S12(2.117m) - 200	0.861	0.139
S12(2.117m) - 300	0.500	0.500
S12(2.117m) - 400	0.199	0.801
S14(4.107m) - 500	0	1.0
Sample - T (°C)	**S9-100 °C**	**S14-500 °C**
S9(3.078m) - 100	1.0	0
S9(3.078m) - 200	0.839	0.161
S9(3.078m) - 300	0.521	0.479
S9(3.078m) - 400	0.175	0.825
S9(3.078m) - 450	0.039	0.961
S14(4.107m) - 500	0	1.0
Sample - T (°C)	**S14-100 °C**	**S14-500 °C**
S14(4.107m) - 100	1.0	0
S14(4.107m) - 200	0.778	0.222

(continued)

Table 5.5 continued

S14(4.107m) - 300	0.403	0.597
S14(4.107m) - 400	0.134	0.866
S14(4.107m) - 450	0.050	0.950
S14(4.107m) - 500	0	1.0
Sample - T (˚C)	**S3-100 °C**	**S3-500 °C**
S3(5.131m) - 100	1.0	0
S3(5.131m) - 200	0.754	0.246
S3(5.131m) - 300	0.390	0.610
S3(5.131m) - 400	0.111	0.889
S3(5.131m) - 500	0	1.0
Sample - T (˚C)	**S8-100 °C**	**S8-500 °C**
S8(10.344m) - 100	1.0	0
S8(10.344m) - 200	0.467	0.533
S8(10.344m) - 300	0.162	0.838
S8(10.344m) - 400	0.052	0.948
S8(10.344m) - 500	0	1.0

A contraction of the Mn-Cl bond length with increasing temperature for each solution is noticeable. For example, the representative octahedral Mn-Cl bond length of 2.51(2) Å at 30 ˚C is around 0.14 Å longer than a typical tetrahedral Mn-Cl bond length of 2.37(2) Å at 500 ˚C (Solution S8, Table 5.4). The Mn-O bond distances of low salinity solutions (0.100 – 0.516 *m*) remain constant (2.16(1) Å) from 30 to 300 ˚C. This is inconsistent with the ~3% increase in the Mn-O bond length for $Mn(H_2O)_6^{2+}$ (Cl-free perchlorate solutions, 25-250 ˚C) interpreted by Koplitz et al. (1994) on the basis of UV-Vis spectroscopy. This discrepancy possibly results from the omission of small amounts of tetrahedral complexes at high temperature in Koplitz et al.'s analysis. For most solutions there seems to be a small contraction of the Mn-O bond distances from room-T to 500 ˚C (~0.05 Å), although this is not statistically significant due to the relatively large errors at high temperature. R-space data for isothermal conditions (400 ˚C) are plotted as a function of chloride concentrations in Figure 5.5; a systematic shift of the position of the main peak reflects an increase in the number of Cl in Mn^{2+} first coordination shell, as illustrated in Figure 5.6d. At 300 ˚C, increasing salinity causes a decrease in coordination number, together with an increase in the number of Cl ligands (Figure 5.6c). The changes in O and Cl ligation numbers as a function of temperature further illustrates the coordination change from octahedral at 30 and 100 ˚C to tetrahedral at 450 and 500 ˚C for both S11 and S14, with the structural transition happening at higher temperature (300–450 ˚C) for S11 compared to 200–400 ˚C for S14 (Figures 5.6a, b).

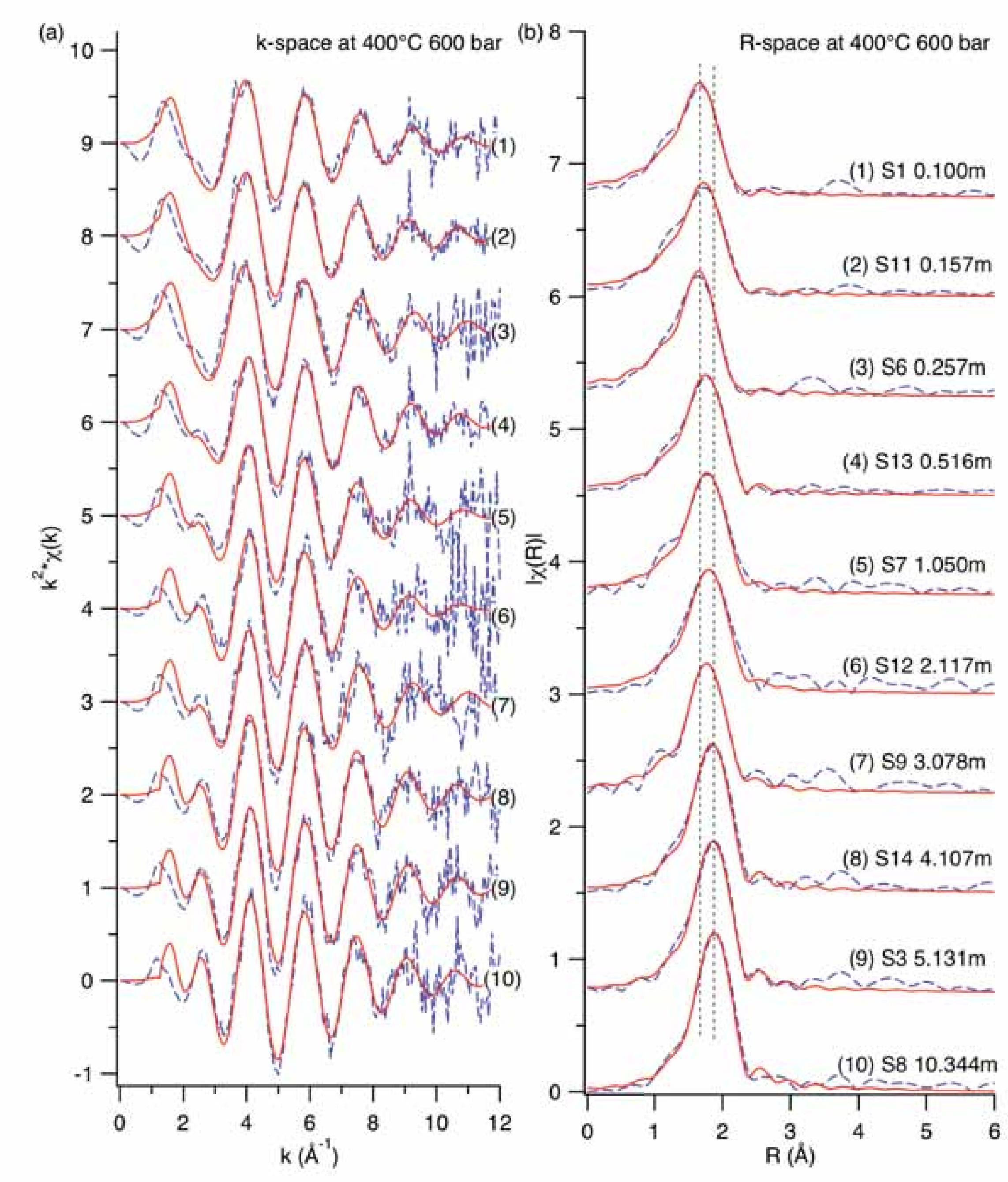

Figure 5.5 Experimental (blue dashed lines) and fitted (red solid lines) EXAFS spectra of all Mn(II) chloride solutions at 400 °C in (a) k-space and (b) R-space. All fits are shown with k^2 weighting.

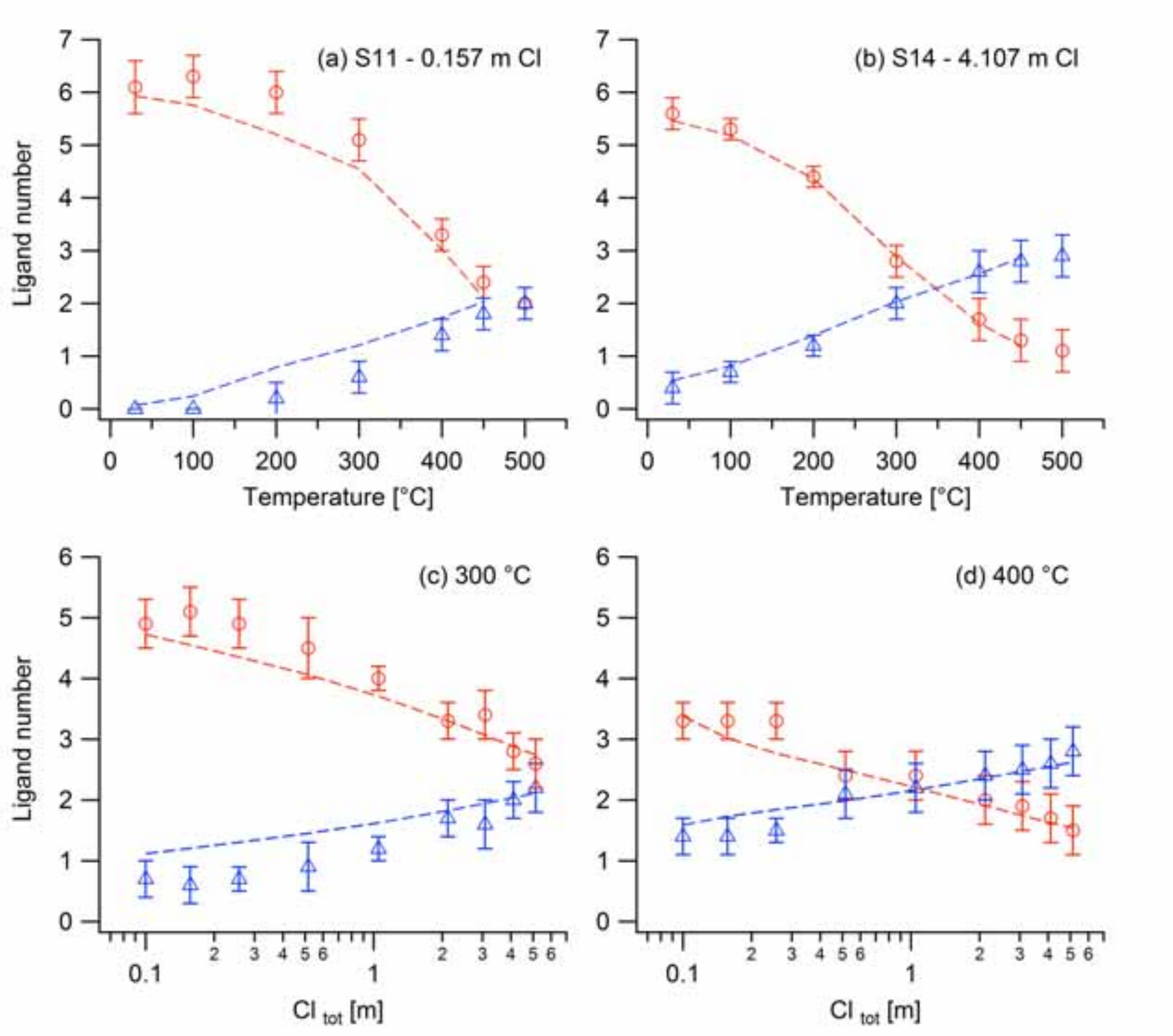

Figure 5.6 Number of oxygen (water molecule; red circles with error bars) and chloride (blue triangles with error bars) ligands in the first shell of Mn^{2+} as a function of temperature for (a) S11 (0.157 *m* Cl) and (b) S14 (4.107 *m* Cl) and as a function of chloride concentration (in log scale) at (c) 300 ˚C and (d) 400 ˚C based on the EXAFS refinements (Table 5.4) and the predictions (dashed lines) based upon the thermodynamic properties in Table 5.8.

5.4.2 Mn-Br solutions

EXAFS data of the Mn-Br solutions were fitted following a similar strategy as for the Mn-Cl solutions, except for the use of a single ΔE_0 for each refinement since it is easier to distinguish the Mn-O and Mn-Br scattering paths. The radial distribution function shows two distinct peaks corresponding to the presence of O and Br within the first shell of Mn for solutions S5 (0.110 *m* Br, Br:Mn molar ratio = 2.04) and S4 (2.125 *m* Br, Br:Mn molar ratio = 33.73) at 500 ˚C (Figure 5.7b). The refined Mn-O bond length of 2.15(1) Å for S5 at 30 ˚C is identical to the bond lengths in the counterpart chloride solutions and with those refined by Chen et al. (2005a, b). At 500 ˚C, the best fit models of $MnBr_{3.0(1.1)}O_{1.3(5)}$ for solution S4 and $MnBr_{2.9(9)}O_{0.8(3)}$ for solution S15 (1.204 *m* Br, Br:Mn molar ratio = 11.47) are similar to the $MnBr_{3.4(1.6)}O_{0.9(4)}$ model identified by Chen et al. (2005b) at 400 ˚C and 310 bar in a solution with a Br:Mn molar ratio of 6 (Table 5.6). The best fit model of $MnBr_{1.7(7)}O_{2.2(1.1)}$ for the low salinity solution S5 at 500 ˚C is also consistent with $MnBr_{1.9(2.4)}O_{1.7(1.3)}$ in a 0.2 *m* $MnBr_2$ solution at 400 ˚C and 310 bar by Chen et al. (2005b). The Mn-O and Mn-Br bond lengths refined in this study (Table 5.6) for tetrahedral Mn(II) complexes are within error of those derived by Chen et al. (2005b). There is no obvious Mn-O bond length contraction upon heating, but the Mn-Br bond length contraction expected for a change from octahedral to tetrahedral coordination was observed: for solution S15, the Mn-Br bond length of 2.58(5) Å) at 100 ˚C is 0.13 Å longer than the typical tetrahedral Mn-Br bond length of 2.45(2) Å obtained at 500 ˚C.

Table 5.6 Summary of EXAFS refinements of Mn bromide solutions at 30 – 500 °C, 600 bar.

T (°C)	ΔE_0 (eV)	Mn-O interaction			Mn-Br interaction			R-range	k-range	R-factor	χ^2
		N_O	$R_{Mn\text{-}O}$ (Å)	σ_O^2 (Å^2)	N_{Cl}	$R_{Mn\text{-}Br}$ (Å)	σ_{Br}^2 (Å^2)				
S5, 0.110 m Br, Br:Mn molar ratio = 2.04											
30	-1.7(0.8)	6.4(0.5)	2.15(0.01)	5.1(1.3)	-	-	-	1-4.3	2.2-11.0	0.028	10.57
200	-4.7(0.7)	5.9(0.4)	2.13(0.01)	5.8(1.0)	-	-	-	1-4.3	2.2-10.5	0.014	2.01
300	-3.3(1.2)	5.9(0.7)	2.13(0.01)	10.4(2.4)*	0.7(0.5)	2.53(0.04)	10.4(2.4)*	1-3	2.2-10.5	0.010	5.47
400	-3.5(1.8)	4.1(0.7)	2.13(0.02)	9.1(3.4)*	1.2(0.7)	2.49(0.02)	9.1(3.4)*	1-3	2.2-10.5	0.021	3.51
500	-1.8(2.6)	2.2(1.1)	2.14(0.03)	16.0(11.9)	1.7(0.7)	2.43(0.01)	6.1(3.4)	1-3	2.2-10.5	0.026	5.52
S15, 1.204 m Br, Br:Mn molar ratio = 11.47											
100	-0.8(1.0)	6.0(0.6)	2.16(0.01)	6.8(2.1)*	0.5(0.4)	2.58(0.05)	6.8(2.1)*	1-4.3	2.2-10.5	0.029	26.11
200	-2.9(1.0)	5.9(0.6)	2.14(0.01)	8.6(2.0)*	0.2(0.4)	2.68(0.17)	8.6(2.0)*	1-4.3	2.2-9.7	0.021	23.44
300	-0.9(1.3)	4.6(0.5)	2.16(0.02)	8.8(2.4)*	0.7(0.5)	2.49(0.03)	8.8(2.4)*	1-3	2.2-10.5	0.013	10.33
350	-2.4(1.7)	4.0(0.6)	2.13(0.02)	9.4(3.2)*	1.0(0.7)	2.47(0.02)	9.4(3.2)*	1-3	2.2-10.5	0.022	37.19
400	-1.0(2.7)	2.8(0.7)	2.14(0.04)	10.3(4.3)*	1.9(1.2)	2.46(0.02)	10.3(4.3)*	1-3	2.2-9.8	0.050	23.77
500	1.0(2.5)	0.8(0.3)	2.18(0.05)	11.6(2.7)*	2.9(0.9)	2.45(0.02)	11.6(2.7)*	1-3	2.2-10.5	0.054	3.04
S4, 2.125 m Br, Br:Mn molar ratio = 33.73											
30	0.8(1.3)	5.6(0.8)	2.18(0.02)	5.9(3.2)*	0.2(0.4)	2.40(0.21)	5.9(3.2)*	1-4.3	2.2-9.8	0.039	14.99
100	-1.9(0.8)	5.9(0.5)	2.15(0.01)	5.9(1.6)*	0.2(0.3)	2.51(0.11)	5.9(1.6)*	1-4.3	2.2-10.2	0.016	14.62
200	-2.1(0.9)	5.5(0.5)	2.15(0.01)	7.5(1.9)*	0.3(0.3)	2.57(0.07)	7.5(1.9)*	1-4.3	2.2-10.2	0.021	16.45
300	-2.6(1.4)	4.9(0.7)	2.13(0.02)	9.2(2.9)*	0.8(0.5)	2.54(0.03)	9.2(2.9)*	1-3	2.2-10.2	0.013	12.77
400	-2.0(2.2)	2.9(0.5)	2.13(0.03)	11.2(3.5)*	2.3(1.1)	2.48(0.02)	11.2(3.5)*	1-3	2.2-10.2	0.032	14.98
500	-3.3(2.9)	1.3(0.5)	2.14(0.04)	9.8(2.9)*	3.0(1.1)	2.43(0.02)	9.8(2.9)*	1-3	2.2-10.5	0.059	5.96

* Debye-waller factor set to be identical for Mn-O and Mn-Br interactions.

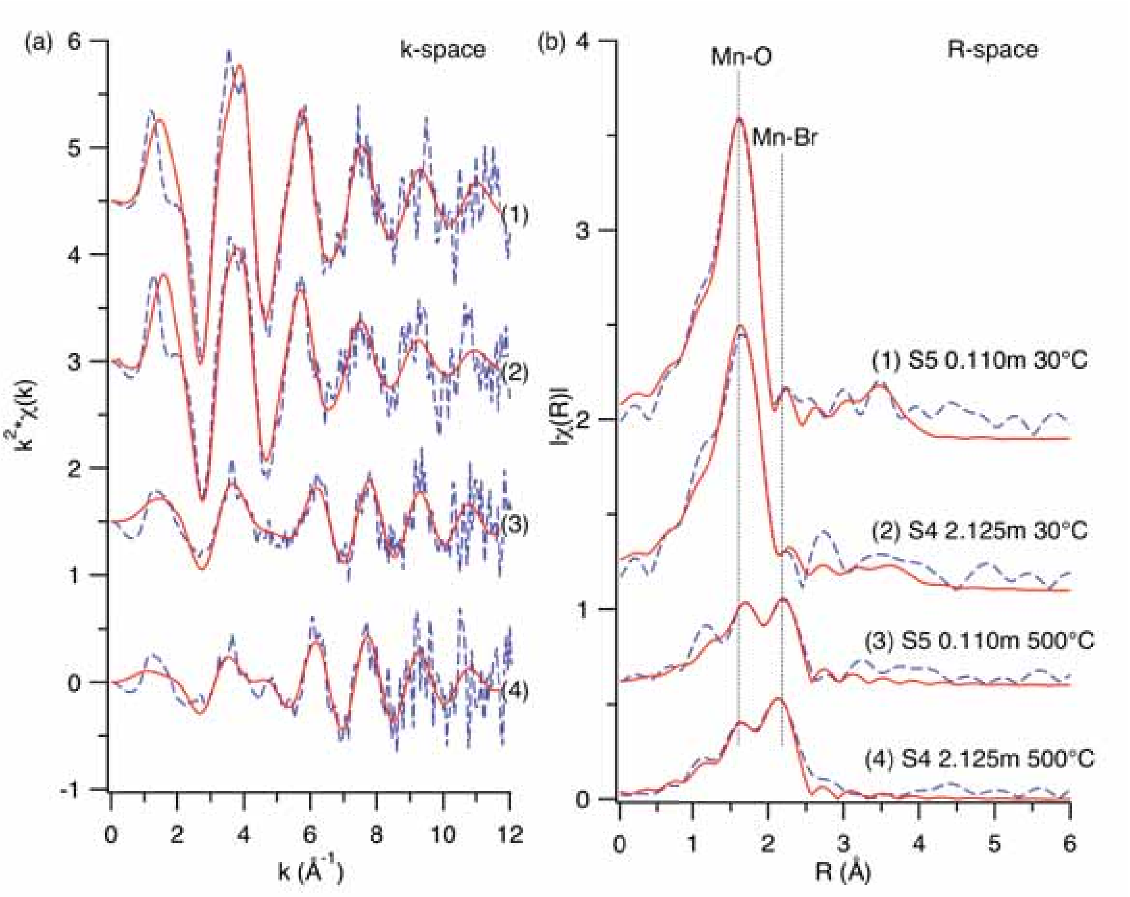

Figure 5.7 Experimental (blue dashed line) and fitted (red solid line) EXAFS spectra of S5 (0.110 m Br) and S4 (2.125 m Br) at 30 °C and 500 °C in (a) k-space and (b) R-space. All fits are shown with k^2 weighting.

5.5 DFT calculations

The results of geometry optimization by DFT for the proposed Mn(II) complexes are summarized in Table 5.7, with detailed structural information listed in the Section 5.8.2. The optimized Mn-O and Mn-Br bond distances were generally longer than the refined EXAFS distances, while Mn-Cl distances were slightly shorter than the EXAFS distances (e.g., 2.16 Å for Mn-O by EXAFS at 30 ˚C in 0.100 *m* Cl solution and 2.21 Å for DFT; 2.37 Å for Mn-Cl by EXAFS at 500 ˚C in 10.344 *m* Cl solution and 2.34 Å for DFT). These discrepancies are in-line with the expected accuracy of the DFT calculations (e.g., Bühl and Kabrede 2006). The most important result from the DFT calculations is that the trends in the variation of the experimental bond lengths are accurately reproduced: a small contraction occurs when geometry changes from octahedral to tetrahedral, and the Mn-O, Mn-Cl and Mn-Br bond lengths increase with increasing number of halide ligands within the same coordination geometry. As a result, averaged Mn-O distances are actually longer, for example, in $MnBr_3(H_2O)^-$ (2.221 Å) than in $Mn(H_2O)_6^{2+}$ (2.21 Å).

Table 5.7 Bond distances for the manganese (II) clusters optimized by DFT. Where several identical ligands are present, the value represents the average distance, with the standard deviation given in parentheses.

Mn(II) Cluster	**Geometry**	**Mn-O (Å)**	**Mn-Cl (Å)**
$Mn(H_2O)_6^{2+}$	Octahedral	2.2081 (0.0156)	-
$MnCl(H_2O)_5^{+}$	Octahedral	2.2568 (0.0113)	2.3657 (0)
$MnCl_2(H_2O)_{4\,(aq)}$ (*cis*)	Octahedral	2.2971 (0.0180)	2.4293 (0.0018)
$MnCl_2(H_2O)_{4\,(aq)}$ (*trans*)	Octahedral	2.2871 (0.0060)	2.4353 (0.0380)
$MnCl(H_2O)_3^{+}$	Tetrahedral	2.1286 (0.0012)	2.2554 (0)
$MnCl_2(H_2O)_{2\,(aq)}$	Tetrahedral	2.1779 (0.0076)	2.2909 (0.0011)
$MnCl_3(H_2O)^{-}$	Tetrahedral	2.2322 (0)	2.3384 (0.0053)
$MnCl_4^{2-}$	Tetrahedral	-	2.3808 (0)
$MnBr(H_2O)_5^{+}$	Octahedral	2.2522 (0.0113)	2.5495 (0)
$MnBr_2(H_2O)_{4\,(aq)}$ (*cis*)	Octahedral	2.2904 (0.0170)	2.5988 (0.0042)
$MnBr_2(H_2O)_{4\,(aq)}$ (*trans*)	Octahedral	2.2645 (0.0077)	2.6420 (0.1297)
$MnBr(H_2O)_3^{+}$	Tetrahedral	2.1295 (0.0005)	2.4145 (0)
$MnBr_2(H_2O)_{2\,(aq)}$	Tetrahedral	2.1695 (0.0199)	2.4576 (0.0015)
$MnBr_3(H_2O)^{-}$	Tetrahedral	2.2210 (0)	2.5012 (0.0069)
$MnBr_4^{2-}$	Tetrahedral	-	2.5495 (0)

5.6 *Ab initio* XANES simulations

5.6.1 Simulations for solid standards

Calculations for Mn(II) solid standards were performed to assess the ability of XANES simulations to reproduce the spectral features of known Mn(II) structures (Figure 5.8). The compounds contain both octahedral and tetrahedral moieties: octahedral $[MnO_6]$ in $MnCO_{3(s)}$, octahedral $[MnCl_2(H_2O)_4]$ in $MnCl_2•4H_2O_{(s)}$, and tetrahedral $[MnCl_4]$ in

$(NEt_4)_2MnCl_{4(s)}$. For $MnCO_{3(s)}$, calculation with a radius of 6 Å using the FDM method reproduced the key spectral features of experimental spectra well (Figure 5.8a). Note that the raw spectrum reproduces accurately the structure of feature F, but the convolution process smoothes out the sharp band at ~6596 eV. The location of this feature corresponds to that of multielectron excitations in the spectra of aqueous complexes (Chen et al., 2005a); such multielectron excitations are not taken into account in the calculations. For $MnCl_2•4H_2O_{(s)}$ and $(NEt_4)_2MnCl_{4(s)}$, the calculated spectra with a radius of 3 Å using the FDM method was in good agreement with the experimental spectrum except for the missing shoulder at around 6548 eV (feature B). Calculations using larger radii (6 Å for $MnCl_2•4H_2O_{(s)}$ by FDM; 7 Å for $(NEt_4)_2MnCl_{4(s)}$ by MT approximation) improved the agreement of feature B (Figure 5.8b, c). Therefore, feature B for $MnCl_2•4H_2O_{(s)}$ and $(NEt_4)_2MnCl_{4(s)}$ is attributed to contributions from beyond the first shell. Overall, such agreements inspire high confidence that *ab initio* XANES simulations can be used to explore the structure of Mn(II) in solutions.

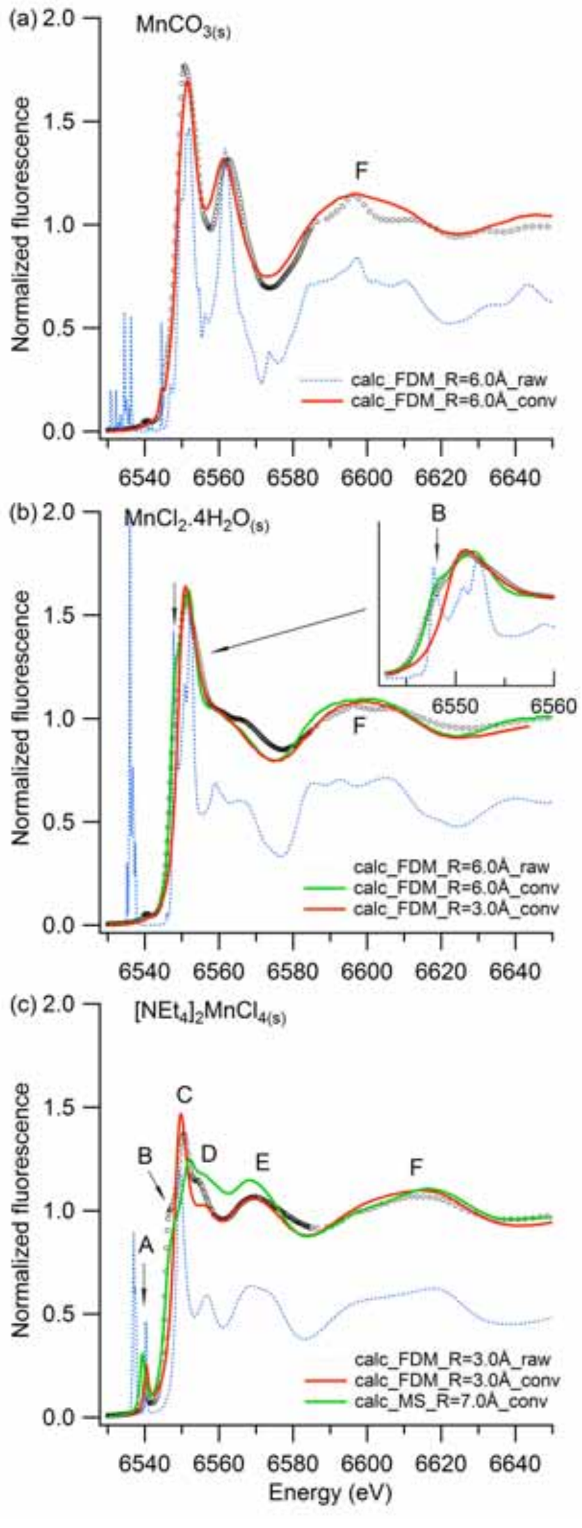

Figure 5.8 Experimental and calculated (both raw and convoluted) XANES spectra for Mn model compounds: (a) $MnCO_{3(s)}$, (b) $MnCl_2.4H_2O_{(s)}$, and (c) $(NEt_4)_2MnCl_{4(s)}$. Open circles are experimental spectra; the calculated raw spectra ('raw') and the convoluted spectra ('conv') with different calculation radius using different methods (FDM: Finite Difference Method, MS: multiple scattering theory) are shown. See text for details.

5.6.2 Simulations of aqueous complexes

In general, the intensity of feature F is miscalculated, because the experimental spectra are affected by multielectron excitations. The calculated XANES spectra based on DFT optimized geometries for a series of octahedral species with increasing Cl substitution exhibit a consistent trend with the spectral evolution observed experimentally at low temperature with increasing salinity (Figure 5.9a): the increase in pre-edge peak (inset in Figure 5.9a) and slight decrease in white line intensity, the shift of white line to lower energy, and reduced oscillation of features D, E, and F were correctly reproduced. The inclusion of H atoms in the calculations affects mainly the intensity of the pre-edge peak. For example, the calculated pre-edge for the $[Mn(H_2O)_6]$ moiety was over-estimated compared to that for $[MnO_6]$ (Figure 5.9c). As these calculations were based on a single rigid configuration and the hydrogen atoms are disordered (Testemale et al., 2009), the overall effect of the H atoms on the XANES spectrum is expected to be small (e.g., Liu et al., 2012). For tetrahedral species, increasing the number of Cl ligands from one to four resulted in the following systematic changes in the calculated XANES spectra: i) progressive growth of feature E, ii) decreased intensity of feature D, and iii) shifted feature D to lower energy leading to a slimmer white line. These trends were consistent with the evolution of experimental spectra at 500 ˚C when salinity increased from 0.100 to 10.344 m (Figures 5.2f and 5.9b). The intensity of features C and E for $[MnCl_4]$ was too high compared to the experimental spectrum of S8 at 500 ˚C. Feature C was too broad and the intensity of feature E was mis-fitted in $[MnCl(H_2O)_3]$ compared to the experimental spectrum of S1 at 500 ˚C (Figure 5.9b). The best agreement with these experimental spectra was obtained by the calculated spectra for $[MnCl_2(H_2O)_2]$ and $[MnCl_3(H_2O)]$ for S1 and S8 at 500 ˚C, respectively. The XANES spectra of the bromide solutions S5 (0.110 *m* Br) and S4 (2.125 *m* Br) at 500 ˚C were well reproduced by the calculations for the $[MnBr_2(H_2O)_2]$

and [$MnBr_3(H_2O)$] clusters, respectively, although the shape and intensity of feature C and E are less distinguishable than in the counterpart Mn chloride complexes (Figure 5.9b).

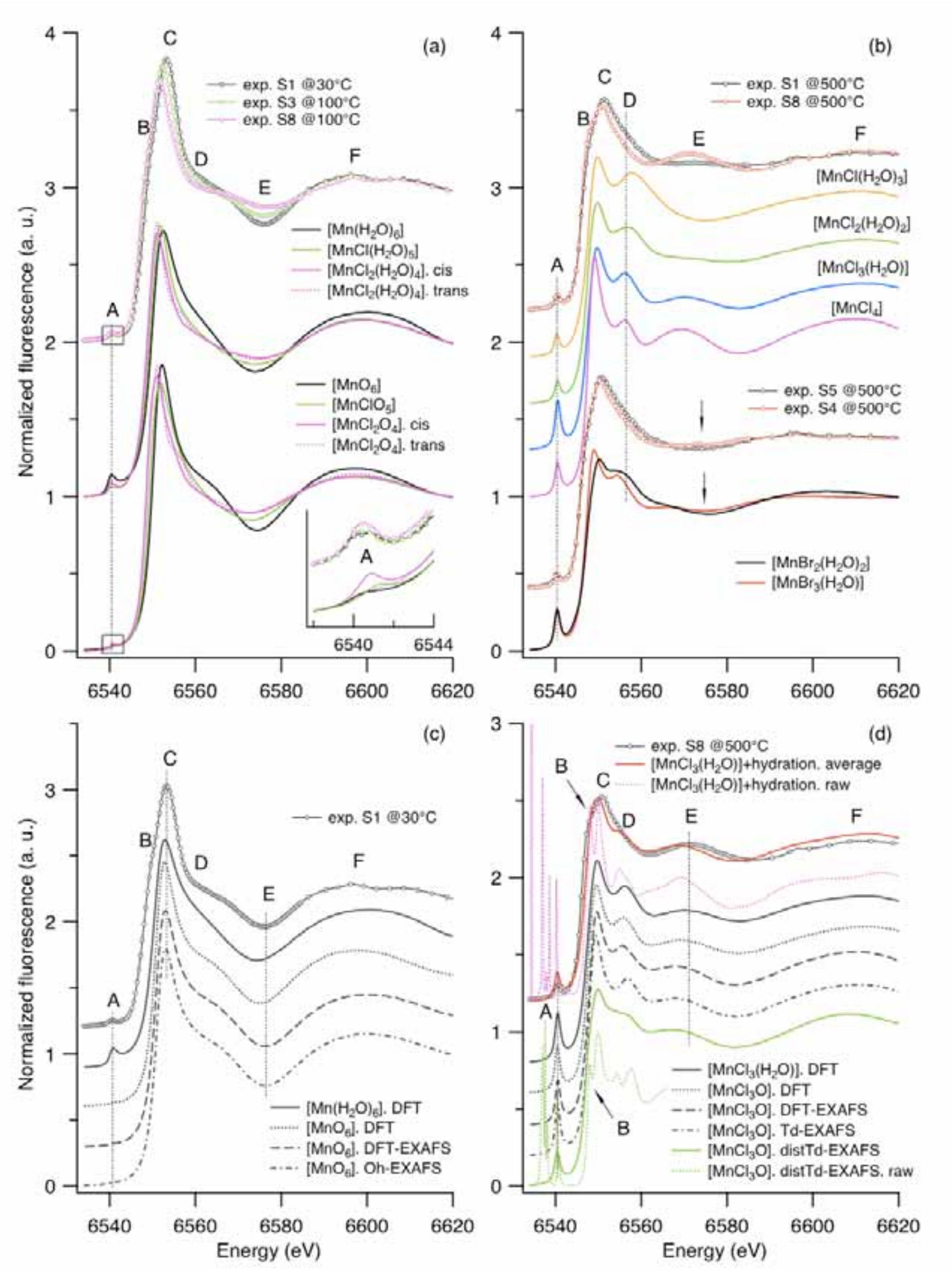

Figure 5.9 Experimental XANES spectra of some representative Mn solutions and calculated XANES spectra of Mn-Cl-O clusters based on DFT-optimized structures (see text for details). The calculated raw spectra were labelled as ‘raw’.

To illustrate the effects of bond lengths and cluster geometry on the XANES spectra of the octahedral $[Mn(H_2O)_6]^{2+}$ and tetrahedral $[MnCl_3(H_2O)]^-$) species (Figures 5.9c and 5.9d, respectively), calculations were conducted on the following structures: DFT optimized structures (Section 5.8.2); highly distorted $[MnCl_3(H_2O)]^-$ (‘disTd’; Section 5.8.2); DFT optimized structures with bond lengths modified to correspond to the EXAFS refined bond lengths; and regular octahedron or tetrahedron with EXAFS bond lengths. Changes in bond lengths resulted in a shift in feature E by ~2 eV (e.g., Testemale et al., 2009). The main disagreement between experimental and calculated spectra for tetrahedral complexes is a double peak for the white line on the calculated spectra, instead of the experimental broad asymmetrical peak (Figure 5.9b, d). The reason might be that the structures used in XANES calculations were rigid and no thermal and structural disorders were taken into account, and the absence of the second hydration shell may also contribute to this discrepancy.

Moreover, the shoulder at 6548 eV (feature B) is relatively more intense on the experimental spectra than on the DFT calculated spectra. In a more strongly distorted tetrahedral structure (labeled ‘disTd’ in Figure 5.9d), a peak at 6548 eV appears on the raw spectrum, resulting in slightly better calculated shape of feature B than the DFT optimized structure. According to Chen et al. (2005b), the growth of feature B with increasing temperature is also affected by the solvent-shared ion pairs Mn•••H_2O•••Cl from the second shell. To assess the impact of hydration beyond the first shell on the XANES spectra, second shell configurations around the $[MnCl_3(H_2O)]^-$ cluster were generated using the classical molecular dynamics (MD) code MOLDY (Refson, 2000). Rigid structures for water (SPC/E model; Berendsen et al., 1987) and the structure of $[MnCl_3(H_2O)]^-$ optimized by the DFT calculation were used for the MD simulations together with the SPC/E potential for water and approximated pair potentials derived from finite cluster calculations for Mn-Cl and Mn-O (see details in Section 5.8.3). Twenty frames from the MOLDY outputs were used as the input for the XANES simulations (calculation radius = 4.5 Å, FDM mode). The resulting twenty convoluted spectra were averaged. This average spectrum is shown (red solid line) together with the raw spectrum of one typical frame (pink dotted line) in Figure 5.9d. The peak at 6548 eV on the raw spectrum corresponds to feature B on the experimental spectrum, confirming the effect of the second shell on this feature. Beyond feature B, the inclusion of the second shell had a minor effect on the convoluted XANES spectrum.

Overall, the XANES simulations confirm the result of the EXAFS analysis that stepwise substitution of H_2O by Cl^- occurs within the octahedral coordination sphere around Mn^{2+} with increasing chlorinity at low temperatures (30 – 100 ˚C), and are consistent with the predominance of $MnCl_2(H_2O)_{2(aq)}$ and $MnCl_3(H_2O)^-$ in low and high salinity solutions at elevated temperatures (i.e., 450 – 500 ˚C). In particular, the intensity of feature E strongly depends on the chloride ligation number of the predominant species: the more Cl^- complexed to Mn^{2+}, the larger the bump is. Therefore, the higher intensity of feature E for $(NEt_4)_2MnCl_{4(s)}$ than for the aqueous solutions (Figure 5.3f) is due to the highest order $[MnCl_4]^{2-}$ moiety in the first shell of $(NEt_4)_2MnCl_{4(s)}$.

5.7 Discussion: Mn(II) speciation in chloride brines

5.7.1 Nature of Mn(II) chlorocomplexes

The combination of qualitative XANES analysis (Section 5.3), quantitative EXAFS refinements (Section 5.4) and DFT/*ab initio* XANES simulations (Sections 5.5/5.6) presents a complete picture of the coordination changes of Mn(II) chloride complexes from ambient to supercritical conditions. At low temperature, chloride anions replace some water groups within an octahedral complex with increasing Cl^- concentration. At 10.344 m Cl_{tot}, 1.6(5) Cl^- at 30 ˚C and 2.0(5) Cl^- at 100 ˚C are bonded to Mn^{2+} (Table 5.4), indicating that a series of octahedral complexes is present, e.g., $MnCl(H_2O)_5^+$ and $MnCl_2(H_2O)_{4(aq)}$. Higher order octahedral complexes such as $MnCl_3(H_2O)_3^-$ and $MnCl_4(H_2O)_2^{2-}$ may exist in highly concentrated chloride solutions from room-T to around 200 ˚C, but these complexes are considered to be minor species because octahedral complexes transform to tetrahedral quickly upon heating above 100 ˚C and they were not detected in our system (salinity: 0.100 – 10.344 *m* Cl) or in the UV-Vis experiments of Suleimenov and Seward (2000). Thus, the octahedral complexes $Mn(H_2O)_6^{2+}$, $MnCl(H_2O)_5^+$, and $MnCl_2(H_2O)_{4(aq)}$ were included in our final speciation model.

The role of solvent on determining the coordination geometry of the Mn(II) halogenide complexes was illustrated by Ozutsumi et al. (1994), who identified a series of five-fold halogenated Mn(II) complexes in a hexamethylphosphoric triamide solution at room temperature (dielectric constant ~30). In contrast, in Cl- or Br-bearing aqueous solutions, Mn(II) complexes exhibit a coordination change from octahedral to tetrahedral upon heating and/or increasing salinity (This study; Chen et al., 2005b). Chen et al. (2005b) identified a family of four-coordinated species: $MnBr(H_2O)_3^+$, $MnBr_2(H_2O)_{2(aq)}$ and $MnBr_3(H_2O)^-$, but found no evidence for the fully halogenated complex $MnBr_4^{2-}$. Similarly, the highest order chloride complex we can identify by combining XANES and EXAFS data was not $MnCl_4^{2-}$ but $MnCl_3(H_2O)^-$. Hence, the available data suggest that $MnCl_4^{2-}$ is only a minor species for Mn transport in brines up to 10 m Cl_{tot}. Similarly, $MnCl(H_2O)_3^+$ is only a minor species in very dilute solutions, and Mn(II) speciation in Cl-bearing solutions at elevated temperatures (⩾ 450 ˚C) consists mainly of two tetrahedral complexes: $MnCl_2(H_2O)_{2(aq)}$ and $MnCl_3(H_2O)^-$ with the ratio of the two species strongly depending on the total Cl^- concentration and the Cl:Mn molar ratio.

Similar to the results for the Mn-Cl system, the EXAFS analysis for the Mn-Br system confirm that: i) tetrahedral Mn(II) bromoaqua complexes dominate Mn speciation at 500 ˚C and 600 bar; ii) $MnBr_2(H_2O)_{2(aq)}$ and $MnBr_3(H_2O)^-$ are the predominant species in solutions with low and high Br concentrations, respectively; and iii) $MnBr_3(H_2O)^-$ is the highest order Mn(II) bromocomplex that could be identified in all bromide solutions of this study. The model $MnBr_{3.4(1.6)}O_{0.9(4)}$ refined by Chen et al. (2005b) from the EXAFS data of a solution at 400 ˚C and 310 bar (Br:Mn ratio = 6) is consistent with the refined models $MnBr_{3.0(1.1)}O_{1.3(5)}$ for S4 and $MnBr_{2.9(9)}O_{0.8(3)}$ for S15 at 500 ˚C and 600 bar in this study. The refined models $MnBr_{2.3(1.1)}O_{2.9(5)}$ for S4 and $MnBr_{1.9(1.2)}O_{2.8(7)}$ for S15 at 400 ˚C and 600 bar suggest the presence of some octahedral component (Table 5.6). The reason could be that decreasing pressure at high temperature favors the formation of tetrahedral complexes (e.g., Lüdemann and Frank, 1967; Kojima et al., 1983, 1984; Suleimenov, 2000). Throughout all temperature and salinity ranges, no evidence of Mn hydroxide complexes has been found and Mn speciation is controlled by halide complexes only, consistent with speciation calculations conducted using the thermodynamic properties of $Mn(OH)^+$ from Shock et al (1997) and $Mn(OH)_{2(aq)}$ regressed from solubility data of Wolfram and Krupp (1996) (Table 5.9).

5.7.2 Thermodynamic analysis

Normalized fluorescence XANES spectra of Mn(II) chloride solutions with a chlorinity range of 0.100 - 5.131 m were used to derive formation constants for Mn(II) chloride complexes following the method described in previous studies (Liu et al., 2007, 2011, 2012; Testemale et al., 2009; Etchmann et al., 2011; Tian et al. 2012) using the BeerOz package (Brugger 2007).

Three octahedral complexes and two tetrahedral complexes were included in the Mn speciation model: $Mn(H_2O)_6^{2+}$, $MnCl(H_2O)_5^{+}$, $MnCl_2(H_2O)_{4(aq)}$, $MnCl_2(H_2O)_{2(aq)}$ and $MnCl_3(H_2O)^{-}$. In this analysis, we assume that the $MnCl^{+}$ and $MnCl_{2(aq)}$ species identified in previous studies at low temperatures (≤ 300 ˚C) have an octahedral geometry. Modified Ryzhenko-Bryzgalin (MRB) parameters (Ryzhenko et al., 1985) for $MnCl(H_2O)_5^{+}$ and $MnCl_2(H_2O)_{4(aq)}$ were regressed using the optimC program (Shvarov, 2008) from the following datasets and weighting scheme (Figures 5.11a, b; Table 5.9). For $MnCl(H_2O)_5^{+}$, the data derived from the solubility experiments of Gammons and Seward (1996) were given a weighting of 0.5 at 25 ˚C and 50 ˚C, because of difficulties in equilibrating solubility experiments at low temperature. The remaining data points (Libuś and Tialowska 1975; Carpenter 1983; Wheat and Carpenter 1988; Gammons and Seward, 1996; Suleimenov and Seward, 2000) were given the weighting of 1.0. For $MnCl_2(H_2O)_{4(aq)}$, the UV-Vis data of Suleimenov and Seward (2000) and the solubility data of Gammons and Seward (1996) were given weightings of 1.0 and 0.8, respectively, to slightly emphasize the newest results. The formation constants of $NaCl_{(aq)}$ and $HCl_{(aq)}$ were taken from Sverjensky et al. (1997) and Tagirov et al. (2001), respectively.

As XANES simulations confirmed that the experimental XANES spectra of S1 at 30 ˚C, S3 at 100 ˚C, S8 at 100 ˚C, S1 and S8 at 500 ˚C were representative of the octahedral and tetrahedral species $Mn(H_2O)_6^{2+}$, $MnCl(H_2O)_5^+$, $MnCl_2(H_2O)_{4(aq)}$, $MnCl_2(H_2O)_{2(aq)}$ and $MnCl_3(H_2O)^-$, respectively, the spectra of these species were fixed from their corresponding experimental spectra. The idea is to limit the number of unknown parameters in the model in order to retrieve formation constants for the two tetrahedral complexes $MnCl_2(H_2O)_{2(aq)}$ and $MnCl_3(H_2O)^-$. As tetrahedral complexes are unstable at low temperatures (30 and 100 ˚C), only the last four datasets (200 - 450 ˚C) were used for XANES fitting. The formation constants for octahedral species were extrapolated from the MRB equation of state, and fixed during the analysis. The refined formation constants for $MnCl_2(H_2O)_{2(aq)}$ and $MnCl_3(H_2O)^-$ are listed in Table 5.8. The uncertainties in the fitted log K values were estimated at the 90% confidence level based on residual maps using the F-distribution factors given by Draper and Smith (1998).

Table 5.8 Formation constants of the aqueous species at 600 bar used in thermodynamic analysis.

Species	**30°C**	**100 °C**	**200 °C**	**300 °C**	**400 °C**	**450 °C**	**References**
$HCl_{(aq)}$	-0.78	-0.96	-0.33	0.79	2.33	3.51	Tagirov et al. (1997)
$NaCl_{(aq)}$	-0.83	-0.54	-0.04	0.61	1.57	2.45	Sverjensky et al. (1997)
$MnCl(H_2O)_5^+$	0.15	0.86	2.04	3.39	5.34	7.02	Libuś and Tialowska (1975) Carpenter (1983) Wheat and Carpenter (1988) Gammons and Seward (1996) Suleimenov and Seward (2000)
$MnCl_2(H_2O)_{4(aq)}$	-5.66	-1.73	1.64	3.98	6.59	8.72	Gammons and Seward (1996) Suleimenov and Seward (2000)
$MnCl_2(H_2O)_{2(aq)}$	-	-	1.04 (<1.55)	4.05 (±0.25)	7.52 (±0.15)	10.58 (±0.49)	Fitted in this study
$MnCl_3(H_2O)^-$	-	-	0.80 (<1.17)	3.76 (±0.25)	7.60 (±0.18)	11.22 (±0.31)	Fitted in this study

The calculated Mn(II) speciation from 200 to 450 ˚C is shown in Figure 5.10. At 200 ˚C, octahedral species predominate Mn speciation; at 300 ˚C tetrahedral species represent less than 30% of all species from 0 to 0.8 m Cl, consistent with the findings of Suleimenov and Seward (2000); at 400 ˚C octahedral species still persist in low salinity solutions but tetrahedral species become predominant with increasing Cl concentration; and at 450 ˚C the octahedral species are negligible, and only two tetrahedral species exist with the fraction of each species depending on the total Cl concentration. The average ligation numbers calculated using the properties in Table 5.8 are in good agreement with the EXAFS refined stoichiometries (Figure 5.6), providing additional evidence that the refined formation constants of $MnCl_2(H_2O)_{2(aq)}$ and $MnCl_3(H_2O)^-$ are valid.

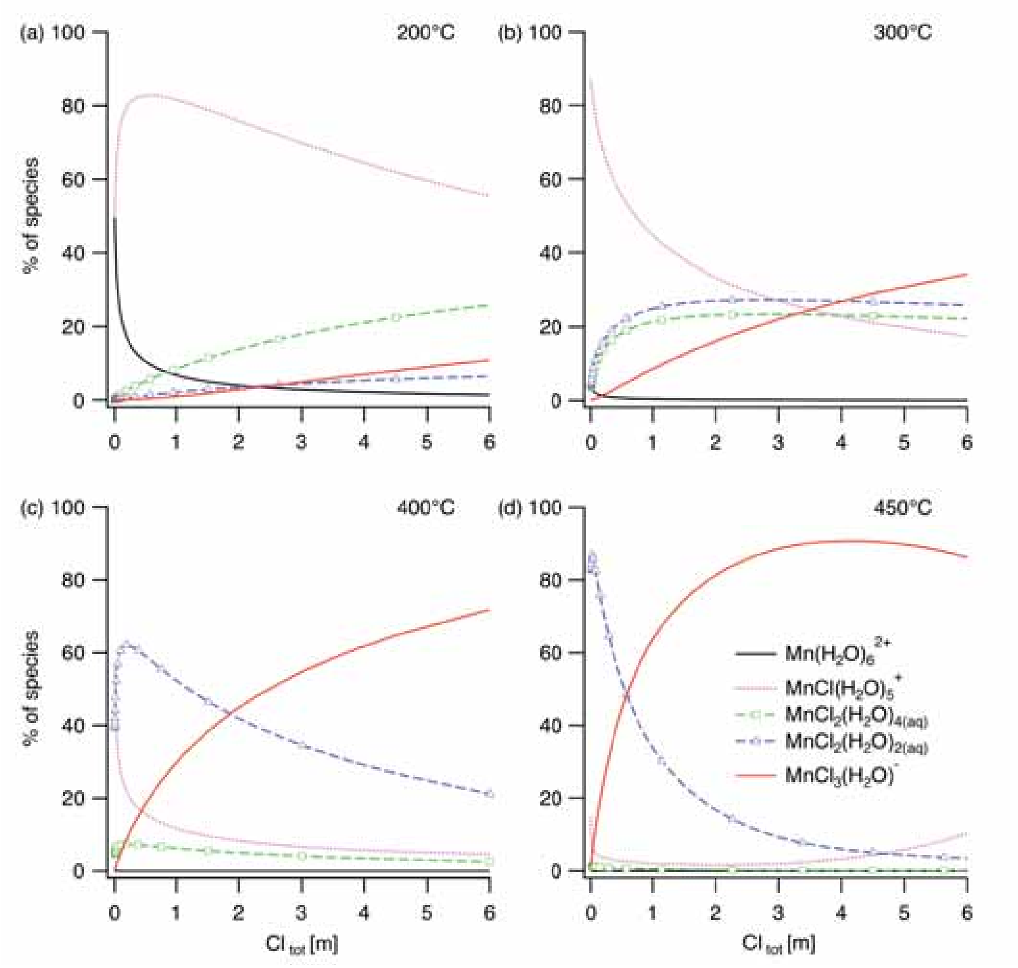

Figure 5.10 Speciation as a function of chlorinity based on the refined thermodynamic properties in Table 5.9 at (a) 200 °C, (b) 300 °C, (c) 400 and (d) 450 °C and 600 bar.

To further test the validity of the thermodynamic model presented here, we checked the compatibility of the properties of $MnCl_2(H_2O)_{2(aq)}$ and $MnCl_3(H_2O)^-$ with the data obtained by Boctor (1985) and Uchida and Tsutsui (2000) at higher temperatures and pressures. In this analysis, we assume that the $MnCl_{2(aq)}$ and $MnCl_3^-$ species identified in these two solubility studies at 1 and 2 kbar from 400 ˚C to 800 ˚C have a tetrahedral geometry. The equilibrium constants for the reaction $MnSiO_{3(s)} + HCl_{(aq)} = MnCl_{2(aq)} + SiO_{2(s)} + H_2O$ at 1 and 2 kbar from 400 to 700 ˚C (Boctor, 1985) were converted to cumulative formation constants for $MnCl_{2(aq)}$ using the thermodynamic properties of $MnSiO_{3(s)}$ from Robie et al. (1978), $HCl_{(aq)}$ from Tagirov et al (1997) and $SiO_{2(s)}$ from Helgeson et al. (1978). Attempting to fit all the data using MRB or HKF resulted in unrealistic pressure parameters, i.e. the extrapolations predicted that the speciation was much more pressure sensitive in the 0-1000 bar region than experiments suggest, making the predictions 1-2.5 orders of magnitude higher than the experimental data at 1 kbar (Figure 5.11c). Thus, in the final analysis, the 1 kbar dataset of Boctor (1985) was discarded, and MRB parameters of $MnCl_2(H_2O)_{2(aq)}$ were regressed from the combination of our data (weighting of 1.0; Table 5.8) and the 2 kbar solubility data from Boctor (1985) (weighting of 0.5 applied for data at 400 – 500 ˚C; and 1.0 for 550 – 700 ˚C). The 1 kbar equilibrium constants for the reaction $MnCl_{2(aq)} + Cl^- = MnCl_3^-$ (Uchida and Tsutsui 2000) were converted to cumulative formation constants for $MnCl_3^-$ by extrapolating the formation constants of $MnCl_{2(aq)}$ to 1 kbar at 400 – 600 ˚C using the newly regressed MRB parameters of $MnCl_2(H_2O)_{2(aq)}$ (Table 5.9). Similarly, MRB parameters of $MnCl_3(H_2O)^-$ were regressed from the combination of our data (Table 5.8) and the 1 kbar solubility data from Uchida and Tsutsui (2000) by equal weighting. The refined formation constants of $MnCl_3(H_2O)^-$ at 600 bar in this study are consistent with the 1 kbar data derived from Uchida and Tsutsui (2000) (Figure 5.11d). The refined MRB parameters of the four Mn species are listed in Table 5.9 and calculated formation constants of $MnCl_2(H_2O)_{2(aq)}$ and $MnCl_3(H_2O)^-$ at 150 – 800 ˚C from water saturated pressure (P_{sat}) to 2 kbar are shown in Table 5.10. Overall, the speciation and thermodynamic model of this study are not only self-consistent but also compatible with previous studies (e.g., Boctor, 1985; Gammons and Seward 1996; Suleimenov and Seward 2000; Uchida and Tsutsui 2000).

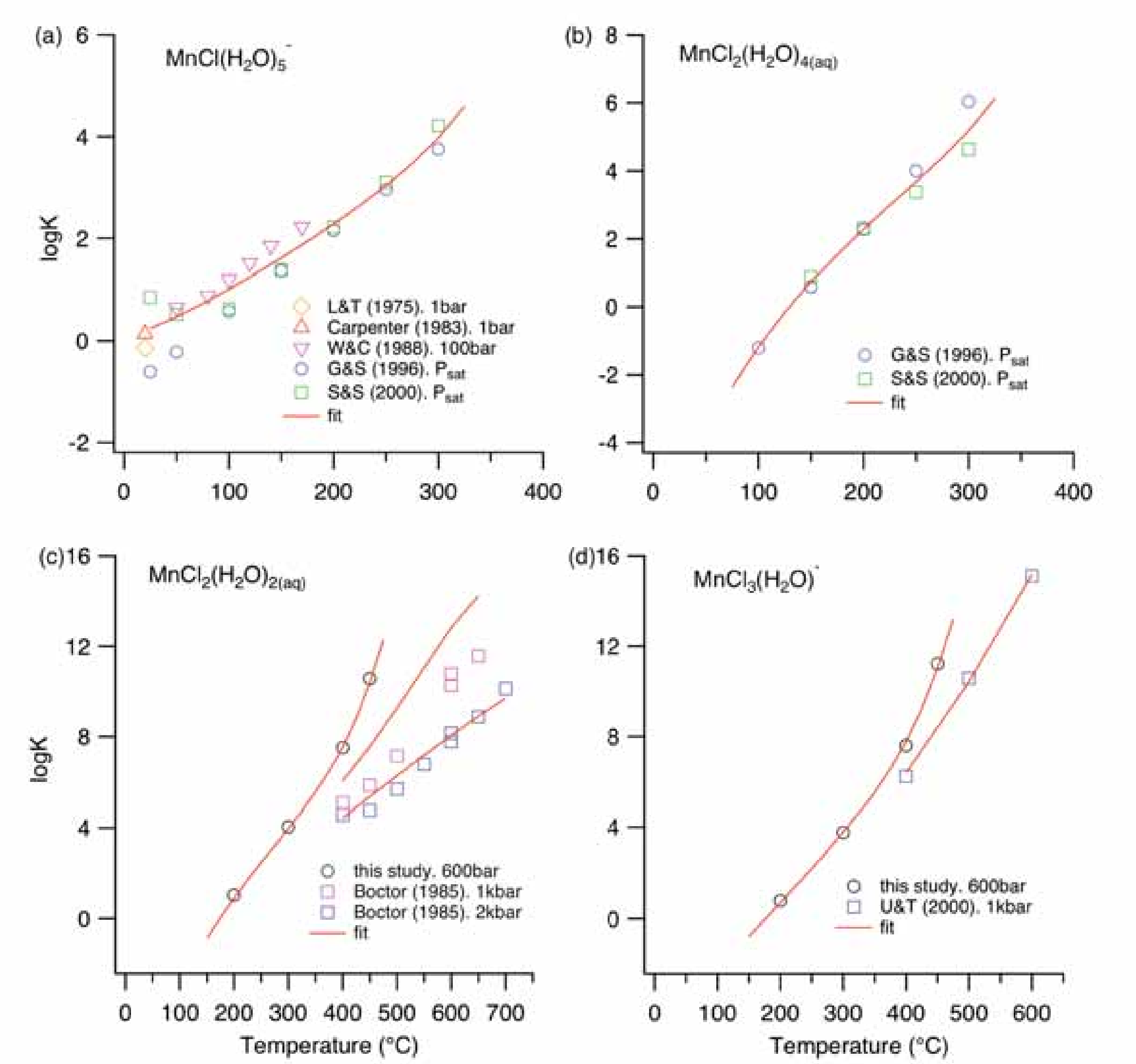

Figure 5.11 Formation constants (log K) of (a) $MnCl(H_2O)_5^+$ determined by experimental data of Libuś and Tialowska (1975), Carpenter (1983), Wheat and Carpenter (1988), Gammons and Seward (1996) and Suleimenov and Seward (2000); (b) $MnCl_2(H_2O)_{4(aq)}$

determined by experimental data of Gammons and Seward (1996) and Suleimenov and Seward (2000); (c) $MnCl_2(H_2O)_{2(aq)}$ determined by this study and derived from 1 and 2 kbar data of Boctor (1985); (d) $MnCl_3(H_2O)^-$ determined by this study and derived from the 1kbar data of Uchida and Tsutsui (2000). The solid lines represent fits to these experimental data using the modified Ryzhenko–Bryzgalin (MRB) model (Ryzhenko et al., 1985) with MRB parameters listed in Table 5.9.

Table 5.9 MRB parameters (*A(zz/a)* and *B(zz/a)*) for $Mn(OH)_{2(aq)}$, $[MnCl(H_2O)_5]^+$, $[MnCl_2(H_2O)_4]_{(aq)}$, $[MnCl_2(H_2O)_2]_{(aq)}$ and $[MnCl_3(H_2O)]^-$.

Species	$log\ K_{(298K)}$	$A_{(zz/a)}$	$B_{(zz/a)}$
$Mn(OH)_{2(aq)}$	9.450	1.806	-748.90
$MnCl(H_2O)_5^+$	0.242	1.276	-191.18
$MnCl_2(H_2O)_{4(aq)}$	-5.293	0.263	963.32
$MnCl_2(H_2O)_{2(aq)}$	-6.936	1.000	679.76
$MnCl_3(H_2O)^-$	-4.627	2.303	-295.96

Table 5.10 Formation constants for $[MnCl_2(H_2O)_2]_{(aq)}$ and $[MnCl_3(H_2O)]^-$ from 150 to 800 °C at water saturated pressure (P_{sat}), 500 bar, 1000 bar and 2000 bar based on the properties in Table 5.9. Note: $[MnCl_2(H_2O)_2]_{(aq)}$ and $[MnCl_3(H_2O)]^-$ are unstable at low temperatures, and only data from 150 to 800 °C are listed.

T (°C)	P_{sat}	500 bar	1000 bar	2000 bar
$MnCl_2(H_2O)_{2(aq)}$				
150	-0.31	-0.79	-1.20	-1.87
200	1.58	1.00	0.54	-0.18
250	3.36	2.60	2.02	1.20
300	5.32	4.15	3.37	2.38
350	8.27	5.88	4.68	3.44
400	-	8.23	6.05	4.42
450	-	12.44	7.56	5.36
500	-	-	9.27	6.28
600	-	-	12.81	8.06
700	-	-	-	9.69
800	-	-	-	11.08

(continued)

Table 5.10 continued

$MnCl_3(H_2O)^-$				
150	-0.44	-0.74	-0.99	-1.40
200	1.18	0.78	0.46	-0.03
250	2.89	2.31	1.88	1.26
300	4.89	3.93	3.29	2.49
350	7.91	5.83	4.78	3.69
400	-	8.43	6.41	4.90
450	-	13.03	8.26	6.12
500	-	-	10.42	7.37
600	-	-	15.19	9.94
700	-	-	-	12.49
800	-	-	-	14.85

5.7.3 Comparison with Fe(II) chloride complexing

Like other first row divalent transition metals (e.g., Fe, Co, Ni, Zn, Cu; Collings et al. 2000; Brugger et al. 2001; Liu et al. 2007, 2011, 2012; Testemale et al. 2009; Tian et al., 2012), the stability of tetrahedral complexes is promoted both by increasing temperature and chlorinity. Compared with Fe(II) chloride complexation, the octahedral to tetrahedral structural transition occurs at higher temperature for Mn(II) complexes (Testemale et al., 2009). The highest order chloride complex identified in this study is the tri-chloro mono-aqua complex $MnCl_3(H_2O)^-$ with $MnCl_4^{2-}$ being unstable through all T-P-salinity range. In contrast, the fully chlorinated tetrahedral complex $[FeCl_4]^{2-}$ has high stability, being the dominant species in concentrated brines at elevated temperature (Testemale et al., 2009). Tetrahedral Mn chloroaqua species (e.g., $MnCl_2(H_2O)_{2(aq)}$ and $MnCl_3(H_2O)^-$) are largely responsible for the high mobility of Mn in Cl-rich fluids in the Earth's crust.

5.8 Annexes

5.8.1 Single crystal x-ray diffraction for $(NEt_4)_2MnCl_{4(s)}$

The $(NEt_4)_2MnCl_4$ crystal (formula: $(C_8H_{20}N)_2[MnCl_4]$) was attached to a glass fiber and mounted on an Oxford Diffraction Xcalibur E diffractometer equipped with an Eos CCD detector. Intensity data were collected at room temperature using Mo*K*α X-radiation (λ = 0.71073 Å) and a detector distance of 46.45 mm. Data collection conditions are given in Table 5.11. The data were processed using the CrysAlisPro program (Oxford Diffraction, 2009) and corrected for Lorentz and polarization effects. An empirical absorption correction was applied using the SCALE3 ABSPACK algorithm, as implemented in CrysAlisPro. The refined unit-cell parameters are a = 9.044(5), b = 9.044(5), c = 15.069(5) Å, V = 1232.6(10) $Å^3$ and Z = 2. Scattering curves for neutral atoms were taken from the International Tables for Crystallography (Wilson, 1992). The mean value of $|E^2-1|$ of 0.763 indicated that the structure is non-centrosymmetric and the systematic absences were consistent with space group $P4_2$/nmc. The structure refinement was initiated in space group $P4_2$/nmc, starting with the atomic coordinates for $(C_8H_{20}N)_2[ZnCl_4]$ of Mahoui (1996) using SHELXL-97 (Sheldrick, 2008). The refinement converged to $R1$ = 7.55% with isotropic displacement parameters for all atoms. Atomic coordinates and site occupancy of each atom in the cell unit are given in Table 5.12.

Table 5.11 Crystal data, data collection and refinement details for $(C_8H_{20}N)_2[MnCl_4]$.

Crystal data	
Formula	$(C_8H_{20}N)_2[MnCl_4]$
Space group	$P4_2$/nmc
a,b,c (Å)	9.044(5), 9.044(5), 15.069(5)
V ($Å^3$), Z	1232.6(10), 2

(continued)

Table 5.11 continued

$F(000)$	701
μ (mm^{-1})	1.449
Absorption correction	empirical
Data collection	
Diffractometer	Oxford Diffraction Xcalibur E
Temperature (K)	293
Radiation	Mo$K\alpha$, λ = 0.71073 Å
θ range (°)	2.63 – 29.19
Detector distance (mm)	46.45
Rotation axes, width (°)	ω
Total no. of frames	233
Collection time per frame (s)	30
h,k,l ranges	-11 → 12, -11 → 11, -20 → 15
Total reflections measured	5420
Data completeness (%)	98.1
Unique reflections	857 (R_{int} = 5.44%)
Refinement	
Refinement on	F^2
$R1^*$ for $F_o > 4\sigma(F_o)$	7.55%
w$R2^\dagger$ for all F_0^2	21.46%
Reflections used $F_o^2 > 4\sigma(F_o^2)$	447
Number of parameters refined	39
$(\Delta/\sigma)_{\max}$	0.0001
$\Delta\rho_{\min}$, $\Delta\rho_{\max}$ (e/Å^3)	0.516, -0.330
GooF	1.322

$^*R1 = \Sigma||F_O|-|F_C|| / \Sigma|F_O|$

$^\dagger wR2 = \Sigma w(|F_O|^2-|F_C|^2)^2 / \Sigma w|F_O|^2)^{1/2}$; $w = 1/[\sigma^2(F_O^2) + (0.042\ P)^2 + 12.60\ P]$;

$P = ([\max \text{ of } (0 \text{ or } F_0^2)] + 2F_C^2)/ 3$

Table 5.12 Atomic coordinates (X, Y, Z * 10^4), equivalent isotropic displacement parameter (U_{eq} * 10^4), and site occupancy of each atom in the cell unit.

Atom	X	Y	Z	U_{eq}	Site occupancy
N	2500	2500	5876(4)	70(2)	1
C(11)	2500	276(16)	4823(8)	79(3)	0.5
C(22)	4560(30)	2500	7000(14)	131(6)	0.5
C(1)	2220(40)	860(20)	5796(12)	109(8)	0.25
C(2)	4200(30)	2920(30)	6011(16)	124(9)	0.25
C(3)	1670(20)	3240(20)	6575(11)	80(5)	0.25
C(4)	1950(20)	3330(20)	5039(13)	109(7)	0.25
C(33)	-10(20)	3030(20)	6600(14)	99(7)	0.25
C(44)	1727(2)	4950(20)	5135(1)	107(7)	0.25
Mn	-2500(2)	2500(20)	2500(1)	64(1)	1
Cl	-406(2)	2500(20)	3405(1)	126(1)	1

5.8.2 DFT optimized geometries for Mn(II) complexes

The positions of each atom from the output of ADF program were in the format of Cartesian coordinates. To show the metal-ligand distances and geometric distortions (bond angles), the Cartesian coordinates were converted to Spherical coordinates via the link: http://www.random-science-tools.com/maths/coordinate-converter.htm. Mn^{2+} is at the origin of coordinates for all structures. These spherical coordinates were also applied in the input files of FDMNES program for *ab initio* XANES simulations. Here, Spherical coordinates for each Mn(II) complex are shown in Table 5.13.

Table 5.13 Spherical coordinates for each Mn(II) complex.

Atom	Metal ligand distance (r, Å)	Polar angle (θ, º)	Azimuthal angle (ϕ, º)
$Mn(H_2O)_6^{2+}$			
Mn	0.00000	0.0000	0.0000
O	2.18802	180.0000	0.0000

(continued)

Table 5.13 continued

O	2.18802	0.0000	0.0000
O	2.21726	90.0000	91.6491
O	2.21726	90.0000	-88.3509
O	2.21899	90.0000	-2.2302
O	2.21899	90.0000	177.7700
H	2.78790	73.9654	82.5084
H	2.78790	73.9654	-97.4916
H	2.78790	106.0350	82.5084
H	2.78790	106.0350	-97.4916
H	2.79312	73.9872	6.7733
H	2.79312	73.9872	-173.2270
H	2.79312	106.0130	6.7733
H	2.79312	106.0130	-173.2270
H	2.88569	164.3630	131.3280
H	2.88569	164.3630	-48.6724
H	2.88569	15.6373	131.3280
H	2.88569	15.6373	-48.6724
$MnCl(H_2O)_5^+$			
Mn	0.00000	0.0000	0.0000
Cl	2.36567	147.5960	80.9392
O	2.24382	87.5906	-10.5598
O	2.24823	32.5150	-93.1377
O	2.25733	87.8040	171.6020
O	2.26229	114.0020	-98.9358
O	2.27226	49.9825	85.4028
H	2.70649	106.1200	162.7750
H	2.73866	100.9530	3.8794
H	2.75304	68.4206	77.4820
H	2.75596	132.6150	-105.9090
H	2.77089	52.4357	110.0800
H	2.77725	109.7550	-78.8257
H	2.83031	70.2627	-6.1057
H	2.83050	48.4319	-105.9890
H	2.83937	17.0761	-115.0010
H	2.84994	87.4735	-170.7340
$MnCl_2(H_2O)_{4\,(aq)}$ *(cis)*			
Mn	0.00000	0.0000	0.0000
Cl	2.42801	137.0010	133.5670
Cl	2.43056	25.0920	155.2510
O	2.27172	97.2733	-126.4250
O	2.29689	82.4124	50.0882
O	2.30836	139.4560	-28.9302

(continued)

Table 5.13 continued

O	2.31137	58.4488	-44.6636
H	2.57502	160.1330	-10.6900
H	2.58793	36.2432	-46.8213
H	2.68107	63.9512	60.4952
H	2.69407	111.1970	-142.1150
H	2.69441	78.6728	-135.2830
H	2.70483	96.8798	64.7881
H	2.85658	127.6060	-9.7953
H	2.87654	64.4462	-25.5411
$MnCl_2(H_2O)_{4\,(aq)}$ (trans)			
Mn	0.00000	0.0000	0.0000
Cl	2.40847	33.5530	-97.9183
Cl	2.46217	146.4610	82.7991
O	2.28064	128.3170	-97.1999
O	2.28328	92.4992	169.6010
O	2.29206	86.1951	-9.1187
O	2.29244	62.0486	81.9104
H	2.65737	82.8328	77.1918
H	2.66853	73.0265	-25.9074
H	2.68888	105.1360	152.9220
H	2.69185	147.4880	-109.0400
H	2.80274	74.4209	164.1840
H	2.81345	115.0120	-112.6120
H	2.82153	53.0682	62.5232
H	2.83179	103.6890	-14.9291
$MnCl(H_2O)_3^+$			
Mn	0.00000	0.0000	0.0000
Cl	2.25544	52.9815	-58.1196
O	2.12767	162.5170	-4.5271
O	2.12825	75.6016	82.3827
O	2.12992	96.8938	-175.6690
H	2.69318	146.0320	-28.6242
H	2.69825	86.8892	-159.3110
H	2.70056	59.3795	71.4736
H	2.71462	92.5446	74.2351
H	2.71560	175.8010	-105.9340
H	2.72166	88.8247	167.4880
$MnCl_2(H_2O)_{2\,(aq)}$			
Mn	0.00000	0.0000	0.0000
Cl	2.29009	42.1647	-177.4956
Cl	2.29171	91.5747	-10.3058
O	2.17249	139.9994	-124.2810

(continued)

Table 5.13 continued

O	2.18323	109.7491	95.9734
H	2.70316	91.9811	104.5985
H	2.71638	108.7188	75.4225
H	2.721324	151.4576	-96.4318
H	2.755439	139.7726	-153.1383
$MnCl_3(H_2O)^-$			
Mn	0.00000	0.0000	0.0000
Cl	2.33230	89.1108	29.8760
Cl	2.34091	37.9230	167.0098
Cl	2.34186	153.9447	-165.0071
O	2.23216	80.1693	-76.2026
H	2.70204	64.6958	-89.7900
H	2.70393	97.6471	-86.1866
Man-made distorted $MnCl_3O$			
Mn	0.00	0	0
Cl	2.37	65	45
Cl	2.37	115	-45
Cl	2.37	115	135
O	2.13	65	-135
$MnCl_4^{2-}$			
Mn	0.00000	0.0000	0.0000
Cl	2.38078	54.7356	45.0000
Cl	2.38078	125.2640	-45.0000
Cl	2.38078	125.2640	135.0000
Cl	2.38078	54.7356	-135.0000
$MnBr(H_2O)_5^+$			
Mn	0.00000	0.0000	0.0000
Br	2.54951	147.6470	80.9598
O	2.23324	86.9617	-10.4820
O	2.25147	87.3168	171.9420
O	2.25467	114.4140	-98.9943
O	2.25989	32.4735	-93.6902
O	2.26164	49.8937	85.0394
H	2.72881	105.5310	163.9110
H	2.74482	133.1170	-106.1990
H	2.75387	68.0105	76.4591
H	2.75499	53.0055	109.7510
H	2.75551	100.4300	3.2655
H	2.76816	110.3120	-78.6802
H	2.81908	69.5135	-6.1382
H	2.83814	86.0217	-170.2610
H	2.84359	17.0410	-115.9710

(continued)

Table 5.13 continued

H	2.84401	48.2655	-106.5300
$MnBr_2(H_2O)_{4\ (aq)}$ (cis)			
Mn	0.00000	0.0000	0.0000
Br	2.59585	144.1600	132.0790
Br	2.60179	33.6068	150.1680
O	2.26625	97.4579	-123.5600
O	2.29050	82.6882	47.2083
O	2.30186	131.0440	-31.3924
O	2.30289	50.2757	-44.7208
H	2.62400	28.4890	-45.8380
H	2.63180	151.7120	-20.5394
H	2.70538	113.0470	-137.2110
H	2.71236	66.2951	59.9459
H	2.71762	80.1956	-134.0410
H	2.72850	99.1432	58.9625
H	2.85251	119.5710	-14.0621
H	2.85875	57.7807	-24.3683
$MnBr_2(H_2O)_{4\ (aq)}$ (trans)			
Mn	0.00000	0.0000	0.0000
Br	2.55035	49.0333	-101.6270
Br	2.73372	131.1400	78.4881
O	2.25478	89.8568	-8.2191
O	2.26179	94.8831	166.1630
O	2.27023	50.2162	80.7341
O	2.27112	148.3560	-98.9390
H	2.59972	169.9910	-112.5030
H	2.60552	71.9593	77.3605
H	2.70596	102.8000	147.1750
H	2.76136	107.8490	-1.0475
H	2.76767	88.1027	-27.3415
H	2.79019	43.7815	56.2238
H	2.79051	76.0303	166.1720
H	2.79463	137.0830	-124.3390
$MnBr(H_2O)_3^+$			
Mn	0.00000	0.0000	0.0000
Br	2.41454	52.8419	-58.0013
O	2.12919	97.2828	-176.7790
O	2.12925	76.3718	83.0822
O	2.13005	163.2380	-0.0751
H	2.69967	147.1900	-26.3836
H	2.70168	60.2261	72.1147
H	2.7018	86.7725	-160.8440

(continued)

Table 5.13 continued

H	2.71216	93.3793	74.8881
H	2.71373	176.4610	-121.1280
H	2.72079	89.8571	166.0600
$MnBr_2(H_2O)_{2\ (aq)}$			
Mn	0.00000	0.0000	0.0000
Br	2.45657	43.4330	179.9070
Br	2.45866	88.0197	-7.5721
O	2.15548	135.2080	-118.3990
O	2.18358	115.6750	97.1350
H	2.70445	98.7697	107.6710
H	2.70688	112.1410	76.0148
H	2.72945	150.2810	-99.4510
H	2.73444	130.9970	-143.4530
$MnBr_3(H_2O)^-$			
Mn	0.00000	0.0000	0.0000
Br	2.49328	89.2355	29.8045
Br	2.50459	153.6480	-165.9760
Br	2.50569	38.5570	166.6920
O	2.22104	80.5439	-76.3325
H	2.69911	64.8704	-89.5700
H	2.70120	97.9224	-86.4115
$MnBr_4^{2-}$			
Mn	0.00000	0.0000	0.0000
Br	2.54946	54.7356	45.0000
Br	2.54946	125.2640	-45.0000
Br	2.54946	125.2640	135.0000
Br	2.54946	54.7356	-135.0000

5.8.3 Classical Molecular Dynamics (MD) simulation

Classical Molecular Dynamics simulation was performed at 500 °C and 600 bar with 5 m Cl^- concentration. The fluid density of 0.7178 g/cm^3 was chosen to correspond to the equation of state of NaCl fluids at the same ionic strength at the pressure and temperature of interest (Driesner, 2007; Driesner and Heinrich, 2007). The coordinates of rigid clusters and parameters of pair potentials are listed in Tables 5.14 and 5.15. The classical MD was run for 500 picoseconds with a time-step of 0.05 femtoseconds. Twenty snapshots were randomly picked up along the whole simulation to calculate the XANES spectra. As

Figure 5.12 shows that the Radial Distribution Function (RDF) of selected twenty frames is consistent with the overall feature, the selected twenty configurations are able to represent the Mn-O pair interaction/distribution (oxygen from free water with the one complexed to Mn^{2+} excluded) of the whole simulation. The cluster radius was set to be 4.5 Å for the FDMNES input. By default, the potential of a total number of around 83 atoms extended to a larger radius of 7.0 Å was taken into account for *ab initio* XANES calculations (Joly, 2012). The effective radii cut-off at 7.0 Å is at the right shoulder of Mn-O pick in the distribution function (Figure 5.12).

Table 5.14 Coordinates of rigid H_2O and $[MnCl_3(H_2O)]$ cluster (in Angstrom).

Atom	**X**	**Y**	**Z**
SPC/E H_2O			
O	0	0	0
H	0.577360	0.816500	0
H	0.577360	-0.816500	0
Optimized $MnCl_3(H_2O)^-$ cluster from ADF			
Mn	0.002206	0.029255	-0.004151
O	0.526737	-2.106668	0.376962
H	0.011158	-2.413509	1.150766
H	0.180436	-2.644694	-0.363967
Cl	-0.991411	-0.236852	-2.108011
Cl	-1.399699	0.352658	1.842445
Cl	2.024310	1.190891	0.032043

Table 5.15 Simulation parameters for classical molecular dynamics.*

Atom	**σ (Å)**	**ε (kcal mol^{-1})**	**q (e)**
O	3.166	0.1554	-0.8476
H	0	0	+0.4238
Na	2.350	0.1300	+1
Cl	4.450	0.1000	-1
Mn	2.591	0.0300	+2

* Parameters from Santosh et al. (2010) and Smith and Dang (1994)

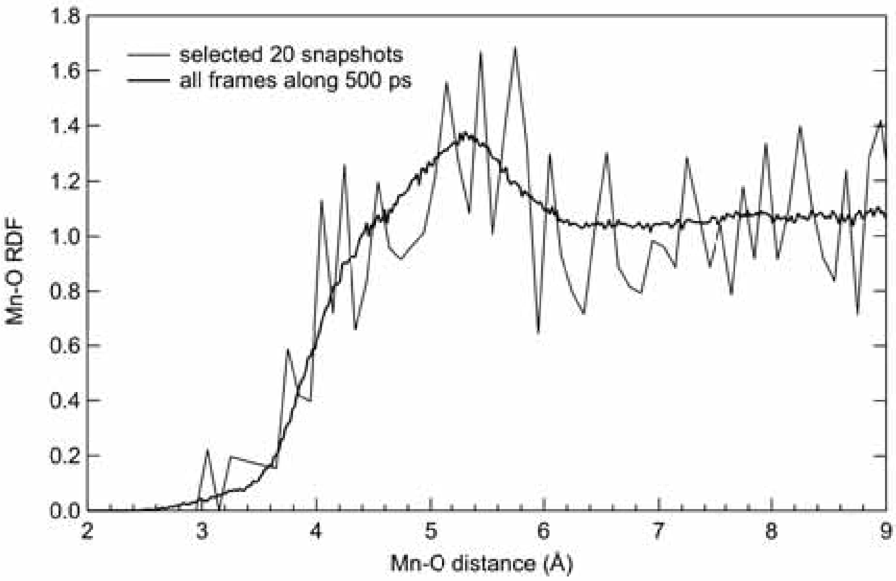

Figure 5.12 Radial Distribution Functions (RDF) of Mn-O for selected 20 snapshots (thin, coarse line) vs all frames along the whole simulation (thick, smooth line).

Acknowledgement: This research was undertaken on the FAME beamline at ESRF, France. The authors thank the ESRF-CRG for the beamtime, and Australian International Synchrotron Access Program for travel funding. Research funding was provided by the Australian Research Council to J.B. (grant DP0878903). The authors thank Prof. David Sherman for his help on DFT calculations. The authors thank Dr Yves Joly for his suggestions on the XANES simulations. The FDMNES calculations were supported by iVEC through the use of the EPIC advanced computing resource located in Perth, Australia. Y.T. acknowledges the University of Adelaide for ASI scholarship.

5.9 References

Ankudinov, A.L., Ravel, B., Rehr, J.J., Conradson, S.D., 1998. Real-space multiple-scattering calculation and interpretation of x-ray-absorption near-edge structure. *Physical Review B* **58**, 7565-7576.

Bazarkina, E.F., Pokrovski, G.S., Zotov, A.V., Hazemann, J.-L., 2010. Structure and stability of cadmium chloride complexes in hydrothermal fluids. *Chemical Geology* **276**, 1-17.

Beagley, B., McAuliffe, C.A., Smith, S.P.B., White, E.W., 1991. EXAFS studies of aqueous solutions of manganese(II) chloride and bromide: structural variations with concentration and interactions with solvent. *Journal of Physics: Condensed Matter* **3**, 7919.

Berendsen, H. J. C., Grigera, J. R., and Straatsma, T. P., 1987. The missing term in effective pair potentials. *The Journal of Physical Chemistry* **91**, 6269-6271.

Boctor, N.Z., 1985. Rhondonite solubility and thermodynamic properties of aqueous $MnCl_2$ in the system $MnO-SiO_2-HCl-H_2O$. *Geochimica et Cosmochimica Acta* **49**, 565-575.

Booth C. H. and Bridges F. (2003) Improved self-absorption correction for fluorescence measurements of extended X-ray absorption fine-structure. The 12th international conference on X-ray absorption fine structure (XAFS XII). *Physica Scripta* **T115**, 202–204.

Borg, S., Liu, W., Etschmann, B., Tian, Y., Brugger, J., 2012. An XAS study of molybdenum speciation in hydrothermal chloride solutions from 25–385 °C and 600 bar. *Geochimica et Cosmochimica Acta* **92**, 292-307.

Brown, I. D. and Altermatt, D., 1985. Bond-valence parameters obtained from a systematic analysis of the inorganic crystal structure database. *Acta Crystallographica B* **41**, 244-248.

Brugger, J., 2007. BeerOz, a set of Matlab routines for the quantitative interpretation of spectrophotometric measurements of metal speciation in solution. *Computers & Geosciences* **33**, 248-261.

Brugger, J., Etschmann, B., Liu, W., Testemale, D., Hazemann, J.L., Emerich, H., van Beek, W., Proux, O., 2007. An XAS study of the structure and thermodynamics of Cu(I) chloride complexes in brines up to high temperature (400 °C, 600 bar). *Geochimica et Cosmochimica Acta* **71**, 4920-4941.

Brugger, J. and Gieré, R., 1999. As, Sb, and Ce enrichment in minerals from a metamorphosed Fe-Mn deposit (Val Ferrera, Eastern Swiss Alps). *Canadian Mineralogist* **37**, 37-52.

Brugger, J., Pring, A., Reith, F., Ryan, C., Etschmann, B., Liu, W., O'Neill, B., Ngothai, Y., 2010. Probing ore deposits formation: New insights and challenges from synchrotron and neutron studies. *Radiation Physics and Chemistry* **79**, 151-161.

Bruyère, R., Prat, A., Goujon, C., Hazemann, J.-L., 2008. A new pressure regulation device using high pressure isolation valves. *Journal of Physics: Conference Series* **121**, 122003-6.

Bunker, G., 2010. *Introduction to XAFS: A Practical Guide to X-ray Absorption Fine Structure Spectroscopy*, 1st ed. Cambridge University Press, New York.

Bühl, M., Kabrede, H., 2006. Geometries of Transition-Metal Complexes from Density-Functional Theory. *Journal of Chemical Theory and Computation* **2**, 1282-1290.

Chalmin, E., Farges, F., Brown, G., 2009. A pre-edge analysis of Mn K-edge XANES spectra to help determine the speciation of manganese in minerals and glasses. *Contributions to Mineralogy and Petrology* **157**, 111-126.

Chantler, J., 1995. Theoretical form factor, attenuation, and scattering tabulation for Z = 1–92 from E = 1–10 eV to E = 0.4–1.0 MeV. *Journal of Physical and Chemical Reference Data* **24**, 71–591.

Chen, Y., Fulton, J., Partenheimer, W., 2005a. A XANES and EXAFS study of hydration and ion pairing in ambient aqueous $MnBr_2$ solutions. *Journal of Solution Chemistry* **34**, 993-1007.

Chen, Y., Fulton, J.L., Partenheimer, W., 2005b. The structure of the homogeneous oxidation catalyst, $Mn(II)(Br^{-1})_x$, in supercritical water: an x-ray absorption fine-structure study. *Journal of the American Chemical Society* **127**, 14085-14093.

Carpenter, R., 1983. Quantitative electron spin resonance (ESR) determinations of forms and total amounts of Mn in aqueous environmental samples. *Geochimica et Cosmochimica Acta* **47**, 875-885.

Cotton, F. A.; Goodgame, D. M. L.; Goodgame, M., Absorption Spectra and Electronic Structures of Some Tetrahedral Manganese(II) Complexes. *Journal of the American Chemical Society* **1962,** *84* (2), 167-172

Cornell, D. H. and Schütte, S. S., 1995. A volcanic-exhalative origin for the world's largest (Kalahari) Manganese field. *Mineralium Deposita* **30**, 146-151.

Davies, A. G. S., Cooke, D. R., and Gemmell, J. B., 2008. Hydrothermal breccias and veins at the Kelian gold mine, Kalimantan, Indonesia: Genesis of a large epithermal gold deposit. *Economic Geology* **103**, 717-757

de Groot, F., Vanko, G., Glatzel, P., 2009. The 1s x-ray absorption pre-edge structures in transition metal oxides. *Journal of Physics: Condensed Matter* **21**, 104207.

Draper, N. R., and Smith, H., 1998. Applied Regression Analysis. John Wiley & Sons, New York.

Driesner, T., 2007. The system H_2O–NaCl. Part II: Correlations for molar volume, enthalpy, and isobaric heat capacity from 0 to 1000 °C, 1 to 5000 bar, and 0 to 1 XNaCl. *Geochimica et Cosmochimica Acta* **71**, 4902-4919.

Driesner, T. and Heinrich, C. A., 2007. The system H_2O-NaCl. Part I: Correlation formulae for phase relations in temperature-pressure-composition space from 0 to 1000 °C, 0 to 5000 bar, and 0 to 1 XNaCl. *Geochimica et Cosmochimica Acta* **71**, 4880-4901.

El Saffar, Z.M., Brown, G.M., 1971. The structure of manganese dichloride tetrahydrate: a neutron diffraction study. *Acta Crystallographica Section B* **27**, 66-73.

Etschmann, B.E., Black, J.R., Grundler, P.V., Borg, S., Brewe, D., McPhail, D.C., Spiccia, L., Brugger, J., 2011. Copper(I) speciation in mixed thiosulfate-chloride and ammonia-chloride solutions: XAS and UV-Visible spectroscopic studies. *RSC Advance* **1**, 1554-1566.

Etschmann, B.E., Liu, W., Testemale, D., Müller, H., Rae, N.A., Proux, O., Hazemann, J.L., Brugger, J., 2010. An in situ XAS study of copper(I) transport as hydrosulfide complexes in hydrothermal solutions (25-592 °C, 180-600 bar): speciation and solubility in vapor and liquid phases. *Geochimica et Cosmochimica Acta* **74**, 4723-4739.

Farges, F., 2005. Ab initio and experimental pre-edge investigations of the Mn K-edge XANES in oxide-type materials. *Physical Review B* **71**, 155109.

Fernandez, D. P., Goodwin, A. R. H., Lemmon, E. W., Sengers, J. M. H. L., and Williams, R. C., 1997. A Formulation for the Static Permittivity of Water and Steam at Temperatures from 238 K to 873 K at Pressures up to 1200 MPa, Including Derivatives and Debye-Hückel Coefficients. *Journal of Physical and Chemical Reference Data* **26**, 1125-1166.

Fulton, J.L., Heald, S.M., Badyal, Y.S., Simonson, J.M., 2003. Understanding the Effects of Concentration on the Solvation Structure of Ca^{2+} in Aqueous Solution. I: The

Perspective on Local Structure from EXAFS and XANES. *The Journal of Physical Chemistry A* **107**, 4688-4696.

Gammons, C.H., Seward, T.M., 1996. Stability of manganese (II) chloride complexes from 25 to 300 °C. *Geochimica et Cosmochimica Acta* **60**, 4295-4311.

Harald G, D., 2010. The “chessboard” classification scheme of mineral deposits: Mineralogy and geology from aluminum to zirconium. *Earth-Science Reviews* **100**, 1-420.

Helgeson, H.C., Delany, J.M., Nesbitt, H.W., 1978. Summary and critique of the thermodynamic properties of rock - forming minerals. *American Journal of Science* **278A**, 1-229.

Hoffmann, M. M., Darab, J. G., Palmer, B. J., and Fulton, J. L., 1999. A transition in the Ni^{2+} complex structure from six-to four-coordinate upon formation of ion pair species in supercritical water: An X-ray absorption fine structure, near-infrared, and molecular dynamics study. *The Journal of Physical Chemistry A* **103**, 8471-8482.

James, R. H., Elderfield, H., and Palmer, M. R., 1995. The chemistry of hydrothermal fluids from the broken spur site, 29°N Mid-Atlantic Ridge. *Geochimica et Cosmochimica Acta* **59**, 651-659.

Joly, Y., 2001. X-ray absorption near-edge structure calculations beyond the muffin-tin approximation. *Physical Review B* **63**, 125120.

Joly, Y., 2012. *FDMNES users' guide*. Institut Néel, CNRS, Grenoble, France.

Joly, Y., Cabaret, D., Renevier, H., Natoli, C.R., 1999. Electron Population Analysis by Full-Potential X-Ray Absorption Simulations. *Physical Review Letters* **82**, 2398.

Kelly, S. D., Hesterberg, D., and Ravel, B., 2008. Analysis of soils and minerals using x-ray absorption spectroscopy. In Methods of Soil Analysis. Part 5. Mineralogical Methods. SSSA Book Series No. 5. (eds. A.L. Ulery and L.R. Drees). pp. 387–463.

Klamt, A., Jonas, V., Bürger, T., and Lohrenz, J. C. W., 1998. Refinement and Parametrization of COSMO-RS. *The Journal of Physical Chemistry A* **102**, 5074-5085.

Klamt, A. and Schuurmann, G., 1993. COSMO: a new approach to dielectric screening in solvents with explicit expressions for the screening energy and its gradient. *Journal of the Chemical Society, Perkin Transactions 2*, 799-805.

Kojima, K., Saida, M., Donoue, M., Matsuda, J., 1983. Pressure and temperature effects on octahedral-tetrahedral equilibria in pyridine solutions of some Cobalt(II) halides. *Bulletin of the Chemical Society of Japan* **56**, 684-688.

Kojima, K., Miyashita, T., Matsuda, J., 1984. Pressure and temperature effects on octahedral-tetrahedral equilibria in pyridine solutions of some Cobalt(II) halides. II. *Bulletin of the Chemical Society of Japan* **57**, 879-880.

Koplitz, L.V., Kim, K., McClure, D.S., 1994. Temperature Dependence of 10Dq for Aqueous HexaaquomanganeseHexaaquomanganese(II). *Inorganic Chemistry* 33, 702-704.

Krause, M.O., Oliver, J.H., 1979. Natural widths of atomic *K* and *L* levels, *Kα* x-ray lines and several *KLL* Auger lines. *Journal of Physical and Chemical Reference Data* **8**, 329-338.

Libuś, Z., Tiałowska, H., 1975. Stability and nature of complexes of the type MCl^+ in aqueous solution (M=Mn, Co, Ni, and Zn). *Journal of Solution Chemistry* **4**, 1011-1022.

Lemmon, E. W., McLinden, M. O. and Friend, D. G. 2000. Thermophysical properties of fluid systems. In *NIST Chemistry WebBook, NIST Standard Reference Database* (eds. W. G. Mallard and P. J. Linstrom). National Institute of Standards and Technology, Gaithersburg, MD. Available from: http://webbook.nist.gov.

Liu, W., Etschmann, B., Foran, G., Shelley, M., Brugger, J., 2007. Deriving formation constants for aqueous metal complexes from XANES spectra: Zn^{2+} and Fe^{2+} chloride complexes in hypersaline solutions. *American Mineralogist* **92**, 761-770.

Liu, W., Borg, S.J., Testemale, D., Etschmann, B., Hazemann, J.-L., Brugger, J., 2011. Speciation and thermodynamic properties for cobalt chloride complexes in hydrothermal fluids at 35–440 °C and 600bar: An in-situ XAS study. *Geochimica et Cosmochimica Acta* **75**, 1227-1248.

Liu, W., Borg, S., Etschmann, B., Mei, Y., Brugger, J., 2012. An XAS study of speciation and thermodynamic properties of aqueous zinc bromide complexes at 25-150 °C. *Chemical Geology* **298–299**, 57-69.

Lüdemann, H.D., Franck, E.U., 1967. Absorptionsspektren bei hohen Drucken und Temperaturen. I: Wäßrige Co(II)- und Ni(II)-halogenid-Lösungen bis zu 500 °C und 6 kbar. *Berichte der Bunsengesellschaft für physikalische Chemie* **71**, 455-460.

Mahoui, A., Lapasset, J., Moret, J., Saint Gregoire, P., 1996. Bis(tetraethylammonium) Tetrachlorometallates, $[(C_2H_5)_4N]_2[MCl_4]$, where M = Hg, Cd, Zn. *Acta Crystallographica Section C* **52**, 2671-2674.

Maslen, E.N., Streltsov, V.A., Streltsova, N.R., Ishizawa, N., 1995. Electron density and optical anisotropy in rhombohedral carbonates. III. Synchrotron X-ray studies of $CaCO_3$, $MgCO_3$ and $MnCO_3$. *Acta Crystallographica Section B* **51**, 929-939.

Mayanovic, R.A., Anderson, A.J., Bassett, W.A., Chou, I., 1999. XAFS measurements on zinc chloride aqueous solutions from ambient to supercritical conditions using the diamond anvil cell. *Journal of Synchrotron Radiation* **6**, 195-197.

Mayanovic, R.A., Anderson, A.J., Bassett, W.A., Chou, I.M., 2009. The structure and stability of aqueous rare-earth elements in hydrothermal fluids: New results on neodymium(III) aqua and chloroaqua complexes in aqueous solutions to 500 °C and 520 MPa. *Chemical Geology* **259**, 30-38.

Mayanovic, R.A., Jayanetti, S., Anderson, A.J., Bassett, W.A., Chou, I.M., 2002. The Structure of Yb^{3+} Aquo Ion and Chloro Complexes in Aqueous Solutions at Up to 500 °C and 270 MPa. *The Journal of Physical Chemistry A* **106**, 6591-6599.

McKibben, M. A. and Williams, A. E., 1989. Metal speciation and solubility in saline hydrothermal fluids - an empirical-approach based on geothermal brine data. *Economic Geology* **84**, 1996-2007

Newville, M., 2001. IFEFFIT: interactive XAFS analysis and FEFF fitting. *Journal of Synchrotron Radiation* **8**, 322-324.

Newville, M., Ravel, B., Haskel, D., Rehr, J.J., Stern, E.A., Yacoby, Y., 1995. Analysis of multiple-scattering XAFS data using theoretical standards. *Physica B* **208**, 154-156.

Olszewski, W., Szymański, K., Zaleski, P., Zając, D.A., 2011. X-ray Absorption near Edge Structure and Extended X-ray Absorption Fine Structure Analysis of Fe(II) Aqueous and Acetone Solutions. *The Journal of Physical Chemistry A* **115**, 13420-13424.

Oxford Diffraction, 2009. *CrysAlis PRO*. Oxford Diffraction Ltd, Yarnton, England.

Ozutsumi, K., Abe, Y., Takahashi, R., Ishiguro, S.-i., 1994. Chloro and Bromo Complexation of the Manganese(II) Ion and Solvation Structure of the Manganese(II), Iron(II), Cobalt(II), Nickel(II), Copper(II), and Zinc(II) Ions in Hexamethylphosphoric Triamide. *The Journal of Physical Chemistry* **98**, 9894-9899.

Parr, R. G. and Yang, W., 1989. *Density-functional theory of atoms and molecules*. Oxford University Press, USA, New York.

Peacock, C. L. and Sherman, D. M., 2004. Copper(II) sorption onto goethite, hematite and lepidocrocite: a surface complexation model based on ab initio molecular geometries and EXAFS spectroscopy. *Geochimica et Cosmochimica Acta* **68**, 2623-2637.

Perdew, J. P., Burke, K., and Ernzerhof, M., 1996. Generalized Gradient Approximation Made Simple. *Physical Review Letters* **77**, 3865-3868.

Proux O., Biquard X., Lahera E., Menthonnex J. J., Prat A., Ulrich O., Soldo Y., Trevisson P., Kapoujyan G., Perroux G., Taunier P., Grand D., Jeantet P., Deleglise M., Roux J. P. and Hazemann J. L. (2005) FAME: a new beamline for X-ray absorption investigations of very-diluted systems of environmental, material and biological interests. *Physica Scripta* **T115**, 970-973.

Pye, C. C. and Ziegler, T., 1999. An implementation of the conductor-like screening model of solvation within the Amsterdam density functional package. *Theoretical Chemistry Accounts: Theory, Computation, and Modeling (Theoretica Chimica Acta)* **101**, 396-408.

Ravel, B., Newville, M., 2005. ATHENA, ARTEMIS, HEPHAESTUS: data analysis for X-ray absorption spectroscopy using IFEFFIT. *Journal of Synchrotron Radiation* **12**, 537-541.

Refson, K., 2000. Moldy: a portable molecular dynamics simulation program for serial and parallel computers. *Computer Physics Communications* **126**, 310-329.

Robie, R.A., Hemingway, B.S., Fisher, J.R., 1978. Thermodynamic properties of minerals and related substances at 298. 15 K and 1 bar (10^5 pascals) pressure and at higher temperatures, USGS-Bulletin-1452.

Roy, S., 1992. Environments and processes of manganese deposition. *Economic Geology* **87**, 1218-1236.

Ryzhenko, B. N., Bryzgalin, O. V., Artamkina, I. Y., Spasennykh, M. Y., and Shapkin, A. I., 1985. An electrostatic model for the electrolytic dissociation of inorganic substances dissolved in water. *Geochemistry International* **22**, 138-144.

Santosh, M. S., Lyubartsev, A. P., Mirzoev, A. A., and Bhat, D. K., 2010. Molecular dynamics investigation of dipeptide-transition metal salts in aqueous solutions. *The Journal of Physical Chemistry B* **114**, 16632-16640.

Seward, T.M., Barnes,H.L.,1997. Metal transport by hydrothermal ore fluids. In: Barnes,H.L. (Ed.), Geochemistry of Hydrothermal Ore Deposits.Wiley, New York, pp. 435–486

Seward, T.M., Driesner, T., 2004. Hydrothermal solution structure: experiments and computer simulations. In: Palmer, D.A., Fernández-Prini, R., Harvery, A.H. (Eds.), Aqueous Systems at Elevated Temperatures and Pressure. Elsevier Academic Press, pp. 149–182.

Sheldrick, G.M., 2008. A short history of SHELX. *Acta Crystallographica A* **64**, 112–122.

Sherman, D. M., 2007. Complexation of Cu^+ in Hydrothermal NaCl Brines: Ab initio molecular dynamics and energetics. *Geochimica et Cosmochimica Acta* **71**, 714-722.

Sherman, D. M., 2009. Electronic structures of siderite ($FeCO_3$) and rhodochrosite ($MnCO_3$): Oxygen K-edge spectroscopy and hybrid density functional theory. *American Mineralogist* **94**, 166-171.

Sherman, D. M., 2010. Metal complexation and ion association in hydrothermal fluids: insights from quantum chemistry and molecular dynamics. *Geofluids* **10**, 41-57.

Shock, E.L., Sassani, D.C., Willis, M., Sverjensky, D.A., 1997. Inorganic species in geologic fluids: Correlations among standard molal thermodynamic properties of aqueous ions and hydroxide complexes. *Geochimica et Cosmochimica Acta* **61**, 907-950.

Shulman, G.R., Yafet, Y., Eisenberger, P., and Blumberg, W.E., 1976. Observations and interpretation of X-ray absorption edges in iron compounds and proteins. *Proceedings of the National Academy of Sciences of the United States of America* **73**, 1384–1388.

Shvarov, Y. V., 2008. HCh: New potentialities for the thermodynamic simulation of geochemical systems offered by windows. *Geochemistry International* **46**, 834-839.

Shvarov, Y.V., Bastrakov, E.N., 1999. HCh, a software package for geochemical equilibrium modeling: user's guide. Record 1999/25. Australian Geological Survey Organisation.

Smith, D. E. and Dang, L. X., 1994. Computer simulations of NaCl association in polarizable water. *The Journal of Chemical Physics* **100**, 3757-3766.

Suleimenov, O.M., Seward, T.M., 2000. Spectrophotometric measurements of metal complex formation at high temperatures: the stability of Mn(II) chloride species. *Chemical Geology* **167**, 177-192.

Susak, N.J., Crerar, D.A., 1985. Spectra and coordination changes of transition metals in hydrothermal solutions: implications for ore genesis. *Geochimica et Cosmochimica Acta* **49**, 555-564.

Sverjensky, D.A., Shock, E.L., Helgeson, H.C., 1997. Prediction of the thermodynamic properties of aqueous metal complexes to 1000 °C and 5 kb. *Geochimica et Cosmochimica Acta* **61**, 1359-1412.

Tagirov, B. R., Zotov, A. V., and Akinfiev, N. N., 1997. Experimental study of dissociation 685 of HCl from 350 to 500 °C and 500 to 2500 bars; thermodynamic properties of HCl^{o}_{aq}. *Geochimica et Cosmochimica Acta* **61**, 4267-4280.

Testemale, D., Argoud, R., Geaymond, O., Hazemann, J.L., 2005. High pressure high temperature cell for x-ray absorption and scattering techniques. *Review of Scientific Instruments* **76**, 043905.

Testemale, D., Brugger, J., Liu, W., Etschmann, B., Hazemann, J.-L., 2009. In-situ x-ray absorption study of iron(II) speciation in brines up to supercritical conditions. *Chemical Geology* **264**, 295-310.

te Velde, G., Bickelhaupt, F. M., Baerends, E. J., Fonseca Guerra, C., van Gisbergen, S. J. A., Snijders, J. G., and Ziegler, T., 2001. Chemistry with ADF. *Journal of Computational Chemistry* **22**, 931-967.

Tian, Y., Etschmann, B., Liu, W., Borg, S., Mei, Y., Testemale, D., O'Neill, B., Rae, N., Sherman, D. M., Ngothai, Y., Johannessen, B., Glover, C., and Brugger, J., 2012. Speciation of nickel (II) chloride complexes in hydrothermal fluids: In situ XAS study. *Chemical Geology* **334**, 345-363.

Tooth, B., Etschmann, B., Pokrovski, G. S., Testemale, D., Hazemann, J. L., Grundler, P., and Brugger, J., 2013. Bismuth Speciation in Hydrothermal Fluids: An X-ray Absorption Spectroscopy and Solubility Study. *Geochimica et Cosmochimica Acta* **101**, 156-172.

Uchida, E., Goryozono, Y., Naito, M., Yamagami, M., 1995. Aqueous speciation of iron and manganese chlorides in supercritical hydrothermal solutions. *Geochemical Journal* **29**, 175-188.

Uchida, E., Haitani, T., Suetsugu, T., Kashima, T., Tsutsui, K., 2003. Experiments on the Element Distribution between the Granodiorite JG-1a and 2M NaCl Hydrothermal Solution at Temperatures of 300 to 800 °C and a Pressure of 1 kb. *Resource Geology* **53**, 155-161.

Uchida, E., Tsutsui, K., 2000. Cation Leaching from the Basalt JB–1a by 2M NaCl Hydrothermal Solutions. *Resource Geology* **50**, 93-102.

Van Lenthe, E. and Baerends, E. J., 2003. Optimized Slater-type basis sets for the elements 1–118. *Journal of Computational Chemistry* **24**, 1142-1156.

Vosko, S. H., Wilk, L., and Nusair, M., 1980. Accurate spin-dependent electron liquid correlation energies for local spin density calculations: a critical analysis. *Canadian Journal of Physics* **58**, 1200-1211.

Westre, T.E., Kennepohl, P., DeWitt, J.G., Hedman, B., Hodgson, K.O., Solomon, E.I., 1997. A multiplet analysis of Fe *K*-edge 1s → 3d pre-edge features of iron complexes. *Journal of the American Chemical Society* **119**, 6297-6314.

Wheat, C.G., Carpenter, R., 1988. $MnCl^+$ and MnSO4 association constants to 170 °C. *Journal of Solution Chemistry* 17, 467-480.

Wilson, A.J.C., Ed., 1992. *International Tables for Crystallography*, vol. C, 883 p. Kluwer Academic, Dordrecht, The Netherlands.

Wolfram, O., Krupp, R.E., 1996. Hydrothermal solubility of rhodochrosite, Mn (II) speciation, and equilibrium constants. *Geochimica et Cosmochimica Acta* **60**, 3983-3994.

Yamamoto, T., 2008. Assignment of pre-edge peaks in K-edge X-ray absorption spectra of 3d transition metal compounds: electric dipole or quadrupole? *X-Ray Spectrometry* **37**, 572-584.

Yardley, B. W. D., 2005. Metal concentrations in crustal fluids and their relationship to ore formation. *Economic Geology* **100**, 613-632.

Zalkin, A., Forrester, J.D., Templeton, D.H., 1964. The Crystal Structure of Manganese Dichloride Tetrahydrate. *Inorganic Chemistry* **3**, 529-533.

Chapter 6

Conclusion

This project mapped the effects of temperature and chlorinity on Ni(II) and Mn(II) speciation in hydrothermal brines, constrained the nature (stoichiometry and geometry) of the high order Ni and Mn chloride complexes, and derived formation constants for tetrahedral Mn and Ni chloride complexes – $NiCl_2(H_2O)_{2(aq)}$, $MnCl_2(H_2O)_{2(aq)}$ and $MnCl_3(H_2O)^-$, which is the primary contribution of this thesis. The second contribution of this project was to use *ab initio* methods of XANES simulations to investigate the speciation of different metal complexes over a wide range of conditions. This method provided additional and supportive information to EXAFS analysis, leading to an overall better understanding of metal speciation in hydrothermal solutions.

6.1 Ni(II) speciation in hydrothermal brines

The combination of XANES and EXAFS analysis has provided consistent information for the coordination change of Ni(II) chloroaqua complexes, from octahedral at ambient temperature to tetrahedral at supercritical conditions (e.g., 434 ˚C, 600 bar), over the chlorinity range of 0.06 - 7.68 m. Increasing temperature results in the coordination change from six-coordinated octahedral to four-coordinated tetrahedral; increasing chlorinity favors the chlorination process (substitution of water by chloride anions) leading to chloride-rich tetrahedral complexes at elevated temperature (i.e., 369 ˚C). Hence, both heating and increase of salinity promote the stability of tetrahedral complexes relative to octahedral complexes. The coordination change of Ni chloroaqua complexes from octahedral to tetrahedral happens at higher temperature and/or higher salinity than the Co analogues (Liu et al., 2011). This project has provided the first set of formation constants and thermodynamic properties of octahedral $NiCl_2(H_2O)_{4(aq)}$ and tetrahedral $NiCl_2(H_2O)_{2(aq)}$ by fitting the XANES spectra of Ni chloride solutions based on the UV-Vis data of Liu et al. (2012b). The highest order Ni chloride complexes identified in this work is not the fully chlorinated $NiCl_4^{2-}$ but the tri-chloro mono-aqua complex $NiCl_3(H_2O)^-$, confirmed by both

EXAFS analysis and XANES simulations. The tri-chloro mono-aqua complex $NiCl_3(H_2O)^-$ is the predominant Ni species at elevated temperature in highly concentrated brines, responsible for the mobility of Ni by chloride-rich fluids in the Earth's crust.

6.2 Mn(II) speciation in hydrothermal brines

Like the study of Ni speciation of chloride complexes, a similar coordination change of Mn(II) chloroaqua complexes has been quantitatively identified by both XANES and EXAFS data analysis from 30 to 550 ˚C at 600 bar with chlorinity range of 0.100-10.344 m. Octahedral species predominate at low temperature (i.e., 30 and 100 ˚C) within the whole salinity range and persist up to ~400 ˚C in low salinity solutions ($m_{Cl} < 1$ m), and tetrahedral species become significant with increasing temperature (i.e., $\geqslant$ 300 ˚C). The highest order chloride complex $MnCl_3(H_2O)^-$ predominated Mn(II) speciation at elevated temperatures (i.e., 450 and 500 ˚C) in highly saline solutions ($m_{Cl} > 3$ m, Cl:Mn ratio > 53), while a lower order chloride complex, $MnCl_2(H_2O)_{2(aq)}$, predominated in weakly saline solutions ($m_{Cl} <$ 0.5 m, Cl:Mn ratio < 10). $MnCl_4^{2-}$ proved to be unstable throughout the whole range of experimental conditions examined. A similar result for Mn speciation of bromide complexes was observed in Mn bromide solutions.

The stability of Mn(II) chloride complexes was found to be similar to those of Ni(II) and Cd(II) chlorides at elevated temperatures in highly saline solutions (Tian et al., 2012; Bazarkina et al., 2010), with the highest order chloride complex – $MCl_3(H_2O)^-$ (M = Ni, Mn, and Cd) differing from the fully chlorinated $FeCl_4^{2-}$ complex identified by Testemale et al. (2009), $CoCl_4^{2-}$ complex identified by Liu et al. (2011a), $ZnCl_4^{2-}$ complex identified by Liu et al. (2007) and Mayanovic et al. (1999) and $ZnBr_4^{2-}$ complex identified by Liu et al. (2012a) under similar conditions using XAS spectroscopy. The first set of formation constants and thermodynamic properties of $MnCl_2(H_2O)_{2(aq)}$ and $MnCl_3(H_2O)^-$ complexes has been derived via XANES data fitting in this work, and tetrahedral $MnCl_3(H_2O)^-$ is responsible for Mn transport and redistribution in chloride-rich fluids in the Earth's crust.

6.3 *Ab initio* XANES simulations to explore structure of hydrothermal solutions

Ab initio XANES calculations based on some clusters structures, whether DFT optimized or man-made, have allowed exploration of the structure of hydrothermal fluids and have provided some independent and supportive information for metal speciation in hydrothermal fluids apart from EXAFS region. The contributions of *ab initio* XANES simulations for this project include:

1) XANES simulations successfully distinguished some metal complexes with different stoichiometry, where EXAFS was ambiguous or had a larger uncertainty. For example, XANES simulations confirmed that the small spectral changes observed at room-T and 100 ˚C with increasing Cl concentration were consistent with stepwise and limited substitution of H_2O by Cl within the octahedral sphere around Ni^{2+} and Mn^{2+}; XANES simulations provided additional evidence for the predominance of tri-chloro one aqua complex – $MCl_3(H_2O)^-$ rather than the fully chlorinated $MnCl_4^{2-}$ and $NiCl_4^{2-}$ in highly saline solutions at elevated temperature; The experimental XANES and EXAFS results of MoO_4^{2-} and distorted octahedral oxo-chloro complexes were correctly reproduced by XANES calculations; The Te-O bond contraction from $Te(OH)_3$ to TeO_3 was also correctly reproduced by XANES calculations, which was difficult to reproduce via EXAFS.

2) XANES simulations provided evidence for a distorted tetrahedral structure rather than a square planar one for the $NiCl_3(H_2O)^-$ complex, confirming that the DFT optimized structure is more realistic than the regular tetrahedral and square planar although the spectral differences are not significant. In addition, XANES simulations suggested that the O-Te-O bond angle and Te-O bond distance of the [TeO_3] moiety may be dynamic and stable in a limited range (e.g., 1.80 - 1.90 Å and 90 - 120°) rather than a rigid structure.

3) XANES simulations allowed retrieval of thermodynamic properties of metal species via XANES fitting, either by validating the assumption that XANES spectrum for each individual species is equal to the corresponding experimental spectrum or by proving the consistency between the retrieved XANES spectrum through thermodynamic fitting and *ab initio* calculated spectrum for some individual spices. In such manner, EXAFS refined stoichiometry, XANES calculations, and thermodynamic fitting are consistent with each other for Ni-Cl and Mn-Cl systems. Thus, *ab initio* XANES simulations have made valuable contributions to the availability of thermodynamic properties of metal species by XANES fitting.

6.4 Future work

This project focused on the understanding of Ni and Mn speciation in chloride solutions at up to 600 bar and 550 ˚C, using XAS techniques. Future work is still needed to better understand the mobility of Mn and Ni in hydrothermal fluids over a wider range of conditions (P, T and fluid composition) and using new complementary techniques. Thus, the following steps are recommended:

1) Bisulphide is believed to be another important ligand responsible for metal transport in some hydrothermal systems, especially in chloride-poor sulphur-rich fluids (e.g., Seward and Barnes, 1997). Hence, investigations of Mn and Ni bisulphide complexation need to be performed to acquire comprehensive knowledge of Mn and Ni geochemistry in hydrothermal fluids.

2) Effects of temperature and salinity were studied in our XAS experiments at constant pressure; hence the effect of pressure on metal speciation needs to be examined in future work as well. As compression at elevated temperature may favour the formation of octahedral complexes according to some qualitative studies of first row transition metal halide complexes (e.g., Lüdemann and Franck, 1967; Kojima et al., 1983, 1984; Seward and Driesner 2004; Suleimenov 2004), *in situ* XAS experiments are expected to identify metal species as a function of pressure at molecular level and to quantify the pressure impact on metal speciation.

3) A number of recent studies have shown that *ab initio* Molecular Dynamics simulations are a powerful tool for probing the behaviour of transition metals in hydrothermal fluids, e.g., Cu(I) chloride complexation by Sherman (2007), Cu(I) bisulfide complexation by Mei et al. (2013), Au(I) bisulfide complexation by Liu et al. (2011b), and Zn(II) chloride complexation by Harris et al. (2003). These studies demonstrate an excellent agreement between the calculated speciation and geometries and those measured by XAS (e.g., Brugger et al., 2007; Pokrovski et al., 2009; Etschmann et al., 2010), and show that the combination of MD simulation and XAS experimental techniques provides deep insights into the nature of metal transport under hydrothermal conditions. MD simulations may improve our understanding of the behaviours of Mn and Ni in three ways: i) formation

constants of Mn and Ni chloride and bisulfide complexes can be calculated by thermodynamic integration, providing an important validation of the experimental values (Bühl et al., 2006; Mei et al., 2013); ii) better understanding of the second shell around Mn and Ni cations can lead to better agreements between *ab initio* XANES calculations and experimental data regarding some fine XANES spectral features (D'Angelo et al. 2006); iii) the cause of different behaviours between Ni-Co, Mn-Fe and Cd-Zn in hydrothermal fluids can be elucidated.

6.5 References

Bazarkina, E. F., Pokrovski, G. S., Zotov, A. V., and Hazemann, J.-L., 2010. Structure and stability of cadmium chloride complexes in hydrothermal fluids. *Chemical Geology* **276**, 1-17.

Bühl, M., Kabrede, H., Diss, R., and Wipff, G., 2006. Effect of Hydration on Coordination Properties of Uranyl(VI) Complexes. A First-Principles Molecular Dynamics Study. *Journal of the American Chemical Society* **128**, 6357-6368.

D'Angelo, P., Roscioni, O. M., Chillemi, G., Della Longa, S., and Benfatto, M., 2006. Detection of Second Hydration Shells in Ionic Solutions by XANES: Computed Spectra for Ni^{2+} in Water Based on Molecular Dynamics. *Journal of the American Chemical Society* **128**, 1853-1858.

Etschmann, B. E., Liu, W., Testemale, D., Müller, H., Rae, N. A., Proux, O., Hazemann, J. L., and Brugger, J., 2010. An in situ XAS study of copper(I) transport as hydrosulfide complexes in hydrothermal solutions (25-592 °C, 180-600 bar): Speciation and solubility in vapor and liquid phases. *Geochimica et Cosmochimica Acta* **74**, 4723-4739.

Gammons, C. H. and Seward, T. M., 1996. Stability of manganese (II) chloride complexes from 25 to 300 °C. *Geochimica et Cosmochimica Acta* **60**, 4295-4311.

Harris, D. J., Brodholt, J. P., and Sherman, D. M., 2003. Zinc complexation in hydrothermal chloride brines: Results from ab initio molecular dynamics calculations. *Journal of Physical Chemistry A* **107**, 1050-1054.

Kojima, K., Miyashita, T., and Matsuda, J., 1984. Pressure and temperature effects on octahedral-tetrahedral equilibria in pyridine solutions of some Cobalt(II) halides. II. *Bulletin of the Chemical Society of Japan* **57**, 879-880.

Kojima, K., Saida, M., Donoue, M., and Matsuda, J., 1983. Pressure and temperature effects on octahedral-tetrahedral equilibria in pyridine solutions of some Cobalt(II) halides. *Bulletin of the Chemical Society of Japan* **56**, 684-688.

Liu, W., Borg, S., Etschmann, B., Mei, Y., and Brugger, J., 2012a. An XAS study of speciation and thermodynamic properties of aqueous zinc bromide complexes at 25–150 °C. *Chemical Geology* **298–299**, 57-69.

Liu, W., Borg, S. J., Testemale, D., Etschmann, B., Hazemann, J.-L., and Brugger, J., 2011a. Speciation and thermodynamic properties for cobalt chloride complexes in hydrothermal fluids at 35–440 °C and 600bar: An in-situ XAS study. *Geochimica et Cosmochimica Acta* **75**, 1227-1248.

Liu, W., Etschmann, B., Foran, G., Shelley, M., and Brugger, J., 2007. Deriving formation constants for aqueous metal complexes from XANES spectra: Zn^{2+} and Fe^{2+} chloride complexes in hypersaline solutions. *American Mineralogist* **92**, 761-770.

Liu, W., Migdisov, A., and Williams-Jones, A., 2012b. The stability of aqueous nickel(II) chloride complexes in hydrothermal solutions: Results of UV–Visible spectroscopic experiments. *Geochimica et Cosmochimica Acta* **94**, 276-290.

Liu, X., Lu, X., Wang, R., Zhou, H., and Xu, S., 2011b. Speciation of gold in hydrosulphide-rich ore-forming fluids: Insights from first-principles molecular dynamics simulations. *Geochimica et Cosmochimica Acta* **75**, 185-194.

Lüdemann, H. D. and Franck, E. U., 1967. Absorptionsspektren bei hohen Drucken und Temperaturen. I: Wäßrige Co(II)- und Ni(II)-halogenid-Lösungen bis zu 500 °C und 6 kbar. *Berichte der Bunsengesellschaft für physikalische Chemie* **71**, 455-460.

Mayanovic, R. A., Anderson, A. J., Bassett, W. A., and Chou, I., 1999. XAFS measurements on zinc chloride aqueous solutions from ambient to supercritical conditions using the diamond anvil cell. *Journal of Synchrotron Radiation* **6**, 195-197.

Mei, Y., Sherman, D. M., Liu, W., and Brugger, J., 2013. Ab initio molecular dynamics simulation and free energy exploration of copper (I) complexation by chloride and bisulfide in hydrothermal fluids. *Geochimica et Cosmochimica Acta* **102**, 45-64.

Oelkers, E. H., Bénézeth, P., and Pokrovski, G. S., 2009. Thermodynamic Databases for Water-Rock Interaction. *Reviews in Mineralogy and Geochemistry* **70**, 1-46.

Pokrovski, G. S., Tagirov, B. R., Schott, J., Hazemann, J.-L., and Proux, O., 2009. A new view on gold speciation in sulfur-bearing hydrothermal fluids from in situ X-ray absorption spectroscopy and quantum-chemical modeling. *Geochimica et Cosmochimica Acta* **73**, 5406-5427.

Seward, T. M. and Barnes, H. L., 1997. Metal transport by hydrothermal ore fluids. In: Barnes, H. L. (Ed.), *Geochemistry of Hydrothermal Ore Deposits*. Wiley, New York.

Seward, T. M. and Driesner, T., 2004. Hydrothermal solution structure: Experiments and computer simulations. In: Donald, A. P., Roberto, F.-P., and Allan, H. H. Eds.), *Aqueous Systems at Elevated Temperatures and Pressures*. Academic Press, London.

Sherman, D. M., 2007. Complexation of Cu^+ in Hydrothermal NaCl Brines: Ab initio molecular dynamics and energetics. *Geochimica et Cosmochimica Acta* **71**, 714-722.

Suleimenov, O. M., 2004. Simple, compact, flow-through, high temperature high pressure cell for UV-Vis spectrophotometry. *Review of Scientific Instruments* **75**, 3363-3364.

Testemale, D., Brugger, J., Liu, W., Etschmann, B., and Hazemann, J. L., 2009. In-situ X-ray absorption study of Iron (II) speciation in brines up to supercritical conditions. *Chemical Geology* **264**, 295-310.

Tian, Y., Etschmann, B., Liu, W., Borg, S., Mei, Y., Testemale, D., O'Neill, B., Rae, N., Sherman, D. M., Ngothai, Y., Johannessen, B., Glover, C., and Brugger, J., 2012. Speciation of nickel (II) chloride complexes in hydrothermal fluids: In situ XAS study. *Chemical Geology* **334**, 345-363.

Appendix A

High-temperature and pressure spectroscopic cell for *in-situ* XAS study of supercritical fluids at the Australian Synchrotron

Y. Tian, J. Brugger, W. Liu, S. Borg, B. Etschmann, B. O'Neill, D. Testemale, J-L. Hazemann, C. Glover, Y. Ngothai, M. Jung and J. Peak (2010) High-temperature and pressure spectroscopic cell for in-situ XAS study of supercritical fluids at the Australian Synchrotron.
Chemeca 2010, Adelaide, S. Australia 2010

NOTE:
This publication is included on pages 170 - 198 in the print copy of the thesis held in the University of Adelaide Library.

Appendix B

Speciation and thermodynamic properties of Manganese(II) and Nickel(II) chloride complexes in hydrothermal fluids: *In situ* XAS study

Y. Tian, J. Brugger, W. Liu, B. Etschmann, S. Borg, D. Testemale, B. O'Neill and Y. Ngothai, (2011) Speciation and Thermodynamic Properties of Manganese(II) and Nickel(II) Chloride Complexes in Hydrothermal Fluids: In situ XAS Study. (abstract only).
Mineralogical Magazine, v. 75 (3), 2011

Appendix C

An XAS study of molybdenum speciation in hydrothermal chloride solutions from 25–385 °C and 600 bar

S. Borg, W. Liu, B. Etschmann, Y. Tian, and J. Brugger (2012) An XAS study of molybdenum speciation in hydrothermal chloride solutions from 25–385 degrees C and 600 bar.
Geochimica et Cosmochimica Acta v. 92, pp. 292-307, September 2012

Appendix D

Speciation of aqueous tellurium(IV) in hydrothermal solutions and vapors, and the role of oxidized tellurium species in gold metallogenesis

Speciation of aqueous tellurium(IV) in hydrothermal solutions and vapors, and the role of oxidized tellurium species in Te transport and gold deposition

Pascal V. Grundler[a,b,h], Joël Brugger[a,b*], Barbara E. Etschmann[a,b], Lothar Helm[c], Weihua Liu[d], Paul G. Spry[e], Yuan Tian[b,g], Denis Testemale[f], and Allan Pring[a,b*]

[a]*Tectonics, Resources and Exploration (TRaX), School of Earth and Environmental Sciences, The University of Adelaide, North Terrace, 5005 Adelaide, South Australia, Australia*

[b]*Division of Mineralogy, South Australian Museum, North Terrace, 5000 Adelaide, South Australia, Australia*

[c]*Groupe de Chimie Inorganique et Bioinorganique, Institut des Sciences et Ingénierie Chimiques, Ecole Polytechnique Fédérale de Lausanne, CH-1015 Lausanne, Switzerland*

[d]*CSIRO Earth Science and Resource Engineering, Clayton, Vic 3168, Australia*

[e]*Department of Geological and Atmospheric Sciences, Iowa State University, Ames, IA 50011-3212, United States*

[f]*Institut Néel, Département MCMF, CNRS-Grenoble, 25 Avenue des Martyrs, BP166, 38042 Grenoble Cedex 09, France*

[g]*School of Chemical Engineering, The University of Adelaide, Adelaide 5000, South Australia, Australia*

[h]*Present address : Paul Scherrer Institute, Laboratory for Nuclear Materials, CH-5232 Villigen PSI, Switzerland*

*Corresponding authors: allan.pring@samuseum.sa.gov.au; joel.brugger@adelaide.edu.au

US ENGLISH

Nomenclature

Tellurium dioxide any form TeO_2

Tellurium dioxide any solid form $TeO_2(s)$

Tellurium dioxide orthorhombic $TeO_2(orth)$

Tellurium dioxide tetragonal $TeO_2(tet)$

Tellurium dioxide gas $TeO_2(g)$

Abstract

Despite the close association between tellurium (Te) and gold (Au) in many epithermal, orogenic, and intrusion-related hydrothermal ore deposits, the hydrothermal chemistry of Te remains poorly understood. We studied the protonation/deprotonation and structure of tellurous acid ($H_2Te^{IV}O_3$) species in aqueous solutions and in water vapor as a function of pH from room-temperature to 505 ˚C using a number of methods: $TeO_2(s)$ solubility in solution and steam, potentiometry, NMR spectroscopy, and *in-situ* XAS spectroscopy.

The solubility of TeO_2 increases by up to a factor 80 between ambient temperature and 200 °C. As the temperature increases, the pH range over which the neutral species $H_2TeO_3(aq)$ dominates to the detriment of the ionic species $H_3TeO_3^+$, $HTeO_3^-$ and TeO_3^{2-} expands. The structure of these species is a trigonal pyramid with the Te atom at its apex, indicating a stereochemically active electron pair. The Te-O bond lengths increase with increasing protonation (i.e. decreasing pH).

Although hydrated tellurite species such as $TeO_2(H_2O)(g)$ and $TeO_2(H_2O)_2(g)$ exist in significant concentrations in vapors equilibrated with $TeO_2(s)$, these species are unlikely to play a significant role in natural systems, because of the high solubility of Te(IV) in the liquid phase under these conditions. Solubility calculations conducted with the new and existing properties confirm the importance of reduced species for the vapor transport of Te, with a partitioning coefficient (K_d = Te concentration in vapor/Te concentration in liquid) up to $>10^5$ in favor of the vapor, and ppm concentrations of Te in reduced vapors at 300 ˚C.

Thermodynamic calculations also show that slightly basic, mildly reduced fluids that can transport Au efficiently as $Au(HS)_2^-$ can also carry significant Te (e.g., ~100 ppb at 300˚C). The calculations also suggest that under magmatic hydrothermal conditions, large amounts of Te can be transported as Te(IV) complexes in oxidized fluids (coexisting with $SO_2(g)$). Reduction of Te(IV) caused by processes such as fluid-rock interaction or fluid mixing will lead to a dramatic decrease in the solubilities of both Te and Au, and to the precipitation of telluride minerals.

Keywords: Tellurium, Experimental Geochemistry, Gold Deposits, X-ray Absorption Spectroscopy, Vapor Transport, Liquid-Vapor partitioning.

1. INTRODUCTION

Tellurium, like its chalcogen congeners, S and Se, has an extensive redox chemistry with oxidation states ranging from –II to +VI. Tellurium is the least common element of group 16 (with the exception of Po), and interest in its chemistry has been growing since the 1990s due to applications in semiconductors and photonic glasses. Some research into the vapor transport of Te was driven by its occurrence as a short-lived fission product in commercial nuclear reactors. The ^{132}Te isotope decays to ^{132}I, an especially hazardous radioisotope because of the biological role of iodine. Tellurium can be released with other volatile elements such as Cs and I during loss of coolant accidents, if the cladding of the fuel rods ruptures due to overheating (>1100 K) (Cordfunke and Konings, 1990; Garisto, 1982, 1992). In the absence of measurements, many of the properties of Te and its compounds have been estimated following the periodic trend set by S and Se (Devillanova, 2007). However, Te sits on the border between non-metals and metals and therefore has some peculiarities that distinguish it from the lighter chalcogens. Its ability to form coordination complexes with chloride, not unlike a metal, illustrates this point (Krebs and Ahlers, 1990; Zingaro, 2006).

In geochemistry, Te is mainly of interest because of its tendency to be associated with Au (Ciobanu et al., 2006; Cook et al. 2009). Recent developments in analytical chemistry also open the way to the use of stable Te isotopes in cosmochemistry (Fehr et al., 2005, 2009; Moynier et al., 2009). Although the body of available data about the stable isotopic variation of Te is still limited, recent studies by Fornadel et al. (2012) reveal a range of $\delta^{130/125}$Te = 1.8 ‰ for Au-Ag-Te minerals from orogenic and low sulfidation epithermal Au-Ag telluride deposits (e.g., Cripple Creek, Colorado; May Day deposit, Colorado; Golden Mile, Kalgoorlie; Bambolla deposit, Mexico; Boulder County deposits, Colorado). Further development of the systematics of stable Te isotopes can be expected and knowledge of Te speciation is critical to the interpretation of any isotopic signature.

The natural abundance of Te is low. It is one of the few elements whose concentration in seawater is not well established, with values ranging from 1 to 30 ng kg^{-1} (ppt; Huang and Hu, 2008; Lee and Edmond, 1985). The crustal abundance of Te is estimated to be 1 μg kg^{-1} (ppb), compared to 4 μg kg^{-1} for Au (Lide, 2003). Yet, high concentrations of Te (10’s to 1000’s of ppm) are found in many Au deposits; in particular, Te is closely associated with Au in many epithermal deposits including Cripple Creek

(Kelley et al., 1998), Emperor, Fiji (Pals and Spry, 2003), and the low-sulfidation Săcărîmb, Romania (Ciobanu et al., 2004), as well as in some "orogenic" Au deposits, such as the giant Golden Mile and the world-class Sunrise Dam deposits in Western Australia (Bateman and Hagemann, 2004; Shackleton et al., 2003; Sung et al., 2007, 2009). Tellurium is also a component of low melting point assemblages (eutectic in the Au-Te system at 689 ˚C; 266 ˚C in the Bi-Te system), and these polymetallic melts have a high affinity for gold and can scavenge gold via melt collector models (Tomkins et al., 2007; Tooth et al., 2008; 2011). Such a liquid-collector mechanism may contribute to the Au-Bi-Te association found in many Au deposits, for example Au skarns (Ciobanu et al., 2010; Cockerton and Tomkins, 2012; Tooth et al., 2011).

The Au-Te association and high Te:Au ratios in many hydrothermal ores indicate the ability of hydrothermal fluids to carry significant quantities of Te. Yet, Te concentrations in modern epithermal waters are low; deep (>500 m) and hot (>200 ˚C) waters from the Lihir (Papua New Guinea) and Wairakei (New Zealand) systems contain up to 4 and 0.4 ppb Te, respectively (Simmons and Brown, 2006). The Lihir water also contained 13 ppb Au. Based on extrapolations from samples heavily contaminated by seawater (≥88%), the hydrothermal fluids at the seafloor Au-bearing Pacmanus hot springs field contained up to 18 ppb Te (Binns et al., 2004). Numerical simulations based on available thermodynamic properties, mostly derived from room-temperature extrapolations (McPhail, 1995), suggest that reduced aqueous fluids have little capacity to carry Te (Fig. 1). Cooke and McPhail (2001) calculated sub-ppt concentrations of Te in 300 ˚C epithermal-type waters, and suggested that the high volatility of reduced Te species (e.g., $H_2Te(g)$; $Te_2(g)$) is responsible for the enrichment of Te in vapor of up to ~0.1 ppm.

These low values contrast with the high Te concentrations found via laser ablation ICP-MS in single fluid inclusions from some porphyry copper and low-sulfidation epithermal deposits. In the Au-Te epithermal system of Roşia Montană, Romania, liquid-vapor inclusions with homogenization temperatures of 233-255 ˚C contained up to 14 ppm Te; one liquid-vapor inclusion with a higher homogenization temperature of 358 ˚C contained 340 ppm Te (Wallier et al., 2006). Two coexisting vapor-only inclusions showed 5.5 and 180 ppm Te, respectively. In one of the liquid-vapor inclusions and one of the vapor inclusions, Te at Roşia Montană coexisted with ppm-levels of Au. Similar Te and Au concentrations (Te concentrations up to 670 ppm, coexisting with Au concentrations up to 13 ppm) were found in fluid inclusions from the porphyry Cu-Mo-Au stage and the transitional quartz-sericite-pyrite stage of the Nevados de Famatina deposit (northwest

Argentina); the final stage of this mineralizing system is a Te-rich high sulfidation system (Pudack et al. 2009). High Te concentrations, with Au below detection limits, were also found in fluid inclusions attributed to the magmatic stage at Nevados de Famatina. Altogether, these data suggest that hydrothermal fluids responsible for the formation of Au-Te deposits may have carried high levels of Te (100's of ppb to ppm), even accounting for the possibility of post-entrapment modifications of the metal concentrations (Lerchbaumer and Audétat, 2012).

The processes leading to the enrichment and the formation of the Te minerals are currently still poorly understood. This is mainly due to the paucity of reliable fundamental data relating to the species present in aqueous systems at elevated temperatures and pressures. Over the last few years progress has been made in this field for the neighboring elements Sb, As and Bi, but not for Te (James-Smith et al. 2010; Pokrovski et al., 2002, 2006; Testemale et al., 2004, 2011). In fact, there are hardly any experimental data on Te transport under hydrothermal conditions. McPhail (1995) mentions tellurite ($TeO_2(s)$) solubility experiments in water up to 80 ˚C but does not provide any detail, whereas Glemser et al. (1964, 1965, 1966) provide measurement of $TeO_2(s)$ solubility in water vapor, but these data have not been used in geochemistry.

The most common Te-bearing minerals in nature are tellurides and native tellurium. Alteration of these primary Te minerals leads to the formation of tellurites and tellurates as secondary minerals (Grundler et al., 2008; Zhao et al., 2009; 2010). Tellurides are highly insoluble under reducing conditions and acidic to neutral pH as reduced Te complexes, but Te(IV) is comparatively much more soluble. Here, we present the first comprehensive study of the speciation of Te(IV) under hydrothermal conditions, based on a combination of experimental data, including mineral solubility, potentiometry, Nuclear Magnetic Resonance (NMR) spectroscopy, and X-ray Absorption Spectroscopy (XAS), in order to provide a molecular-level understanding of Te transport as tellurite species (Brugger et al. 2010). We use the new data together with existing thermodynamic properties to investigate the role of oxidized Te species in the formation of gold deposits.

2. MATERIALS AND METHODS

2.1. Materials

Tellurium dioxide (TeO_2) 99.999% powder was obtained from Strem Chemicals Inc, Newburyport MA and used to prepare solutions for the potentiometric titrations and in the vapor solubility experiments at 170 °C. Powder of $^{125}TeO_2$ (98.00% isotopic purity) was obtained from Isoflex USA, San Francisco CA, and used to prepare the sample for the NMR measurements. Coarse TeO_2 powder 99+% was acquired from Aldrich and used for the solubility experiments below 100 °C. A boule of $TeO_2(s)$ (paratellurite; α-TeO_2) was obtained from Abal OptoTek Co. Ltd., Putian, China, and used for the solubility experiments at 200 °C and above. Syringe filters with a supor® membrane (hydrophilic polyethersulfone; 0.45 μm) from Acrodisc (Pall Corp.) allowed solid particles to be removed from the sample solutions. Details of other chemical reagents used are given in Appendix A1.

2.2. Analytical methods

NMR spectra were recorded on Bruker AvanceII-400 and Avance-200 spectrometers equipped with BBO BB $\{^1H\}$ 10 mm probe heads. ^{125}Te chemical shifts were measured with respect to sodium trimethylsilylpropansufonate (TMSPS) and referenced to dimethyltellurium (0.0 ppm) using the method recommended by Harris et al. (2001). For work at temperatures above the boiling point of water, 10 mm outer diameter sapphire NMR tubes with a titanium screw cap were used (Cusanelli et al., 1996). To minimize the amount of solution lost to the headspace as vapor, a PTFE rod was placed above the solution inside the sapphire tubes.

pH measurements were made with a 692 pH/ion-meter from Metrohm or a 510 pH/ion-meter from Eutech Instruments. Both instruments were calibrated daily with 3 standard pH buffers ($pH_{25^\circ C}$ = 4.00, 7.00 and 10.00; accuracy 0.01 pH units). Tellurium concentrations were determined using an Agilent ICP-MS with Ar as the carrier gas/plasma. The ^{130}Te isotope was selected due to its high natural abundance and the absence of interference from other elements present in solution. Recovery levels were monitored by analyzing simultaneously for ^{115}In mixed into the flow as an internal standard. This compensated for possible matrix effects due to the use of different buffers.

2.3. Software

Geochemist's Workbench (GWB; Bethke, 2007) was used to calculate the pH of solutions at all temperatures and to perform simulations in the water-Au-Te-S-Cl system. The geochemical modeling software HCh (Shvarov and Bastrakov, 1999) was used to obtain the properties of water above the critical point. Data fitting was done in Matlab, using either the Visualiseur/Optimiseur software (Yerly, 2010) or in-house code. Helgeson-

Kirkham-Flowers (HKF) equation of state parameters for Te aqueous species were calculated using the OptimB software (Tanger and Helgeson, 1988; Shvarov, 1993).

As the dissociation constants of the various buffers are unequally temperature dependent, it was not practical to maintain a constant ionic strength over the whole pH and temperature ranges covered. As a consequence, it was necessary to calculate activity coefficients of the Te species for each solution composition and temperature. The OLI StreamAnalyzer 2.0 software was used for this purpose (OLI Systems, Morris Plains NJ; (Wang et al., 2002; 2004). We used the interaction parameters included in the default OLI databank, except for concentrated solutions of $HClO_4$ and $NaClO_4$ solutions, for which interaction parameters were obtained by regression of available isopiestic, mean stoichiometric activity coefficients and density data (See Appendices A2 and A3 for details).

3. EXPERIMENTAL PROCEDURES

3.1. Tellurite solubility in aqueous solutions

Buffer solutions for solubility determination were based on acetate, ammonium, borate, carbonate, phosphate or sulfate with sodium or chloride (for NH_4^+) as a counter ion (Table 1). Perchloric acid solutions were also used to obtain data at high acidity. Sodium chloride (about 1 m) was added to a selection of buffer solutions to investigate its possible influence on the solubility. The solubility of TeO_2(tet) (Appendix A4) was determined in two ways. Below 100 °C, 100 mL glass bottles (ISO 4796) containing buffer solutions in contact with TeO_2(tet) powder were kept in a temperature-controlled environment (water bath or drying oven) for several weeks. Solutions were first equilibrated at 80 °C and sampled at least two times at this temperature at 4 weeks intervals to check for steady state. The same solutions were then equilibrated at 25 °C and sampled following the same procedure. The nature of the solid was checked by powder XRD at the end of the runs. Solution samples were taken from the bottles with single use plastic syringes and filtered through a 0.45 μm polyethersulfone membrane to remove suspended TeO_2 particles. Syringe and filter were warmed to be at the same temperature as the solution, prior to sampling. Concentrated hydrochloric acid was added to each aliquot, in order to ensure that TeO_2(s) did not precipitate upon cooling/storage. For a few samples, special care was taken not to disturb the solution prior to sampling. These samples were not filtered and no difference in Te concentration was observed in comparison with the filtered samples. Before analysis, the sample solutions were diluted (by weight) to be within the calibration range (20-1,000 ppb) of the ICP-MS instrument. Repeat analyses over several weeks did not reveal any significant change.

Above 100 °C, PTFE cells in a stainless steel casing were used. These cells are fitted with a PTFE insert, creating two compartments separated by a sieve (Fig. 2). This allows a fragment of the TeO_2(tet) boule to be brought into contact with the solution, and then to separate it again from the solution just by turning the hot cell up-side down (e.g., Liu et al. 2001; Seward 1976). Once steady state is reached (minimum 4 weeks at 200 °C), the cells were turned to separate both phases and a day later allowed to cool down to room temperature over a few hours. The piece of TeO_2(tet) was recovered, rinsed with water (which was recovered) and acetone, and then allowed to dry in air. The weight difference before and after heating was recorded (Appendix A5), allowing the solubility to be calculated using the known amount of solution initially added to the cell. The solution itself was also recovered, and the cell and insert were rinsed with concentrated hydrochloric acid; this was added to the previously recovered solution. The weights of all recovered fractions were recorded in order to compute initial Te concentrations. The sample was then diluted for ICP-MS analysis; dilution factors varied between 2 to 1000, depending upon Te concentrations.

3.2. Tellurite solubility in steam

Two methods were used to investigate the solubility of TeO_2(s) in steam. For the first method, shards of a TeO_2(tet) crystal were placed with water at the bottom of a titanium cell (30 mm inside diameter and 180 mm in depth) fitted with two round pieces of titanium mesh sitting in the upper third. The mesh, acting like a sieve, prevents solid particles of TeO_2(tet) and drops of solution from being carried with the steam during the sampling. The cell, with a 60 cm long stainless steel (SS) tube connected to the lid, was placed in the middle third of a vertical furnace with three heating units. The temperature gradient over the length of the Ti cell was estimated to be 5 °C. The upper third of the furnace was set to a 10 °C higher target temperature than the cell to prevent the premature condensation of the steam in the SS tube. Outside the furnace, a pressure gauge and a Ti valve with graphoil packing were connected to the SS tube. The cell was allowed to equilibrate for at least two days in the furnace before the first sampling, which was then repeated once a day for three to four days. Samples were taken by opening the valve and condensing the escaping vapor into a few grams of concentrated hydrochloric acid. The amount of condensate was determined by weight difference. Temperature and pressure were recorded at the time of sampling. The Te content in the condensate was determined by ICP-MS.

At lower temperatures, larger volumes of vapor were required due to the lower densities and solubilities. Therefore, a second experimental method was used. A 3 liter round-bottom glass flask containing a precisely weighed amount of water (1.5 g) was fitted with a Y-connector. A small flask containing TeO_2 powder was connected to one side, and the other side was fitted with a glass stopcock valve. The water was frozen with the help of dry ice and the flask evacuated to 10 mbar. The evacuated flask was then placed in an oven at 170 °C for 10 days in order to allow the steam inside the flask to equilibrate with the TeO_2 powder. The flask was then removed from the oven and allowed to cool first in an air stream and then with dry ice, to condense the entire vapor. The flask was then filled with nitrogen, opened, and rinsed using a few milliliters of hydrochloric acid. The sample mixed with hydrochloric acid was analyzed for Te by ICP-MS.

3.3. NMR titrations

The weakly complexing organic buffers tris(hydroxymethyl)aminomethane, piperazine-N,N'-bis(2-butanesulfonic acid) and N,N'-diethyl-N,N'-bis(3-sulfopropyl)ethylenediamine (Kandegedara and Rorabacher, 1999) were used in addition to those used for the solubility experiments. Trifluoromethanesulfonic acid was used as an alternative to the thermally less stable perchloric acid to reach high acidity. Solution characteristics are listed in Table 2. Typically, the sapphire NMR tubes were loaded with TeO_2 powder enriched in ^{125}Te (98%), 2.25 ml of buffer solution, and 0.25 ml of TMSPS/D_2O. The pH was measured after mixing (Table 2), and the tube was introduced in the thermostated NMR spectrometer and left to equilibrate for at least 30 min. ^{1}H and ^{125}Te spectra were recorded alternatively. Parameters for ^{125}Te spectra acquisition were as follows: pulse length 9.5 μs, spectral width 100 kHz, repetition rate 2 s, accumulation of between 5k and 100k scans. The temperature in the NMR probe was measured with a 100 Ω Pt resistor immersed in a standard 10 mm NMR tube containing a high boiling point liquid. Due to long acquisition times (several hours in cases of low solubility) for the ^{125}Te spectra, they were not all recorded in duplicate, but ^{1}H spectra were recorded before and after each ^{125}Te spectrum. Differences in the ^{125}Te chemical shift resulting from referencing to the two different ^{1}H NMR spectra were less than 0.1 ppm. Two samples made from the same acetate/NaCl solution were run separately and yielded virtually identical chemical shifts of 1738.18 ppm.

3.4. Potentiometric titrations

The dissociation constants of tellurous acid at high pH were determined by potentiometric titration at constant ionic strength (I = 1 m, $NaClO_4$) by adding $HClO_4$ to a solution of TeO_2 in NaOH/$NaClO_4$ (0.1 m/0.9 m). For the duration of the titration, the sample was kept at constant temperature (±0.1 °C) in a jacketed beaker connected to a thermostated water bath (25-80 °C).

3.5. X-ray absorption spectroscopy

Tellurium K-edge (31,814 eV) X-ray Absorption Near Edge Structure (XANES) and Extended X-ray absorption Fine Structure (EXAFS) spectra were measured at the 20-BM-B (XOR/PNC sector) beamline at the Advanced Photon Source (APS), in Chicago, USA, and at beamline 30-BM (FAME) at the European Synchrotron Radiation Facility (ESRF) in Grenoble, France. Details of the beam line set-up, experimental cells and temperature calibration are described in Appendix A6.

4. RESULTS AND DISCUSSION

4.1. Aqueous chemistry of the tellurite ion

The aim of this section is to provide a quantitative assessment of the nature and stability of tellurous acid ($H_2TeO_3(aq)$) and its protonation/deprotonation products (see equations (2)-(4) below) in aqueous solutions up to 200 °C, using a combination of solubility experiments, potentiometric measurements, and NMR studies.

4.1.1. Solubility of TeO_2(tet) in aqueous solution as a function of pH

The solubility of TeO_2(tet) was investigated as a function of temperature (25 to 200 °C), NaCl concentration (0-1 m), and pH. The solubility goes through a minimum around pH 4 (Fig. 3). At this minimum, the main aqueous species is the neutral $H_2TeO_3(aq)$. A powder X-ray diffraction analysis of the solid TeO_2 that was in contact with the saturated solution indicated that it consisted of the tetragonal polymorph (paratellurite). $H_2TeO_3(aq)$ can either undergo protonation to yield a cationic species (i.e., $H_3TeO_3^+$) or lose H^+ and form the tellurite anions $HTeO_3^-$ and TeO_3^{2-}. Either way the ionic species are more soluble and, as a consequence, the solubility increases under either basic or strongly acidic conditions.

Tellurium (IV) is known to form several complexes with the chloride anion (Krebs and Ahlers, 1990); however, high chloride concentrations (> 1 m, up to saturation) and low pH

(> 1 m HCl) are required (Milne, 1991). As these conditions were not encountered in the present study (≤1 m NaCl), the presence of chloro-complexes in the solutions investigated is negligible. Therefore, the presence of chloride has no significant effect on Te solubility, but NaCl has a buffering effect on the ionic strength of the solution. This can be observed in a reduced scatter among the data points corresponding to chloride solutions (Fig. 3). Equations (1)-(4) describe the equilibria occurring in solution. The square brackets represent the analytical concentrations of the species and γ_i their respective activity coefficients. Calculations have shown that the water activity in these solutions is very close to unity (0.97-1.00). Therefore, in the following, we assume both $a(H_2O)$ and $a(TeO_2(tet))$ to be unity:

$$\mathrm{TeO_2(tet) + H_2O(l) = H_2TeO_3}(aq); \quad K_s = [\mathrm{H_2TeO_3}(aq)]\gamma_{\mathrm{H_2TeO_3}(aq)} \tag{1}$$

$$\mathrm{H_3TeO_3^+ = H_2TeO_3}(aq) + \mathrm{H^+}; \quad K_{a_0} = \frac{a_{\mathrm{H^+}}[\mathrm{H_2TeO_3}(aq)]\gamma_{\mathrm{H_2TeO_3}(aq)}}{[\mathrm{H_3TeO_3^+}]\gamma_{\mathrm{H_3TeO_3^+}}} \tag{2}$$

$$\mathrm{H_2TeO_3}(aq) = \mathrm{HTeO_3^- + H^+}; \quad K_{a_1} = \frac{a_{\mathrm{H^+}}[\mathrm{HTeO_3^-}]\gamma_{\mathrm{HTeO_3^-}}}{[\mathrm{H_2TeO_3}(aq)]\gamma_{\mathrm{H_2TeO_3}(aq)}} \tag{3}$$

$$\mathrm{HTeO_3^- = TeO_3^{2-} + H^+}; \quad K_{a_2} = \frac{a_{\mathrm{H^+}}[\mathrm{TeO_3^{2-}}]\gamma_{\mathrm{TeO_3^{2-}}}}{[\mathrm{HTeO_3^-}]\gamma_{\mathrm{HTeO_3^-}}} \tag{4}$$

The total analytical Te concentration is given by equation (5):

$$c_{Te} = \left[\mathrm{H_3TeO_3^+}\right] + \left[\mathrm{H_2TeO_3}(aq)\right] + \left[\mathrm{HTeO_3^-}\right] + \left[\mathrm{TeO_3^-}\right] \tag{5}$$

Combining and rearranging equations (1)-(5) yields equation (6), which describes the total Te solubility (analytical concentration as determined in the present study by ICP-MS) as a function of pH (defined as $-\log_{10}\left(a_{\mathrm{H^+}}\right)$):

$$\log c_{\mathrm{Te}} = \log\left(\frac{K_s}{\gamma_{\mathrm{H_2TeO_3}(aq)}} + \frac{[\mathrm{H^+}]K_s}{K_{a_0}\gamma_{\mathrm{H_3TeO_3^+}}} + \frac{K_{a_1}K_s}{a_{\mathrm{H^+}}\gamma_{\mathrm{HTeO_3^-}}} + \frac{K_{a_2}K_{a_1}K_s}{\left(a_{\mathrm{H^+}}\right)^2\gamma_{\mathrm{TeO_3^{2-}}}}\right) \tag{6}$$

A least squares fit of this equation to the experimental data, listed with the corresponding activity coefficients in Appendix A4, yielded numerical values for the equilibrium constants, which are summarized in Table 3. Unfortunately, the high solubility of TeO_3^{2-} prevented the precise determination of the Te concentrations at pH above 10, and, consequently, no data covering a sufficient pH range (at least up to pH 12) were available for the determination of K_{a2} (Equation 4). For the fitting procedure the value for pK_{a2} was kept at 10 (value constrained by potentiometric and NMR measurements; see sections 4.1.2 and 4.1.3). Setting it to 9 or 11 did not affect the values obtained for the other parameters beyond the error range.

4.1.2. Potentiometric titrations

Since data on pK_{a2} cannot be accessed from the solubility measurements, potentiometric titrations at constant ionic strength (I = 1 m, $NaClO_4$) and variable T were performed (Fig. 4; Appendix A7). The quality of the response of the pH electrode (Eutech) decreased with increasing temperature; nevertheless, it was possible to collect data up to 80 °C. The titration curve for a weak dibase (TeO_3^{2-}) by a strong acid ($HClO_4$) in the presence of a strong base (NaOH) is given by equation (7) (see Appendix A8 for the derivation of the equation), where n is the number of moles of the subscripted species, mw the molecular weight of the subscripted species, X is the mass fraction of subscripted species in the titrant solution, and m_a is the mass of titrant. Activity coefficients and other fixed parameters are listed in Table 4.

$$\boxed{\frac{\dfrac{n_{\mathrm{Te}}K_W\left(2\gamma_{\mathrm{HTeO_3^-}}\gamma_{\mathrm{H_2TeO_3}(aq)}K_W+\gamma_{\mathrm{TeO_3^{2-}}}K_{b1}\gamma_{\mathrm{H_2TeO_3}(aq)}a_{\mathrm{H^+}}\right)}{\gamma_{\mathrm{HTeO_3^-}}\gamma_{\mathrm{TeO_3^{2-}}}K_{b2}K_{b1}a_{\mathrm{H^+}}^2+\gamma_{\mathrm{TeO_3^{2-}}}K_{b1}\gamma_{\mathrm{H_2TeO_3}(aq)}a_{\mathrm{H^+}}K_W+\gamma_{\mathrm{H_2TeO_3}(aq)}K_W^2\gamma_{\mathrm{HTeO_3^-}}}-\dfrac{n_{\mathrm{NaOH}}\gamma_{\mathrm{NaOH}}K_b a_{\mathrm{H^+}}}{\gamma_{\mathrm{Na^+}}K_W+\gamma_{\mathrm{NaOH}}K_b a_{\mathrm{H^+}}}-m_{\mathrm{H_2O}}^s\left(\dfrac{a_{\mathrm{H^+}}}{\gamma_{\mathrm{H^+}}}-\dfrac{K_W}{\gamma_{\mathrm{OH^-}}a_{\mathrm{H^+}}}\right)}{X_{\mathrm{H_2O}}^a\left(\dfrac{a_{\mathrm{H^+}}}{\gamma_{\mathrm{H^+}}}-\dfrac{K_W}{\gamma_{\mathrm{OH^-}}a_{\mathrm{H^+}}}\right)-\dfrac{X_{\mathrm{HClO_4}}^a\gamma_{\mathrm{HClO_4}}K_a}{mw_{\mathrm{HClO_4}}\left(a_{\mathrm{H^+}}\gamma_{\mathrm{ClO_4^-}}+\gamma_{\mathrm{HClO_4}}K_a\right)}}=m_a} \quad (7)$$

pK_{a2} values from the fitting are listed in Table 5 and fit curves plotted in Figure 5. Making the same assumptions as described below in section 4.1.4, equation (12) can also be applied to obtain $\Delta_rH°$ and $\Delta_rS°$ (Table 5) from these temperature-dependent pK_{a2} values.

4.1.3. ^{125}Te NMR studies

To complement the data obtained by solubility and potentiometric experiments, the acid-base equilibrium was further investigated via ^{125}Te NMR. This analytical method has the ability to cover the pH range of -1 to 14. However, a minimum concentration of ~1 mM of the NMR-active nuclei is required to obtain spectra within a reasonable timeframe (few hours). By using isotopically enriched Te (98% ^{125}Te; natural abundance ~7%) and working at elevated temperatures (higher solubility), it was possible to collect the data shown in Figure 6.

Chemical shifts display a clear variation as a function of pH which is, however, not monotonic (Fig. 6; Appendix A9, A10). To understand this, one has to consider that the chemical shift is controlled by the shielding tensor, which has two contributions. First, the diamagnetic component, which reflects the electron density around the nucleus of interest, and hence is related to the effective charge on the atom. Were this term to dominate the shielding tensor, a gradual change in chemical shift when going from a cationic to a neutral and then to an anionic species would be expected. This possibly accounts for the variation at high pH where the addition of a proton (eq (4)) produces an increase in chemical shift (deshielding). The second component to the shielding tensor is the paramagnetic term, which is controlled by intramolecular currents and depends in a complex way on coupling between occupied and virtual molecular orbitals. Theoretical calculations have shown that the paramagnetic contribution dominates the shielding tensor in the case of ^{125}Te (Ruiz-Morales et al., 1997). The paramagnetic contribution cannot be related in a simple way to structural or chemical information relevant here. However, it is noteworthy that the ^{77}Se chemical shifts of selenite species follow a similar pattern as those of ^{125}Te in tellurite species (Kolshorn and Meier, 1977). The similarity in chemical shifts for ^{77}Se and ^{125}Te in a number of analogous compounds was noted by McFarlane and McFarlane (1973). In selenites, the ^{77}Se chemical shift correlates with the Se-O σ-bond force constant (Kolshorn and Meier, 1977), providing some insight into the nature of the Se-O bond. To the best of our knowledge, in the case of Te, only the force constant of the TeO_3^{2-} species (4.41 mdyn/Å) has been reported (Siebert, 1954). Therefore, such a correlation cannot be confirmed for tellurites, but by analogy one can predict that the Te-O σ-bond force constant would decrease across the following series: $H_3TeO_3^+ > TeO_3^{2-} > H_2TeO_3 > HTeO_3^-$. Even in the absence of a quantitative understanding of the physical causes for the variation of the chemical shift, the pH dependence of the chemical shifts can be used to obtain quantitative data on acid-base equilibria.

To be able to observe individual signals by NMR for two sites in chemical exchange, the difference in resonance frequencies between the nuclei in each site must be larger than the exchange frequency between the two sites. In the present case, the observed maximum difference in resonance frequencies is a few tens of kHz. This means that only reactions with rates slower than about 10^4 s^{-1} will lead to well-resolved individual NMR lines. In the present case, the presence of only an averaged line shows that the protonation-deprotonation rates on the tellurites species are much faster. This is not unusual as proton exchange reactions are among the fastest reactions to occur in aqueous solution with half-lives as low as 10^{-9} s (Eigen, 1964). The observed chemical shift (δ_{obs}) is an average of the chemical shifts of the different Te species as they are in a fast chemical exchange on the NMR time scale. Each species contributes to δ_{obs} in proportion to its mole fraction χ, i.e.:

$$\delta_{\mathrm{obs}} = \chi_{\mathrm{H_3TeO_3^+}}\delta_{\mathrm{H_3TeO_3^+}} + \chi_{\mathrm{H_2TeO_3}(aq)}\delta_{\mathrm{H_2TeO_3}} + \chi_{\mathrm{HTeO_3^-}}\delta_{\mathrm{HTeO_3^-}} + \chi_{\mathrm{TeO_3^{2-}}}\delta_{\mathrm{TeO_3^{2-}}} \tag{8}$$

with
$$\chi_{\mathrm{H_3TeO_3^+}} = \frac{\left[\mathrm{H_3TeO_3^+}\right]}{\left[\mathrm{H_3TeO_3^+}\right]+\left[\mathrm{H_2TeO_3}(aq)\right]+\left[\mathrm{HTeO_3^-}\right]+\left[\mathrm{TeO_3^{2-}}\right]}. \tag{9}$$

The other mole fractions are defined in an analogous way. Combining the equations for the mole fraction with equations (2)-(4), and rearranging them to introduce them into equation (8) yields equation (10).

$$\delta_{\mathrm{obs}} = \frac{\dfrac{a_{\mathrm{H^+}}\gamma_{\mathrm{H_2TeO_3}(aq)}}{K_{a_0}\gamma_{\mathrm{H_3TeO_3^+}}}\delta_{\mathrm{H_3TeO_3^+}} + \delta_{\mathrm{H_2TeO_3}(aq)} + \dfrac{K_{a_1}\gamma_{\mathrm{H_2TeO_3}(aq)}}{\gamma_{\mathrm{HTeO_3^-}}a_{\mathrm{H^+}}}\delta_{\mathrm{HTeO_3^-}} + \dfrac{K_{a_2}K_{a_1}\gamma_{\mathrm{H_2TeO_3}(aq)}}{\gamma_{\mathrm{TeO_3^{2-}}}a_{\mathrm{H^+}}^2}\delta_{\mathrm{TeO_3^{2-}}}}{\dfrac{a_{\mathrm{H^+}}\gamma_{\mathrm{H_2TeO_3}(aq)}}{K_{a_0}\gamma_{\mathrm{H_3TeO_3^+}}} + 1 + \dfrac{K_{a_1}\gamma_{\mathrm{H_2TeO_3}(aq)}}{\gamma_{\mathrm{HTeO_3^-}}a_{\mathrm{H^+}}} + \dfrac{K_{a_2}K_{a_1}\gamma_{\mathrm{H_2TeO_3}(aq)}}{\gamma_{\mathrm{TeO_3^{2-}}}a_{\mathrm{H^+}}^2}} \tag{10}$$

As for the solubility experiments, the activity of water was assumed to be unity; the activity coefficients of the Te(IV) complexes and pH were calculated for each solution at the required temperature (Appendices A9 and A10). The results of the fit are given in Table 6, and plotted in Figure 6. Two curves are plotted; one corresponds to an ionic strength of 1 m whereas in the second case it is at infinite dilution (I = 0 m). The scatter of the experimental points is due to the fact that the actual ionic strength of the samples is located between these two limiting cases. However experimental errors also contribute to it. The upper limit of the temperature range of the instrument used is 140 °C, the temperature was stable within ±2 °C. In the case of $p\mathrm{K}_{a0}$, $p\mathrm{K}_{a1}$ and $p\mathrm{K}_{a2}$, a comparison of the values obtained from the NMR experiments and the two other methods is possible and shows that the NMR values are systematically higher (Fig. 5), although with the exception of pK_{a0} the differences can be considered to be within the experimental error. A possible explanation for this systematic deviation could be the fact that the NMR samples contain 10% D_2O. In the case of the second dissociation for selenious acid,

$$\mathrm{HSeO_3^-} = \mathrm{SeO_3^{2-}} + \mathrm{H^+} \tag{11}$$

the $\mathrm{pK_a}$ in D_2O is higher by 0.54 than in H_2O (Salomaa et al., 1969). However, the change in the ionization constant in mixed solvent (H_2O/D_2O) does not follow linearly the mole fraction of D and in the case of low D content the change tends to be less than such a linear relation would predict (Laughton and Robertson, 1969). Therefore, the contribution from addition of D_2O can be conservatively estimated to result in an observed increase by 0.05 units, which is within experimental error.

4.1.4. Comparison with previous solubility studies and recommended thermodynamic properties

TeO_2(s) dissolves easily in alkaline solutions. The Na_2O-TeO_2-H_2O system was investigated at 25 °C resulting in the identification of several solid phases such as Na_2TeO_3(s), $Na_2TeO_3 \cdot 5H_2O$(s), $Na_2Te_3O_5 \cdot 3H_2O$(s), $Na_2Te_3O_7 \cdot 5H_2O$(s), or $Na_2Te_4O_9 \cdot 5H_2O$(s) (Lavut and Vorob'eva, 1960); Te concentrations ranged from 0.026 m in 40 wt% NaOH up to 4.5 m in solutions in equilibrium with the solid phases $Na_2TeO_3 \cdot 5H_2O$(s) and $Na_2Te_3O_5 \cdot 3H_2O$(s). Lithium tellurite is reported to have a retrograde solubility with increasing temperature: 12.65 wt% at 30 °C down to 5.86 wt% at 80 °C (Breusov et al., 1965). TeO_2(s) also has the ability to dissolve in acidic solutions and this characterizes it as an amphoteric compound. The solubility goes through a minimum in the pH range 3.8 to 4.5 at 25 °C (Cheng, 1961; Issa and Awad, 1954). Consequently, any comprehensive investigation of the solubility of this compound needs to also consider the acid-base equilibria involved (equations (2)-(4)). Masson (1976) noted a wide divergence among the values reported in the literature for the acid dissociation constants of the tellurites. Consequently, she performed her own experimental investigations to complement the available data and to attempt to resolve the discrepancies, which resulted in the following recommended values: $\log K_{a0} = 2.8 \pm 0.2$, $\log K_{a1} = 6.08 \pm 0.06$ and $\log K_{a2} = 9.56 \pm 0.02$, and a minimum solubility at 25 °C of 1.2×10^{-5} M (Table 3). All studies to date were conducted at or near room temperature, but McPhail (1995) launched an experimental investigation aimed at extending the available data for the TeO_2-H_2O system to 80 °C. Unfortunately, the full details of his investigation were not published. The solubility of TeO_2(s) was found to increase almost by a factor of ten between 25 °C and 80 °C: $\log K_s = -5.03$ to -4.12. McPhail (1995) also reported values for the first two acid dissociation constant: $\log K_{a0} = -2.83$ to -2.33 and $\log K_{a1} = -6.38$ to -5.99.

Our pK_s values determined from the solubility experiments are ~0.4-0.3 logK unit lower than the experimental values of McPhail (1995) at 25-80 ˚C (Table 3). At 200 ˚C, our value of pK_S (2.72) is close to McPhail's (1995) extrapolation (2.88). There is an excellent agreement between our pK_{a0} value at 25 °C and those reported by McPhail (1995) and Masson (1976). However, with increasing temperature the values drift apart. In the case of

pK_{a1} excellent agreement is found at 80 °C, which contrasts with a difference in more than one pK unit between the values reported for 25 °C previously and in this study. For pK_{a2}, our potentiometric value for $H_2TeO_3^+$ at 25 ˚C is 0.5 log unit higher than that obtained by Masson (1976) and selected by McPhail (1995). At 80 ˚C, the pK_{a2} values obtained from potentiometric titration (9.68) and NMR (9.96) are lower than the estimate of McPhail (1995). The observed temperature dependence of pK_{a2} is opposite from the trend predicted by McPhail (1995).

In general, the values obtained are equal or lower than the ones given by McPhail (1995), suggesting that there may be some systematic cause (e.g., activity coefficient model; calculation of buffer pH). However, in the absence of a detailed account of the measurements and data analysis, it is not possible to resolve these inconsistencies.

Plotting the pK values versus reciprocal T yields straight lines (Fig. 5; R^2 listed in Table 3). This means that the enthalpy change of the reaction is constant over the experimental temperature range (i.e., the heat capacity $\Delta_r C_p$ is constant and close to zero). Equation (12) derived from the van't Hoff equation is therefore a reasonable approximation to describe the temperature dependence of K over the temperature range covered here. As McPhail (1995) noted, a similar behavior is also observed for the solubility of other oxides such as SiO_2 and TiO_2 over a comparable temperature range.

$$\ln K = -\frac{\Delta_r H^\circ}{RT} + \frac{\Delta_r S^\circ}{R} \qquad (12)$$

This allows the enthalpy $\Delta_r H^\circ$ and entropy $\Delta_r S^\circ$ of reaction to be estimated from a simple linear regression; the resulting values are listed in Table 3.

Table 7 summarizes the thermodynamic parameters for the aqueous species from the consolidated data of the solubility determination, the potentiometric titrations and the NMR measurements. The last line in Table 7 lists the values proposed for $\Delta_f G^\circ_{298}$ in the compilation by McPhail (1995). There is good agreement between the respective values of both sets. Some of the difference can possibly be related to the different values taken for the properties of $H_2O(l)$ and $TeO_2(s)$ (in the present study from Barin (1995)).

To assist in using the new properties in geochemical modeling, we extrapolated the data to allow simulation over a wide range of conditions. We follow the approach implemented in the HCh software (Shvarov and Bastrakov, 1999). Due to the limited dataset, full fitting to the revised Helgeson-Kirkham-Flowers (HKF) equation of state of Shock et al. (1997) is not feasible; instead, we use the HKF formalism to describe one 'basis species', and then describe the related species using the modified Ryzhenko-Bryzgalin model (MRB) (Borisov and Shvarov, 1992) parameters: the pK of reaction linking the new species to other 'basis' species under standard conditions (25 ˚C and 1 bar) and two empirical fit parameters, A and B. The resulting equation of state parameters and extrapolated properties are listed in Table 8. We selected $HTeO_3^-$ as the basis species. Attempts to use the neutral $H_2TeO_3(aq)$ complex with the empirical correlations among HKF coefficients developed for neutral species by Plyasunov and Shock (2001) led to poor fits. The correlations of Plyasunov and Shock (2001) for neutral species are based on the free energy of the hydration reaction, $H_2TeO_3(g) = H_2TeO_3(aq)$; based on the properties of $H_2TeO_3(g)$ developed in the current study (section 4.2), $\Delta_h G^0_{298K}$ = -117 kJ mol^{-1}. This value is significantly more negative than that of the compounds considered by Plyasunov and Shock (2001) (-75 kJ mol^{-1}) in developing their correlations.

4.2. TeO_2(s) solubility in water vapor

Previous studies showed that the volatility of TeO_2(s) is significantly enhanced in the presence of steam (water vapor), because of the formation of $TeO_2{\cdot}xH_2O(g)$ species (Glemser and Haeseler, 1962; Glemser et al., 1964; 1965, 1966; Malinauskas et al., 1970). The stoichiometry of the volatile Te species is dependent on the vapor pressure: at low steam pressure (≤ 1 bar, 450-700 °C), $TeO(OH)_2(g)$ is present whereas at higher pressures (3 to 455 bar, 418 °C and 470 °C), $Te(OH)_4(g)$ is the main Te-bearing species (Glemser et al., 1964, 1965, 1966). These studies used a mass transport apparatus to investigate the TeO_2-steam system. Steam, sometimes mixed with a carrier gas, was allowed to flow over heated $TeO_2(s)$ where it reacted to form $TeO_2{\cdot}xH_2O(g)$ species. The vapor was then condensed and analyzed to obtain the concentration of Te carried in the vapor phase. Malinauskas et al. (1970) reproduced the low pressure results obtained by Glemser et al. (1964), but their attempt to confirm the presence of $TeO(OH)_2(g)$ by mass spectrometry failed due to the Te/steam mixture reacting with the material of their instrument. In addition, Malinauskas et al. (1970) reported the presence of a dimeric species under dry conditions. Other studies (Cordfunke and Konings, 1990; Garisto, 1982, 1992) mainly review the low pressure data from the work of Glemser et al. (1964, 1965, 1966) and Malinauskas et al. (1970), and draw speciation diagrams relevant to nuclear reactor safety.

In the present study, a different experimental approach was used. The vapor phase above a solution saturated with TeO_2(tet) was sampled directly. The reaction was investigated at two temperatures (315 ° and 385 °C). The second temperature was just above the critical temperature (T_c = 374 °C). In this case, after each sampling the pressure in the autoclave decreased and it was, therefore, possible to collect samples at different pressures for the same temperature. Results are listed in Table 9.

The measured vapor solubilities of TeO_2(tet) are plotted together with the data from Glemser et al. (1964; 1966) in Figure 7. These data have been treated together to compute thermodynamic parameters for use in reactive transport modeling. The data from Malinauskas et al. (1970) were not included as no listing of individual data points were given.

The Gibbs free energy of formation from the elements ($\Delta_f G_i^{P,T}$) for vapor species i is:

$$\Delta_f G_i^{P,T} = \Delta_f G_i^0 - S_i^0 \left(T - T_R\right) + \int_{T_R}^{T} c_p(T)dT - T\int_{T_R}^{T} \frac{c_p(T)}{T} dT + RT\ln\left(f_i\right) \tag{13}$$

where $\Delta_f G_i^0$ is the Gibbs free energy of formation under the reference conditions (T_R=298.15 K, P_R = 1 bar); S_i^0 is the entropy at T_R, P_R; $c_p(T)$ is molal isobaric heat capacity of the gas at 1 bar (P_R); and $f_i = \gamma_i P$, where γ_i is the fugacity coefficient. For the Te vapor species, the fugacity coefficient is fixed at unity.

The temperature dependence of the heat capacity of each species was approximated using the polynomial equation:

$$c_p(T) = a_0 + a_1 T + \frac{a_2}{T^2} + \frac{a_3}{T^{0.5}} + a_4 T^2 + a_5 T^3 \tag{14}$$

The reactions involved in the vapor experiments are:

$$TeO_2(s) + nH_2O(g) = TeO_2(H_2O)_n(g), \text{ with } n = 0, 1, 2 \tag{15}$$

The Gibbs free energy change of these three reactions is related to the Gibbs free energy of formation of the individual species by:

$$\Delta_r G_i^{P,T} = \Delta_f G^{P,T}_{\mathrm{TeO_2(H_2O)_n(g)}} - n\Delta_f G^{P,T}_{\mathrm{H_2O(g)}} - \Delta_f G^{P,T}_{\mathrm{TeO_2(s)}} \tag{16}$$

$\Delta_f G^{P,T}_{H_2O(g)}$ was calculated using the improved Peng-Robinson equation of state of Stryjek and Vera (1986), as coded in the HCh software. A value of $\Delta_f G^{P,T}_{TeO_2(s)}$ was taken from Barin (1995) (Table 10). The data for the dry vaporization equilibrium of TeO_2(tet), which was not reinvestigated here, were also taken from Barin (1995).

The Gibbs free energy of formation from the elements under standard conditions, entropy, and heat capacity functions from the $TeO_2 \cdot H_2O$(g) and $TeO_2 \cdot 2H_2O$(g) species were retrieved via non-linear least squares refinement, minimizing a residual function defined as $(\log(\exp) - \log(\text{calc}))^2 / (\log(\exp))^2$ (Table 10; Fig. 7). Our two 1 bar experimental points

(Table 9) have Te concentrations that are almost two orders of magnitude too low, and were excluded from the fit. This may indicate that an equilibration time of 10 days was not sufficient (section 3). In addition, the high P (>300 bar) data collected by Glemser et al. (1966) at 691 K were also excluded; these data points define an anomalous steep trend (slope between 8 and 12) on a plot of log f_{Te} vs. log f_{H2O} (Fig. 7). Although this may indicate the presence of highly hydrated Te complexes, there are not enough data to interpret the speciation. In addition, the dataset at 691 K appears to be anomalous, since at higher T (e.g. 743 K) and higher pressures there is little evidence for highly hydrated Te(IV) vapor species.

4.3. The structure of tellurite species by XAS

In-situ X-ray absorption spectroscopy techniques were employed to further characterize the predominant Te(IV) species and to determine their coordination structures in hydrothermal solutions. XANES and EXAFS spectra of aqueous solutions containing Te(IV) were recorded under ambient conditions (APS) and up to 505 °C and 800 bar (ESRF). A list of the solutions studied under various conditions is given in Table 11.

4.3.1. Qualitative XANES analysis

Te(IV) coordination in solids is characterized by a strong lone electron pair effect: Te sits at the apex of distorted trigonal pyramids [TeO_3], on an equatorial position in distorted trigonal dipyramids [TeO_4], or in intermediate coordinations [TeO_{3+1}]. As a result of this range in coordinations, Te–O bond distances vary substantially in Te(IV) minerals, ranging from 1.78 to 3.41 Å (see Fig. 7 in Grundler et al., 2008), with an average bond distance of 2.20 Å. Similar coordination geometries were found for the Te(IV) ion in tellurite glasses, based on the experimental studies of Yamamoto et al. (1994) and Blanchandin et al. (2000), and the theoretical studies of Jiang and Spence (2004) and Strömberg et al. (1985).

Figure 8a compares the Te K-edge XANES spectra collected on metallic tellurium, $Te(OH)_6$(s) (a tellurate salt containing Te(VI) in octahedral coordination), and the tellurite salts K_2TeO_3(s) (containing Te(IV) coordinated by three oxygens at 1.82 Å; Andersen et al., 1989) and TeO_2(tet) (containing Te(IV) coordinated by two oxygens at 1.90 Å and two oxygens at 2.11 Å) with some spectra for Te(IV) in aqueous solutions.

TeO_2(tet) displays two peaks at ~31868 eV and 31900 eV, (C_1 and C_2) but K_2TeO_3(s) shows a single broad peak in this region. In addition, the white line (feature A) is sharper and more intense in TeO_2(tet), so that the shoulder B appears to be relatively more prominent in K_2TeO_3(s). Yamamoto et al. (1994) interpreted these differences to reflect differences among the [TeO_3] (as in K_2TeO_3(s)) and [TeO_4] (TeO_2(tet)) moieties. The solution spectra collected at high pH have spectra similar to that of K_2TeO_3(s), and all experimental solutions have a single broad peak at C, consistent with the [TeO_3] moiety according to Yamamoto et al. (1994). At low pH, the white line (feature A) appears to become sharper and more intense (e.g., Sol4 at 100 ˚C). Note that the slight difference between the spectra of Sol1 and Sol2 reflect differences in the resolutions of the two beam lines used in this study (monochromators Si(220) at ESRF and Si(111) at APS; see Appendix A6).

Figure 8b shows spectra of three different solutions measured as a function of temperature. Overall, the individual solutions show little spectral variation with temperature, the main difference being small changes in the relative intensity of the shoulder (position B) relative to the white line (position A). As the temperature increases, the spectra for Sol4 ($pH_{25^\circ C}$ 1.56) show a slight decrease in the intensity of the white line and a slight edge shift. The spectra for the last two temperatures are very similar (316 and 456 °C); metallic Te precipitated upon further heating. The spectrum for Sol6 ($pH_{25^\circ C}$ 2.01) at 212 °C resembles Sol4 at 100 °C and as the temperature increases the shoulder B appears to broaden, whereas the white line remains roughly constant. Sol4 and Sol6, which have similar $pH_{25^\circ C}$ (~2), follow the same spectral trend with increasing temperature, but the evolution starts at a lower temperature in Sol4, as the sulfate buffer (Sol4) has a stronger temperature dependence than the phosphate buffer (Sol6). At 100 ˚C, the white line for Sol5 (near neutral) is lower than that for Sol4 (acidic), and the shoulder B is similar in size and energy as that for TeO_2(tet); this could indicate the presence of TeO_2(tet) in suspension at 100 ˚C in Sol5; however, the absence of a double peak at C suggest that the aqueous complex still dominates this experimental spectrum.

4.3.2. EXAFS

To quantify the coordination structure of the tellurite species, EXAFS data were analyzed with the HORAE package (Ravel and Newville, 2005), using FEFF version 6 (Rehr et al., 1992). The data used in the EXAFS fit ranged from k = 2.0 to 10.0 $Å^{-1}$. The fitting was done in R-space in the range [1.0 – 3.4 Å], with a Hanning window and multiple k^n weighting (n=1, 2 and 3) to diminish correlations between variables. Selected 'end-member' (i.e. most different) spectra were refined (Fig. 9).

Various models were tested on the three room T solutions to determine the most likely speciation: (i) Te bonded to three equidistant O atoms, (ii) Te bonded to three O atoms at three different distances, (iii) Te bonded to four equidistant O atoms, (iv) Te bonded to four O atoms at four different distances, and (v) Te bonded to three equidistant O atoms plus another O atom at a different distance. The fit with Te bonded to three equidistant O atoms resulted in the best fit (model (i); Table 12), both visually and with the best goodness of fit parameters. Fitting with three different oxygen distances (model ii) did not improve the fit; refining all the variables resulted in unphysical values so a number of parameters had to be constrained. Even this did not result in an improved fit for any of the three experimental solutions. All fits involving four oxygen atoms (models iii and iv) were poor. Fitting the data with three equidistant plus another oxygen atom at a different distance (model v) resulted in a fit that visually was almost as good as Te bonded to three equidistant oxygen atoms, however the fitting parameters were not as good. Using the χ_{red}^2 test of Kelly et al. (2008), it could be determined that there is a statistically significant difference in the fitting parameters of models (i) and (v) and that TeO_3 (model i, with three equidistant oxygen atoms) is the better model. Although there is no statistically significant difference between the models (i) and (ii), there is no advantage in using the more complicated model. Thus, EXAFS confirms that [TeO_3] is the dominant Te species in these solutions.

On the basis of fits using model (i), the Te-O bond length at room T increases with decreasing pH, expanding from 1.83(2) Å at pH > 10 (Sol1) to 1.90(1) Å at pH < 0 (Sol8). This is consistent with a change in speciation from [TeO_3^{2-}] at high pH to [$Te(OH)_3^+$] at low pH (Fig. 1). The protonation of oxygen leads to a weakening, and consequently lengthening, of the Te-O bond by withdrawing electron density between the Te and O atoms. The bond length stayed relatively constant (almost within 1σ-error; Table 12) when heating from room temperature (Sol2) to 456 °C (Sol4). These bond lengths compare well with previously published bond lengths of Te-O in solid compounds (see section 4.3.1).

4.3.3. Ab-initio XANES calculations

XANES spectra for selected stoichiometries and geometries of Te(IV) complexes were calculated *ab-initio* using the FDMNES package (Joly 2001), following the procedure outlined in Brugger et al. (2007), Testemale et al. (2009) and Etschmann et al. (2010, 2011). Jiang and Spence (2004) presented *ab-initio* Te *K*-edge XANES calculations for Te(IV) in TeO_3, TeO_{3+1} and TeO_4 configurations, using the Muffin Tin (MT) approximation to solve the Schrödinger equation and calculate the final states and resulting absorption cross sections. In this study, we used the Finite Difference Method (FDM) to solve the Schrödinger equation, which allows for a totally free potential shape; this is of particular interest for low symmetry and/or non-dense structures (Joly, 2001), as is the case for the Te(IV) complexes affected by a stereochemically active lone electron pair (see Appendix A11 for details of the calculations).

Calculations of Te K edge spectra for three compounds in which Te exists in different coordinations illustrate the level of accuracy achieved by the calculations (Fig. 10). In K_2TeO_3(s) (Andersen et al., 1989, ICSD 65640), Te(IV) exists as a trigonal pyramidal [TeO_3] moiety (Fig. 10b). The calculated spectrum (FDM, 6 Å) agrees well with the experimental spectrum (Fig. 10a). In particular, the white line (A) and the shoulder (B) are accurately reproduced. The only discrepancy is the band (C): there is one broad peak on the experimental spectrum, whereas there are two small peaks on the calculated raw spectrum. The spectrum calculated using the MT approximation shows a much poorer agreement; in particular, the shoulder (B) is poorly reproduced. The large difference between FDM and MT modes can be attributed to the low local symmetry (trigonal pyramid TeO_3) around Te(IV) (Andersen et al., 1989; Joly, 2001; Testemale et al., 2004).

In TeO_2(tet), Te is bonded in a TeO_4 moiety, with two O atoms at 1.902 Å and two others at 2.105 Å (Worlton and Beyerlein, 1975; ICSD 34422; Fig. 10d). The spectrum calculated based on Worlton and Beyerlein (1975)'s crystallographic unit-cell shows features B, C1, and C2 that are red-shifted by ~3 eV relative to feature A. Reducing the unit cell dimensions by 2% resulted in a spectrum that agreed well with the experimental data (Fig. 10c). The remaining disparities include a slightly higher white line and a less significant peak (shoulder B); the latter feature, however, corresponds to a sharp peak on the raw spectrum. An important observation is that the C1 - C2 doublet, which in some earlier studies was believed to be related to Te coordination (3 versus 4; Yamamoto et al., 2004), is actually related to second shell contributions: the calculated spectrum with a cluster size of 3 Å (TeO_4 moiety) shows a single peak. Again, the MT calculations are less accurate than the FDM calculations, with a wider white line (A). The spectrum of telluric acid, $Te^{VI}(OH)_6$(s), in which Te exists in octahedral coordination with 6 OH^- anions (Falck and Lindqvist, 1978; ICSD 2390; Fig. 10f) was also calculated. The structure is quite symmetrical, so there is little difference between the spectra calculated using the MT or FDM methods (Fig. 10e).

Based on *ab-initio* XANES calculations using the MT approximation, Jiang and Spence (2004) concluded that the intensity of the shoulder B (i.e. the ratio of intensities of the white line (A) and shoulder (B)) in Te K-edge spectra can be used to distinguish between [TeO_3] and [TeO_4] moieties. Figures 8a and 11a show that the main difference in the spectra of aqueous Te(IV) species is this ratio, with basic solutions showing a relatively lower white line (A) and higher shoulder (B). However, our *ab-initio* XANES calculations show that these differences are not necessarily due to a change in coordination from 3 to 4 (Figure 11c); deprotonation (Fig. 11a), Te-O bond distances (Fig. 11a), and the O-Te-O bond angles (Fig. 11b) all affect the relative intensities of the A and B features (see Appendix A12 for details). Altogether, these effects show that $Te(OH)_3^+$ (stable under highly acidic conditions) and TeO_3^{2-} (stable under highly basic conditions; Fig. 1a) can both share a three-fold coordination, as suggested by the EXAFS analysis.

5. GEOLOGICAL IMPLICATIONS

The main aim of the experimental studies is to identify the main species responsible for metal mobility and to provide thermodynamic properties that can be used for modeling mineral solubility and reactive transport in complex geological environments (Brugger et al. 2010). Although experiments cover limited ranges in P, T, and fluid composition, semi-empirical methods (e.g., HKF equation of state; Shock et al. 1997) allow the results to be extended over conditions ranging from low-temperature epithermal deposits to high-temperature intrusion-related deposits. In this section, we focus on calculations of Au-Te and Ag-Au-Te systems at 200 and 300 ˚C based on the new data generated in this study and properties from the literature. Using these calculations, we discuss the conditions under which Au, Ag, and Te can be transported in hydrothermal fluids and the role of liquid-vapor partitioning in the formation of Au-Te deposits.

5.1. Modeling mineral solubility in the Au-Te-(Ag)-H_2O system

Calculations of the speciation and solubility of Te and Au in coexisting brine and vapor for the system Au-Te-H_2O-S-Cl at 300 ˚C at vapor saturation pressure (85.8 bar) are shown in Figure 12. These diagrams are based on full chemical speciation calculations for a closed system with the following composition: 1 molal Cl^- (5.5 wt% NaCl), 10 ppm Te, 1 ppm Au, and 0.1 molal (3200 ppm) S. The chosen concentration of Te (10 ppm) reflects the ppm-levels of Te measured in fluid inclusions from magmatic fluids associated with epithermal-style mineralization (Pudack et al., 2009; Wallier et al., 2006). Note that contrary to activity-activity diagrams (e.g., Zhang and Spry, 1994), diagrams based on full speciation calculations do not assume fixed activities of components such as Te; instead, the total amount of Te in the modeled system is fixed, and the mass partition of Te between aqueous species and minerals is calculated at each point in the diagram. The calculations were performed over a range of pH and $\log f O_2(g)$, with Na^+ used to balance the charges, using Geochemist's Workbench (Bethke, 2007). This package calculates only fugacities for vapor species; Te concentrations in the vapor phase were estimated using the ideal gas approximation with the water densities from the water equation of state of Lemmon et al. (2000, NIST database). Thermodynamic properties for the reduced aqueous and vapor Te species were taken from McPhail (1995); other Te species are listed in Table 13. Properties for Au species were taken from the review in Usher et al. (2009).

Figure 12a shows the minerals coexisting with the solution and the vapor in the modeled system. At $fO_2(g) > \sim -22$, the solubility of Te and Au is larger than the amount available in the modeled closed system (i.e., Te ≥ 10 ppm; Au ≥ 1 ppm), and consequently no Au or Te mineral is present. The assemblage of calaverite + native tellurium is stable under a large range of reducing conditions, well into the fields where aqueous Te speciation is dominated by oxidized Te(IV) species (Fig. 12b). As pointed out by previous studies (Cooke and McPhail, 2001; McPhail, 1995), the solubility of Te is low under reducing conditions (methane stable) at acidic to neutral pHs (Fig. 12b). Under basic condition, mildly reduced, Au-rich (≥ 300 ppb; Au transported as $Au(HS)_2^-$) solutions can carry up to 100 ppb Te (Fig. 12b,c). These calculations emphasize the fact that fluids that can transport Au efficiently as $Au(HS)_2^-$ can also carry significant Te. Cook et al. (2009) note that such geochemical conditions exist in some epithermal environments (hematite-pyrite stability) and in orogenic systems (typical neutral to alkaline pH, low-salinity, CO_2-rich fluids), explaining the greater abundance of Au telluride deposits in such geological settings.

Native tellurium rarely coexists with calaverite in gold deposits (e.g., Golden Mile, Golding, 1978; Emperor, Pals and Spry, 2003; Perama Hill, Voudouris et al., 2011). Native tellurium has not been reported from deposits in which Te-rich fluid inclusions were analyzed (Roşia Montană, Tamas et al. 2006; Nevados de Famatina, Losada-Calderón and McPhail, 1996). The presence of native tellurium in the model most probably reflects the fact that important chemical elements are missing from the model. Aside from Ag- and Ag-Au tellurides (discussed in the following paragraphs), Te is found mainly in minerals such as coloradoite (HgTe; e.g., Golden Mile deposit, Australia, Shackleton et al., 2003), goldfieldite ($Cu_{12}(Te,Sb,As)_4S_{13}$; e.g., Nevados de Famatina, Losada-Calderón and McPhail, 1996) in orogenic and epithermal-style deposits; or as Bi-tellurides, mainly in reduced intrusion-related deposits (Ciobanu et al. 2009).

The system Au-Ag-Te better represents what is observed for precious metal tellurides in gold deposits. In such deposits, calaverite more commonly coexists with native gold (e.g., Golden Sunlight deposit, Montana, Spry et al., 1997) or the Ag-bearing tellurides, krennerite or petzite (e.g., Golden Mile deposit, Australia, Shackleton et al., 2003), whereas native tellurium primarily coexists with the silver-bearing tellurides (sylvanite, hessite, and stützite) (e.g., Kobetsuzawa and Kawazu deposits, Japan, Nakata and Komuru, 2011; Golden Sunlight, Spry and Thieben, 2000). Modeling this Ag-Au-Te-H_2O system is currently limited by our poor understanding of the thermodynamics of Ag-Au-Te minerals. Data exist only for petzite (Echmaeva and Osadchii, 2009), but there are no data for sylvanite and krennerite, or for higher-temperature metastable phases (α- or γ-phases above 120 °C; Bindi et al., 2005). Calaverite, although formally a Au-Te mineral, can contain similar amounts of Ag as sylvanite (Zhao et al. 2013). In addition, the assemblages observed may be affected by protracted histories of (re)-crystallization during cooling, often complicated by overprinting events (Cook et al. 2009). Zhao et al. (2013) showed experimentally that such complex textures and assemblages (calaverite of different composition; petzite; hessite) can also result from single stage hydrothermal alteration, via interaction among fluid-mediated interface coupled dissolution-reprecipitation reactions and solid-state reactions.

We show in Figure 13 the results of a simulation of the Ag-Au-Te system; the model system is similar to Figure 12 (1 ppm Au, 10 ppm Te, 1 m Cl^-, 0.1 m S), with the addition of 10 ppm Ag to the bulk composition. The properties of Ag-chlorocomplexes recommended by Pokrovski et al. (2012) were used, together with hessite data are from Mills (1974) and Afifi et al. (1988). Because of the limited thermodynamic dataset for Ag-Au-Te phases, such diagrams must be used with care in interpreting phase relationships. However, the diagram represents qualitatively the evolution observed experimentally by Zhao et al. (2013) for the hydrothermal alteration of sylvanite. Importantly, the addition of Ag to the system Au-Te does not alter the topology of the solubility gradients (compare Figs. 13b and 12c), showing that the Au-Te system is useful for understanding Au and Te transport and deposition. Similarly, the Te vapor partitioning remains similar in the Ag-bearing and Ag-free models (Figs. 13d, 12f).

A relatively common feature of epithermal and orogenic gold deposits is that tellurides form in more than one stage over a range of physicochemical conditions. As was pointed out by Pals and Spry (2003), Au-rich tellurides generally form prior to Ag-rich tellurides in a variety of deposits (e.g., Gies deposit, Zhang and Spry, 1994; Golden Sunlight, Spry et al., 1997; Emperor, Pals and Spry, 2003), whereas Cooke and McPhail (2001), for example, showed the opposite paragenetic trend in the Acupan deposit, Philippines. Numerical simulations by Cooke and McPhail (2001), taking into account a wide variety of depositional processes including redox gradients, boiling, fluid mixing, and condensation, showed that hessite is expected to precipitate first, assuming a starting concentration of 7 ppb Ag^+, 30 ppb Au and 3.7 10^{-6} ppb Te at $pH_{300^\circ C}$ of 5.65 and $\log fO_2$ of -33. Calculations here suggest that the calaverite-hessite-tellurium assemblage controls Au-Ag-Te in solution under reducing conditions. Paragenetic sequences of particular deposits mainly reflect the ratios of metals in the parent hydrothermal fluid and the reaction path, which controls which minerals become saturated first. For example, Figure 13b shows that upon reduction, a fluid containing 10 ppm Te and Ag, and 1 ppm Au, will precipitate first native silver, then hessite, and finally calaverite (+/- native tellurium) at pH corresponding to the $H_2CO_3(aq)/HCO_3^-$ buffer at 300°C. Under near-neutral pH, hessite is followed by calaverite (+/- native tellurium).

5.2. Vapor partitioning of tellurium

In natural geological systems, there is an increasing body of field evidence that supports the concept that Te can be carried in the vapor phase. For example, Greenland and Aruscavage (1986) showed that Te occurs in the particulate fraction of eruptive emissions from the Kilauea volcano, Hawaii. Larocque et al. (2008) reported the presence of calaverite and a Au-Cu telluride (likely kostovite, $AuCuTe_4$) in vesicles in pumice at Volcán Popocatépetl, Mexico, while Fulignati and Sbrana (1998) identified native tellurium as a sublimate in altered rocks of La Fossa volcano, Italy. Although the presence of Au-bearing tellurides reported by Larocque et al. (2008) may suggest that significant Au is also transported in the vapor phase, calculations using the stability constants provided by Zezin et al. (2011) for $AuS(H_2S)_n(g)$ and $AuS(H_2O)_m(g)$ show that Au concentrations in the vapor are extremely low ($<10^{-9}$ ppb Au) at 300°C and P_{sat} and that Te/Au ratio is extremely high under ore-forming conditions.

In epithermal deposits, McPhail (1995) noted that vapor transport was likely to play a major role in Te transport, given the relatively high volatility of Te as reduced species such as $H_2Te(g)$ and $Te_2(g)$ (Fig. 12d). Cooke and McPhail (2001) produced elegant numerical simulations emphasizing the likely role of phase separation and preferential Te partitioning into the vapor for the deposition of metals in epithermal environments. Figure 12d shows the concentration of Te and the predominant Te species in a vapor coexisting with an aqueous solution at the conditions of our simulation as a function of pH and log $f\,O_2(g)$; and Figures 12f and 13d show the partitioning coefficient K_d, defined as:

$$K_d = \frac{[\mathrm{Te}]_{vap}}{[\mathrm{Te}]_{liq}}, \qquad (17)$$

where $[\mathrm{Te}]_{vap}$ and $[\mathrm{Te}]_{liq}$ are the total concentrations of Te (in ppm) in the vapor and liquid, respectively. These figures illustrate the strong preference of Te for the vapor phase under moderately reducing conditions (i.e., $f\,H_2S(g) \geq f\,SO_2(g)$) for acidic to moderately basic pHs; the vapor will carry >10 ppb Te under these conditions, with K_d reaching in excess of 10^6. Under oxidizing conditions, Te partitions into the liquid phase, although a vapor will still carry ppt-levels of Te.

In summary, calculations of vapor partitioning in the Au-Te and Ag-Au-Te systems at 300 °C show that calaverite and native tellurium coexist over a broad range of fO_2 and pH conditions, for which, under reduced conditions, these minerals are in equilibrium with Te predominantly in the vapor phase, whereas at higher fO_2 conditions they are in equilibrium with Te primarily in an aqueous phase.

5.3. Reduced or oxidized Te species in Te transport and gold deposition

The Te and Au concentrations found in modern geothermal fluids, in particular the deep, basic, CO_2-rich fluids from Lihir (>200°C; 0.4 ppb Te, 13 ppb Au; Simmons and Brown, 2006), correspond well with the predictions from our thermodynamic model (Fig. 12). However, high Te concentrations, such as those measured in fluid inclusions at Roşia Montană and Nevados de Famatina, can develop in either basic solutions, or under highly reduced or highly oxidized conditions (Fig. 12b,d). High Te:Au ratios, such as those found in these inclusions, also require similar conditions (Fig. 12e).

This raises the possibility that the Te-rich fluid inclusions represent oxidized (SO_2-only) magmatic fluids, since such fluids can carry high levels of both Te and Au. Reduction of those fluids, e.g. via fluid mixing or fluid-rock interaction, would cause reduction of Te(IV), which would lead to the precipitation of telluride minerals:

$$2\,TeO_3^{2-} + Au(HS)_2^{-} + 3\,H^{+} = AuTe_2(s) + 2\,HS^{-} + 2.5\,H_2O + \mathbf{1.75\,O_2(g)} \quad (18)$$

This mechanism would be very efficient, given the low solubility of telluride minerals. Te(IV) is also likely to be a strong oxidant, i.e. promoting the rate of fluid-rock interaction. Under highly reducing conditions, Te can be transported as polytelluride complexes such as Te_2^{2-} (Brugger et al. 2012). In this case, the precipitation of (Ag)-Au-tellurides is an oxidation reaction:

$$Te_2^{2-} + Au(HS)_2^- + H^+ + 0.25\ O_2(g) = AuTe_2(s) + 2\ HS^- + 0.5\ H_2O \qquad (19)$$

In this case, oxidants would be provided SO_4^{2-} and Fe^{3+}, which can form via fluid-rock interaction from reduced fluids during cooling (e.g., Golden Mile deposit; Evans et al. 2006).

Although aqueous telluro-gold species are unknown in nature, various workers have speculated their presence in hydrothermal solutions and that they may be important in the formation of precious metal minerals. Such species have included $Au(Te_2)^-$, $Au_2(Te_2)^o$, and $Au(Te_2)_2^{3-}$ (Seward, 1973), $AuHTe_{(aq)}$ and $AuTe_2^-$ (McPhail, 1995), and $Au(HTe)_2^-$ (Cook and McPhail, 2001) although Cook and McPhail predicted that concentrations of $Au(HTe)_2^-$ were likely to be 14 orders of magnitude lower than those of $Au(HS)_2^-$. Based on the concentration of Au, Ag, and Te in arsenian pyrite in Carlin- and epithermal-type deposits, and the poor correlation between Au and Te as well as between Ag and Te, Kesler et al. (2007) proposed that the Te:Au, and Te:Ag ratios were so low that Te-precious metal complexes were not primary species for the transport of Au in hydrothermal solution. However, as pointed out by previously by Brugger et al. (2012), polytellurides in highly basic and reducing fluids could possibly act as ligands for precious metal tellurides in a manner similar that proposed for polysulfides (Mei, 2013; Pokrovski and Dubrovinsky 2011; Tossell, 2012). The formation of $[Au_3Te_4]^{3-}$ and $[Au_2Te_4]^{2-}$ as products of electrochemical dissolution of $AuTe_2$ (Warren et al. 1993) and the recognition of the polyatomic ligands $[Au_2(TeS_3)_2]^{2-}$, $[Ag_2Te(TeS_3)_2]^{2-}$, and $[Ag_2Te(TeSe_3)_2]^{2-}$ by Chung et al. (1995) further fuels speculation that precious metal-telluride complexes may be important in hydrothermal solutions although experimental studies of such complexes are yet to be conducted.

ACKNOWLEDGEMENTS

We are grateful to Aoife McFadden for helping with the ICP-MS analyses and potentiometric titrations. Travel to APS and ESRF was supported by the Australian

Synchrotron Research Program, which was funded by the Commonwealth of Australia under the Major National Research Facilities Program and the Australian Research Council (ARC) through the Centre for Green Chemistry. The use of the Advanced Photon Source was supported by the U.S. Department of Energy, Office of Science, Basic Energy Sciences, under Contract No.W-31-109-Eng-38. We thank Dale Brewe (20-BM-B) and Stacey Borg for help with data collection at the APS. This research was conducted as part of an ARC discovery project grant to PVG and AP, and an ARC Professorial Fellowship to JB.

REFERENCES

Afifi, M., Kelly, W. C. and Essene, E. J. (1988) Phase relations among tellurides, sulphides, and oxides: I. Thermochemical data and calculated equilibria. *Econ. Geol.* **83**, 377-394.

Andersen, L., Langer, V., Stromberg, A. and Stromberg, D. (1989) The structure of K_2TeO_3 - an experimental and theoretical study. *Acta Crystallogr. Sect. B* **45**, 344-348.

Barin, I. (1995) *Thermochemical data of pure substances*, 3rd ed. VCH, Weinheim.

Bateman, R. and Hagemann, S. (2004) Gold mineralisation throughout about 45 Ma of Archaean orogenesis: protracted flux of gold in the Golden Mile, Yilgarn craton, Western Australia. *Mineral. Deposita* **39**, 536-559.

Bethke, C.M. (2007) *Geochemical and Biogeochemical Reaction Modeling*, 2nd ed. Cambridge University Press, Cambridge.

Bindi, L., Rossell, M. D., Van Tendeloo, G., Spry, P. G. and Cipriani, C. (2005) Inferred phase relations in part of the system Au-Ag-Te: an integrated analytical study of gold ore from the Golden Mile, Kalgoorlie, Australia. *Miner.Petrol* **83**, 283-293.

Binns, R.A., Dotter, L.E. and Blacklock, K.A. (2004) Chemistry of borehole fluids collected at Pacmanus, Papua New Guinea, ODP leg 193. In *Proceedings of the Ocean Drilling Program, Scientific Results.* Texas A&M University, College Station, Texas, pp. 1-15.

Blanchandin, S., Champarnaud-Mesjard, J.C., Thomas, P. and Frit, B. (2000) Crystal structure of $Nb_2Te_4O_{13}$. *J. Alloys Compd.* **306**, 175-185.

Borisov, M.V. and Shvarov, Y.V. (1992) *Thermodynamics of geochemical processes*. Moscow State University Publishing House, Moscow.

Breusov, O.N., Revzina, T.V. and Druz, N.A. (1965) Preparation and properties of lithium tellurite. *Russ. J. Inorg. Chem.* **10**, 1084-1085.

Brugger, J., Etschmann, B., Liu, W., Testemale, D., Hazemann, J.L., Emerich, H., van Beek, W. and Proux, O. (2007) An XAS study of the structure and thermodynamics of Cu(I) chloride complexes in brines up to high temperature (400 °C, 600 bar). *Geochim. Cosmochim. Acta* **71**, 4920-4941.

Brugger, J., Pring, A., Reith, F., Ryan, C., Etschmann, B., Liu, W. H., O'Neill, B. and Ngothai, Y., (2010) Probing ore deposits formation: New insights and challenges from synchrotron and neutron studies. *Radiation Physics and Chemistry* **79**, 151-161.

Brugger, J., Etschmann, B., Grundler, P., Liu, W., Testemale, D. and Pring, A. (2012). XAS evidence for the stability of polytellurides in hydrothermal fluids up to 599 ˚C, 800 bar. *American Mineralogist*, 97, 1519-1522.

Cheng, K.L. (1961) Analysis of lead telluride with an accuracy to better than 0.1%. *Anal. Chem.* **33**, 761-764.

Chung, D.-Y., Huang, S.-P., Kim, K.-W. and Kanatzidis, M.G. (1995) Discrete complexes incorporating heteropolychalcogenide ligands: ring and cage structures in $Au_2(TeS_3)_2]^{2-}$, $[Ag_2Te(TeS_3)_2]^{2-}$, and $[Ag_2Te(TeSe_3)_2]^{2-}$. *Inorg. Chem.* **34***,* 4292-4293.

Ciobanu, C.L., Birch, W.D., Cook, N.J., Pring, A. and Grundler, P.V. (2010) Petrogenetic significance of Au–Bi–Te–S associations: The example of Maldon, Central Victorian gold province, Australia. *Lithos* **116**, 1-17.

Ciobanu, C.L., Cook, N.J., Damian, G., Damian, F.and Buia, G., (2004) Telluride and sulphosalt associations at Săcărîmb. *IAGOD Guidebook Series* **12**, 145-186.

Ciobanu, C.L., Cook, N.J. and Spry, P.G. (2006) Preface – Special Issue: Telluride and selenide minerals in gold deposits – how and why? *Mineral. Petrol.* **87**, 163-169.

Ciobanu, C. L., Cook, N. J., Pring, A., Brugger, J., Danyushevsky, L. V. and Shimizu, M. (2009) 'Invisible gold' in bismuth chalcogenides. *Geochim. Cosmochim. Acta* **73**, 1970-1999.

Cockerton, A. B. D. and Tomkins, A. G. (2012) Insights into the Liquid Bismuth Collector Model Through Analysis of the Bi-Au Stormont Skarn Prospect, Northwest Tasmania. *Econ. Geol.* **107**, 667-682.

Cook, N.J., Ciobanu, C.L., Spry, P.G. and Voudouris, P. (2009) Understanding gold-(silver)-telluride-(selenide) mineral deposits. *Episodes* **32**, 249-263.

Cooke, D.R. and McPhail, D.C. (2001) Epithermal Au-Ag-Te mineralization, Acupan, Baguio district, Philippines: Numerical simulations of mineral deposition. *Econ. Geol.* **96**, 109-131.

Cordfunke, E.H.P. and Konings, R.J.M. (1990) Thermochemical data for reactor materials and fission products. North Holland, Amsterdam, p. 695.

Cusanelli, A., Frey, U., Richens, D.T. and Merbach, A.E. (1996) The slowest water exchange at a homoleptic mononuclear metal center: variable-temperature and variable-pressure ^{17}O NMR study on $[Ir(H_2O)_6]^{3+}$. *J. Am. Chem. Soc.* **118**, 5265-5271.

Devillanova, F.A. (2007) Handbook of Chalcogen Chemistry. The Royal Society of Chemistry, Cambridge, p. 884.

Echmaeva, E. A. and Osadchii, E. G. (2009) Determination of the thermodynamic properties of compounds in the Ag-Au-Se and Ag-Au-Te systems by the EMF method. *Geology of Ore Deposits* **51**, 247-258.

Eigen, M. (1964) Proton transfer, acid-base catalysis, and enzymatic hydrolysis. Part I: Elementary processes. *Angew. Chem. Int. Ed. Engl.* **3**, 1-19.

Etschmann, B.E., Black, J., Grundler, P., Borg, S., Brewe, D., McPhail, D.C., Spiccia, L. and Brugger, J. (2011) Copper(I) speciation in mixed thiosulfate-chloride and ammonia-chloride solutions: XAS and UV-Visible spectroscopic studies, R*SC Advances* **1**, 1554-1566.

Etschmann, B.E., Liu, W., Testemale, D., Müller, H., Rae, N.A., Proux, O., Hazemann, J.L. and Brugger, J. (2010) An in situ XAS study of copper(I) transport as hydrosulfide complexes in hydrothermal solutions (25-592 °C, 180-600 bar): Speciation and solubility in vapor and liquid phases. *Geochim. Cosmochim. Acta* **74**, 4723-4739.

Evans, K. A., Phillips, G. N. and Powell, R. (2006) Rock-buffering of auriferous fluids in altered rocks associated with the Golden Mile-Style mineralization, Kalgoorlie Gold Field, Western Australia. *Econ. Geol.* **101**, 805-817.

Falck, L. and Lindqvist, O., (1978) X-ray refinement of structure of cubic telluric acid. *Acta Cryst.* **B34**, 3145-3146.

Fehr, M.A., Rehkamper, M., Halliday, A.N., Hattendorf, B. and Gunther, D., (2009) Tellurium isotope compositions of calcium-aluminum-rich inclusions. *Meteorit. Planet. Sci.* **44**, 971-984.

Fehr, M.A., Rehkamper, M., Halliday, A.N., Wiechert, U., Hattendorf, B., Gunther, D., Ono, S., Eigenbrode, J.L. and Rumble, D. (2005) Tellurium isotopic composition of the early solar system - A search for effects resulting from stellar nucleosynthesis, Sn-126 decay, and mass-independent fractionation. *Geochim. Cosmochim. Acta* **69**, 5099-5112.

Fornadel, A.P., Spry, P.G., Mathur, R.D., Jackson, S.E. and Chapman, J.B. (2012) Methods for the determination of Te isotope systematics of minerals in the system Au-Ag-Te by MC-ICP-MS. *Mineral. Mag.* **76 (6)**, 1714.

Fulignati, P. and Sbrana, A. (1998) Presence of native gold and tellurium in the active high-sulfidation hydrothermal system of the La Fossa volcano (Vulcano, Italy). *J. Volcanol. Geotherm. Res.* **86**, 187-198.

Garisto, F. (1982) Thermodynamics of iodine, cesium and tellurium in the primary heat-transport system under accident conditions. Atomic Energy of Canada Limited, Pinawa, Manitoba, p. 53.

Garisto, F. (1992) Thermodynamic behaviour of tellurium at high temperatures. Atomic Energy of Canada Limited, Pinawa, Manitoba, p. 31.

Glemser, O., and Haeseler, R.V. (1962) Über gasförmige Hydroxide des Molybdäns und Wolframs. *Z. Anorg. Allg. Chem.* **316**, 168-181.

Glemser, O., Haeseler, R.V. and Müller, A. (1964) Über gasförmiges $TeO(OH)_2$. *Z. Anorg. Allg. Chem.* **329**, 51-55.

Glemser, O., Mueller, A. and Schwarzkopf, H. (1965) Über die Reaktion von TeO_2 mit Wasserdampf bei höheren Drucken und Temperaturen. *Naturwissenschaften* **52**, 129-130.

Glemser, O., Mueller, A. and Schwarzkopf, H. (1966) Über die Reaktion von TeO_2 und CrO_3 mit Wasserdampf bei höheren Drucken, Omagiu Raluca Ripan. Editura Acedemiei Republici Socialiste Romania, Bucarest, pp. 253-262.

Golding, L.Y. (1978) Mineralogy, geochemistry and origin of the Kalgoorlie gold deposits, Western Australia. Ph. D. thesis, Univ. of Melbourne.

Greenland, L.P., and Aruscavage, P.J. (1986) Volcanic emissions of Se, Te, and As from Kilauea Volcano, Hawaii. *J. Volcanol. Geotherm. Res.* **27**, 195-201.

Grundler, P.V., Brugger, J., Meisser, N., Ansermet, S., Borg, S., Etschmann, B., Testemale, D. and Bolin, T. (2008) Xocolatlite, $Ca_2Mn^{4+}{}_2Te_2O_{12}\cdot H_2O$, a new tellurate related to kuranakhite: Description and measurement of Te oxidation state by XANES spectroscopy. *Am. Mineral.* **93**, 1911-1920.

Harris, R.K., Becker, E.D., Cabral de Menezes, S.M., Goodfellow, R. and Granger, P.(2001) NMR nomenclature. Nuclear spin properties and conventions for chemical shifts. *Pure Appl. Chem.* **73**, 1795-1818.

Huang, C., and Hu, B. (2008) Speciation of inorganic tellurium from seawater by ICP-MS following magnetic SPE separation and preconcentration. *J. Sep. Sci.* **31**, 760-767.

Issa, I.M., and Awad, S.A. (1954) The amphoteric properties of tellurium dioxide. *J. Phys. Chem.* **58**, 948-951.

James-Smith, J., Cauzid, J., Testemale, D., Liu, W., Hazemann, J.-L., Proux, O., Etschmann, B., Philippot, P., Banks, D., Williams, P. and Brugger, J. (2010) Arsenic speciation in fluid inclusions using X-ray Absorption Spectroscopy. *Am. Mineral.* **95**, 921-932.

Jiang, N., and Spence, J.C.H. (2004) Intermediate-range structure of tellurite glasses from near-edge absorption spectra. *Phys. Rev. B* **70**, 184113.

Joly, Y. (2001) X-ray absorption near-edge structure calculations beyond the muffin-tin approximation. *Phys. Rev. B* **63**, 125120.

Kandegedara, A. and Rorabacher, D.B. (1999). Noncomplexing tertiary amines as “better” buffers covering the range of pH 3-11. Temperature dependence of their acid dissociation constants. *Anal. Chem.* **71**, 3140-3144.

Kelley, K.D., Romberger, S.B., Beaty, D.W., Pontius, J.A., Snee, L.W., Stein, H.J. and Thompson, T.B. (1998) Geochemical and geochronological constraints on the genesis of Au-Te deposits at Cripple Creek, Colorado. *Econ. Geol.* **93**, 981-1012.

Kelly, S., Hesterberg, D. and Ravel, B. (2008) Analysis of soils and minerals using X-ray absorption spectroscopy (Chapter 14). In: *Methods of Soil Analysis, Part 5. Mineralogical Methods*. Soil Sciences Society of America, Madison, USA, pp. 387-463.Kesler, S.E., Deditius, A.P. and Chryssloulis, S. (2007) Geochemistry of Se and Te in arsenian pyrite: New evidence for the role of Se and Te hydrothermal complexes in Carlin and epithermal-type deposits. In *Au-Ag-Te-Se deposits, Proceedings of the 2007 Field Workshop* (Espoo, Finland, August 26-31, 2007). Geological Survey of Finland Guidebook 53, p. 85-95.

Kesler, S.E., Deditius, A.P., and Chryssloulis, S., 2007, Geochemistry of Se and Te in arsenian pyrite: New evidence for the role of Se and Te hydrothermal complexes in Carlin and epithermal-type deposits. In Kojonen, K. K., Cook, N.J. and V.J. Ojala (eds.), Au-Ag-Te-Se deposits, *Proceedings of the 2007 Field Workshop (Espoo,* *Finland, August 26-31, 2007)*. Geological Survey of Finland Guidebook 53, p. 85-95.

Kolshorn, H. and Meier, H. (1977) Selenium-77 magnetic resonance. pH dependence of the chemical shift of ^{77}Se in aqueous selenious acid. *J. Chem. Res. (S)*, 338-339.

Krebs, B. and Ahlers, F.-P. (1990) Developments in chalcogen-halide chemistry. *Adv. Inorg. Chem.* **35**, 235-317.

Larocque, A.C.L., Stimac, J.A., Siebe, C., Greengrass, K., Chapman, R. and Melja, S.R. (2008) Deposition of high-sulfidation Au assemblage from a magmatic volatile phase, Volcán Popocatépetl, Mexico. *J. Volcanol. Geotherm. Res.* **170**, 51-68.

Laughton, P.M. and Robertson, R.E. (1969) Solvent isotope effects for equilibria and reactions. In Coetzee, J.F., Ritchie, C.D. (Eds.), Solute-solvent interactions. Marcel Dekker, New York, pp. 399-538.

Lavut, E.A. and Vorob'eva, O.I. (1960) Solubility in the Na_2O-TeO_2-H_2O system at 25°. *Russ. J. Inorg. Chem.* **5**, 880-882.

Lerchbaumer, L. and Audétat, A. (2012) High Cu concentrations in vapor-type fluid inclusions: An artifact? *Geochim. Cosmochim. Acta* **88**, 255-274.

Lee, D.S. and Edmond, J.M. (1985) Tellurium species in seawater. *Nature* **313**, 782-785.

Lemmon, E.W., McLinden, M.O., Friend, D.G., (2000). *Thermophysical properties of fluid systems*. National Institute of Standards and Technology, Gaithersburg, MD.

Lide, D.R. (2003) Handbook of Chemistry and Physics. CRC Press, Boca Raton, Florida.

Liu, W., McPhail, D. C. and Brugger, J.(2001) An experimental study of copper(I)-chloride and copper(I)-acetate complexing in hydrothermal solutions between 50 ºC and 250 ºC and vapour saturated pressure. *Geochim. Cosmochim. Acta* **65**, 2937-2948.

Losada-Calderón, A. J. and McPhail, D. C.(1996) Porphyry and high-sulfidation epithermal mineralization in the Nevados del Famatina mining district, Argentina. *Society of Economic Geologists, Spec Publ* **5**, 91–118.

Malinauskas, A.P., Gooch, J.W. and Redman, J.D. (1970) The interaction of tellurium dioxide and water vapor. *Nucl. Appl. Technol.* **8**, 52-57.

Masson, M.R. (1976) Some equilibrium constants of tellurous acid. *J. Inorg. Nucl. Chem.* **38**, 545-548.

McFarlane, H.C.E. and McFarlane, W. (1973) Studies of tellurium shielding by heteronuclear magnetic double resonance in a representative series of compounds. *J. Chem. Soc., Dalton Trans.* **22**, 2416-2418.

McPhail, D.C. (1995) Thermodynamic properties of aqueous tellurium species between 25 and 350°C. *Geochim. Cosmochim. Acta* **59**, 851-866.

Mei, Y., Sherman, D.M., Liu, W. and Brugger, J. (2013) Complexation of gold in S_3^--rich hydrothermal fluids: evidence from ab-initio molecular dynamics simulations. *Chem. Geol.* **347**, 34–42.

Mills, K.C. (1974) *Thermodynamic data for inorganic sulphides, selenides and tellurides*. Butterworths, London.

Milne, J.B. (1991) Hexachlorotellurate(IV) hydrolysis equilibira in hydrochloric acid. Measurement by Raman and ^{125}Te NMR spectroscopy and a reconsideration of earlier spectrophotometric results. *Can. J. Chem.* **69**, 987-992.

Moynier, F., Fujii, T. and Albarède, F. (2009) Nuclear field shift effect as a possible cause of Te isotopic anomalies in the early solar system - An alternative explanation of Fehr et al. (2006 and 2009). *MeteoritPlanet. Sci,* **44**, 1735–1742.

Nakata, M. and Komuru, K. (2011) Chemistry and occurrences of native tellurium from epithermal gold deposits in Japan. *Resour. Geol.* **61**, 211-223.

Pals, D.W. and Spry, P.G. (2003) Telluride mineralogy of the low-sulfidation epithermal Emperor gold deposit, Vatukoula, Fiji. *Mineral. Petrol.* **79**, 285-307.

Plyasunov, A.V. and Shock, E.L. (2001) Correlation strategy for determining the parameters of the revised Helgeson-Kirkham-Flowers model for aqueous nonelectrolytes. *Geochim. Cosmochim. Acta* **65**, 3879-3900.

Pokrovski, G.S. and Dubrovinsky, L.S. (2011) The S_3^- ion is stable in geological fluids at elevated temperatures. *Science* **331**, 1052-1054.

Pokrovski, G.S., Borisova, A.Y., Roux, J., Hazemann, J.-L., Petdang, A., Tella, M. and Testemale, D. (2006) Antimony speciation in saline hydrothermal fluids: A combined X-ray absorption fine structure spectroscopy and solubility study. *Geochim. Cosmochim. Acta* **70**, 4196-4214.

Pokrovski, G.S., Zakirov, I.V., Roux, J., Testemale, D., Hazemann, J.-L., Bychkov, A.Yu.and Golikova, G.V. (2002) Experimental study of arsenic speciation in vapor phase to 500°C: implications for As transport and fractionation in low-density crustal fluids and volcanic gases. *Geochim. Cosmochim. Acta* **66**, 3453-3480.

Pokrovski, G. S., Roux, J., Ferlat, G., Jonchiere, R., Seitsonen, A. P., Vuilleumier, R. and Hazemann, J.-L. (2012) Silver in geological fluids from in situ X-ray absorption spectroscopy and first-principles molecular dynamics. *Geochim Cosmochim Acta*. http://dx.doi.org/10.1016/j.gca.2012.12.012.

Pudack, C., Halter, W. E., Heinrich, C. A. and Pettke, T. (2009) Evolution of magmatic vapor to gold-rich epithermal liquid: the porphyry to epithermal transition at Nevados de Famatina, Northwest Argentina. *Econ. Geol.* **104**, 449-477.

Ravel, B. andNewville, M. (2005) ATHENA, ARTEMIS, HEPHAESTUS: data analysis for X-ray absorption spectroscopy using IFEFFIT. *J. Synchr. Rad.* **12**, 537-541.

Rehr, J.J., Albers, R.C., and Zabinsky, S.I. (1992) High-order multiple-scattering calculations of x-ray-absorption fine structure. *Phys. Rev. Lett.* **69**, 3397-3400.

Robie, R. A. and Hemingway, B. S. (1995) Thermodynamic properties of minerals and related substances at 298.15 K and 1 bar (10^5 Pascals) pressure and higher temperatures. U.S. Geol. Surv Bull. 2131.

Ruiz-Morales, Y., Schreckenbach, G., and Ziegler, T. (1997) Calculation of ^{125}Te chemical shifts using gauge-ncluding atomic orbitals and density functional heory. *J. Phys. Chem. A* **101**, 4121-4127.

Salomaa, P., Hakala, R., Vesala, S. and Aalto, T. (1969) Solvent deuterium isotope effects on acid-base reactions. III. Relative acidity constants of inorganic oxyacids in light and heavy water. Kinetic applications. *Acta Chem. Scand.* **23**, 2116-2126.

Seward, T.M. (1973) Thio complexes of gold and transport of gold in hydrothermal solutions. *Geochim. Cosmochim. Acta* **37**, 379-399.

Seward, T. M. (1976) The stability of chloride complexes of silver in hydrothermal solutions up to 350°C. *Geochim. Cosmochim. Acta* **40**, 1329-1341.

Shackleton, J.M., Spry, P.G. and Bateman, R. (2003) Telluride mineralogy of the Golden Mile deposit, Kalgoorlie, Western Australia. *Can. Mineral.* **41**, 1503-1524.

Shock, E.L., Sassani, D.C., Willis, M., and Sverjensky, D.A. (1997) Inorganic species in geologic fluids: Correlations among standard molal thermodynamic properties of aqueous ions and hydroxide complexes. *Geochim. Cosmochim. Acta* **61**, 907-950.

Shvarov, Y. V. (1993) UT-HEL: IBM computer code for calculating the HKF revised equation of state parameters for aqueous species. Moscow State University.

Shvarov, Y. and Bastrakov, E. (1999) HCh : a software package for geochemical equilibrium modelling: user's guide, AGSO record. Australian Geol. Surv. Org., Canberra, p. 61.

Siebert, H. (1954) Kraftkonstante und Strukturchemie. V. Struktur der Sauerstoffsäuren. *Z. Anorg. Allg. Chem.* **275**, 225-240.

Simmons, S.F. and Brown, K.L. (2006) Gold in magmatic hydrothermal solutions and the rapid formation of a giant ore deposit. *Science* **314**, 288-291.

Spry, P.G., Foster, F., Truckle, J. and Chadwick, T.H. (1997) The mineralogy of the Golden Sunlight gold-silver telluride deposit, Montana, U.S.A. *Mineral. Petrol.* **59**, 143-164.

Spry, P.G. and Thieben, S.E. (2000) The distribution and recovery of gold in the Golden Sunlight gold-silver telluride deposit, Montana, U.S.A. *Mineral. Mag.* **64**, 31-42.

Strömberg, A., Wahlgren, U. and Lindqvist, O. (1985) A theoretical study of the geometrical properties of tellurite complexes. *Chem. Phys.* **100**, 229-235.

Stryjek, R. and Vera, J.H. (1986). PRSV: an improved Peng-Robinson equation of state for pure compounds and mixtures. *Can. J. Chem. Eng.* **64**, 323-333.

Sung, Y.H., Ciobanu, C.L., Pring, A., Brugger, J., Skinner, W., Cook, N.J. and Nugus, M. (2007) Tellurides from Sunrise Dam gold deposit, Yilgarn Craton, Western Australia: a new occurrence of nagyágite. *Mineral. Petrol.* **91**, 249-270.

Sung, Y.-H., Brugger, J., Ciobanu, C. L. , Pring, A., Skinner, W., Danyushevsky, L. V. and Nugus, M. (2009) Invisible gold in arsenian pyrite and arsenopyrite from a multistage Archaean gold deposit: Sunrise Dam, Eastern Goldfields Province, Western Australia. *Mineral. Depos*. **44**, 765-791.

Tanger, J. C. I. and Helgeson, H. C.(1988) Calculation of the thermodynamic and transport properties of aqueous species at high pressures and temperatures: Revised equations of state for the standard partial molal properties of ions and electrolytes. *Am. J. Sci.* **288**, 19-98.

Tamas, C. G., Bailly, L., Ghergari, L., O'Connor, G. and Minut, A. (2006.) New occurrences of tellurides and argyrodite in Rosia Montana, Apuseni Mountains, Romania, and their metallogenic significance. *Can Mineral.* **44**, 367-383.

Testemale, D., Brugger, J., Liu, W.H., Etschmann, B., and Hazemann, J.L. (2009) In-situ X-ray absorption study of Iron(II) speciation in brines up to supercritical conditions. *Chem. Geol.* **264**, 295-310.

Testemale, D., Hazemann, J.-L., Pokrovski, G.S., Joly, Y., Roux, J., Argoud, R. and Geaymond, O. (2004) Structural and electronic evolution of the $As(OH)_3$ molecule in high temperature aqueous solutions: An X-ray absorption investigation *J. Chem. Phys.* **121**, 8973-8982.

Testemale, D., Pokrovski, G. S. and Hazemann, J. L. (2011) Speciation of As(III) and As(V) in hydrothermal fluids by in situ X-ray absorption spectroscopy. *Europ. J. Mineral.* **23**, 379-390.

Tomkins, A.G., Pattison, D.R.M. and Frost, B.R. (2007) On the initiation of metamorphic sulfide anatexis. *J. Petrol.* **48**, 511-535.

Tooth, B., Brugger, J., Ciobanu, C. and Liu, W. (2008) Modeling of gold scavenging by bismuth melts coexisting with hydrothermal fluids. *Geology* **36**, 815-818.

Tooth, B., Ciobanu, C.L., Green, L., O'Neill, B. and Brugger, J. (2011) Bi-melt formation and gold scavenging from hydrothermal fluids: An experimental study. *Geochim. Cosmochim. Acta* **75**, 5423-5443.

Tossell, J.A. (2012) Calculation of the properties of the S_3^- radical anion and its complexes with Cu^+ in aqueous solution. *Geochim. Cosmochim. Acta* **95**, 79-92.

Usher A., McPhail, D.C. and Brugger, J. (2009) A spectrophotometric study of aqueous Au(III)-halide-hydroxy complexes at 25 ˚C. *Geochim Cosmochim Acta* **73**, 3359-3380.

Voudouris, P., Melfos, V., Spry, P.G., Moritz, R., Papavassiliou, C., Falalakis, G. and Eleftheroglou, T. (2011) Mineralogy and geochemical environment of formation of the Perama Hill high-sulfidation epithermal Au-Ag-Te-S deposit, Petrota Graben, NE Greece. *Mineral. Petrol.* **103**, 79-100.

Wallier, S., Rey, R., Kouzmanov, K., Pettke, T., Heinrich, C.A., Leary, S., O'Connor, G., Tamas, C.G., Vennemann, T. and Ulrich, T. (2006) Magmatic fluids in the breccia-hosted epithermal Au-Ag deposit of Rosia Montana, Romania. *Econ. Geol.* **101**, 923-954.

Wang, P., Anderko, A. and Young, R.D. (2002) A speciation-based model for mixed-solvent electrolyte systems. *Fluid Phase Equilib.* **203**, 141-176.

Wang, P., Springer, R.D., Anderko, A. and Young, R.D. (2004) Modeling phase equilibria and speciation in mixed-solvent electrolyte systems. *Fluid Phase Equilib.* **222–223**, 11-17.

Warren, C.J., Ho, D.M., Bocarsly, A.B. and Haushalter, R.C. (1993) Electrochemical synthesis of a new gold-tellurium polyanion by the cathodic dissolution of a gold telluride ($AuTe_2$) electrode: structure ot telluroaurate ($Au_3Te_4^{3-}$). *J. Amer. Chem Soc.*

Worlton, T.G. and Beyerlein, R.A. (1975) Structure and order parameters in the pressure-induced continuous transition in TeO_2. *Phys. Rev. B* **12**, 1899-1907.

Yamamoto, H., Nasu, H., Matsuoka, J. and Kamiya, K. (1994) X-ray absorption fine structure (XAFS) study on the coordination of Te in $PbO-TiO_2-TeO_2$ glasses with high third-order optical non-linearity. *J. Non-Cryst. Solids* **170**, 87-96.

Yamamoto, T. (2008) Assignment of pre-edge peaks in K-edge x-ray absorption spectra of 3d transition metal compounds: Electric dipole or quadrupole? *X-Ray Spectrometry* **37**, 572-584.

Yerly, F. (2010) Visualiseur/Optimiseur, 2.3.7 ed, Lausanne.

Zezin, D. Y., Migdisov, A. A. and Williams-Jones, A. E. (2011) The solubility of gold in H_2O-H_2S vapour at elevated temperature and pressure. *Geochim. Cosmochim. Acta* **75**, 5140-5153.

Zhang, X. and Spry, P.G. (1994). Calculated stability of aqueous tellurium species, calaverite and hessite at elevated temperatures. *Econ. Geol.* **89**, 1152-1166.

Zhao, J., Xia, F., Pring, A., Brugger, J., Grundler, P.V. and Chen, G. (2010) A novel pre-treatment of calaverite by hydrothermal mineral replacement reactions. *Minerals Eng.* **23**, 451-453.

Zhao, J., Brugger, J., Grundler, P., Xia, F., Chen, G. and Pring, A. (2009). Mechanisms and kinetics of a mineral transformation under hydrothermal conditions: Calaverite to metallic gold. *Am. Mineral* **94**, 1541-1555.

Zhao, J., Brugger, J., Xia, F., Nogthai, Y., Chen, G. and Pring, A. (2013) Dissolution-reprecipitation vs. solid state diffusion: Mechanism of mineral transformations in sylvanite, $(AuAg)_2Te_4$, under hydrothermal conditions. *American Mineralogist.* 98, 19–32, 2013.

Zingaro, R.A. (2006) Polonium: Inorganic Chemistry In Scott, R.A. (Ed.), Encyclopedia of Inorganic Chemistry. John Wiley & Sons, Ltd, New York, p. 8.

APPENDIX D

Table 1. Buffer solutions used for solubility experiments

Buffer/Electrolyte	Concentration (mol kg^{-1})	pH_{mes} 25°C	pH_{calc} 25°C	pH_{calc} 80°C	pH_{calc} 200°C
$HClO_4$	0.509	0.38	0.44	0.45	0.52
$HClO_4$	0.0514	1.42	1.37	1.38	1.42
Sulfate	1.957	-0.50	-0.43	-0.37	-0.04
Sulfate	0.185	0.81	0.79	0.86	0.96
Phosphate	0.369	1.30	1.36	1.53	2.02
Sulfate	0.199	1.73	1.65	2.15	3.58
Phosphate	0.200	2.10	2.13	2.39	3.13
Sulfate	0.199	2.39	2.43	2.99	4.44
Phosphate	0.200	2.97	3.03	3.30	4.06
Acetate	0.199	4.14	4.19	4.27	4.77
Acetate	0.200	4.61	4.65	4.73	5.22
Acetate	0.200	5.53	5.62	5.68	6.16
Phosphate	0.201	6.67	6.62	6.59	7.05
Phosphate	0.201	7.63	7.51	7.47	7.90
Borate	0.200	9.30	9.29	8.90	8.72
Carbonate	0.200	9.84	9.77	9.47	9.42
Ammonium	0.200	9.62	9.35	7.94	5.98
Ammonium/NaCl	0.186/1.074	9.31	9.39	7.97	6.05
Sulfate/NaCl	0.199/0.988	1.34	1.38	1.85	3.10
Phosphate/NaCl	0.200/1.008	1.74	1.99	2.24	3.02
Sulfate/NaCl	0.199/0.997	2.02	2.16	2.70	4.00
Phosphate/NaCl	0.200/1.012	2.62	2.91	3.17	3.97
Acetate/NaCl	0.199/1.001	3.92	4.07	4.13	4.54
Acetate/NaCl	0.200/0.999	4.40	4.61	4.65	5.06
Acetate/NaCl	0.200/0.999	5.36	5.68	5.68	6.08
Phosphate/NaCl	0.201/1.004	6.16	6.35	6.32	6.78
Phosphate/NaCl	0.201/1.001	7.12	7.27	7.24	7.69
Borate/NaCl	0.200/0.999	8.89	9.29	8.66	8.31

Table 2. NMR solutions characteristics

Sample ID	Buffer/electrolyte***	Concentration** (mol kg^{-1})	pH_{mes} 25°C	pH_{calc} 25°C	pH_{calc} 80°C	pH_{calc} 140°C
Te_aq028	$HClO_4$	0.105	0.97	1.06		1.08
Te_aq026	$HClO_4$/$NaClO_4$	0.097 / 0.807	0.82	1.10		1.13
Te_aq040	$HClO_4$	0.913	-0.06	0.11		0.14
Te_aq006	$HClO_4$	0.863	0.13	0.14		0.19
Te_aq046	HOTf	2.615	-0.30	-0.44*		-0.42*
Te_aq030	Sulfate	0.0653	1.33	1.51		1.97
Te_aq044	Phosphate	0.0761	1.73	1.87		2.29
Te_aq032	Sulfate	0.0522	1.72	1.81		2.75
Te_aq050	Sulfate/$NaClO_4$	0.0440 / 0.975	1.64	1.75		2.29
Te_aq037	Sulfate	0.0398	1.71	1.82		2.61
Te_aq020	Sulfate	0.205	2.13	2.25		3.53
Te_aq035	Sulfate	0.0448	1.86	1.95		2.97
Te_aq033	Phosphate	0.0911	2.59	2.74		3.35
Te_aq029	NaOH	1.019	13.6	13.85		11.5
Te_aq024	Phosphate	0.119	11.7	11.5		10.2
Te_aq019	Acetate/NaCl	0.191 / 0.837	4.37	4.60		4.811
Te_aq016	Acetate/NaCl	0.191 / 0.837	4.38	4.60		4.811
Te_aq015	Acetate	0.180	4.67	4.66		4.94
Te_aq043	PIPBS	0.0405	4.75	4.59*		3.86*
Te_aq022	Acetate	0.179	4.62	4.66		4.94
Te_aq031	Acetate/$NaClO_4$	0.0987 / 0.805	4.46	4.49		4.70
Te_aq023	Carbonate	0.0996	9.84	9.88		9.46
Te_aq039	Acetate	0.167	4.61	4.66		4.94
Te_aq047	DESPEN	0.0836	5.62	5.44*		4.31*
Te_aq049	PIPBS/$NaClO_4$	0.0397 / 0.992	4.38	4.50*		3.74*
Te_aq012	TRIS/$NaClO_4$	0.0875 / 0.974	6.18	8.01*		5.97*
Te_aq017	Carbonate/NaCl	0.0944 / 0.838	9.59	9.57		9.17
Te_aq018	Phosphate/NaCl	0.0990 / 0.807	6.27	6.42		6.56
Te_aq048	Carbonate	0.0979	9.56	9.53		9.16
Te_aq021	Phosphate	0.0996	6.75	6.74		6.89
Te_aq027	Borate/$NaClO_4$	0.0986 / 0.0183	8.79	8.82		8.28
Te_aq045	Carbonate	0.0878	9.30	9.35		9.00
Te_aq042	Borate	0.167	9.20	9.27		8.74
Te_aq025	Phosphate	0.0975	7.61	7.69		7.82
Te_aq038	Phosphate/$NaClO_4$	0.0820 / 0.989	6.35	6.82		7.03
Te_aq036	Phosphate	0.0834	6.96	6.93		7.09
Te_aq051	Borate	0.047	9.26	9.28	8.89	
Te_aq052	Carbonate	0.104	9.33	9.52	9.22	
Te_aq053	Phosphate	0.098	11.8	11.94	11.0	
Te_aq054	Carbonate	0.093	9.04	9.37	9.05	
Te_aq055	Borate/$HClO_4$	0.0097/0.018	8.73	8.94	8.67	
Te_aq056	Carbonate /NaCl	0.099/0.797	9.28	9.58	9.28	
Te_aq057	NaOH	0.997	n/a	13.8	12.4	
Te_aq058	Borate/NaCl	0.044/0.915	8.90	8.83	8.70	
Te_aq059	Phosphate	0.096	7.74	7.69	7.66	
Te_aq060	Phosphate /NaCl	0.096/0.715	7.38	7.42	7.39	
Te_aq061	Phosphate/NaCl	0.098/0.626	11.3	11.9	11.0	
Te_aq062	Carbonate /NaCl	0.104/0.856	8.85	9.18	8.89	

* Calculated using Geochemist's Workbench (Bethke, 2007)

** for anions, charge balance is Na^+/H^+

*** HOTf: trifluoromethanesulfonic acid. DESPEN: N,N'-diethyl-N,N'-bis(3-sulfopropyl)ethylenediamine. PIPBS: piperazine-N,N'-bis(2-butanesulfonic acid). TRIS: tris(hydroxymethyl)aminomethane. Heavy water, D_2O, was added (10%) to all NMR samples to allow the instrument to lock and a trace amount of sodium trimethylsilylpropanesulfonate (TMSPS) was added as a reference for chemical shift.

APPENDIX D

Table 3. Solubility and dissociation constants determined from the solubility experiments. Numbers in brackets represent standard deviations. R^2 correspond to linear regression lines plotted in Figure 5.

	pK_S		pK_{a_0}			pK_{a_1}		
	This study	McPhail (2005)	This study	McPhail (2005)	Mason (1976)	This study	McPhail (2005)	Mason (1976)
$\log K_{25°C}$	4.64(0.15)	5.03	2.81(0.20)	2.83	2.8(0.2)	5.18(0.19)	6.38	6.08(0.06)
$\log K_{80°C}$	3.79(0.04)	4.12	2.22(0.09)	2.60		5.95(0.06)	5.99	
$\log K_{200°C}$	2.72(0.05)	2.88†	1.08(0.18)	1.78†		6.63(0.11)	7.00	
$\Delta_r H°_{298°C}$ (kJ mol^{-1})	29.684		27.059			-22.286		
$\Delta_r S°_{298°C}$ (J mol^{-1} K^{-1})	10.9		35.8			-174.9		
R^2	0.9991		0.9926			0.9809		

Notes: pK_{a2} was fixed to 10 at all 3 temperatures during the refinement of solubility data. †Extrapolated (maximum experimental temperature of 80 ˚C).

Table 4. Activity coefficients and other parameters used for the fitting of the potentiometric titration data using eq(7).

T-ID	a_{H_2O}	$\gamma_{H_2TeO_3}$	$\gamma_{HTeO_3^-}$	$\gamma_{TeO_3^{2-}}$	γ_{OH^-}	γ_{H^+}	$\gamma_{ClO_4^-}$	γ_{Na^+}	γ_{HClO_4}	γ_{NaOH}	pK_w	pK_a	pK_b
25-21	0.9692	0.9692	0.6877	0.2007	0.6562	0.8332	0.6877	0.6881	1.00	1.00	14.000	-5	-5
25-15	0.9687	0.9687	0.6876	0.2004	0.6562	0.8351	0.6876	0.6880	1.00	1.00	14.000	-5	-5
60-14	0.9677	0.9677	0.6710	0.1784	0.6576	0.8133	0.6710	0.6708	1.00	1.00	13.041	-5	-5
60-20	0.9684	0.9684	0.6710	0.1790	0.6572	0.8100	0.6710	0.6714	1.00	1.00	13.041	-5	-5
80-22	0.9689	0.9689	0.6597	0.1657	0.6428	0.7917	0.6597	0.6600	1.00	1.00	12.619	-5	-5
80-28	0.9690	0.9690	0.6598	0.1658	0.6427	0.7913	0.6598	0.6602	1.00	1.00	12.619	-5	-5

Table 5. Dissociation constants pK_{a2} from potentiometric titrations (curves shown on Figure 5) and enthalpies and entropies for $H_3TeO_3^+$ derived from the T dependence.

T (°C)	This Study	McPhail (2005)	Masson (1976)
25.0	10.02 ± 0.01	9.56	9.56(0.02)
25.0	10.08 ± 0.01		
60.0	9.91 ± 0.01		
60.0	9.78 ± 0.01		
80.0	9.67 ± 0.03	10.59	
80.0	9.66 ± 0.01		
$\Delta_r H°_{298}$ (kJ mol^{-1})	13.730 ± 2.1		
$\Delta_r S°_{298}$ (J mol^{-1} K^{-1})	-146.6 ± 6.5		
R^2	0.89		

Table 6. Parameters from ^{125}Te NMR titration. Numbers in brackets represent standard deviations from the Least Squares fit.

	80 °C, 1 bar		140 °C, 3.6 bar	
$\delta_{H_3TeO_3^+}$ (ppm)			1609	(6)
$\delta_{H_2TeO_3}$ (ppm)			1745	(5)
$\delta_{HTeO_3^-}$ (ppm)	1795	(2)	1802	(11)
$\delta_{TeO_3^{2-}}$ (ppm)	1747	(2)	1733	(10)
pK_{a_0}			2.56	(0.1)
pK_{a_1}			6.67	(0.4)
pK_{a_2}	9.96	(0.1)	9.76	(0.3)

Table 7. Thermodynamic parameters at standard conditions from linear regression of the solubility, NMR and potentiometric data.

	Log K_s TeO_2(s) + H_2O = **H_2TeO_3(aq)**	Log K_{a0} **$H_3TeO_3^+$** = H_2TeO_3(aq) + H^+	Log K_{a1} H_2TeO_3(aq) = **$HTeO_3^-$** + H^+	Log K_{a2} $HTeO_3^-$ = **TeO_3^{2-}** + H^+
pK_{298}	4.63	2.87	5.25	10.02
$\Delta_rG°_{298}$ (kJ mol^{-1}) *	26.430	16.384	29.925	57.143
$\Delta_rH°_{298}$ (kJ mol^{-1})	29.684±0.9	27.059±2	-24.323±5	7.580±3
$\Delta_rS°_{298}$ (J mol^{-1} K^{-1})	10.9±3	35.8±7	-182.0±13	-166.3±9
$\Delta_fG°_{298}$ (kJ mol^{-1}) *	**-480.292**	**-496.676**	**-450.367**	**-393.224**
$\Delta_fH°_{298}$ (kJ mol^{-1}) *	**-579.569**	**-606.628**	**-603.891**	**-596.311**
$S°_{298}$ (J mol^{-1} K^{-1})	**155**	**119**	**-27**	**-193**
$\Delta_fG°_{298}$ (kJ mol^{-1}) (McPhail, 1995)	**-474.6**	**-490.7**	**-438.2**	**-384**

K_{a0} value from NMR excluded from the evaluation. $\Delta_fG°_{298}$, $\Delta_fH°_{298}$ and $S°_{298}$ for H_2O(l) and TeO_2(s) taken from the compilation by Barin (1995) (-237.141, -285.830 kJ mol^{-1} & 69.95 J mol^{-1} K^{-1}, resp. -269.581, -323.423 kJ mol^{-1} & 74.057 J mol^{-1} K^{-1}). $\Delta_fG°_{298}$(H^+(aq)) = 0 by convention. *Note that the number of significant figures does not reflect the accuracy.

APPENDIX D

Table 8. Parameters for extrapolating thermodynamic properties of Te(IV) species to high temperature and pressure.

	$HTeO_3^-$ †		**$H_2TeO_3(aq)$ ***	**$H_3TeO_3^+$ ***	**TeO_3^{2-} ***
$^a\Delta_fG°_{298}$	-450.567 kJ mol^{-1}	$pK_{298°C}$	5.225	8.012	-10.068
$S°_{298}$	-27.1 J mol^{-1} K^{-1}	A	-0.182	-0.151	0.148
c1	309.44697 J mol^{-1} K^{-1}	B	729.5	595.9	-591.2
c2 10^{-4}	-104.603 J mol^{-1} K^{-1}				
ω 10^{-5}	4.1581 J/mol				

† The modified Helgeson-Kirkham-Flowers (HKF) equation of state parameters (Tanger and Helgeson, 1988).

- **Ryzhenko-Bryzgalin parameters (Borisov and Shvarov, 1992).**

Table 9. Results for the solubility of Te(IV) in H_2O(g). Density (ρ_w), and fugacity (f_w) of water were calculated with the OLI SteamAnalyzer software below the critical point and above with the HCh software. The fugacity of Te (f_{Te}) is the product of mole fraction (χ_{Te}) and total pressure.

T (°C)	P_{tot} (bar)	log(χ_{Te})	log(ρ_w)	f_w	$f_{Te} \times 10^5$
170±1	1	-8.13	-3.308	0.9936	7.41 10^{-4}
170±1	1	-7.94	-3.308	0.9936	1.14 10^{-3}
317±2	105±5	-7.092	-1.238	80.27	0.8498
315±2	100±5	-7.159	-1.269	77.31	0.6940
315±2	100±5	-7.064	-1.269	77.31	0.8634
385±2	240±5	-4.765	-0.656	155.96	412.5
385±2	240±5	-4.166	-0.656	155.96	1639
385±2	238±5	-5.046	-0.656	155.23	213.9
385±2	238±5	-5.086	-0.656	155.23	195.4
385±2	230±5	-5.277	-0.757	153.34	121.6
381±2	205±5	-5.075	-0.895	142.72	172.4
383±2	187±5	-5.070	-0.991	136.57	159.3
382±2	170±5	-5.343	-1.070	127.81	77.2

Table 10. Thermodynamic properties for Te(IV) gaseous species.

	$TeO_2(s)$	$TeO_2(g)$	$TeO_2 \cdot H_2O(g)$	$TeO_2 \cdot 2H_2O(g)$
$\Delta_f G^0$ [J/mol]	-269581	-65482	-363451	-497859
S^0 [J/mol/K]	74.057	274.998	504.26	1293.47
V0 [J/bar]	2.85			
Cp function	0.9817 -1.089×10^{-2} T -3.702×10^{3} T^{-2} -5.495×10^{2} $T^{-0.5}$ + 9.375×10^{-6} T^2	98.53 -3.165×10^{-2}T -4.29×10^{5} T^{-2} -746.8 $T^{-0.5}$ $+ 1.615\times10^{-5}$ T^2 -2.97×10^{-9} T^3	-3.94814×10^{2} + 0.64663 T + 4 .8926$\times10^{-2}$ T^{-2}	-2.26437×10^{3} + 3.03995 T
Data sources	Barin (1995)	Barin (1995)	This study	This study

Table 11. XAS sample specifications

Sample ID	**Measurement conditions**	**Facility**	**Composition**	**$pH_{25^\circ C}$**
Sol1	ambient	APS	0.055 m TeO_2 in 1 m NaOH	>10
Sol2	ambient	ESRF	0.45 m TeO_2 in 1.2 m NaOH	>10
Sol3	ambient	APS	0.025 m TeO_2in borate buffer	9.24
Sol4	800 b, 30-503 °C	ESRF	*TeO_2(tet) in HSO_4^-/SO_4^{2-} buffer	1.56
Sol5	800 b, 30-409 °C	ESRF	*TeO_2(tet) in $H_2PO_4^-/HPO_4^{2-}$ buffer	6.72
Sol6	800 b, 30-503 °C	ESRF	*TeO_2(tet) in $H_3PO_4/H_2PO_4^-$ buffer	2.01
Sol7	ambient	APS	0.011 m TeO_2 in 5 m $HClO_4$	<0
Sol8	ambient	APS	0.024 m TeO_2 in 9.9 m $HClO_4$	<0

* Solubility experiment.

Table 12. EXAFS refinement parameters

Sample ID, T	**Ligand**	**n**	**R (Å)**	**σ^2**	**E0**	**χ^2_{red}**	**R-factor**	**k-weighting**	**k-range**	**R-range**
Sol1, 25 ˚C	O	3 (fix)	1.83(2)	0.008(2)	8(2)	1186	0.031	1,2,3	2-10	1-3
Sol8, 25 ˚C	O	3 (fix)	1.90(1)	0.0005(14)*	10.00(1)	1186	0.031	1,2,3	2-10	1-3
Sol2, 25 ˚C	O	3 (fix)	1.873(7)	0.0018(6)	10.8(8)	1186	0.031	1,2,3	2-12	1-3
Sol 4, 100 ˚C	O	3 (fix)	1.91(2)	0.001 (fix)	10(3)	86	0.048	1,2,3	2-10	1-3
Sol4, 220 ˚C	O	3 (fix)	1.89(2)	0.002(1)	10(2)	39	0.016	1,2	2-10	1-2.5
Sol4, 480 ˚C	O	3 (fix)	1.88(3)	0.005(2)	10(4)	39	0.016	1,2	2-10	1-2.5

Table 13. Thermodynamic properties recommended in this study.

Reaction	**Temperature [˚C]**									**Reference**
	25	50	60	100	150	200	250	300	350	
Aqueous species										
$H_3TeO_3^+ = H_2TeO_3(aq)+H^+$ ($\log K_{a0}$)	-2.79	-2.43	-2.31	-1.88	-1.46	-1.14	-0.87	-0.62	-0.32	This study
$H_2TeO_3(aq) = HTeO_3^-+H^+$ ($\log K_{a1}$)	-5.22	-5.57	-5.69	-6.07	-6.39	-6.61	-6.84	-7.17	-7.98	This study
$HTeO_3^- = TeO_3^{2-} + H^+$ ($\log K_{a2}$)	-10.07	-9.89	-9.83	-9.58	-9.29	-9.04	-8.86	-8.84	-9.25	This study
Minerals										
$Te(s) + H_2O(l) + O_2(g) = H_2TeO_3(aq)$	42.62	38.64	37.21	32.26	27.38	23.54	20.48	18.04	16.23	*
$TeO_2(s)+H_2O(l) = H_2TeO_3(aq)$ ($\log K_s$)	-4.61	-4.21	-4.07	-3.59	-3.14	-2.77	-2.44	-2.07	-1.53	This study
Calaverite+$1.5H_2O+2.25O_2(aq)+H^+ = 2H_2TeO_3(aq)+Au^+$	80.92	74.30	71.89	63.39	54.75	47.74	41.95	37.10	32.99	Mills (1974)
Hessite + $2 H^+ + 1.5 O_2(aq) = 2 Ag^+ + H_2TeO_3(aq)$	54.17	49.89	48.34	42.90	37.44	33.07	29.48	26.47	23.85	Mills (1974); Afifi et al. (1988)
Petzite+$4 H^+ + 3 O_{2(g)} = 3 Ag^+ + Au^+ + 2 H_2TeO_3(aq)$	95.5	88.0	85.2	75.7	66.0	58.1	51.6	46.0	-	Echmaeva and Osadchii, 2009
Gaseous species										
$H_2TeO_3(aq) = TeO_2(g)+H_2O(l)$	-31.14	-27.97	-26.84	-22.90	-19.02	-15.97	-13.55	-11.65	-10.29	Barin (1995)
$H_2TeO_3(aq)=TeO_2(H_2O)(g)$	-20.49	-17.55	-16.52	-13.09	-9.90	-7.56	-5.83	-4.58	-3.81	This study
$H_2TeO_3(aq)+H_2O(l)=TeO_2\cdot 2(H_2O)(g)$	-38.49	-31.45	-29.06	-21.35	-14.73	-10.30	-7.31	-5.31	-4.14	This study

* Tellurium(s) properties from Robie and Hemingway (1995).

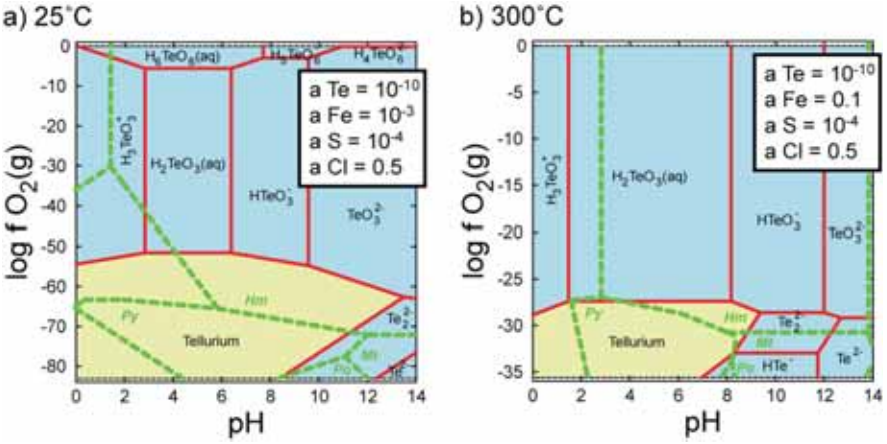

Figure 1. Solubility of native tellurium and predominance fields of aqueous Te species as a function of pH and oxygen fugacity at 25 ˚C and 300 ˚C and water-saturated pressures, using thermodynamic properties collected by McPhail (2005).

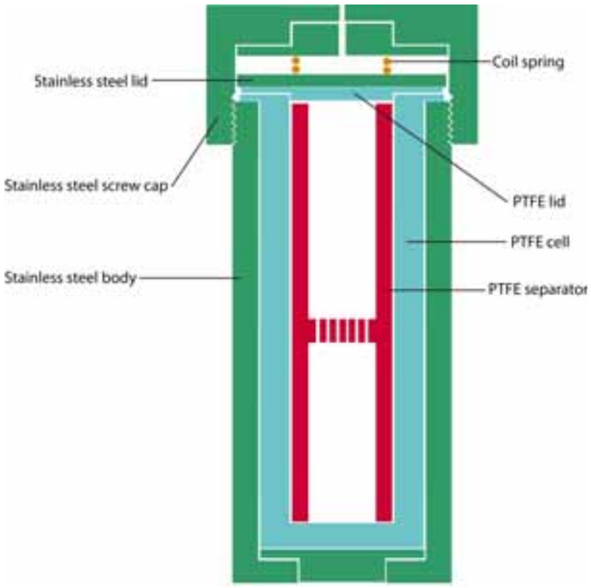

Figure 2. Schematic section (not to scale) through the PTFE-stainless steel cell used for the solubility experiments at 200 °C. Total height 12 cm, outside diameter of the body 5 cm, inner volume 15 ml. The inside is divided in two compartments by a separator with an H shaped longitudinal section. Holes (0.5-1 mm) drilled through the horizontal plate allow the solution to pass from one compartment to the other when the cell is turned up side down. The solid piece of TeO_2 remains on one side and thus can be separated from the solution once equilibrium is reached and before the cell is cooled down.

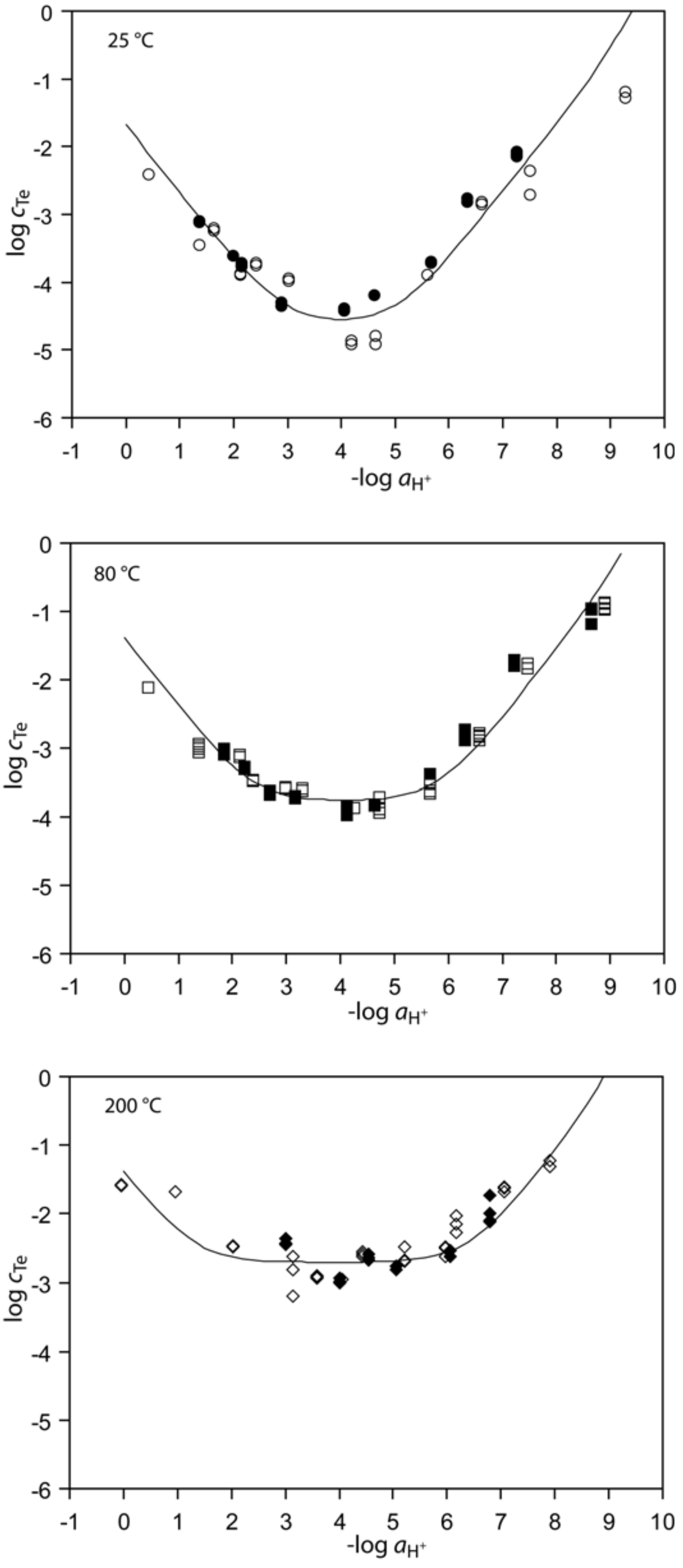

Figure 3. Solubility of TeO_2 as a function of pH at three different temperatures (25, 80 and 200 °C). Solid symbols correspond to solutions where NaCl was added. Curves corresponds to solubility at I = 1 m using equation (6) with the activity coefficients listed in Table A4 (appendix).

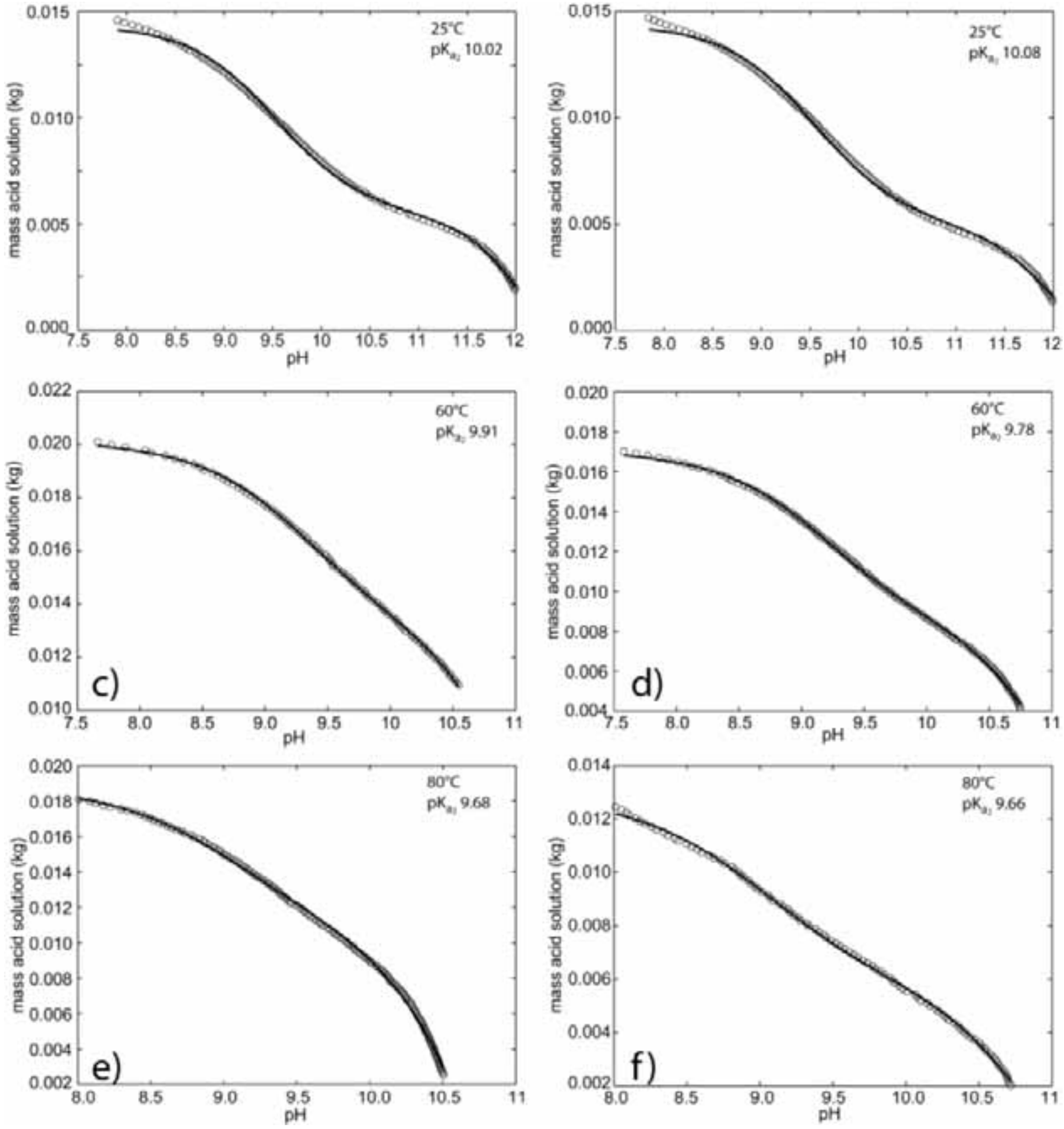

Figure 4. Potentiometric titration curves at different temperatures of solutions of TeO_2 in NaOH with perchloric acid and $NaClO_4$ as background electrolyte. Open circles represent experimental data, solid lines are best fit according to eq (7).

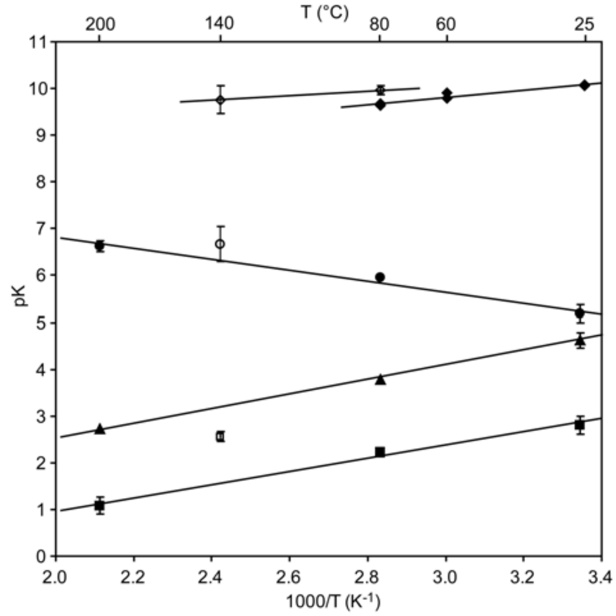

Figure 5. Plot of pK vs the reciprocal temperature. From solubility determination ■ pK_{a0}, ▲ pK_s, ● pK_{a1}; from potentiometry ◆ pK_{a2}; from NMR □ pK_{a0}, ○ pK_{a1}, ◇ pK_{a2}. Lines represent linear regressions (NMR data points for pK_{a0} and pK_{a1} not included).

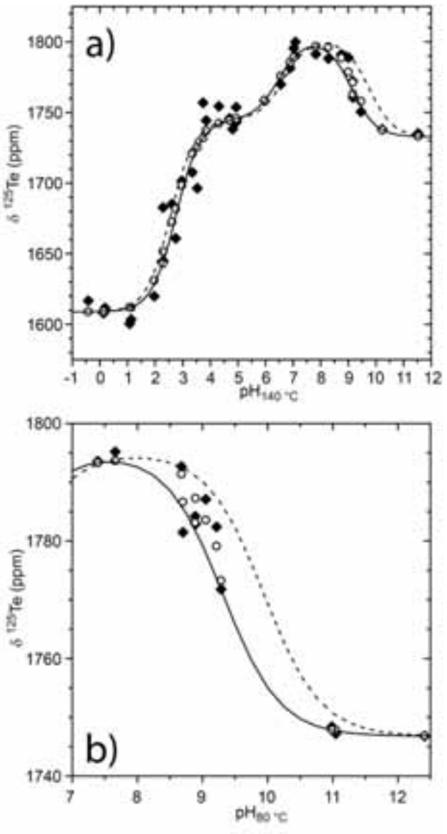

Figure 6. ^{125}Te NMR chemical shifts as a function of pH. Black diamonds experimental points, open circles calculated points using parameters from best fit according to eq (10). Solid line best fit at I = 1 m, and dashed line best fit at I ~0 m. a) at 140°C b) at 80°C.

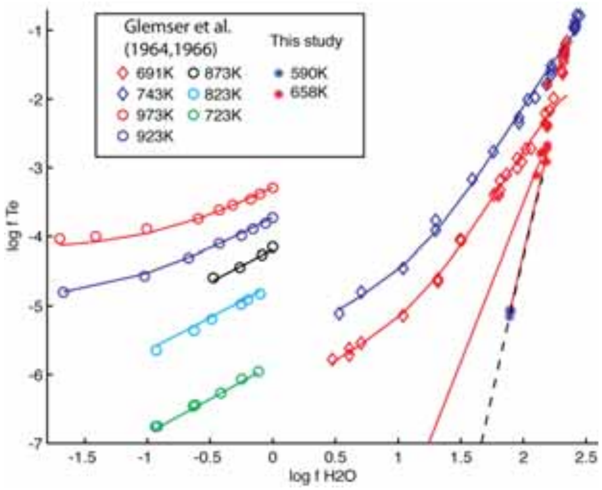

Figure 7. Activity-activity diagram for Te(IV) hydroxides in steam. Except for the vapor saturation curve (black dashed line), all lines represents isotherms and were calculated using eqs (13) to (16) and the parameters listed in Table 10. Open circles correspond to data from Glemser et al. (1964; 1966), other points this study.

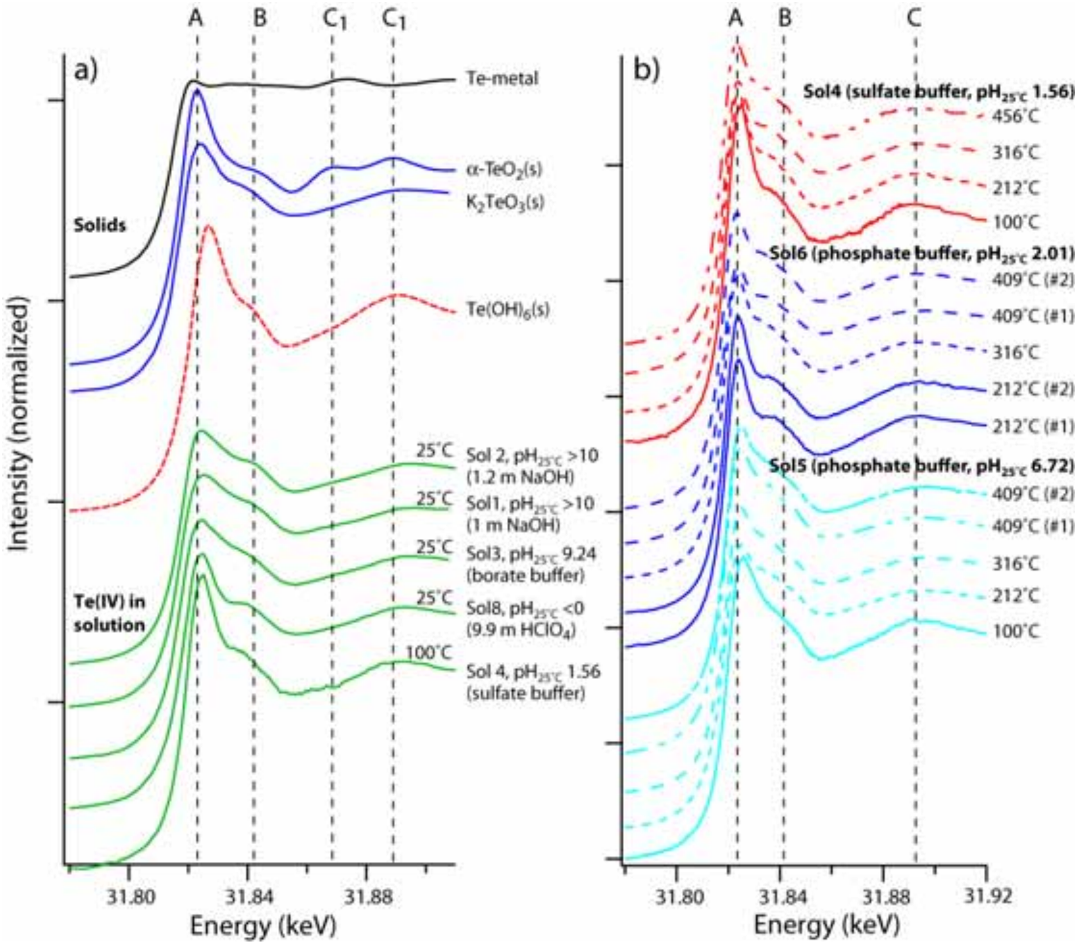

Figure 8. Te K-edge XANES data on standards and solutions. (a) XANES spectra from standards and some selected solutions; (b) Effect of temperature on XANES spectra. A, B, C define the centroids of the main peaks; see section 4.3.1 in the text.

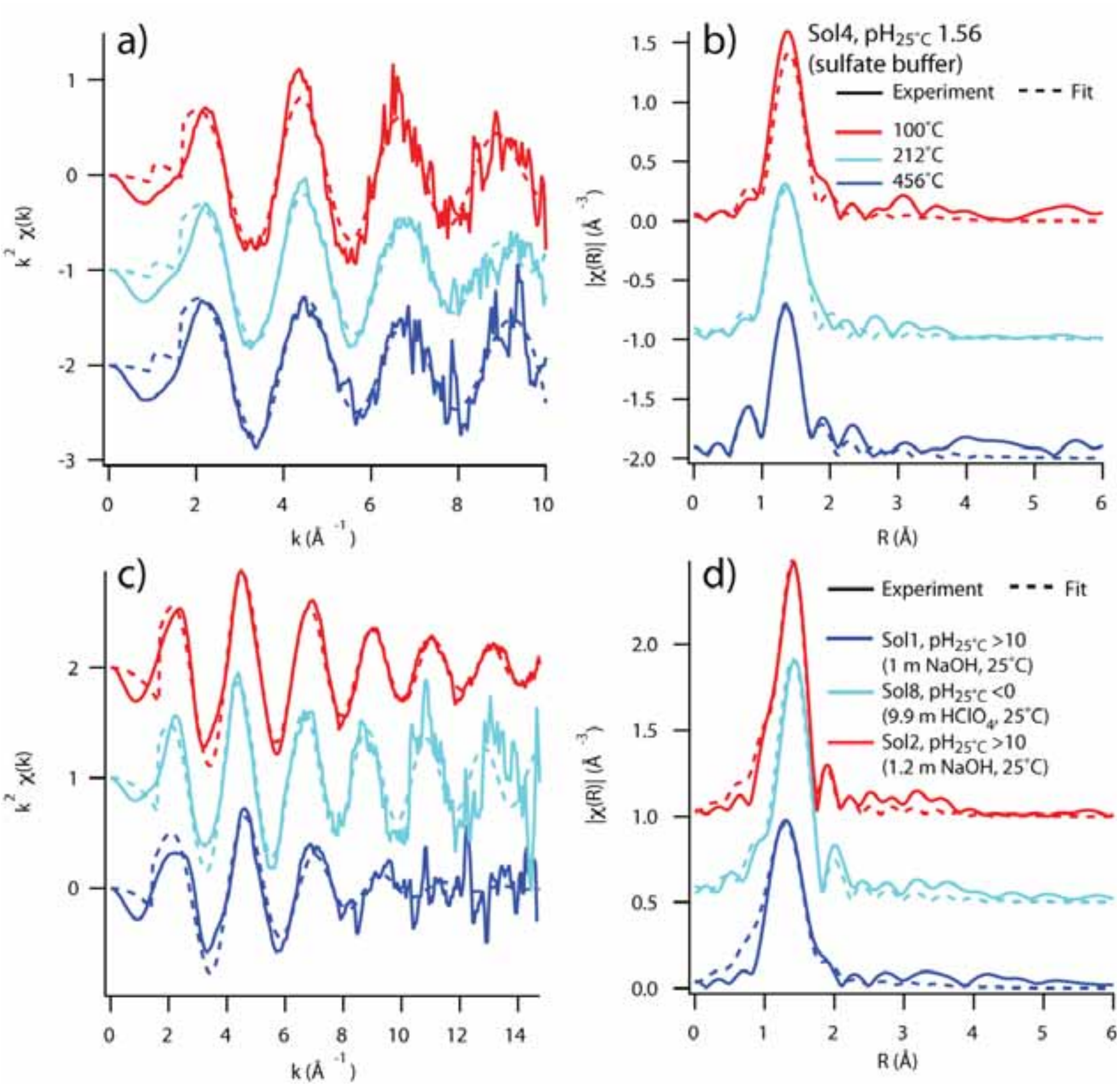

Figure 9. Te K-edge EXAFS spectra of Te(IV)-bearing solutions; only the fits with three equidistant oxygens are shown (Table 12). (a,b) Sol4 (TeO_2 in sulfate buffer, pH$_{25°C}$ ~ 1.56) at selected temperatures, 800 bar, shown in k-space (a) and R-space (b). (c,d) Room temperature spectra of Te(IV) in highly acidic and highly basic solutions, shown in k-space (c) and R-space (d).

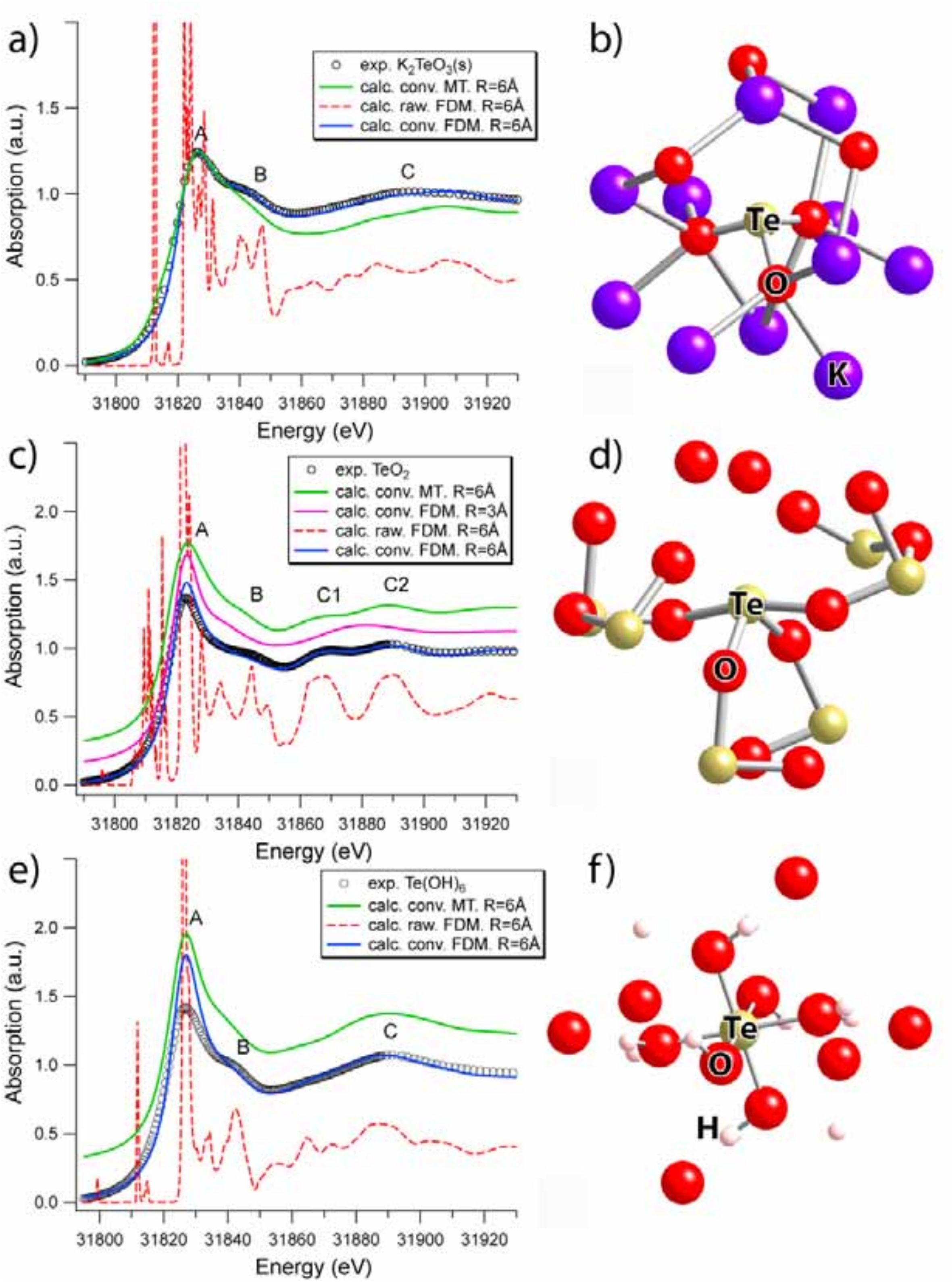

Figure 10. Te K-edge XANES calculations on selected standards: K_2TeO_3(s) (a,b), TeO_2(s) (c,d) and $Te(OH)_6$(s) (e,f). (a,c,e) Measured and calculated spectra; (b,d,f) local structure within a 6 Å distance from the central Te atom.

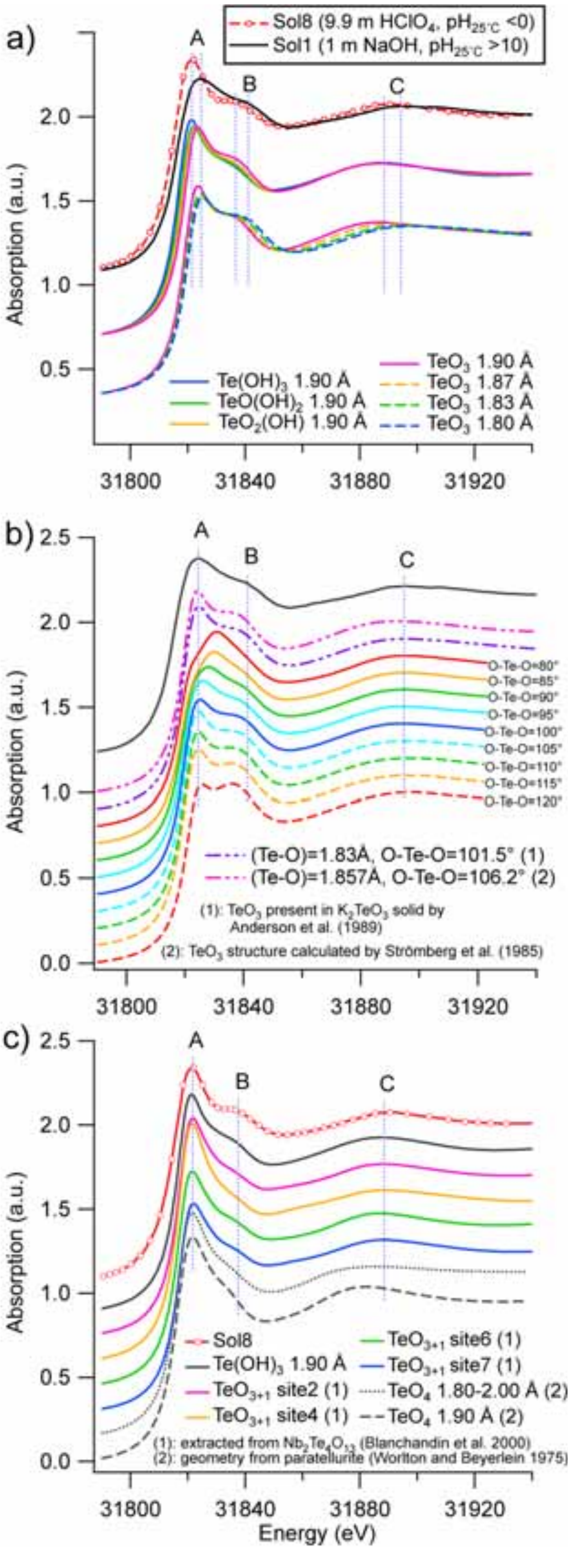

Figure 11. Te K-edge XANES calculations on for selected aqueous complexes: a) effect of deprotonation and bond length contraction in K edge, b) basic solution with various O-Te-O angles, c) acid solution with different Te models.

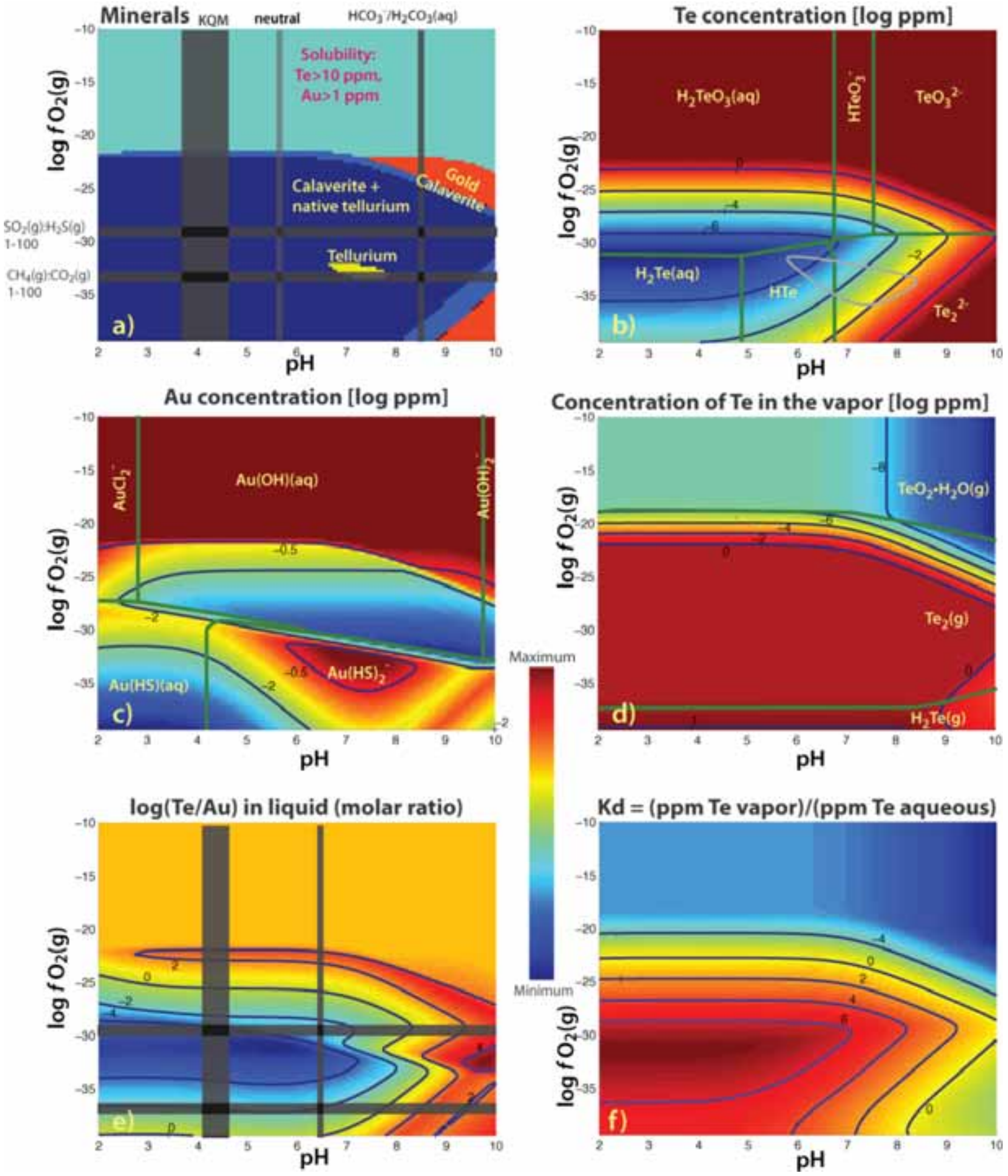

Figure 12. Calculations of the speciation and solubility of Te and Au in the brine and vapor for the system Au-Te-H_2O-S-Cl at 300 ˚C at vapor saturation pressure (85.8 bar). The diagrams are based on full chemical speciation calculations for a closed system with the following composition: 1 molal Cl^-, 10 ppm Te, 1 ppm Au, and 0.1 molal S. KQM: K-feldspar-quartz-muscovite buffer, for aK^+ 1 to 0.1. The grey line in (B) is the 0.320 ($10^{-0.5}$) ppm contour for gold.

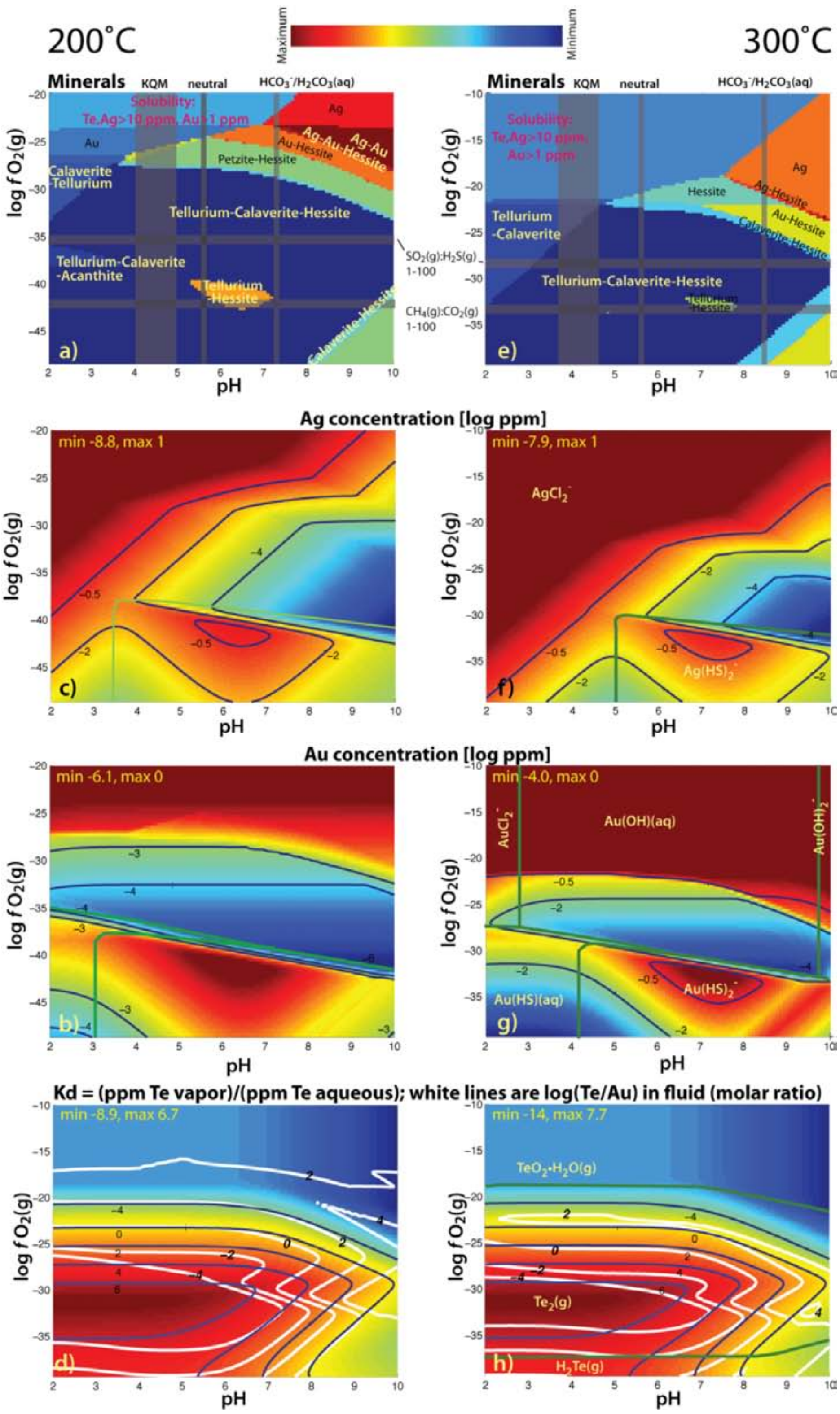

Figure 13. Calculations of the speciation and solubility of Ag and Au in the brine and vapor for the system Ag-Au-Te-H_2O-S-Cl at 200 ˚C and 300 ˚C at vapor saturation pressure. The diagrams are based on full chemical speciation calculations for a closed system with the following composition: 1 molal Cl^-, 10 ppm Te, 10 ppm Ag, 1 ppm Au, and 0.1 molal S. KQM: K-feldspar-quartz-muscovite buffer, for aK^+ 1 to 0.1.